



ScuDo
Scuola di Dottorato ~ Doctoral School
WHAT YOU ARE, TAKES YOU FAR



Doctoral Dissertation
Doctoral Program in Civil and Environmental Engineering (33.th cycle)

Computational Wind Engineering Simulations for the Design of Sand Mitigation Measures around Railway Tracks

Marko Horvat

* * * * *

Supervisors

Prof. L.Bruno, Supervisor
dr. sc. S.Khris, Co-supervisor

Politecnico di Torino
December 18th, 2020

This thesis is licensed under a Creative Commons License, Attribution - Noncommercial-NoDerivative Works 4.0 International: see www.creativecommons.org. The text may be reproduced for non-commercial purposes, provided that credit is given to the original author.

I hereby declare that, the contents and organization of this dissertation constitute my own original work which does not compromise in any way the rights of third parties, including those relating to the security of personal data. This Thesis will be subjected to a three-year-long embargo to protect innovative results of industrial interests. The Reviewers and Jury members are subjected to a Non-Disclosure commitment.

.....
Marko Horvat
Turin, December 18th, 2020

Summary

The engineering interest about the windblown sand has been significantly growing in the last years. The large ongoing infrastructure projects in deserts require robust, cost-effective and high-performance solutions. This PhD Thesis deals with the application of the general Computational Wind Engineering design approach to developing new, innovative Sand Mitigation Measure (SMM) employed to protect desert railways. The Thesis is developed within the H2020-MSCA-ITN-2016 "*Sand Mitigation along Railway Tracks*" (SMaRT) European project under the Grant Agreement No 721798.

The scientifically based problem setting, design framework and the quantitative assessment of the sand mitigation measures are, at the present time, not sufficiently developed in the literature. The Thesis, at first, introduces an exhaustive problem setting in the form of the innovative classification of the problems sand is causing around railways, analogously to equivalent actions in civil engineering. Sand Serviceability Limit States involve railway partial loss of capacity and passenger discomfort. Conversely, Sand Ultimate Limit States involve service interruption and passengers unsafe conditions. Additionally, the new classification of sand mitigation measures is introduced, based on their relative position to the railway infrastructure and their working principle. Source-Path-Receiver categorization follows. The classifications are introduced to provide an orienting framework for the research and design activities within the Thesis.

Two innovative sand mitigation measures are developed. At first, the Path SMM called *Shield for Sand* is optimized in the sense of minimizing the cost-to-performance ratio with the Gradient-based and Genetic algorithm models. Additionally, an innovative Receiver SMM, called *Sand Blower* is designed from scratch. For the design, a deeper insight into the aerodynamic behavior of unmitigated railway systems is necessary. Therefore, a detailed numerical sensitivity analysis is carried out by varying the geometric parameters of the railway substructure, comprising of ballast and embankment. Moreover, typical conventional and non-conventional superstructure systems are tested. In particular, standard rails, tubular tracks, humped sleepers, and humped slab are considered. From the mentioned, humped sleepers applied on the most gentle ballast and embankment show the most promising results. In the light of this, the *Sand Blower* has been designed, applied

to that railway system.

This Thesis develops through the following chapters according to the objective methods and the applications mentioned above. The introduction to the study is presented in **Chapter 1**.

Chapter 2 is devoted to the state of art. In particular, this chapter starts with the definition of the sand action in analogy to other actions in civil engineering. After, the thorough description of the innovative classifications of sand limit states and the sand mitigation measures are given. The chapter finishes with the best practices and guidelines on sand mitigation strategy.

The description of the mathematical and numerical methods is given in **Chapter 3**. Briefly, the mathematical aspects of the Navier-Stokes equations are complemented by their numerical discretization in Finite Volume Method (FVM). The second part of the chapter deals with the description of Gradient-based optimization and the Genetic algorithm.

In **Chapter 4**, the design process of innovative sand mitigation measure *Shield for Sand* is given. The conceptual and preliminary design are briefly tackled, due to the fact they are not developed within the Thesis. They are followed by the detailed description of detailed design, optimization process and the verification of the optimized geometry by the higher fidelity numerical model.

Chapter 5 is devoted to the investigation of the aerodynamics of the unmitigated railway systems in the form of a thorough sensitivity study of both substructure and superstructure. The best performing combination is used in the conceptual and preliminary design of the *Sand Blower*.

In the final chapter, the conclusions and the future perspectives are detailed and critically discussed.

The Thesis aims at providing original contributions on four specific aspects. First, the innovative classification of sand limit states and sand mitigation measures is proposed to ground the design framework under which new mitigation measures can be designed in rationale-based approach. Previously, the most commonly adopted approach in sand mitigation has been an iterative heuristic approach based on trials and errors. Second, each individual stage of the design is covered by the application of the framework on two innovative sand mitigation measures. Third, a wide computational study of unmitigated railway systems is given, which is essential in the design of Receiver sand mitigation measures. Fourth, quantification of the aerodynamic performance is estimated by introducing the performance metrics based on the single-phase wind flow, to meet the engineering requirements during the early stages of the design process.

Acknowledgements

I would like to sincerely thank my supervisors for continuous support during the research. I thank prof. Luca Bruno for his guidance and dedication he showed throughout the PhD. I would also like to thank Dr. Sami Khris for everything I have learned from him about the numerical approaches and their industrial worth. The research for the Thesis has been carried out within the project: “Sand Mitigation around Railway Tracks” (SMaRT). I would like to express my gratitude to the key people of the project. In particular, prof. Giles Wiggs from Oxford University for the opportunity to familiarize myself with the topic of Geomorphology. Dr. Nicolas Coste and Dr. Eric Delboulbe for all the effort and time provided to me during the industrial secondment at Optiflow Company. Prof. Luigi Preziosi from Politecnico di Torino for showing me the details of multiphase flows from mathematical point of view. For every contribution to my Thesis, I would like to thank my colleagues Dr. Lorenzo Raffaele, Roberto Nuca, Ciaran Nash and Dr. Andrea Lo Giudice.

The SMaRT project was conducted in the framework of Marie Skłodowska-Curie Actions (MSCA), Innovative Training Networks (ITN), European Industrial Doctorate (EID), call H2020-MSCA-ITN-2016 (www.smart-eid.eu). The project received funding from the European Union Horizon 2020 research and innovation program under the Grant Agreement No 721798. The special mention deserve the industrial partner organizations Ansaldo STS, Astaldi, and Salcef group, whose contribution is highly appreciated.

Computational resources, without which the research would not have been possible, were provided by Optiflow Company and HPC@POLITO, a project of Academic Computing within the Department of Control and Computer Engineering at Politecnico di Torino (<http://www.hpc.polito.it>).

I would like to express my sincere gratitude to the reviewers of the thesis, prof. Hrvoje Jasak and prof. Gianni Bartoli. Their remarks significantly improved the quality of the Thesis.

Contents

List of Tables	X
List of Figures	XI
Abbreviations	XIX
Nomenclature	XXI
1 Introduction	1
1.1 Desert Railway Overview	3
1.1.1 Past Railways across Deserts	3
1.1.2 Present Railways across Deserts	4
1.1.3 Future Railways across Deserts	6
1.2 General Design Framework	6
2 Windblown Sand Effects on Railways: State of Art	11
2.1 Sand Action	11
2.2 Windblown Sand Limit States	14
2.2.1 Sand Ultimate Limit States	15
2.2.2 Sand Serviceability Limit States	17
2.3 Windblown Sand Mitigation Measures	22
2.3.1 SMM Categorization Criteria in the Literature	22
2.3.2 Sand Mitigation Measure Categorization: the New Proposal	23
2.3.3 Source Sand Mitigation Measures	26
2.3.4 Path Sand Mitigation Measure	31
2.3.5 Receiver Sand Mitigation Measures	41
3 Methods	47
3.1 Computational Approaches in Turbulent Flows	47
3.2 Mathematical Model	48
3.2.1 Mass Conservation	49
3.2.2 Momentum Conservation	49
3.2.3 Energy Conservation	51

3.2.4	Constitutive Laws	51
3.2.5	Turbulence Modelling	51
3.2.6	Initial and Boundary Conditions	56
3.3	Finite Volume Method	57
3.3.1	Discretization of the Convective Term	58
3.3.2	Discretization of the Diffusion Term	59
3.3.3	Discretization of the Source/Sink Term	60
3.3.4	Interpolation Schemes	60
3.3.5	Discretization of the Temporal Derivative Term	62
3.4	Optimization Approach	62
3.4.1	General Work-Flow of Aerodynamic Optimization	63
3.4.2	Gradient-Based Optimization	64
3.4.3	Genetic Algorithm Optimization	64
3.4.4	Aerodynamic Optimization in Civil Engineering: an Overview	65
3.5	Computational Wind Engineering and Wind Tunnel Testing in Rail- way Aerodynamics: an Overview	67
4	Computationally-Based Design of Innovative Path Sand Mitiga- tion Measures	73
4.1	Conceptual and Preliminary Design of <i>Shield for Sand</i>	73
4.1.1	Detailed Design and Optimization Setup	75
4.2	Specific Computational Approach	79
4.3	Preliminary Sensitivity Study	82
4.3.1	Preliminary Sensitivity Study for the One-Panel Deflector	82
4.3.2	Preliminary Sensitivity Study for the Two-Panel Deflector	89
4.4	Optimization	92
5	Computationally-Based Design of Innovative Receiver Sand Miti- gation Measures	97
5.1	Field Evidences of Sand Sedimentation Patterns around Railways	97
5.2	Setup of the Study	101
5.2.1	Railway Systems	101
5.2.2	Setup of the Vanes	103
5.2.3	Specific Computational Approach	103
5.2.4	Incoming Wind Flow and Sand Features	106
5.3	Generation of the Numerical Grids	107
5.4	Results	108
5.4.1	Unmitigated Railway Systems	108
5.4.2	Preliminary Design of the Receiver Sand Mitigation Measure	127
5.4.3	Final Performance Assessment of the Receiver Sand Mitiga- tion Measure	135

5.4.4	Performance Assessment of the Receiver Sand Mitigation Measure under Yawed Winds	139
6	Conclusion	145
6.1	Outlines of Path SMMs	146
6.2	Outlines of Receiver SMMs	147
	Bibliography	151

List of Tables

2.1	Correlation between types of mitigation measure and sand moving processes.	25
2.2	Correlation between types of mitigation measure and Sand Limit States.	25
5.1	Synopsis of conventional and non-conventional railway systems. . .	101

List of Figures

1.1	General sand-induced problems: a) pipeline in desert (explicit publishing permission from the owner of the photo: gordontour@Flickr), b) invading sand dunes in front of a city [reprinted from: 190, with the permission from Elsevier], c) encroached single building (explicit publishing permission from the owner of the photo: Nouar Boulghobra), d) sand-invaded palm plantation (explicit publishing permission from the owner of the photo: Nouar Boulghobra), e) sand covered road (explicit publishing permission from the owner of the photo: Yann Arthus-Bertrand), f) railway in desert (courtesy of Astaldi).	2
1.2	a) Number of cited references classified by the year of publication, b) classification of references according to the research area, c) increasing trend of filed patents through years.	2
1.3	Grasplatz railway station along the Aus to Lüderitz railway before (a) and after (b) sand dune encroaching (permission to reuse under a Creative Commons Attribution License; owner of the photos: Klaus Dierks [68]).	4
1.4	Historical railways.	5
1.5	Map of currently in service, under construction, and proposed railways.	7
1.6	Scheme of the computationally-based SMM design.	7
2.1	a) Scheme of the sand transport modes [redrawn from: 191], b) wind-sand interaction in saltation.	12
2.2	Sand rose of Drift Potential (DP)s and Resultant Drift Potential (RDP) [redrawn from: 90].	13
2.3	Framework scheme of the safety standards.	14

2.4	Sand Ultimate Limit States. Civil works: a) full sand coverage by an encroaching dune (explicit publishing permission from the owner of the photo: Giles Wiggs), b) partial sand coverage by the sand blown from a sandy plane. Track superstructure: c) jammed turnout, d) detail of the sand accumulation in the gap. Rolling stock: e) running train derailment [reprinted from: 242, with the permission from the editor], f) train window breaking [reprinted from: 52, with the permission from Elsevier].	16
2.5	Sand Serviceability Limit States. a) Partial obstruction of embankment culverts. Ballast contamination induced problems: b) Rail corrugation [reprinted from: 238, with the permission from Elsevier, photocredit: W. R. Tyfour], c) Track drainage malfunction [reprinted from: 78, with the permission from Elsevier]. d-h) Levels of ballast contamination. Corrosion of track superstructure elements due to salt content in sand: i) contamination of fasteners and rail web, j) degradation of sleepers [reprinted from: 78, with the permission from Elsevier], k) corrosion of rail head (courtesy of Astaldi). l) contamination of turnout moving components. Sand wearing induced issues: m) thin sand layer on the downwind rail head (incoming wind from left to right, courtesy of Astaldi), n) detail of the downwind rail head [reprinted from: 137, with the permission from Voestalpine], o) wearing-induced cracks on the rail head [reprinted from: 137, with the permission from Voestalpine], p) wheel profiling [reprinted from: 137, with the permission from Voestalpine]. Sand accumulation around Wheel Detectors: q) sand free WD, r) partially buried WD, s) fully covered WD.	18
2.6	Conceptual scheme of the Source, Path and Receiver SMM classification.	24
2.7	Scheme of the proposed SMM categorization.	26
2.8	Layer system. a) Natural sand crusting, b) asphalt-latex mixture layer [reprinted from: 248, with the permission to reuse under a Creative Commons Attribution License].	28
2.9	Structured Hedge system: a) straw checkerboard [reprinted from: 104, with the permission to reuse under a Creative Commons Attribution License], b) polyethylene-net checkerboard [reprinted from: 272, with the permission from Elsevier], c) stones checkerboard [reprinted from: 272, with the permission from Elsevier], d) array of line-like obstacles [reprinted from: 149, with the permission to reuse under a Creative Commons Attribution License].	28

2.10	Checkerboard Hedge system: a) Isolated flow regime inside cells (cells geometry scale: $Dz \approx 2Dx$), b) corresponding qualitative sedimentation levels in a cell [redrawn from: 148, sand sedimentation levels scale: $Dz \approx 6Dx$], c) initial unstable condition of empty cells [reprinted from: 104, with the permission to reuse under a Creative Commons Attribution License], d) stable concave surface [reprinted from: 104, with the permission to reuse under a Creative Commons Attribution License], e) stable flat surface [reprinted from: 193, with the permission from Elsevier].	29
2.11	Unstructured Hedge system: a) gravel surface [reprinted from: 150, with the permission from Elsevier], b) large roughness elements [reprinted from: 96, with the permission from Elsevier], c) trees planted over dunes near a railway.	30
2.12	Path SMMs: surface-like (a,b), volume-like (c,d,e).	32
2.13	Path SMM arrangement configurations: a) wind direction orthogonal to the longitudinal railway axis, b) skewed wind direction.	32
2.14	Wind flow mean streamlines and related sedimentation levels around: (a,b) solid Straight vertical wall (SVW) barriers [redrawn from: 11, 116], (c,d) very low porosity fences [$\beta < \beta_0$, redrawn from: 71, 116], (e,f) low porosity fences [$\beta_0 < \beta < \beta_c$, redrawn from: 260, 116], (g,h) high porosity fences [$\beta > \beta_c$, redrawn from: 260, 116]. Sand sedimentation levels scale: $Dz = 5Dx$	33
2.15	Fences with smeared porosity. Homogeneous anisotropic turbulence generators: a) vertical slats, b) horizontal slats. Homogeneous isotropic turbulence generators: c) grid fence, d) nylon net fence, e) holed fence, f) fractal fence (a-e redrawn from [71], f redrawn from [162]).	35
2.16	Fences with localized porosity: a) spire-shaped [redrawn from: 27], b) leaf-shaped [redrawn from: 273].	35
2.17	Fences with deflecting porosity: a) guide plates downwind rectangular openings [redrawn from: 50], b) array of inclined slats [redrawn from: 53].	36
2.18	Fences with smeared porosity: a) traditional fence protecting a palm plantation (explicit publishing permission from the owner of the photos: Nouar Boulghobra); b) nylon net fence [reprinted from: 151, with the permission to reuse under a Creative Commons Attribution License]. Fences with localized porosity: c) concrete fence [reprinted from: 273, with the permission from Elsevier].	36

2.19	Artificial dune growing: a) scheme of the process [redrawn from: 248, sand sedimentation levels scale: $Dz = 5Dx$, Fence 1 (t1) - placed in December 1962, Fence 2 (t2) - placed in January 1963, Fence 3 (t3) - placed in March 1964, Fence 4 (t4) - placed in March 1966, final shape - July 1968], b) a questionable application to stop the windblown sand (explicit publishing permission from the owner of the photo: Nouar Boulghobra).	37
2.20	Geometry of aerodynamically-shaped solid barriers: a) common Straight Vertical Wall, b) pioneering shape by [184], c) [183], d) recent patent Shield for Sand [41]. Thick solid lines indicate the cross-section of the aerodynamic-effective surfaces.	38
2.21	Shape induced differences in wind flow mean streamlines [from computational simulations in 39] and sand sedimentation levels [from wind tunnel tests in 116, 44]: comparison between <i>Shield for Sand</i> (a,c,e) and a SVW (b,d,f).	38
2.22	Straight Vertical Wall examples: a) precast r.c. modules [owner of the photo: R. Méndez, 164]; b) slanted, overlapped modules [reprinted from: 273, with the permission from Elsevier]; c) alignment of vertical sleepers (curtsey of Astaldi). Straight Vertical Wall sedimentation patterns: d) free-standing concrete wall [explicit publishing permission from the owner of the photo: Nouar Bolghobra, 30]; e) gabion wall adjacent to the toe of the railway embankment (curtsey of Astaldi); f) horizontally stacked sleepers (explicit publishing permission from the owner of the photo: Nouar Bolghobra).	39
2.23	Volume-like SMMs. Wind flow mean streamlines around a) a dyke [redrawn from: 188], and b) a ditch [redrawn from: 220]. Sand sedimentation levels around c) a dyke [redrawn from: 116], and d) a ditch. Examples of actual volume-like SMMs during field trials: e) a dyke [reprinted from: 186], and f) a ditch [reprinted from: 186].	40
2.24	Aerodynamic-based Receiver SMMs: jet roofs. a) Historical example from [198], b) patent redrawn from [103], c) patent redrawn from [207].	42
2.25	Aerodynamic-based Receiver SMMs. Venturi effect-based: a) humped sleepers scheme. Streamlines in the section: x-z (b), x-y (c). d) humped sleepers [reprinted from: 201, with the permission to reuse under a Creative Commons Attribution License]. Qualitative sand accumulation levels in the section: x-z (e), x-y (f).	43
2.26	Sand-resistant Receiver SMMs. The ballastless track slab systems: a) longitudinal continuous support, the T-Track system (explicit publishing permission from the owner of the photo: Giles Wiggs), b) the continuous slab [reprinted from: 164, with the permission from El Confidencial]. c) the lubricant-free turnout [reprinted from: 137, with the permission from Voestalpine].	45

2.27	Failure of Receiver SMMs: a) the T-Track covered by sand (explicit publishing permission from the owner of the photo: Ciaran Nash), b) the continuous humped slab covered by sand [reprinted from: 164, with the permission from El Confidencial], c) the lubricant-free turnout jammed by sand (courtesy of Astaldi).	46
3.1	General polyhedral control volume in FVM. Redrawn from [125].	58
3.2	Face interpolation - central differencing scheme.	59
3.3	Face interpolation - definition of nodes.	60
3.4	Work-flow of the optimization process.	63
3.5	Work-flow of genetic algorithm optimization.	65
4.1	Shield for Sand conceptual design (a) and a render along a desert railway line (b).	74
4.2	Detailed design for N=1 scenario: (a) cross-section; (b) isometric view. N=2 scenario: (c) cross-section; (d) isometric view.	76
4.3	Above ground geometrical setup with one (a) and two (b) steel panels.	77
4.4	Mean streamlines around <i>Shield for Sand</i> baseline solution, structures and characteristic lengths of the local flow, after [39] (a). Structural parameters, with wind-induced bending and overturning moments (b).	78
4.5	2D computational domain (not in scale). All the lengths are given in relation to barrier height H . $u(z)$ -line represents the incoming logarithmic velocity profile.	79
4.6	Automatically-generated numerical grids: a) around a barrier with low circular angle; b) around a barrier with high circular angle.	81
4.7	$N = 1$ - Sampling plan for sensitivity study.	83
4.8	$N = 1$ - Flow structures and characteristic quantities around differently shaped barriers: limit case close to SVW (a), example between two limit cases (b), most deflected simulated case (c).	84
4.9	$N = 1$ - Pressure coefficient over barrier height: upwind surface (a), downwind surface (b).	85
4.10	$N = 1$ - Bulk metrics related to performance: along-wind projection $L_{R,u}$ (a), vertical projection $H_{R,u}$ (b), and recirculation area A_R (c) of the upwind sand trapping vortex.	86
4.11	$N = 1$ - bulk metrics related to cost: moment M_1 at the deflector base (a), overall base moment M_0 (b).	87
4.12	$N = 1$ - Synopsis of the sensitivity study (SS): samples in the cost-performance plane (a), streamlines around selected samples (b).	87
4.13	$N = 1$ - Trend of the goal function versus the design parameters.	89
4.14	$N = 2$ - Synopsis of the sensitivity study (SS): samples in the cost-performance plane (a), streamlines around selected samples (b).	90
4.15	$N = 2$ - Trend of the goal function in the overall design space (a), trend of the goal function versus pairs of the design parameters (b,c,d).	91

4.16	Gradient-Based Optimization (GBO) and Genetic Algorithm Optimization (GAO) objective function for each function evaluation (a) and estimated error (b).	92
4.17	Summary of the samples from the sensitivity study (SS) on the $c/c_0 - p/p_0$ plane (a), GBO and GAO paths for $N = 1$ (b) and $N = 2$ (c,d).	93
4.18	Optimal shapes from GBO (a) and GAO (b).	94
5.1	Observed sand sedimentation patterns around railways. General patterns around the railway (a) and the substructure (b, c). Local Patterns around standard railway system (d, e). Different granulometry of sedimenting particles (f, g). Local patterns around non-conventional track systems (h,i). Pattern due to yawed incoming wind (j). Inferred prevailing wind directions from left to right in all pictures. Photocredits: pictures a, h, j - C. Nash and G. Wiggs, University of Oxford, SMaRT members; pictures b, c, f - F. Genta, Astaldi Company, SMaRT partner organization; pictures d, e, g - M. Horvat, C. Nash and R. Nuca, SMaRT early stage researchers; picture i - [201], with the permission to reuse under a Creative Commons Attribution License.	98
5.2	Values of common geometrical parameters in mm, with reference to EB.1 cross section.	102
5.3	Synopsis of vane geometries. a) General 2D case; b) main geometrical vane parameters of the studied cases; c) 3D vane geometry.	104
5.4	Scheme of computational domain and boundary conditions (not in scale - superstructure not drawn for the sake of clarity).	104
5.5	Ratio τ_0/τ_t at the inlet boundary as a function of d_s and U_{10}	107
5.6	Numerical grid around the ground and side surfaces of a standard railway (a), close up view around the rail (b).	107
5.7	Grid sensitivity to domain track-wise length L_y	109
5.8	Wind flow around railway: a) Streamlines and vorticity; p1)-p7) vertical profiles of the velocity components at different positions across the railway system.	111
5.9	Global flow features and potential sedimentation zones: a) reference flow topology; b) skin friction coefficient; c) shear stresses for different incoming reference velocities; d) potential sedimentation, erosion and backward erosion zones.	112
5.10	Global upwind (a) and downwind (b) sedimentation lengths.	113
5.11	Local flow patterns (left column) and potential sedimentation, erosion and backward erosion zones (right column).	115
5.12	Local erosion (a) and sedimentation (b) normalized areas for EB.SS cases.	116

5.13	u_y velocity component along the track-wise direction for non-conventional 3D superstructures (NC.2-NC.4). s.v.f. refers to the streamline visualization field.	117
5.14	Flow patterns for non-conventional (NC) cases (incoming wind from left to right).	119
5.15	Potential sedimentation, erosion and backward erosion patterns for NC cases (incoming wind from bottom).	120
5.16	Local erosion (a) and sedimentation (b) normalized areas for NC cases.	121
5.17	Effects of differently-yawed wind flow on standard Railway Systems (RS) (EB.1) aerodynamics.	122
5.18	Flow patterns for NC.3 cases at different yaw angles.	124
5.19	Flow patterns for NC.4 cases at different yaw angles.	125
5.20	Potential sedimentation, erosion and backward erosion patterns along non-conventional railway systems under differently yawed wind-flow (incoming wind from below).	126
5.21	Sedimentation (a) and erosion (b) normalized areas for selected cases under differently-yawed wind flow.	127
5.22	Local flow features in terms of aerodynamics (left column) and potential sedimentation, erosion and backward erosion zones (right column) for Standard Sleepers (SS) cases.	129
5.23	Graphs of erosion (a), sedimentation (b), and backward erosion (c) for SS cases integrated over the upper ballast surface.	130
5.24	Local flow features in terms of aerodynamics (left column) and potential sedimentation, erosion and backward erosion zones (right column) for Humped Sleepers (HS) cases.	133
5.25	Graphs of erosion (a), sedimentation (b), and backward erosion (c) for HS cases integrated over the upper ballast surface.	135
5.26	Flow patterns for unmitigated SS, HS and <i>Sand Blower</i> cases (incoming wind from left to right).	136
5.27	Potential sedimentation, erosion and backward erosion patterns for unmitigated SS, HS and <i>Sand Blower</i> cases (incoming wind from left to right).	138
5.28	Local erosion (a), sedimentation (b) and backward erosion (c) normalized areas for <i>Sand Blower</i>	139
5.29	Potential sedimentation, erosion and backward erosion patterns for unmitigated SS, HS and <i>Sand Blower</i> cases at different yaw angles.	140
5.30	Averaged values of local erosion (a), sedimentation (b) and backward erosion (c) normalized areas for <i>Sand Blower</i> at different yaw angles.	141
5.31	Local erosion (a), sedimentation (b) and backward erosion (c) normalized areas for <i>Sand Blower</i> at $\theta_0 = 75^\circ$ for a given gap presented in subfigure (d).	142

5.32	Local erosion (a), sedimentation (b) and backward erosion (c) normalized areas for <i>Sand Blower</i> at $\theta_0 = 60^\circ$ for a given gap presented in subfigure (d).	143
5.33	Local erosion (a), sedimentation (b) and backward erosion (c) normalized areas for <i>Sand Blower</i> at $\theta_0 = 45^\circ$ for a given gap presented in subfigure (d).	144

Abbreviations

ABL Atmospheric Boundary Layer.

BC Boundary conditions.

CWE Computational Wind Engineering.

DNS Direct Numerical Simulations.

DP Drift Potential.

FVM Finite Volume Method.

GAO Genetic Algorithm Optimization.

GBO Gradient-Based Optimization.

HS Humped Sleepers.

IC Initial conditions.

IPC *International Patent Classification*.

LES Large Eddy Simulations.

LIC Line Integral Convolution.

NC non-conventional.

PVC Percentage Void Contamination.

RANS Reynolds-averaged Navier-Stokes.

RDD Resultant Drift Direction.

RDM Resultant Drift Magnitude.

RDP Resultant Drift Potential.

RS Railway Systems.

s.v.f. streamline visualization field.

SBO Surrogate-Based Optimization.

SLS Sand Limit State.

SMM Sand Mitigation Measure.

SRM Sand Removal Machine.

SS Standard Sleepers.

SSLS Sand Serviceability Limit State.

SST Shear Stress Transport.

SULS Sand Ultimate Limit State.

SVW Straight vertical wall.

WDs Wheel Detectors.

Nomenclature

ρ air density.

θ yaw angle.

β optical porosity.

Ω fluid domain.

ϕ general transported variable.

μ dynamic viscosity.

ν kinematic viscosity.

ω specific dissipation rate of the turbulent kinetic energy.

η gradient step.

ε dissipation rate of the turbulent kinetic energy.

α central angle of an arc.

Δ distance between the optimal goal function and the goal function at a given iteration.

λ track-wise wavelength of the aerodynamic structures.

\check{G} the minimum goal function from sensitivity study.

\tilde{P}_k source of the turbulent kinetic energy.

τ^* dimensionless form of wall shear stresses.

$\nu_{c,s}$ collision sand viscosity.

$\nu_{eff,s}$ effective viscosity of sand.

ϕ_i goal function at the given iteration.

ρ_s sand density.

ν_s molecular sand viscosity.

ν_t turbulent kinematic viscosity (or eddy viscosity).

α_t tangency angle.

$\nu_{t,s}$ turbulent sand viscosity.

τ_w wall shear stresses.

Δt time step.

AR aspect ratio.

A_R cross-sectional recirculation area.

A_S cross-sectional sedimentation area.

BR blockage ratio.

C_0 roughness constant.

C_f dimensionless skin friction coefficient.

C_p coefficient of pressure.

F_i normalized mass flux through the face.

G goal function.

H total height.

$H_{R,u}$ vertical recirculation length.

$H_{S,u}$ vertical sedimentation length.

Kn Knudsen Number.

$L_{R,u}$ horizontal recirculation length.

$L_{S,u}$ horizontal sedimentation length.

M aerodynamic moment.

Ma Mach Number.

Q sand transport rate.

Q_h heat source.

Re Reynolds Number.

S total curvilinear length.

T_r arbitrary time period.

T_{ref} reference time period.

V volume.

W track-wise wavelength of the geometric structures.

c cost metric.

c_e wind exposure factor.

d sand grain diameter.

e specific energy of the system.

e_i internal energy.

h height of the vertical wall.

k turbulent kinetic energy.

k_s sand grain roughness height.

n^+ dimensionless wall distance (commonly represented by y^+ in literature).

n_p cell center height.

n_w cell height.

p performance metric.

p_s static pressure.

q sand flux.

q_p stagnation pressure.

r radius of an arc.

s curvilinear length of an arc.

t time coordinate.

u wind velocity magnitude.
 u_* shear velocity.
 $u_{*,eff}$ effective shear velocity.
 $u_{*,t}$ threshold shear velocity.
 u_s sand particle velocity.
 z_0 aerodynamic roughness length.
A matrix of coefficients.
b external force field (gravity).
I identity tensor.
n normal vector.
q_h heat flux.
s_i face area vector.
T stress tensor.
u velocity vector.
x spatial coordinates.

Chapter 1

Introduction

Parts of the work presented in this chapter are published by the author in peer-reviewed article [40].

The engineering interest about windblown sand is dictated by the harmful interactions that sand can have with a number of structures and infrastructures in arid environments [170], such as pipelines [134], industrial facilities [3], towns [269], single buildings [204, 27], farms [247], roads [199], and railways (see Figure 1.1). The research done within the Thesis is driven by the real world technical problems. In particular, the wind-induced accumulation of sand is one of the specific key design challenges threatening safety, affecting serviceability and maintenance of railways in arid and desert regions. To cope with the issues *Sand Mitigation Measures* (SMMs) are applied.

A growing demand for windblown sand mitigation design and maintenance has been observed in the last decade and it is expected to further increase in the next 20-30 years. The increasing interest in windblown sand mitigation is demonstrated by the growing number of published studies and filed patents in the recent years. A non-exhaustive survey of studies versus the year of publication is shown in Figure 1.2 (a), while non-exhaustive survey of patents on SMM design versus the filing year is shown in Figure 1.2 (c). The included references are the ones cited in the Thesis. The patents have been acquired through *Orbit* ©; patent database. The following technologies are taken into account with their corresponding classification codes by the *International Patent Classification* (IPC): i.) *Snow fences or similar devices* (E01F 7/02), e.g. devices affording protection against sand drifts or side-wind effects; and ii.) *Fencing* (E04H 17/00), e.g. fences, enclosures, corrals. Multidisciplinarity in windblown sand mitigation is testified by the chart in Figure 1.2 (b), which shows the distribution of the peer-reviewed studies cited in the Thesis, over the addressed research fields. Given the high diversity in research fields, scientific affiliations have been grouped in three main research areas, i.e. engineering disciplines, environmental sciences, and applied mathematics and physics. Studies classified as environmental sciences deal with Geology, Ecology, Geography.



Figure 1.1: General sand-induced problems: a) pipeline in desert (explicit publishing permission from the owner of the photo: gordontour@Flickr), b) invading sand dunes in front of a city [reprinted from: 190, with the permission from Elsevier], c) encroached single building (explicit publishing permission from the owner of the photo: Nouar Boulghobra), d) sand-invaded palm plantation (explicit publishing permission from the owner of the photo: Nouar Boulghobra), e) sand covered road (explicit publishing permission from the owner of the photo: Yann Arthus-Bertrand), f) railway in desert (courtesy of Astaldi).

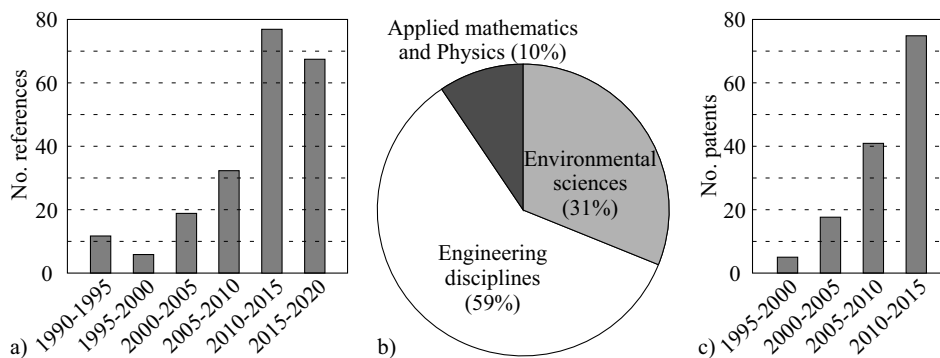


Figure 1.2: a) Number of cited references classified by the year of publication, b) classification of references according to the research area, c) increasing trend of filed patents through years.

In the engineering disciplines the following subareas are included; Civil, Mechanical, Geotechnical, and Transport Engineering. It is worth stressing that the most of the cited studies in the Thesis cover more than one scientific area. For the sake of simplicity, the studies dealing with multidisciplinary topics are included under a single area in the chart.

Despite the development of the ad-hoc studies for specific projects, a systematic and comprehensive problem setting and solving is still missing. Furthermore, a common nomenclature about windblown-sand-induced effects on railways does not exist. Authors publishing from different scientific backgrounds refer to characteristic phenomena by different nomenclature: e.g. *sand disasters* [52, 216], *sand damage* [51], *aeolian hazard* [29, 204, 226], *sand risk* [31], or a combination of mentioned nomenclature [18].

1.1 Desert Railway Overview

To better grasp the idea of the windblown sand problems, a brief overview of railways crossing the deserts is given. The existing railways and the railways which are planned to be built in the recent future present the potential size of the sand mitigation market. In the ideal case, protection from sand is designed at the stage of the infrastructure design. Conversely, for the railways built without the protection, the SMMs can be applied a posteriori.

1.1.1 Past Railways across Deserts

Historically, the first railways along deserts have been built by colonial countries. The British military railway was built at the end of the 19th century (1897-1899) from Wadi Halfa to Abu Hamed over the Nubian desert [Sudan 252, 253]. The French railway (1910) extends over the wide area from Oran to Colomb-Bechar in the Kénadsa desert in Algeria [253] and was built in the framework of the never finished Trans-Saharan Railway project (1870-1941) [106]. The best example of a German railway is the line from Aus to Lüderitz (1906) over the Namib desert in Namibia [68]. The Hejaz Railway was built from Damascus to Medina, through the arid Hejaz region of Saudi Arabia and was a part of the Ottoman railway network built from 1900 to 1908 with German advice and support [177]. At the present time, most of the mentioned lines are partially or totally decommissioned, and their remnants buried by the accumulated windblown sand or encroaching dunes. Example of the Grasplatz railway station along the Aus to Lüderitz railway before and after the sand hazardous effect can be seen in Figure 1.3 (a) and (b).

From the reviewed literature, the first SMMs for railways have been empirically tested along the Kundian-Mianwali section of the Sher Shah-Attock line in the arid Punjab province of Pakistan (probably built in 1891, surely in service in 1910,) [198]. The 550 km long Dammam-Riyadh line is the first pioneering modern railway whose design systematically addressed the windblown sand challenges (Kingdom of Saudi Arabia, 1947-1950, today in service). The team of American designers guided by J.H. Gildea tackled the problem of “*Combating the engineering obstacles of locating track on sands that drift constantly like snow. It was, in fact, this similarity to snow*”

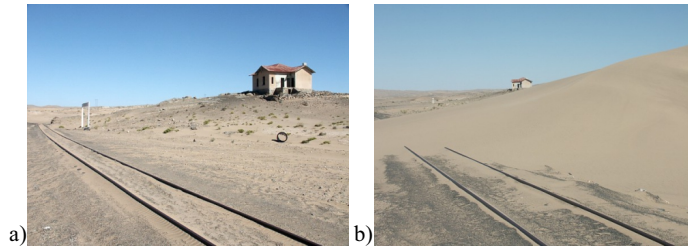


Figure 1.3: Grasplatz railway station along the Aus to Lüderitz railway before (a) and after (b) sand dune encroaching (permission to reuse under a Creative Commons Attribution License; owner of the photos: Klaus Dierks [68]).

that provided an important key to solving the difficulty. As strong prevailing north-west winds, known in Arabia as chamals, kept the sand in continual movement, engineers employed plows and spreaders. Such tools have previously been proven efficient in snow operations and are employed in desert regions to level and clear wavelike dunes. Fences comparable to snow fences were erected along the right of way. Heavy coatings of crude oil were applied and the heavy crust thus created not only held the sand firm beneath it, but provided a surface over which the blowing sand would not hold.” [107]. It is worth pointing out that engineers were applying technology known from the snow mitigation, even though sand and snow have strikingly different physical properties. Moreover, the first influential book on the physics of windblown sand has been published 10 years before [10]. In other words, at early stages of the development, SMMs were suffering the scarce transfer of knowledge from the base and specialist research fields (e.g. Aeolian Geomorphology, Fluid and Porous Mechanics, Wind Engineering) to the Transportation and Civil Engineering design practice.

In 1956, 40 km of the Batou-Lanzhou railway was constructed in the south of the Tengger Desert, China [171]. The railway was massively buried by mobile dunes since its construction. In the following years, a procedure for establishing artificial ecosystem on mobile dunes was started by application of straw checkerboards over the mobile sand source [153]. This technique has been widely used in China along a number of railway lines. For the full list of the railway lines, interested readers are referred to [263]. All the mentioned historical lines can be seen in Figure 1.4.

1.1.2 Present Railways across Deserts

At the present time, most of the in-service railway lines crossing deserts and aeolian sand regions are located in the north-western China with the total length of about 10,000 km [146, 147, 51]. For example, the Lanzhou-Xinjiang line across the Gobi desert (1,904 km, completed in 1990) [52], the Xining-Lhasa line along

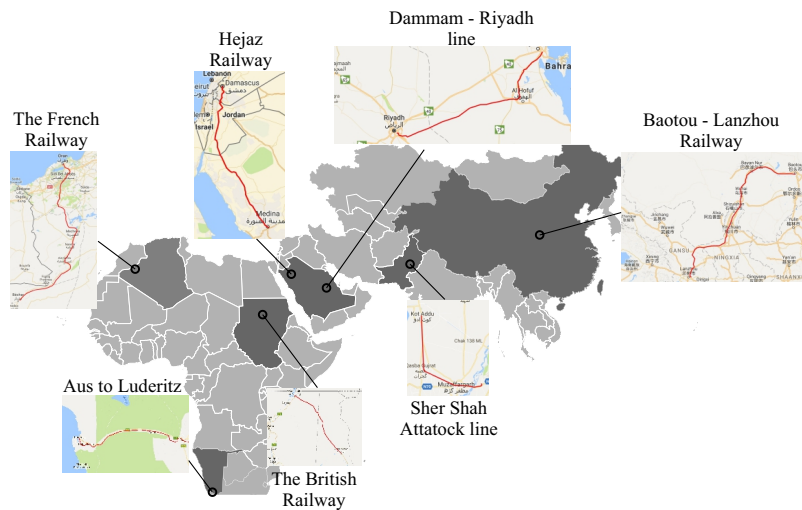


Figure 1.4: Historical railways.

the Tibet plateau (1,956 km, completed in 2006), the Linhai-Ceke line across the Ulanbuhe, Yamaleike, and the Badain Jaran Deserts (707 km, completed in 2009). Despite the tremendous effort of the Chinese scientific community in the past 15 years, China has the greatest windblown sand disaster distribution along its railway network [52]. The Linhai-Ceke line seems to be one of the most vulnerable ones. In the first year of operation, over 10,000 workers were mobilized and CNY 71 million was spent on windblown sand induced maintenance. Service was suspended for two months in the spring of 2010. In the first 36 days after passenger service was introduced in the November 2010, sand storms buried the track for 27 days and caused 51 service disruptions. Sand storms have reduced the effective speed on eight sections of track between Suhongtu to Swan Lake to 25 km/h [172].

A report of sand hazards from India was given in a detailed survey of railways in the desert and semi desert areas of Rajasthan in [176]. An overall length of about 1,250 km is prone to windblown sand in the Jodhpur and Bikaner Divisions of the north-western Railway. The survey includes the list of windblown-sand-induced accidents per year (1 to 2 derailments, 3 to 7 days of service disruptions) and manpower lost on the sand removal activities (about 1,480 man-day per year).

Apart from the Far East, most of the in-service desert railways are located in the Middle East - North Africa (MENA) region. The cited Dammam-Riyadh line in Kingdom of Saudi Arabia (KSA) has recently suffered a service suspension due to a windblown-sand-induced train derailment. The precise mapping of the in-service railway lines along sandy areas is available for the Iranian railway Network: the overall length of 416 km [267] is exposed to windblown sand, with severe operational difficulties in the Bafgh-Mashhad line along the Lout desert. At the present

time, two other main lines are in the testing and commissioning stage in the Arabic peninsula. The North-South Railway is a 2,400 km long railway project in KSA [2]. The so-called phase 1 of the Etihad Rail network is a 266 km long line from Shah and Habshan to Ruwais in the United Arab Emirates. In the same time, the 450 km long Haramain High Speed rail between Medina and Mecca is under construction. Despite the ad-hoc dedicated studies during the design phase [186], the construction advancement is suffering significant delays due to the windblown sand accumulation along the line under construction and the retrofitting of the designed SMMs, among others, e.g. [128, 97].

On the other side, some desert trains in Africa are converted into touristic attractions thanks to the windblown sand (e.g. the Oriental Desert Express in Oujda-Bouarfa, Morocco or the Desert Express in Windhoek-Swakopmund, Namibia).

1.1.3 Future Railways across Deserts

In the short and mid term, the railway lines in desert and arid regions are expected to rapidly grow, particularly in the MENA region. The Arab Countries are conceiving, evaluating and building a large railway network at different scales. The Arab Network Railway (ANR, preliminary study by the consortium Italferr-Dar El Omran, 2009-2012) is a 30,000 km long, high-speed/high-capacity railway network conceived to connect all the Arab League Countries across the Middle East and North Africa. It is worth pointing out that the length of a single project is more than twice the overall European high-speed railway network currently in operation and under construction. The Gulf Railway (GR) is a 2,217 km long project proposed to connect six Arab Gulf Co-operation Council (GCC) member states. In this framework, national railway networks are currently under design and/or construction, e.g. the Oman, UAE and KSA ones. The corresponding investments are significant. For instance, the Middle East Countries have allocated about USD 260 billion to build 40,000 km of railway tracks up to 2030 [119]. Map of the mentioned currently in service, in construction, and proposed railways are shown in Figure 1.5.

1.2 General Design Framework

The proposed general design framework can be seen in Figure 1.6. It is defined in analogy to the best practices in Computational Wind Engineering (CWE).

Generally speaking, the design of a product follows the presented path in Figure 1.6. Such approach is suited for the design of SMMs whose working principle relies on modifying the local wind flow to promote the desired effect. A proper preparation for the design process starts with the *Problem Setting*. It is aimed at the understanding of the physical working principles and the investigation of the

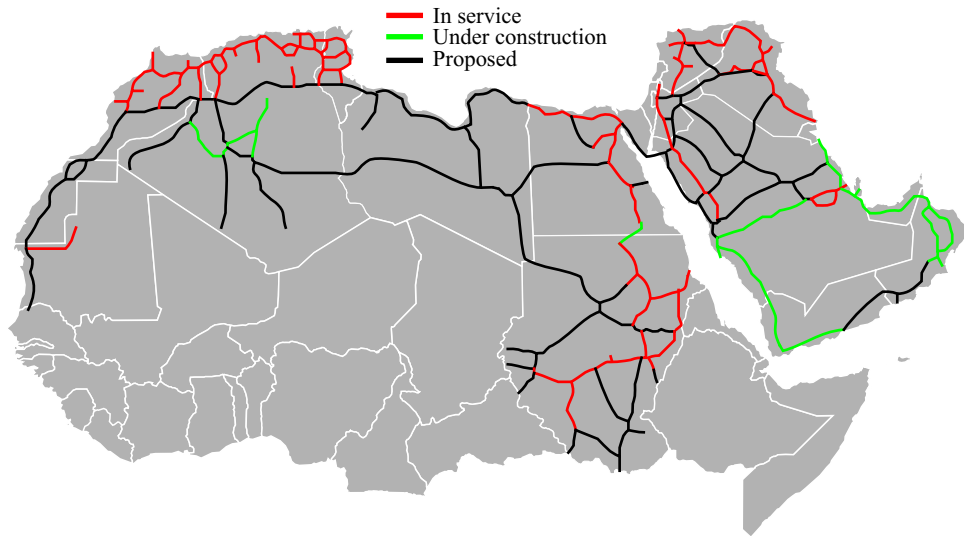


Figure 1.5: Map of currently in service, under construction, and proposed railways.

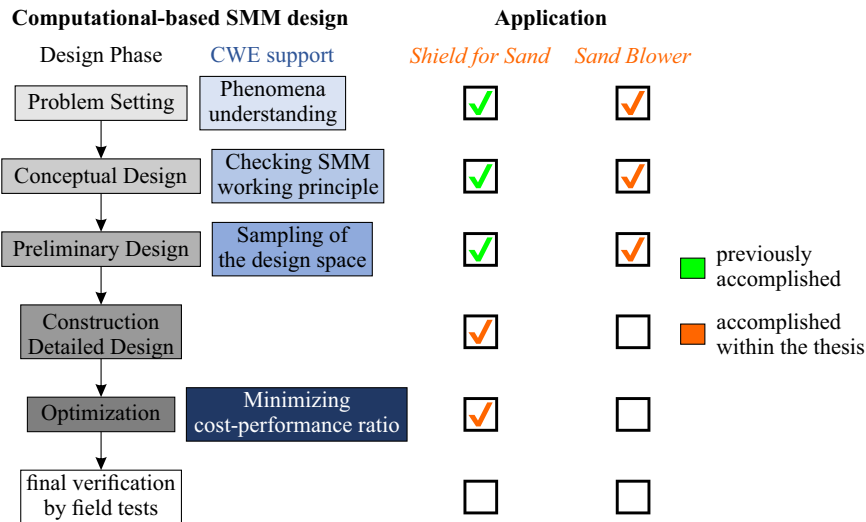


Figure 1.6: Scheme of the computationally-based SMM design.

state of art. The CWE approach is one of the tools which can be used to successfully fulfill the phase by exhaustive simulation campaign and critical comparative assessment of the existing solutions. The goal is to pinpoint the weaknesses of the commonly adopted approaches in literature and to find promising design solutions, if any, which could be improved in the subsequent phases of the design process. Knowledge gathered in the problem setting evokes design ideas which

are conceptualized by following the engineering practices in the *Conceptual Design* phase. Simple, quick and cost-effective CWE simulations can be employed to check the working principles of the innovative design solution. The promising ideas are further tested in the *Preliminary Design*. At this phase, the critical variables have to be chosen for the performance assessment in order to shed additional light onto the working principle of the innovative design solution. To cope with this issue, the CWE simulations can be used in the form of non-exhaustive parametric study in which the characteristic geometric parameters are varied. Such a study shows how sensitive the innovative design solution is to the input parameters and which part of the design solution requires special attention in the next phases. At this point, designer should have a deep understanding of the working principle. A detailed description of geometry is given in the *Detailed Design* phase. Special attention should be given to each construction member, and the way they are incorporated in the final assembly of the product should be defined. The ratio of the production cost defined in the detailed design and the performance metric defined in the preliminary design results in the goal function. The definition of the goal function naturally leads to the *Optimization* phase. The goal is to find the optimally-behaving shape of the innovative design solution by minimizing the goal function. The design parameters at which the minimum is found, define the shape of the optimal solution. Coupling of the CWE simulations and the optimization algorithms can be employed as a tool to carry out such a study. Optimization is usually time consuming and requires vast numerical resources, making it not always justifiable for every Civil Engineering structure. However, optimization is essential in the design of kilometers-long SMMs where the cost is of utmost importance, e.g. *Shield for Sand*. The properly optimized design solution should at the end of the design process be tested. In the industrial and scientific community dealing with sand mitigation, the most accepted approach are the field measurements. Due to the fact that the field tests are out of the scope of this Thesis, they are not covered herein.

The design part of the Thesis revolves around applying and critically describing the results obtained at each phase of the design framework. To cope with the current industrial needs of the SMaRT project, the phases are applied on two different SMMs. In particular, i.) a barrier responsible for trapping most of the sand far from the railway, the so-called *Shield for Sand*; ii.) a mitigation measure to be positioned close to the railway and protect pointwise railway equipment, the so-called *Sand Blower*.

In the case of *Shield for Sand*, the steps of problem setting, conceptual and preliminary design are skipped, because they have been previously covered by the SMaRT team [41]. The detailed design is carried out by adopting semi-finished products already existing in the infrastructure industry. The detailed design is not supported by the CWE simulations, but is carried out in the form of detailed three-dimensional geometrical models. The materials used in a combination with

the industrial and physical constraints leads to the calculation of the production costs. Moreover, the aerodynamic shape of *Shield for Sand* has been optimized by coupling of the CWE simulations with the gradient-based and genetic algorithm optimization. Conversely, the design of the *Sand Blower* started from scratch. Due to the fact that the aerodynamics of railway systems is only partially described in the literature, an extensive simulation campaign is performed. Understanding of the aerodynamic behavior is unavoidable in the case of *Sand Blower*, because the geometry of the SMM itself interacts with the geometry of the railway, and it cannot be treated independently. In the process, a potentially well-performing, unmitigated railway system is discovered and it is used in the conceptual and preliminary design of the *Sand Blower*. Additionally, a parametric study has been performed in the form of the two-dimensional CWE simulations. The most promising solution is further presented in its three-dimensional form, and the results are quantitatively compared to the other significant unmitigated and mitigated railway systems.

In order to deal with the open issues described in this chapter, the research within the Thesis first covers an innovative categorizations of both the windblown-sand-induced performance deficiencies of the railway system and the sand mitigation techniques. The new nomenclature has been proposed within the Thesis which allows the introduction of the general design framework for SMMs. The framework is science-oriented and is introduced to replace the semi-heuristic, trial-and-error approach previously preferred in the area of sand mitigation.

The structure of the Thesis follows the time line of the research. In **Chapter 1**, introduction is given with a focus on the motivation and the reason why a general design framework is essential. In **Chapter 2**, the state of art in the form of the innovative classifications of both, sand induced problems and SMMs are thoroughly described. **Chapter 3** deals with the modelling approaches, in particular their mathematical and numerical aspects. In **Chapters 4** and **5** respectively, description of the design optimization and the conception of a completely new design solution is given. **Chapter 6** outlines the most significant findings of the Thesis.

Such structure completely correlates with the goals of the Thesis, and with the tasks defined in the Work Package 1 of the SMaRT project. In particular: i) the review of the state of art of the existing SMMs and sand induces problems; ii.) a comparative study of unmitigated and mitigated railway systems using CWE; iii.) the conceptual design of innovative SMMs; iv.) the development of innovative performance assessment metrics for SMMs.

Kyyyyy

Chapter 2

Windblown Sand Effects on Railways: State of Art

Parts of the work presented in this chapter are published by the author in a peer-reviewed article [40].

The chapter deals with the innovative aspects of the work presented in the Thesis. In particular, the definition of *Sand Action* and the corresponding definition of *Sand Ultimate Limit States* and *Serviceability Limit States*, and the proposed classification of SMMs.

2.1 Sand Action

In the research within this study, windblown sand is treated as an environmental variable action, in analogy to other actions in engineering areas, such as thermal action [84], fire action [81], corrosion [224], wind action [83], windblown snow [82] or ice action [63]. The probabilistic modelling of the environmental actions is mandatory because of their inborn variability. Windblown sand action is defined as the *amount of sand carried by the incoming wind* undisturbed by the infrastructure, in analogy to the incoming mean wind velocity in wind engineering practice.

Windblown sand transport is a complex phenomenon resulting from the interaction of the two physical subsystems, i.e. the wind and the sand. Depending on the grain diameter d , sand is transported in different modes of motion, i.e. creeping ($d > 0.5$ mm), saltation ($0.5 > d > 0.07$ mm) and suspension ($d < 0.07$ mm) [10, 214] (Figure 2.1 a). Among them, saltation is recognized as the mechanism which mainly contributes to the overall transported sand mass [136]. In the following, only the sand grains with diameter in the range from 0.07 – 2 mm are taken into account, because an ensemble of particles with smaller diameter is defined as dust with much different physical properties, e.g. [191, 101], which are transported over very long distances in the processes called short and long-term suspension.

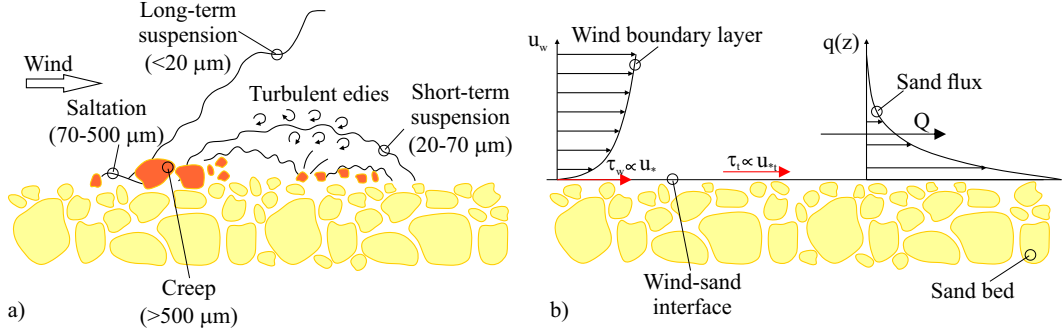


Figure 2.1: a) Scheme of the sand transport modes [redrawn from: 191], b) wind-sand interaction in saltation.

Windblown sand saltation flux q results from the shear stress τ_w induced by the wind over the sand bed (Figure 2.1 b). τ_w is proportional to the rate of change of the wind velocity u_w in the vertical direction ($\tau_w \propto \partial u_w / \partial z$) and is usually expressed in the form of wind shear velocity $u_* = \sqrt{\tau_w / \rho}$, where ρ is the air density. If the shear stress acting on the sand bed exceeds a certain threshold ($u_* > u_{*,t}$), sand grains are entrained into the lower part of the Atmospheric Boundary Layer (ABL), the grain bouncing is triggered and saltation occurs. The resulting sand flux $q(z)$ [$\text{M L}^{-2} \text{T}^{-1}$] is defined as the product of the sand grain velocity $u_s(z)$ and the sand density $\rho_s(z)$, whose distribution follows a decreasing exponential function in the vertical direction [275]. The sand transport rate Q [$\text{M L}^{-1} \text{T}^{-1}$] is a bulk metric derived from the sand flux by its integration in the vertical direction, i.e. $Q = \int_0^\infty q(z) dz$. However, Q is usually estimated by the semi-empirical models, reviewed in [72], [136], [215]. Among them, the most often applied are the so-called modified Bagnold type models in which Q is a function of the effective shear velocity $u_{*,eff}$ [195], defined as:

$$Q \propto u_{*,eff} \propto f(u_*) - f(u_{*,t}). \quad (2.1)$$

These models do not take into account the variability of wind and sand. DP is introduced in [90] to account for the *variability of the wind* in average, and to evaluate the cumulative value of sand transport rate. For a given wind direction θ , DP is expressed as:

$$DP = \frac{T}{\Delta t} \frac{1}{n} \sum_{i=1}^n Q_{i,\Delta t} \Delta t, \quad (2.2)$$

where n is the number of Q_i instances taken into account used to average the value of DP over an arbitrary time period ($T_r = n\Delta t$). Q_i is the i -th value of sand drift, evaluated by means of one of the Q semi-empirical models. Δt is the sampling time (e.g. 10 min), and a $T_{ref}/\Delta t$ is a factor used to normalize DP to the time scale

of the arbitrarily chosen reference time. The DP [$M L^{-1} T_{ref}^{-1}$] defined in such a way is giving an averaged amount of sand mass accumulated over the unit length in the cross-wind direction and over the reference time period T_{ref} . $T_{ref} = 1$ year is usually adopted in the field of sand mitigation. DP is graphically represented by the so-called sand rose, with an example shown in Figure 2.2.

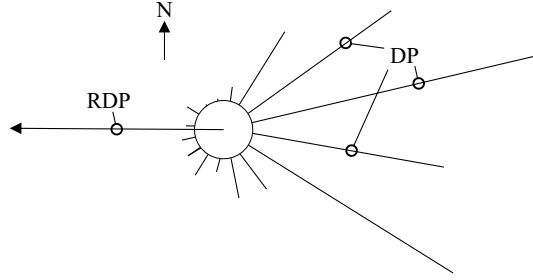


Figure 2.2: Sand rose of DPs and RDP [redrawn from: 90].

Each arm of the sand rose represents DP from a given direction towards the center circle. The RDP is computed as the vector sum of drift potentials, and is defined by the Resultant Drift Magnitude (RDM) and Resultant Drift Direction (RDD). These quantities are called potentials because they refer to the ideal sand bed, i.e. actual ground surface properties (e.g. sand or vegetation covering) are not taken into account. The framework proposed in [90] is currently widely applied in a number of scientific and technical fields, e.g. highway engineering [73], railway engineering [272, 52, 256], geomorphology and environmental sciences [9, 274, 262, 108, 28].

The effects of the *variability of the sand* on the threshold shear velocity ($u_{*,t}$) have been investigated in a number of papers, reviewed in [197]. The effects of the variability of $u_{*,t}$ on the windblown sand transport has been recently assessed in [195] for a number of the Q semi-empirical models. The evaluation of DP in a fully-probabilistic approach is firstly introduced by [196], where both the variability of wind and sand are taken into account. In this approach, DP is a random variable, described not only by its averaged value but also by higher statistical moments and percentiles. The probabilistic description of DP paves the way towards the definition of the sand action design value, in the general semi-probabilistic approach used in Civil Engineering for other environmental variable actions [80]. The design value of sand action DP_d is defined with the semi-empirical expression:

$$DP_d = \gamma_{DP} DP_k = \gamma_{dp} \gamma_{Sd} DP_k. \quad (2.3)$$

The characteristic value DP_k is defined as an upper limit with the specified probability of not being exceeded during the reference period. DP_k is directly obtained by the probability density function of DP. The partial factor γ_{DP} accounts for both

sand action inborn uncertainties defined by the partial factor (γ_{dp}), and modelling uncertainties defined by (γ_{sd}). The values of the partial factors for sand action are not specified in the current state of art, and further research is needed. The partial factor γ_{DP} depends on the limit state, and on the component of the railway infrastructure that attains it.

2.2 Windblown Sand Limit States

The sand sedimentation around the railways infrastructure unavoidably leads to problems in the operability of the railway traffic. In general terms, under a given windblown sand action (input) the overall infrastructure (system) is characterized by the resulting level of performance (output). In a performance-based design perspective, the same framework provides guidelines for a proper railway design under a given sand action, with the respect to the targeted performances.

In the scope of the present work, the focus is on the railway infrastructure, defined as the set of 4 *railway components*: i.) Civil works; ii.) Railroad equipment; iii.) Signalling system; iv. Rolling stock. The Sand Limit State (SLS) are introduced herein as threshold performance levels, beyond which the railway no longer fulfills the relevant design criteria. SLS are set in analogy to the other safety formats in different branches of Civil Engineering, e.g. [80]. SLS are further classified in Sand Ultimate Limit State (SULS) and Sand Serviceability Limit State (SSLS) as follows: i.) attaining SULS involves service interruption and/or passengers unsafe conditions; ii.) attaining SSLS involves the railway partial loss of capacity and/or passenger discomfort. The windblown SLSs are adopted as the main classification criterion, while the railway components attaining them as the secondary (see Figure 2.3).

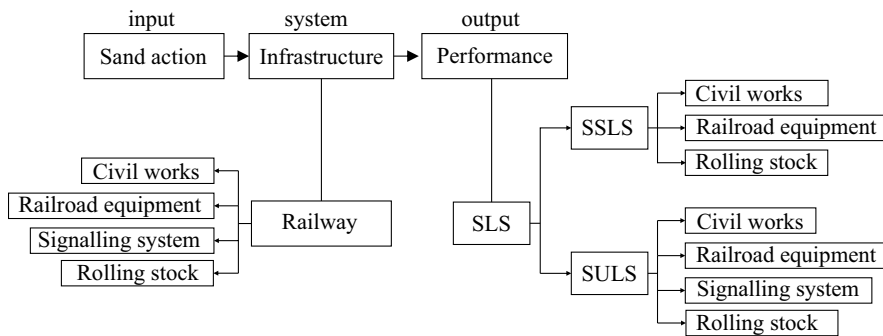


Figure 2.3: Framework scheme of the safety standards.

2.2.1 Sand Ultimate Limit States

The Sand Ultimate Limit State is mainly attained by the civil works, e.g. embankment or cutting buried by the sand. Because of the unavoidable interaction of the civil works, railroad equipment, and rolling stock the trains attain SULS in turn. The remaining reviewed system components (i.e. signalling system) do not suffer SULS. Under SULS, the windblown sand completely inhibits infrastructure operation. Hence, SULS are attained on the whole, or a section of the railway.

Civil Works

Schematically, railway body is susceptible to be buried by windblown sand under two conditions:

- the railway line crosses a migrating dune field, i.e. an area covered by transverse or barchan dunes (Figure 2.4 a). Such dunes advance with little or no change in the shape and dimension [236]. The velocity of barchan dunes varies with the dune height. For example, a 3 m high dune propagates at a velocity from 15 to 60 m/yr, while a 15 m high dune with a velocity ranging from 4 to 15 m/yr [4]. Dune encroachments across railway lines are reported in [171] and [68];
- the railway line crosses an area where the ground surface is covered by a thin sand sheet. The railway body (embankment and/or cutting) or simply railroad equipment of the at-grade sections (ballast bed, slab or rails) act as the obstacles to the incoming wind flow, inducing a deceleration of the flow at the upwind toe and a recirculation region downstream [255]. The reduction of the wind velocity and the shear stresses promotes sedimentation of the windblown sand over the infrastructure, resulting in a partially (Figure 2.4 b) or fully covering of the railway body. The degree of coverage depends, besides the incoming sand transport rate, on the passed time. Regardless of the degree of coverage, the sedimented sand induces the railway SULS when it compromises the infrastructure safety or operation. A number of site observations document railway covering in the literature, e.g. [272, 186, 92, 52].

Track Superstructure

Analogously to the civil works, the track superstructure of the at-grade sections (ballast bed, slab or rails) promotes sedimentation of the windblown sand over the track. Windblown sand can jam the railroad switches (also named turnouts, Figure 2.4 c). The sand accumulates in the gap between the linked tapering rail and the diverging outer rail (Figure 2.4 d), and prevents the correct operation of switches,

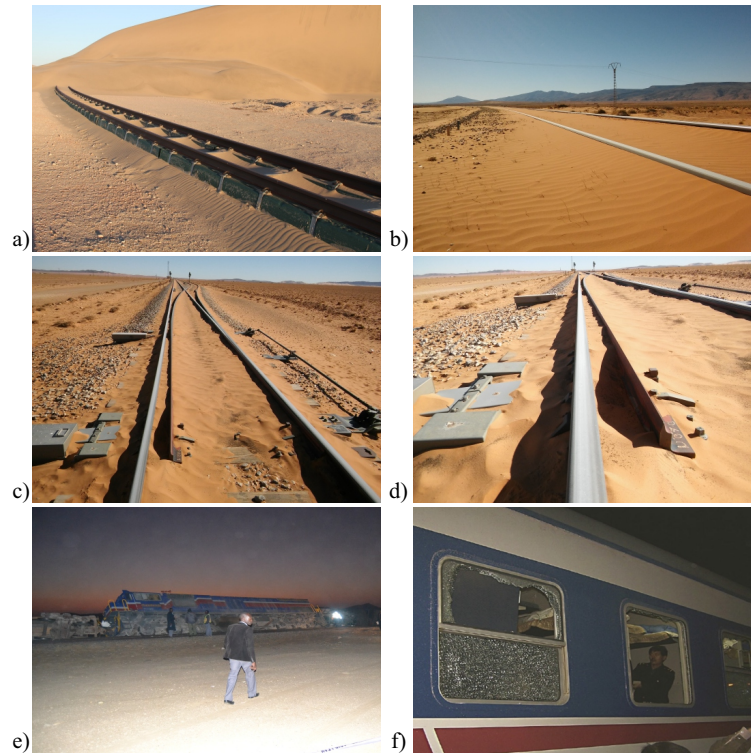


Figure 2.4: Sand Ultimate Limit States. Civil works: a) full sand coverage by an encroaching dune (explicit publishing permission from the owner of the photo: Giles Wiggs), b) partial sand coverage by the sand blown from a sandy plane. Track superstructure: c) jammed turnout, d) detail of the sand accumulation in the gap. Rolling stock: e) running train derailment [reprinted from: 242, with the permission from the editor], f) train window breaking [reprinted from: 52, with the permission from Elsevier].

analogously to the snow and ice in cold conditions. In such condition, service interruption is mandatory since switch malfunction may lead to train derailment or head-on collision.

Rolling Stock

The following conditions are recognized as SULSs of rolling stock:

- the sand covering of the railway platform can induce derailment of running trains (Figure 2.4 e), as reported by e.g. [176], [242];
- in general, the overturning of running trains is mainly due to crosswind [12]. The contribution of the suspended sand in the crosswind flow has been recently studied in [258], [245] and [243] by the CWE simulations. According

to the study in [245], for very high crosswind speed (about 50 m/s) the overturning moment caused by the sand grains on the running train is about 20% of the overall aerodynamic overturning moment. To the author's best knowledge, there is no experimental evidence to date;

- parked trains acting as the further obstacle to windblown sand and promoting sand sedimentation around them. Trains parked even for relatively short period of time can get trapped during windblown sand events with high sand drift, e.g. one night [92]. In the mentioned case, sand had to be manually removed to allow the train departure;
- breaking of the train windows by windblown sand in conjunction with high wind speed, shown in Figure 2.4 (f) [52]. An experimental study has demonstrated that windblown sand, especially with the sand grain diameter of about 5-6 mm, can significantly reduce the window glass ultimate pressure strength [259].

2.2.2 Sand Serviceability Limit States

The Sand Serviceability Limit State is attained by every component of the railway infrastructure. Under SSLS, windblown sand affects only a component of the railway. However, SSLS reverberate on the overall railway system performance, notably its speed. Significant speed reduction along sandy block are reported in [176, 267, 172].

Civil Works

The SSLS attained by the civil works is a partial obstruction of the railway embankment culverts by the sedimented windblown sand. Even if this is a recurrent issue on the field (Figure 2.5 a), it is scarcely studied in the scientific literature, with an exception in [216].

Track Superstructure

The following track superstructure SSLS are identified:

- ballast contamination (or ballast fouling) due to windblown sand is the most common example of SSLS. The sand acts as an external source of fine material (defined as the surface spillage in [213]) infiltrating from the upper surface of the ballast bed. In the normal conditions, surface spillage contributes to about 7% of the ballast contamination, but it largely prevails in the desert environment. Attainment of ballast contamination is generally defined by referring to the permitted level of fouling, quantitatively expressed by a suitable fouling metric, e.g. Fouling Index [213], Void Contaminant Index [230],

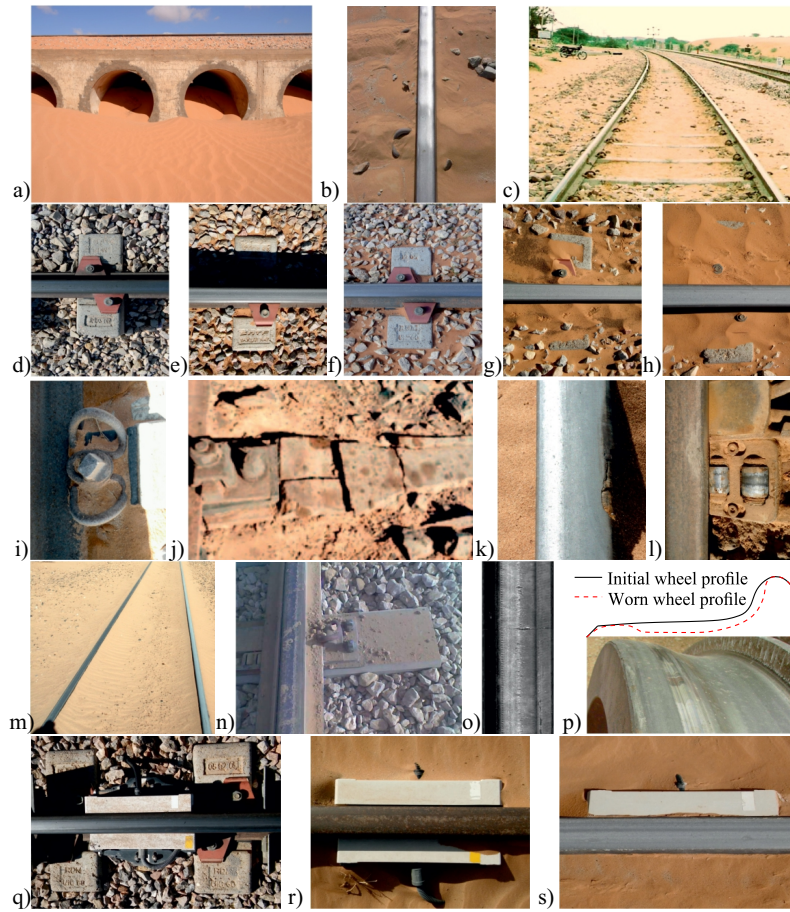


Figure 2.5: Sand Serviceability Limit States. a) Partial obstruction of embankment culverts. Ballast contamination induced problems: b) Rail corrugation [reprinted from: 238, with the permission from Elsevier, photocredit: W. R. Tyfour], c) Track drainage malfunction [reprinted from: 78, with the permission from Elsevier]. d-h) Levels of ballast contamination. Corrosion of track superstructure elements due to salt content in sand: i) contamination of fasteners and rail web, j) degradation of sleepers [reprinted from: 78, with the permission from Elsevier], k) corrosion of rail head (courtesy of Astaldi). l) contamination of turnout moving components. Sand wearing induced issues: m) thin sand layer on the downwind rail head (incoming wind from left to right, courtesy of Astaldi), n) detail of the downwind rail head [reprinted from: 137, with the permission from Voestalpine], o) wearing-induced cracks on the rail head [reprinted from: 137, with the permission from Voestalpine], p) wheel profiling [reprinted from: 137, with the permission from Voestalpine]. Sand accumulation around Wheel Detectors: q) sand free WD, r) partially buried WD, s) fully covered WD.

or Percentage Void Contamination (PVC) [87]. Different allowable limits of PVC have been applied for different track standards and ballast depths. As an example, according to [118], for a concrete sleeper track with a 250 mm thick ballast, the allowable limit of PVC equals 30%. This limit is used to specify a ballast-cleaning process. The requirement of the ballast cleaning is to clean the minimum depth of 100 mm. Figures 2.5 (d-h) show the different levels of ballast contamination along the same railway line: clean ballast $0\% \leq \text{PVC} < 20\%$ (Figure 2.5 d); moderately-contaminated $20\% \leq \text{PVC} < 30\%$ to fouled ballast $\text{PVC} \geq 30\%$ (Figure 2.5 e, f); fully-buried ballast (Figure 2.5 g); fully-covered ballast (Figure 2.5 h). In the literature, there is a number of well-documented ballast contamination site observations, e.g. [272, 268, 92, 237]. Ballast layer fouling leads to:

- increasing of the stiffness and decreasing of the damping of ballast bed and rail support modulus. That causes an increase of the train-induced vibrations and additional damage to the superstructure components of the track, such as sleepers, rail pads and rails (see e.g. in-situ observation in [268] along the Iranian Bafgh-Mashhad railway, and laboratory full-scale box tests in [120]). The received share of axle load for under-wheel sleeper and sleeper bending moments are significantly higher in sand-fouled ballast than in the clean one [265]. Ballast fouling percentages of 12% and 50% involve a growth of the rail support modulus of about 182% and 454%, respectively [79];
- accumulation of the permanent deformation, increasing the surface deviation of the track [75];
- rail corrugation, as observed in-situ in [237] along the Aqaba Railway, Jordan (Figure 2.5 b). This is a phenomenon characterized by the route-wise periodic patterns on the rail head [238]. Besides negatively affecting the train induced dynamics, such anomalies result in environmental noise pollution as well. Affected rails are called the squealing or roaring rails [161];
- decreasing of the ballast drainage capacity, as observed in-situ in [5] (Figure 2.5 c). The test results in [230] show that a 5% increase of the Void Contaminant Index decreases the hydraulic conductivity by a factor of around 1,500 for the ballast contaminated by fine clayey sand;
- corrosion and degradation of the fastening system, e.g. r.c. sleeper and rail due to the salt content of the sand sedimented around them (Figure 2.5 i, j and k, respectively). To the best knowledge of the author, no specific studies about windblown desert sand are published on the topic, apart from qualitative observations of corrosion test in a saline mist chamber on a specially coated clip and its metallic screw [47];

- sand-induced effects on the dynamic behavior of the fastening systems. Laboratory dynamic bending load tests conducted in [47] on a single fastening system show that the sand penetrates the gaps between the upper surface of the pad and the rail foot. A significant increase of the overall stiffness of the fastening system of about +44% results;
- the windblown sand sedimented around railroad switches enters and becomes trapped in their components. This, in turn, leads to abrasive wear [254], increasing of the friction between sliding/rolling components (Figure 2.5 l), decreasing of the performance and durability of greases and lubricants [137];
- rail grinding induced by the thin sand layer sedimented on the wheel-rail contact interface. This SSLS has been first recognized along the heavy-haul North-South Railway in the Kingdom of Saudi Arabia [92, 137, 111], and more recently along the Haramain High Speed railway [86]. The thickness of the sand layer on the head of the rail is estimated in the order of a millimeter. The sand covered rail head is easily recognizable by its matte surface, compared to the shiny sand free rail head (e.g. the right and left hand rails in Figure 2.5 m, respectively). When a train travels on a rail covered by a thin sandy layer, it crushes sand grains and increases wearing (Figure 2.5 n). The physical phenomena that result in sand sedimentation on the rail head are scarcely investigated in scientific literature. In the study [111], it is conjectured this is due to the aerodynamic effects of the passing trains: the underside of the vehicle induces lifting of the sand previously sedimented in between rails, analogously to the well-known ballast lifting by high speed trains. Analogous effects are expected in the wake of the train. These train-induced lifting is expected to induce the sand covering of both rails, because related aerodynamic phenomena are symmetric in average. However, in-situ observations, e.g. [92] often reveal the asymmetric sand covering of the rails, i.e. covered downwind and sand-free upwind the rail head (e.g. Figure 2.5 m). The following explanation is proposed. The incoming wind flow separates at the head of the upwind rail. Here, the flow acceleration promotes the sand erosion and stops the sedimentation. Conversely, the low-speed flow recirculation in the track gauge promotes the windblown sand sedimentation around the downwind face of the rail gauge and on its head. This qualitative reading should be confirmed by the future quantitative studies. The sandy layer increases the friction coefficient up to approximately twice the value commonly seen in Europe or North America [111]. This induces adhesive vertical and gauge face wearing rates 18 to 24 times higher than an analogous North American railway [111]. A worn rail head with crack patterns on its surface is shown in Figure 2.5 (o). Because of the asymmetric sand sedimentation, in [92] it is estimated that the head of the downwind rail wears 2-3

times faster than the upwind rail, resulting in three-times more frequent rail replacement.

Rolling Stock

The rolling stock may attain the following SSLs:

- sand-induced wheel profiling results from the same aerodynamic phenomenon that induces rail grinding, i.e. the windblown sand sedimentation on the wheel-rail contact interface. Severe wheel wear problems have been observed on rolling stock operating along the heavy-haul North-South Railway in the Kingdom of Saudi Arabia [92, 137, 111] and along the Haramain High Speed railway [86]. The wheels adopted in four months track test along the Haramain line recorded very low performances in terms of durability, reaching the end of life within around 130,000 km [86]. Analogously, in [92] it is estimated that the wheel wears 2-3 times faster than the normal rate, and wheel replacement is 2-3 times more frequent. Both flange wear and hollow wheel occur (Figure 2.5 p [137]). According to [111], the wearing process is amplified along almost completely tangent alignments usually occurring in railway lines across deserts. Here, the wheel running bands consistently make contact with the same portion of the rail profile;
- sand impact on high-speed running trains. Premature wear of the train elements, especially the leading vehicle, may occur because of the high relative speed caused by the motion of high-speed trains in sand-laden air. Such a limit state has not been observed up to now in the field, but preliminary investigations have been recently proposed in the literature [182].

Signalling System

A number of signalling devices are often mounted on modern railways to detect and transmit rolling stock information. All of them are prone to be buried by sedimented sand, and damaged by mechanical sand removal operations. However, the sedimented sand is expected to affect their operability to a different extent, depending on their working principles. Even if, to the best knowledge of the author, scientific studies or technical specifications are not available in the literature, some devices are listed below:

- Wheel Detectors (WDs) are part of Axle Counting System, mounted on the side of the rail, and usually based on inductive sensor technology. Such sensors are traditionally [91] and widely used to measure train position or speed in desert environments. Due to their working principle, they are generally independent of sedimented sand [117]. Sand free, partially buried and fully covered WDs are shown in Figure 2.5 (q-s), respectively;

- balises are transmission units which communicate with the passing train. They are a part of the automatic train protection system. They are mounted along the center line of the track, and based on the Magnetic Transponder Technology. Its main function is to transmit and/or receive signals through the air gap between the balise and the train [239]. The sand covering induces the impairment in the balise performance, analogously to other debris [232]. The European mandatory requirements for achieving air-gap interoperability specify detailed functional and non-functional requirements for the balise and consider specific environmental conditions [239]. In particular, balise must fulfill the Input/Output characteristics when applying a 20 mm thick dry sand covering. At the time being, such a thickness can be tentatively adopted to quantify the SLS of balises;
- hot box and hot wheel defect detectors are mounted across the whole gauge, and based on infrared optics. Their working principle is expected to be strongly affected by sedimented sand covering.

The following partial remarks can be synthetically drawn about SLS:

- the verification of the railway line and its components at SLS is mandatory in order to cope with the safety issues;
- the undesired effects at SLS can be mitigated, but not completely removed.

2.3 Windblown Sand Mitigation Measures

Effective, durable, robust and sustainable SMMs are mandatory in order to satisfy the conditions at both SLS and SLS defined above. In the reviewed literature, there is a number of SMMs proposed in the past, notably in the last decade. Their rationale collection is needed in order to give an orienting framework to railway owners, designers, general contractors, and railway operators among the available technical solutions.

2.3.1 SMM Categorization Criteria in the Literature

Historically, the first SMMs categorization attempt has been presented in [198]. In his pioneering survey, Rahim proposes an early categorization of *methods adopted from time to time to deal with the evil*. Rahim's classification is driven by the two ordering criteria: space-extent and time-length. The first criterion allows distinguishing between: i.) country-wide measures, i.e. *to eradicate the evil from the country as a whole by a coordinated effort between various department like Forest, Irrigation, Road and Railways*; and ii.) narrow-strip measures, i.e. *arresting the onslaught of the sand dunes onto the railway track [...] in the narrow strip of*

the land belonging to the railway. The first group, also called *reclamation of the sand drifts* analogous to *solutions against desertification* in the current language, is no further articulated by Rahim. Conversely, the time-length criterion is further applied to the narrow-strip SMMs, so that permanent, semi-permanent and temporary SMMs are sorted by decreasing initial cost and increasing maintenance frequency and related variable costs. The Rahim’s time-length categorization has been recently revised in [264], where reference is made to the short-term and long-term approaches to the windblown sand challenges. In [133, 134], objective-based categorization is introduced. It is firstly applied to SMMs adopted for oil-field operations, with four selected objectives: i.) destruction or stabilization of sand dunes; ii.) diversion of wind-blown sand; iii.) direct and permanent stoppage or impounding of sand before the object to be protected; and iv.) rendition of deliberate aid to sand movement so as to avoid deposition over the object. Analogously, four other objectives are adopted in [248]: i.) enhancement of the deposition of entrained sand; ii.) enhancement of the transportation of sand; iii.) reduction of the sand supply; and iv.) deflection of the moving sand. Objective-driven classification with reference to the SMMs employed along the Qinghai-Tibet railway is recently given in [51]: i.) sand-resistance engineering measure; ii.) sand-stabilization engineering measure; and iii.) sand-guidance engineering measure. Finally, it is worth citing the somewhat hybrid categorization proposed in [226], resulting in three categories: i.) protection management; ii.) stabilization management; and iii.) land management.

In the author’s opinion, each criterion has its pros and cons. The space-extent and time-length based categorizations are technically sound, because they lie in the design dimensions, but they fail in guaranteeing the categorization uniqueness: a single kind of SMM (e.g. straw checkerboard) can belong to both country-wide measures and narrow-strip ones, while the time-length of a SMM (e.g. a sand trapping ditch) strongly depends on its capacity (e.g. its size). The objective-based categorization are directly informative once the design goals are fixed, but once more, it does not guarantee the categorization uniqueness: the same SMM (e.g. a porous fence) can be adopted to reach multiple objectives, e.g. enhancement of the deposition of entrained sand, reduction of the sand supply, deflection of the moving sand in [248]. Furthermore, such categorization is not directly defining the SMM spatial location.

2.3.2 Sand Mitigation Measure Categorization: the New Proposal

In the following, a new categorization of the SMMs is proposed with the goal of partially contributing in overcoming the previously mentioned shortcomings. The categorization criterion follows the SMM location with respect to the sand course. An innovative *Source-Path-Receiver* (SPR) scheme results (see Figure 2.6):

1. *Source* SMMs are directly located over the sand source (dunes or loose sand sheets), whatever the spacing between the sand source and the infrastructure is. They are almost independent from the type of infrastructure.
2. *Path* SMMs are located along the windblown sand path ranging from the sand source to the infrastructure. They depend on the overall geometry of the infrastructure, e.g. point-wise or line-like infrastructure components.
3. *Receiver* SMMs are directly located on the infrastructure (e.g. the railway or its shoulder). As a result, they strongly depend on the type of the infrastructure.

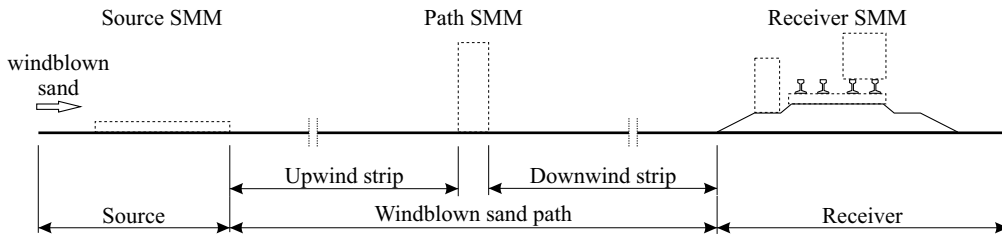


Figure 2.6: Conceptual scheme of the Source, Path and Receiver SMM classification.

SPR categorization can be complemented by the recognized SMM working principles from the reviewed literature: i.) the sand-modifying, where the mitigation is achieved by modifying the properties of sand; ii.) the aerodynamic, where the mitigation is carried out by changing the local wind flow; and iii.) the sand-resistant, where the mitigation is achieved by improving the material properties of the infrastructure component to be protected. Such major differences in the working principles results from the multidisciplinary in windblown sand mitigation. In this overview, the focus is put on the aerodynamic-based SMMs.

It is also worth pointing out that SPR categorization is consistent with a complementary criterion based on the windblown sand processes. The windblown sand movement is described by the three main processes: erosion, transport, and sedimentation, i.e. ETS model as defined in [190]. The sand-modifying and Aerodynamic SMMs aim at controlling, promoting and/or preventing such processes. Table 2.1 shows the correlation between the SPR classification and ETS processes.

The working principle of source SMMs is mainly based on preventing sand source erosion. Path SMMs aim at controlling sand transport by driving the wind flow and/or promoting sand sedimentation at the safe distance from the infrastructure. Receiver SMMs are applied to control the transport of windblown sand by deflecting it from the infrastructure, and/or by promoting the erosion of the sedimented

Table 2.1: Correlation between types of mitigation measure and sand moving processes.

	1. Source	2. Path	3. Receiver
Erosion	Prevented		Promoted
Transport		Controlled	Controlled
Sedimentation		Promoted	Prevented

sand. Once the sand is eroded from the infrastructure by the Receiver SMM, the further sedimentation is prevented.

Finally, the proposed SPR scheme corresponds to the introduced SLS. Correlation between the SPR classification and SLS is shown in Table 2.2.

Table 2.2: Correlation between types of mitigation measure and Sand Limit States.

	1. Source	2. Path	3. Receiver
SULS	✓	✓	
SSLS			✓

Source and Path SMMs are mainly addressed to mitigate massive sand erosion and transport upwind the infrastructure, i.e. reducing the sand flux responsible for SULS. However, even if such SMMs exhibit high sand trapping performance, it is not likely that they completely trap the whole incoming windblown sand and cope with SSLS. Receiver SMMs are employed to cope with SSLS once the Path and Source SMMs remove the threat of SULS. The aerodynamic Receiver SMMs are addressed to avoid the local sedimentation on the railway body of small amount of sand filtered by Source and Path SMMs. The sand-resistant Receiver SMMs are ad-hoc modified track superstructure components characterized by increased sand resistance, i.e. increased lifetime.

Bearing in mind the matching of the SPR categorization with ETS and SLSs, the proposed classification also offers a new rationale to the combined use of complementary SMMs, as recently proposed by other authors, e.g. in [51, 257, 53, 54]. It is, however, worth to be stressed that the proposed SPR categorization does not necessarily cover any potential sand mitigation strategy that can be imagined. Figure 2.7 shows the synoptic scheme of the proposed categorization, and anticipates the sub-categories reviewed in the following.

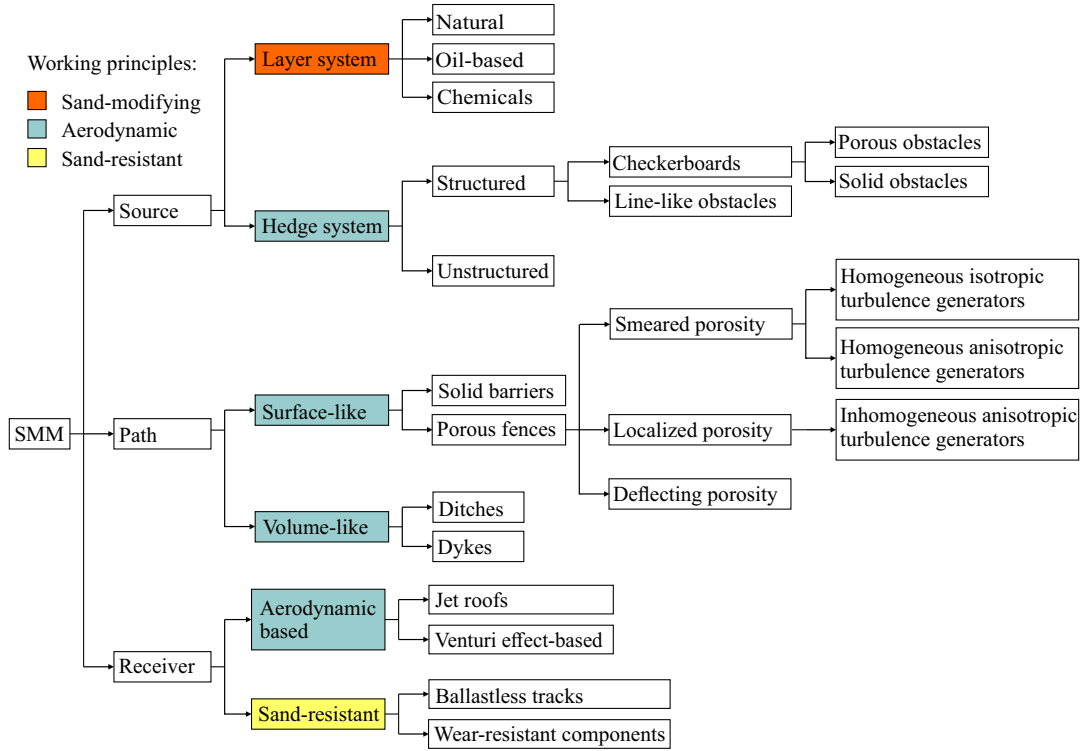


Figure 2.7: Scheme of the proposed SMM categorization.

2.3.3 Source Sand Mitigation Measures

Source SMMs aim at reducing incoming windblown sand flux by: i.) reducing erosion from localized sand sources (e.g. sand dunes) and/or smeared sources (e.g. loose sand sheets); or ii.) stopping mobile dunes, such as marching (e.g. Barchan dunes) or unstable dunes, (e.g. transverse dunes evolving in barchanoid chains). Such measures have been mainly developed and applied in International [157] and National [e.g. 225, 246, 19, 206] Country-wide systematic actions against desertification. In this perspective, the ten-kilometers-wide green belts are by far wider than the railway corridor, and its objectives are beyond the funding capabilities and the scope of the railway promoters. At a smaller scale, such measures have been also applied in tens-of-meter-wide areas to control small dune fields, single dunes or loose sand sheet in the infrastructure corridor, e.g. [3, 150, 51]. In the following, desertification literature is referenced regarding the technique categorization, while engineering bibliographic references are given for infrastructure applications. The approach usually involves short-term, temporary stabilization of the sand surface, followed by progressive, long-term, permanent stabilization by means of vegetational covering. Source SMMs can be further divided into *Layer systems*, also called mulching techniques [21], and *Hedge systems* [131], on the basis

of their working principle.

Layer System

The idea behind the layer systems is taken from the nature, where it was observed that the sand layer is prone to crusting. Figure 2.8 (a) shows a naturally crusted surface of sand. The crusting phenomenon relies on increasing of cohesive forces between the sand grains, consequently increasing the erosion threshold $u_{*,t}$ by cementing the sand surface. In such a way, the incoming sand flux is reduced according to the Eq. 2.1. The moisture content of dry sand is approximately 0.2 – 0.6% depending on the moisture of the surrounding atmosphere. When a sand layer is wet, moisture is retained by sand as a surface film. Thus, cohesion results from the tensile forces between water molecules and sand grains. A content of moisture above 4% fully stops the sand grain movement, at least under the incoming wind speed tested in wind tunnel experiments in [20] and [126]. Salt in low concentrations can significantly raise the erosion threshold, even without increased content of moisture. Salt and other cementing agents act as cement at points of grain contacts. The cementing effect can be achieved by artificially increasing the moisture content or other cementing agents like salt, clay skins, fungal hyphae, algae and lichens [192]. According to the material used, the layer SMMs can be divided into: i.) the natural material layers, such as soil, salty water, biological crust; ii.) the oil-based layers, such as asphalt, see Figure 2.8 (b) [248, 8], high gravity waxy oil, crude oil [3]; and iii.) layers made of chemical products [231, 218].

Besides the growth of the erosion resistance they induce, materials applied in the layer SMMs should satisfy industrial criteria such as durability, water solubility, cost, environmental effects and in-situ availability, among others. In the example of the asphalt-latex mixture used as a layer SMM shown in Figure 2.8 (b), the mixture is laid using a pressure injection technique which achieves penetration up to 28 mm. The penetration depth is an important parameter in order to avoid the destruction of the layer due to dune movements. For a thicknesses lower than 10 mm, dune movements cause the collapse of the treated surface making the SMM ineffective [248].

Hedge System

The hedge system involves discontinuous, closely-spaced obstacles placed on the ground to increase its aerodynamic roughness length (z_0), and in turn, to locally reduce the shear stress at the wind-sand interface. Indeed, a decrease in wind shear stress leads to a reduction of the sand transport rate (see Eq. 2.1). Obstacles could be arranged in a regular or irregular patterns, resulting in two hedge sub-categories: i.) the structured hedge system; and ii.) the unstructured hedge system.

Structured hedge systems can be divided into the pointwise obstacles and the

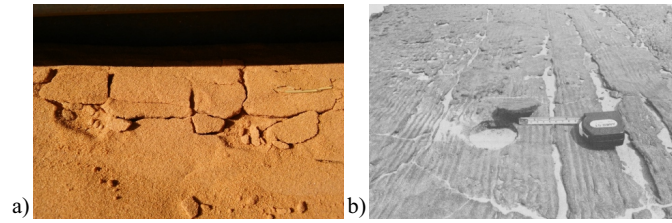


Figure 2.8: Layer system. a) Natural sand crusting, b) asphalt-latex mixture layer [reprinted from: 248, with the permission to reuse under a Creative Commons Attribution License].

checkerboard systems. Some examples of the pointwise obstacles as an SMM are reported in [95, 94]. The checkerboard solution (Figure 2.9 a-c) is the most widely adopted structured hedge system, since the early field tests along the Baotou-Lanzhou railway in the 1950s [153]. Small obstacles are usually manually arranged in an orthogonal and equally spaced alignments, resulting in square cells. About half of the obstacle is buried in the sand, while the other half is above the ground level and exposed to the wind. An SMM example similar to the checkerboard system is shown in Figure 2.9 (d). A structured array of line-like obstacles are arranged orthogonally to the prevailing wind direction. As a result, it is only effective for the orthogonal winds. Several materials are used depending on the in-situ availability, and according to this criterion structured hedge system can be further divided in:

1. the porous obstacles, built from straw [Figure 2.9 a, 263], reed [73], polyethylene-net [Figure 2.9 b, 51], and coconut leaves [Figure 2.9 d, 149];
2. the solid obstacles, e.g. stones [Figure 2.9 c, 272].

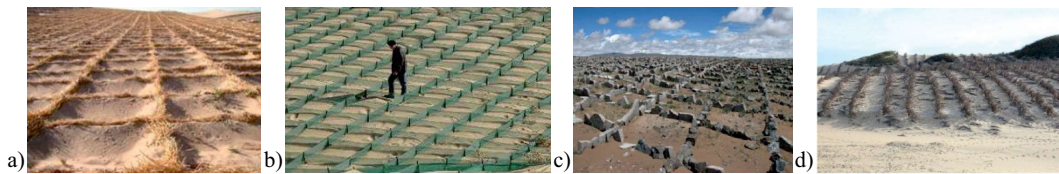


Figure 2.9: Structured Hedge system: a) straw checkerboard [reprinted from: 104, with the permission to reuse under a Creative Commons Attribution License], b) polyethylene-net checkerboard [reprinted from: 272, with the permission from Elsevier], c) stones checkerboard [reprinted from: 272, with the permission from Elsevier], d) array of line-like obstacles [reprinted from: 149, with the permission to reuse under a Creative Commons Attribution License].

The aerodynamic working principle of checkerboard system is qualitatively shown in Figure 2.10. Generally speaking, the flow regime inside a cavity (i.e. the checkerboard cell) mostly depends on the aspect ratio $AR = w/h$, where w is the width and h the height of the cell [179]. As a result, three characteristic flow regimes are defined [23]: i.) skimming flow ($AR \leq 1.5$), where only a single vortex appears inside of a cavity; ii.) wake interference flow ($1.5 \leq AR \leq 2.5$), where the main vortex is significantly shifted downwind and a stable secondary counter rotating vortex appears; and iii.) isolated flow ($AR \geq 2.5$), where the flow is qualitatively similar to the flow around an isolated obstacle, i.e. a large vortex appears downwind the obstacle, the flow reattaches and again separates in front of the downwind obstacle. In the real world applications along railways, the cell side length usually varies from 1 to 3 m, and the exposed height is from 10 to 30 cm respectively, resulting in an $AR \approx 10$. Hence, the flow inside the cell should correspond to the isolated flow regime. Figure 2.10 (a) shows the conjectured flow regime for an array of cells bounded by solid obstacles. Recirculating vortices drain energy from the

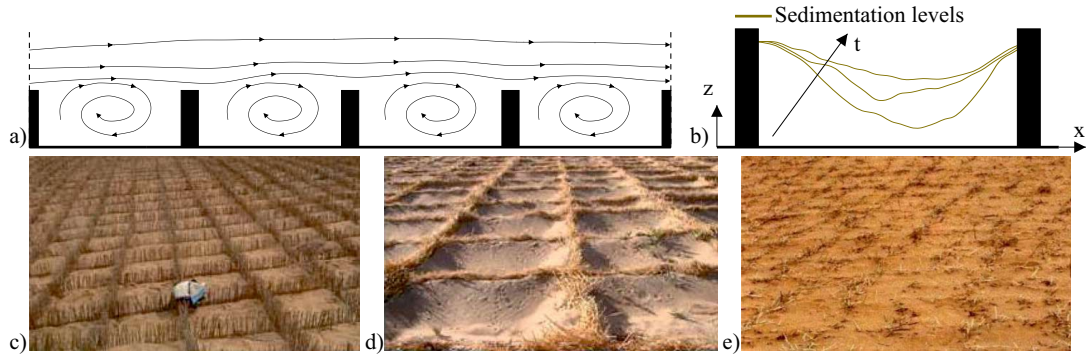


Figure 2.10: Checkerboard Hedge system: a) Isolated flow regime inside cells (cells geometry scale: $Dz \approx 2Dx$), b) corresponding qualitative sedimentation levels in a cell [redrawn from: 148, sand sedimentation levels scale: $Dz \approx 6Dx$], c) initial unstable condition of empty cells [reprinted from: 104, with the permission to reuse under a Creative Commons Attribution License], d) stable concave surface [reprinted from: 104, with the permission to reuse under a Creative Commons Attribution License], e) stable flat surface [reprinted from: 193, with the permission from Elsevier].

incoming wind flow, by reducing the mean wind velocity. The reduction of wind velocity near the ground can be accounted for via the increase of the aerodynamic roughness length to about 0.015 m, i.e. about 1,000 time greater than the one of a flat sandy surface.

The sand level evolution inside a cell is qualitatively given in Figure 2.10 (b). The arrow crossing the sand levels depicts the trend of the sedimentation process.

Figure 2.10 (b) is complemented by Figure 2.10 (c), (d) and (e), where the real world examples of the sand level inside cells are shown. The two vortices inside the initially empty cell promote sand sedimentation close to the inner side of the obstacles (see Figure 2.10 c). At the equilibrium between erosion and sedimentation, two different stable conditions result in the cell, differently reducing wind velocities [193]:

- a concave sand surface with a the aspect ratio ranging between 1:10 and 1:8 (see Figure 2.10 d). In this configuration, the SMM is working properly and is preventing further erosion;
- a flat sand surface at the top of the exposed part (see Figure 2.10 e).

When the checkerboard is completely buried by sand, it is unable to further promote sand sedimentation and it becomes a sand source in turn. As a result, manual sand removal maintenance is required. Alternatively, vegetation growth may be promoted inside the cells, once the sand inhibits most of the cell volume. Since the evaporation rate is inversely proportional to the aerodynamic roughness [61], the adoption of checkerboards allows for an increase in sand bed moisture and in turn to the promotion of vegetation growth. Despite the number of scientific studies devoted to the topic of sand sedimentation around checkerboard system, the critical values of the full set of parameters inducing the transition from the favorable (i) to the unfavorable equilibrium condition (ii) are still not clearly defined. For a recent review of sand sedimentation in the checkerboards, see [148].



Figure 2.11: Unstructured Hedge system: a) gravel surface [reprinted from: 150, with the permission from Elsevier], b) large roughness elements [reprinted from: 96, with the permission from Elsevier], c) trees planted over dunes near a railway.

Unstructured hedge solutions are often employed in the form of gravels spread on the sandy surface (Figure 2.11 a). However, attention should be paid to the both, gravels size and covering ratio since they can be buried by sand leading to an increment in the sand source [150]. Irregular vegetation pattern could be also ascribed to this subcategory. An attempt to mimic a natural vegetation pattern by arranging large-size roughness elements, such as straw bales, is described in [96] (Figure 2.11 b). Since they do not require water for their maintenance, they

could be preferred to the plant-based SMMs. Permanent stabilization of sand is possible with an artificial vegetation layer upwind the infrastructure planned to be protected. However, attempts of vegetative stabilization should consider the inter-relationships between several physical and biological habitation factors, most importantly the quantity of available water. A vegetation system around a single oasis takes the form of shelterbelts. For more details, the interested readers are referred to the recent in-situ observation at the Minqin oasis, Badai Jaran Desert and Tengger Desert (in Gansu Province) [159]. A vegetation system along line-like infrastructures takes the form of upwind and downwind vegetation belts. This vegetation solution has been adopted in the recent past along the Jing-Tong Railway [129] and the Tarim Desert Highway crossing the Taklamakan Desert [73]. An example is shown in Figure 2.11 (c).

2.3.4 Path Sand Mitigation Measure

The goal of Path SMMs is the promotion of sand sedimentation, achieved by controlling windblown sand transport, i.e. by driving the local wind flow in turn. The wind flow is modified by reducing the longitudinal component of its velocity and/or by promoting flow recirculation. Due to the amount and variety of Path SMMs proposed in the literature, they are further divided into two subcategories, according to a geometric criterion:

1. the above-ground Surface-like SMMs, i.e. solid barriers and porous fences (Figure 2.12 a,b);
2. the volume-like SMMs, i.e. ditches, dikes and ridges (Figure 2.12 c,d,e).

Such a classification is also compliant with the sedimentation mechanism they induce. The surface-like SMMs promote sedimentation along the upwind and/or downwind strips (see Figure 2.6), while the volume-like SMMs additionally allow sand sedimentation over and inside them. Whatever the geometry of Path SMMs, they can be arranged in two main configurations, as shown in Figure 2.13. Both the configurations tend to preserve the angle of attack $\alpha = 90^\circ$ between the direction of the prevailing wind and the SMM longitudinal axis. In the case of skewed winds with respect to the railway longitudinal axis, ($\theta \neq 90^\circ$, as shown in Figure 2.13 b), the SMM modules are slanted and their tips overlap along the wind.

Since the current state of the art does not allow a comparative and comprehensive quantitative assessments of every Path SMM, qualitative schemes representing the morphodynamics of sand accumulation are provided in the following subsections.

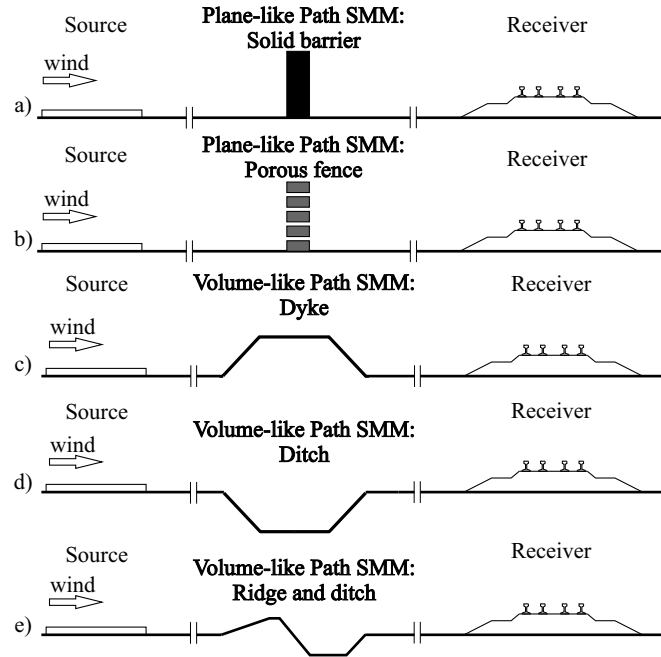


Figure 2.12: Path SMMs: surface-like (a,b), volume-like (c,d,e).

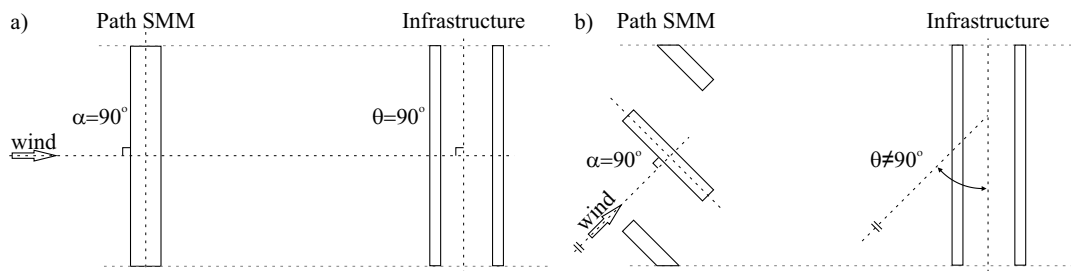


Figure 2.13: Path SMM arrangement configurations: a) wind direction orthogonal to the longitudinal railway axis, b) skewed wind direction.

Surface-Like

The optical porosity β is the degree of permeability of a surface-like SMM, i.e. the percentage ratio of the open area to the total area [142]. It is commonly considered as the most important parameter controlling the performances of straight vertical surface-like SMMs of a given height. Based on that, surface-like SMMs can be further divided into two main categories:

1. porous fences, if $\beta > 0$;
2. solid barriers, if $\beta = 0$.

Porous fences have been widely investigated in the scientific literature since the early aerodynamic studies at the beginning of the 20th century, e.g. [15], and the pioneering applications to control windblown snow, e.g. [88] and windblown sand, e.g. [163]. The research activity about fences has been recently reviewed with respect to the wind loads [93], the aerodynamics [113], and the induced morphodynamics [144, 244]. Conversely, the scientific studies on solid barriers are surprisingly scarce, and usually limited to the aerodynamics [11, 98, 143] and sand morphodynamics [116, 60] of SVW. In the following, straight vertical surface-like SMMs are reviewed first, and solid SVWs are viewed as a limit case of porous fences with $\beta = 0$. Solid barriers with shapes other than the straight vertical plane are scrutinized as well.

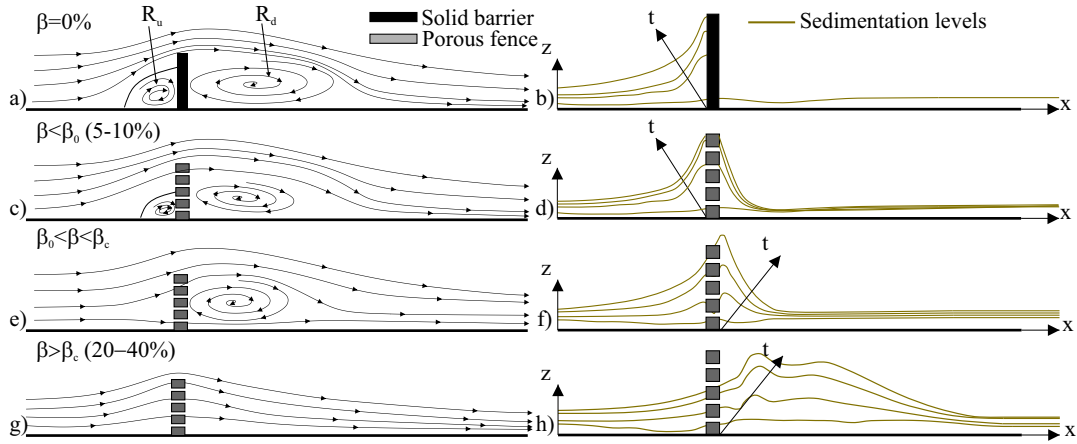


Figure 2.14: Wind flow mean streamlines and related sedimentation levels around: (a,b) solid SVW barriers [redrawn from: 11, 116], (c,d) very low porosity fences [$\beta < \beta_0$, redrawn from: 71, 116], (e,f) low porosity fences [$\beta_0 < \beta < \beta_c$, redrawn from: 260, 116], (g,h) high porosity fences [$\beta > \beta_c$, redrawn from: 260, 116]. Sand sedimentation levels scale: $Dz = 5Dx$.

Figure 2.14 collects the results from a number of experimental studies in order to describe the evolution of both the wind pattern and the sand sedimentation process versus the porosity ratio. The wind pattern around zero porosity SVW barriers, Figure 2.14 (a) [11], is characterized by a large reversed flow region in the wake of the barrier (R_d) and by a stable clockwise vortex upwind of the barrier (R_u) below the stagnation point. R_u reduces the wind shear stress close to the ground and promotes upwind sand sedimentation in turn, Figure 2.14 (b) [116], acting as a sand trapping vortex. As a result, the larger the upwind vortex, the higher the upwind sand accumulation potential, i.e. the maximum amount of trapped sand volume [39]. An increment of the porosity, Figure 2.14 (c) [71], induces the shrinking of the stable clockwise vortex R_u . The watershed value $\beta_0 \approx 5 - 10\%$ is defined as the one at which R_u vanishes. Given the non-zero porosity, sand sedimentation occurs on

both sides of the fence with a downwind steep slope, Figure 2.14 (d) [116]. However, most of the sedimentation still occurs upwind of the fence. A further increment of the porosity induces the growth of R_d , Figure 2.14 (e) [260]. This occurs in the interval $\beta_0 < \beta < \beta_c$, where β_c is defined as the porosity value at which the reversed flow region in the wake of the barrier R_d vanishes, too. Most of the sedimentation occurs downwind from the fence and the downwind slope is shallower, Figure 2.14 (f) [116]. For values of β greater than the critical value $\beta_c \approx 20 - 40\%$ [144], the flow is dominated by the bleed flow through the fence openings, Figure 2.14 (g) [259]. Sand sedimentation is no longer induced by the reversed flow downwind the fence, but simply by the velocity defect in its wake, Figure 2.14 (h) [116]. The porosity $\beta_{opt} \approx 40 - 50\%$ is widely established as the optimal value in the terms of the sand trapping overall efficiency [208, 27], defined as the maximum volume of accumulated sand per fence unit length, irrespectively of where sedimentation occurs. Fences with β higher than 50% are rarely used, because of their low sand trapping efficiency [116].

The variability of the values of β_0 , β_c and β_{opt} testify that the porosity ratio, i.e. a macroscopic feature, cannot summarize all the relevant parameters that drive the aerodynamics and sand morphodynamics of porous fences. Besides the porosity ratio, sand sedimentation depends on a number of other parameters. Some of them are not directly related to the SMM (e.g. environmental and experimental setup, related incoming wind conditions, measurement uncertainties), while others are related to SMM features, such as the size, shape, distribution and orientation of openings and solid elements [144]. Based on that, porous fences are herein further divided into three subcategories: i.) the fences with smeared porosity; ii.) the fences with localized porosity; and iii.) the fences with deflecting porosity.

Fences with *smeared porosity* are fences whose openings have characteristic length(s) several orders of magnitude smaller than the fence characteristic length, i.e. its height. Some schemes of the most common types of smeared porous fences are given in Figure 2.15. Further division of smeared porosity fences is made according to the induced wake turbulence properties. In particular, porous fences will induce anisotropic turbulence when the opening characteristic length distribution is constant, but differs between vertical and horizontal dimensions (Figure 2.15 a, b), while they will induce isotropic turbulence when opening characteristic length distribution is the same in both dimensions (Figure 2.15 c, d, e, f). The induced wake turbulence, i.e. grid-generated turbulence in the literature [234, 138], has a characteristic length scale of the same order of magnitude of the solid element size. Among the latter, fractal porous fences have been recently proposed in [162]. They are expected to induce multiple wake turbulence characteristic length scales.

Fences with *localized porosity*, also called turbulence generators or wind weakeners in the literature, are characterized by openings having characteristic length(s) of the same order of magnitude of, or one order of magnitude smaller than, the fence height. Accordingly, the wake turbulence characteristic length scale is of the

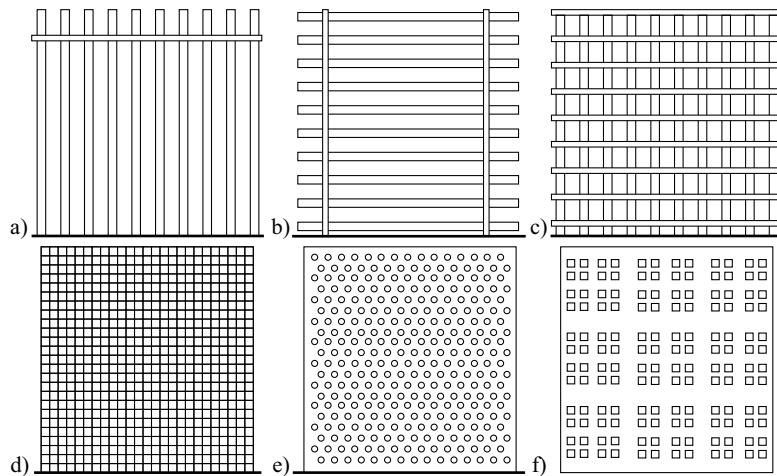


Figure 2.15: Fences with smeared porosity. Homogeneous anisotropic turbulence generators: a) vertical slats, b) horizontal slats. Homogeneous isotropic turbulence generators: c) grid fence, d) nylon net fence, e) holed fence, f) fractal fence (a-e redrawn from [71], f redrawn from [162]).

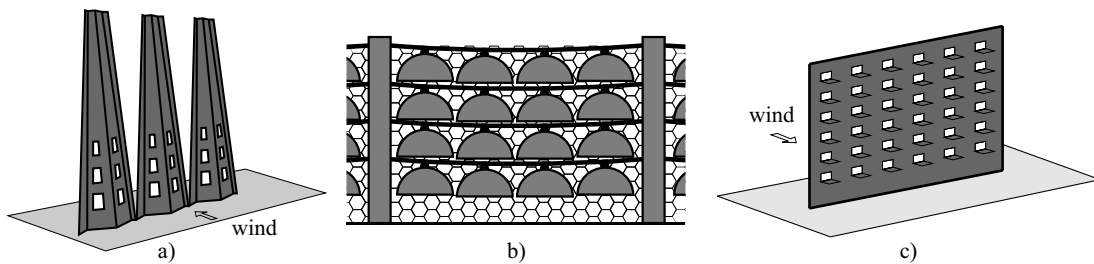


Figure 2.16: Fences with localized porosity: a) spire-shaped [redrawn from: 27], b) leaf-shaped [redrawn from: 273].

same order of magnitude of the characteristic scale of the local mean flow, and strongly interacts with it. Some examples of localized porosity fences are given in Figure 2.16: an alignment of spire-shaped glass-fiber modules shown in Figure 2.16 (a) [27] is analogous to spires usually adopted in boundary layer wind tunnels; an array of leaf-shaped concrete modules hanged by suspension cables shown in Figure 2.16 (b) [273, 51].

Fences with *deflecting porosity* include solid elements inclined out of the fence plane, such as vanes, slats or plates. Some of these fences were patented in the last decades [158, 205], but only recent scientific studies have been devoted to study their aerodynamic and sand morphodynamic behavior [50, 53]. Figure 2.17 shows the deflecting porosity fences studied in the cited articles. Both deflecting porosity

fences are intended to guide the flow upwards. The working principle of the deflecting inclined elements is twofold: i.) guiding the mean bleed flow along target directions, i.e. downward, upward or laterally; and ii.) reducing the wake turbulence intensity with respect to the classic porous fences.

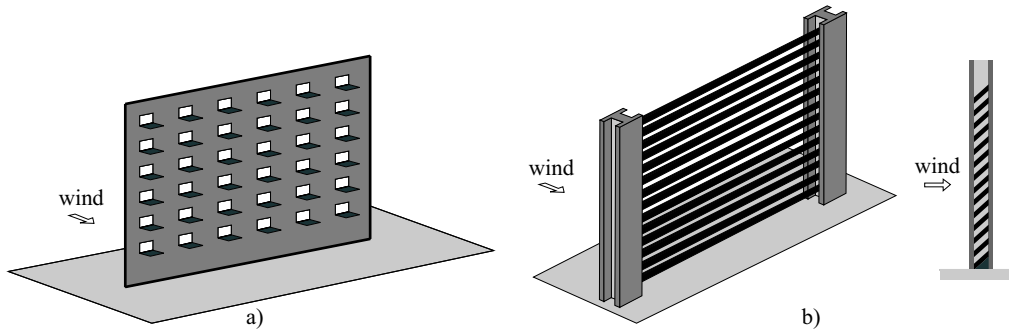


Figure 2.17: Fences with deflecting porosity: a) guide plates downwind rectangular openings [redrawn from: 50], b) array of inclined slats [redrawn from: 53].

Fences with *homogenous porosity* are one of the oldest type of built SMMs [133]. A traditional example is given in Figure 2.18 (a). Such fences have been developed through the years in order to improve their durability and maintainability, resulting in e.g. polymer nets (Figure 2.18 b). An actual example of fences with localized porosity made by reinforced concrete panels is given in Figure 2.18 (c).



Figure 2.18: Fences with smeared porosity: a) traditional fence protecting a palm plantation (explicit publishing permission from the owner of the photos: Nouar Boulghobra); b) nylon net fence [reprinted from: 151, with the permission to reuse under a Creative Commons Attribution License]. Fences with localized porosity: c) concrete fence [reprinted from: 273, with the permission from Elsevier].

Porous fences with smeared porosity are often applied to promote the rapid growth of artificial bell-shaped dunes in coastal regions to protect residential areas from the hazardous effects of both wind and water [208]. Figure 2.19 (a) shows a six-year-long dune growing process. First, a single porous fence is installed where the

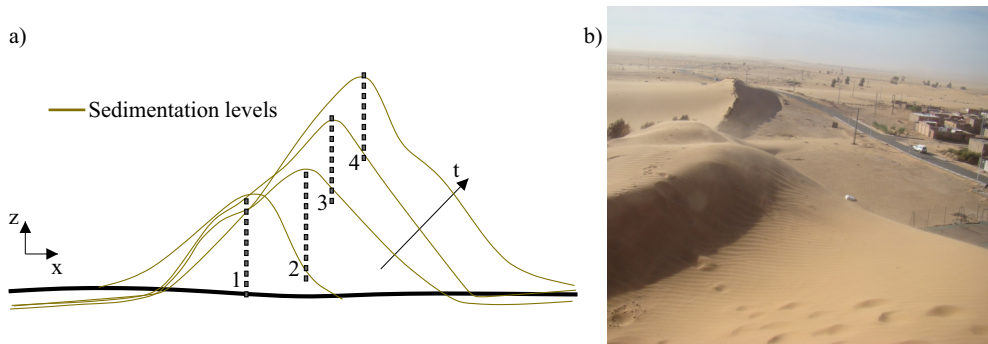


Figure 2.19: Artificial dune growing: a) scheme of the process [redrawn from: 248, sand sedimentation levels scale: $Dz = 5Dx$, Fence 1 (t_1) - placed in December 1962, Fence 2 (t_2) - placed in January 1963, Fence 3 (t_3) - placed in March 1964, Fence 4 (t_4) - placed in March 1966, final shape - July 1968], b) a questionable application to stop the windblown sand (explicit publishing permission from the owner of the photo: Nouar Boulghobra).

dune is needed. When the accumulation of the sand exceeds the height of the barrier, a second barrier is positioned on top of the accumulated sand. The process is repeated each time a fence is buried. The numbers depicted in Figure 2.19 (a) indicate the order in which porous fences were positioned. An example of questionable application of artificial dune growing for windblown sand mitigation of a village in the desert is shown in Figure 2.19 (b), where porous fences are used to shape a dune upwind from the road. The dune upwind slope acts as a launching pad for the incoming windblown sand. In the figure, it can be seen that, even though a massive dune was created upwind the road, sand is still partially covering it.

Actual porous fences are usually straight and vertical, even if inclined porous windscreens have been investigated [67]. Conversely, the shape of *solid barriers* greatly affects the local wind pattern around them, and the sedimentation process in turn. To the author's best knowledge, existing solid barriers having different shapes with respect to the SVW are scarcely investigated in scientific literature so far. The parameters driving their design and controlling their performance have been systematically and rigorously discussed only recently [39]. However, solid barriers with alternate shapes have been heuristically designed and patented as SMMs in the past. Some examples are given in Figure 2.20. λ -shaped wooden barrier for railway applications is patented in [184]. Analogously, a λ -shaped precast r.c. barrier to be used as SMM for agroforestry applications is given in [183]. Very recently, the SMaRT team [41] have patented a novel solid barriers called *Shield for Sand*, equipped with an ad-hoc conceived upper windward concave deflector aimed at making the extent of the vortex upwind the barrier as large as possible even for high sedimentation levels. The conceptual design of *Shield for Sand* has been

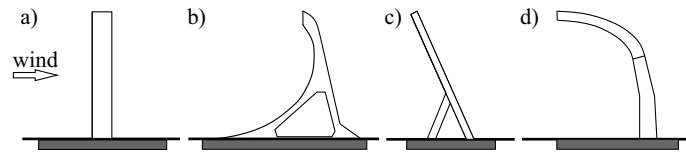


Figure 2.20: Geometry of aerodynamically-shaped solid barriers: a) common Straight Vertical Wall, b) pioneering shape by [184], c) [183], d) recent patent *Shield for Sand* [41]. Thick solid lines indicate the cross-section of the aerodynamic-effective surfaces.

carried out by computational simulations [39], and its performance assessment by wind tunnel test [44].

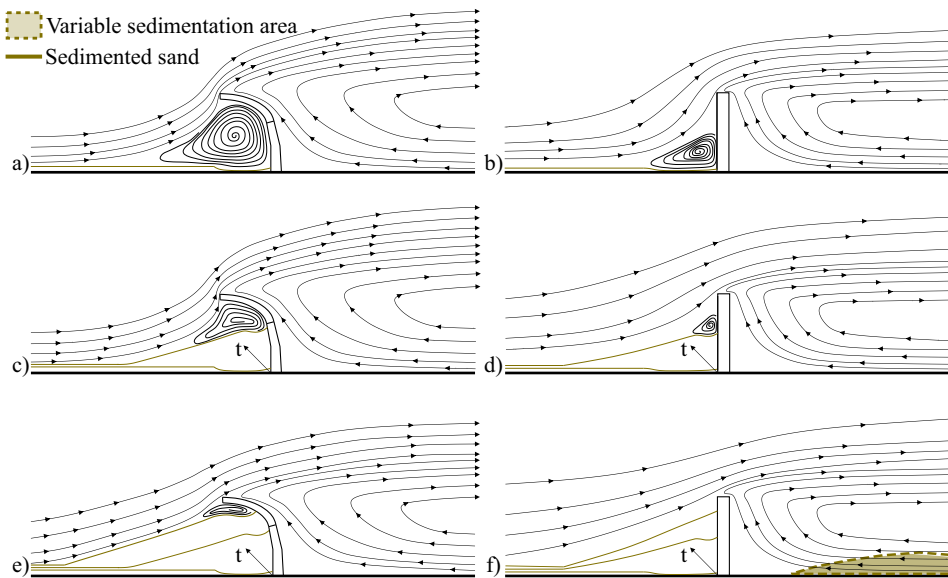


Figure 2.21: Shape induced differences in wind flow mean streamlines [from computational simulations in 39] and sand sedimentation levels [from wind tunnel tests in 116, 44]: comparison between *Shield for Sand* (a,c,e) and a SVW (b,d,f).

Figure 2.21 shows the comparison between SVW and *Shield for Sand* induced aerodynamics and morphodynamics for three different sedimentation levels. Both shape and size of the upwind clockwise vortex for about the same level of accumulation change significantly by varying the geometry of the solid barrier. In particular, *Shield for Sand* induces a larger upwind vortex with respect to SVW for low (Figure 2.21 a-b) and moderate (Figure 2.21 c-d) sedimentation levels. Higher upwind accumulation potential and trapping efficiency result in turn. The vortex upwind SVW vanishes for high sedimentation levels (Figure 2.21 f), while being still present

upwind *Shield for Sand* (Figure 2.21 e). The sedimented sand upwind SVW results in a launching pad for incoming windblown sand [116], i.e. windblown sand crosses over the SMM and contaminates the downwind strip and the railway. The severity of contamination depends on the wind field in the wake, the position of the reattachment point along the downwind strip, and the width of the strip itself, i.e. variable or uncertain sedimentation area in Figure 2.21 (f). Conversely, properly-shaped solid windward concave barriers prevent such undesired phenomena until the sedimentation level reaches the barrier height.

To the author’s best knowledge, SVWs are the only kind of solid barriers proposed and tested up to now in actual design practice. For instance, a 4 m-high, basic SVW has been proposed as an SMM in the preliminary design of the Segment 1 of the Oman National Railway Network [122]. A 1.5 m-high Jersey-like wall has been recently built along the Mecca-Medina high speed railway in Saudi Arabia [164], showing questionable performances. Some real world SVWs applied as SMM along railways are given in Figure 2.22 (a-c). The sand sedimentation level around them is low. Conversely, high sedimentation levels around other SVWs are shown in Figure 2.22 (d-f). SVWs are made of different materials and components,

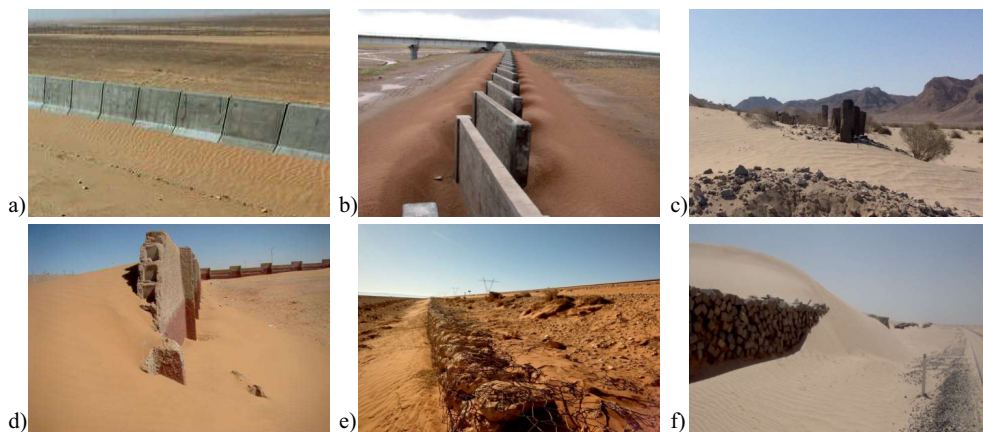


Figure 2.22: Straight Vertical Wall examples: a) precast r.c. modules [owner of the photo: R. Méndez, 164]; b) slanted, overlapped modules [reprinted from: 273, with the permission from Elsevier]; c) alignment of vertical sleepers (curtesy of Astaldi). Straight Vertical Wall sedimentation patterns: d) free-standing concrete wall [explicit publishing permission from the owner of the photo: Nouar Bolghobra, 30]; e) gabion wall adjacent to the toe of the railway embankment (curtesy of Astaldi); f) horizontally stacked sleepers (explicit publishing permission from the owner of the photo: Nouar Bolghobra).

built ad-hoc (e.g. Figure 2.22 b, d, e), obtained by adapting elements from other applications (e.g. Jersey barrier in Figure 2.22 a) or by recycling decommissioned

ones (e.g. sleepers in Figure 2.22 c and f). Some of the SVWs shown in Figure 2.22 are not necessarily intended as SMMs, e.g. courtyard perimeter wall, flood barrier, and sleeper stock in Figure 2.22 (d), (e), and (f), respectively. However, they clearly show the upper limit of the sedimentation (Figure 2.22 d). The subsequent transport of sand grains over the embankment shoulder (Figure 2.22 e), or the progressive burying of the downwind strip and railway track (Figure 2.22 e) is possible.

Volume-Like

Volume-like path SMMs share the same working principle of the surface-like ones: the goal is to decrease the incoming wind velocity, induce the recirculation flow around them, and promote sand sedimentation. To the author’s best knowledge, there are no published scientific papers specifically dealing with the aerodynamics and sand morphodynamics around dykes or ditches intended as SMMs. Hence, in the Thesis, the dyke and ditch aerodynamics is regarded equivalent to upward/backward facing step and axisymmetric cavity, respectively (schemes in Figure 2.23 a, b). The corresponding qualitative schemes of sand sedimentation levels are shown in Figure 2.23 (c,d). Sand accumulation over ditches and dykes is

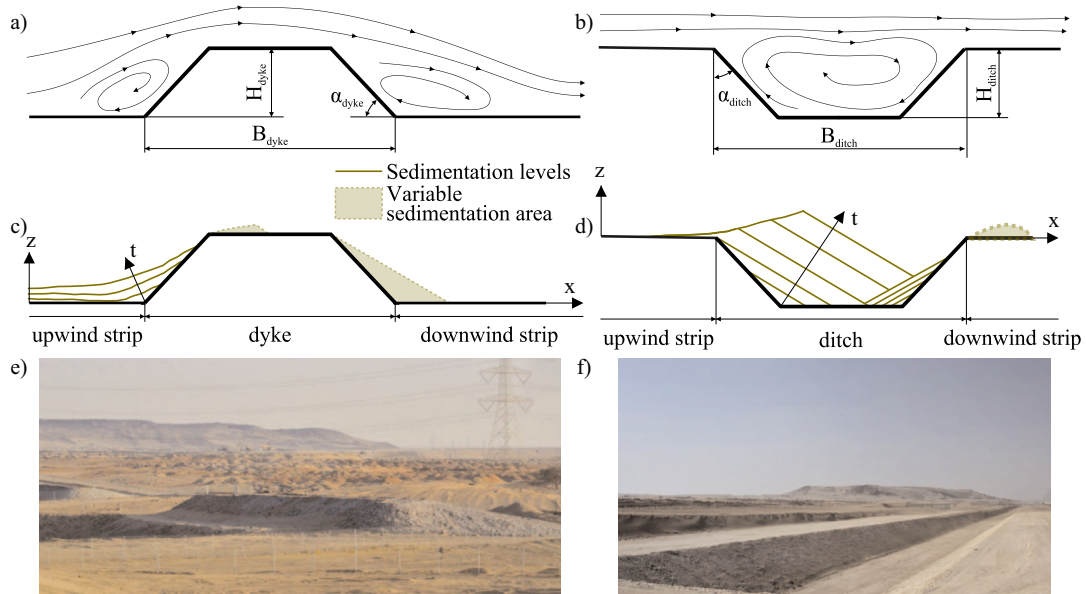


Figure 2.23: Volume-like SMMs. Wind flow mean streamlines around a) a dyke [redrawn from: 188], and b) a ditch [redrawn from: 220]. Sand sedimentation levels around c) a dyke [redrawn from: 116], and d) a ditch. Examples of actual volume-like SMMs during field trials: e) a dyke [reprinted from: 186], and f) a ditch [reprinted from: 186].

mainly affected by their geometric parameters, i.e. height (H), width (B) and slope (α). Dykes induce flow recirculation and consequently sand sedimentation mainly on the upwind slope, while ditches reverse the flow promoting sedimentation mainly inside the cutting. At the equilibrium between sedimentation and erosion, the sand accumulated along the upwind shoulder of the dyke reduces its slope angle up to about 10 degrees [139], i.e. the upwind vortex disappears, the upwind slope acts as a launching pad for incoming windblown sand, the sand crosses the dyke and contaminates the downwind strip. It follows that the accumulation potential of a dyke is expected to be relatively low compared to its volume. Conversely, the accumulation potential of a ditch is close to its volume, provided that its cross-section is properly shaped, so that the vortex inside the cutting is maintained at high sedimentation levels as well. From the economic point of view, ditches and dykes involve construction costs higher than the surface-like path SMMs, because of the large amount of excavation and required earth-moving works. In the recent years, dykes, ditches or a combination of the both have been proposed for different railway projects along the Arabian peninsula [185, 186, 42, 59].

In general, maintenance is mandatory to periodically remove sand sedimented around both, the surface-like and the volume-like Path SMMs. Solid barriers have to be cleaned upwind before sand trapping efficiency dramatically decreases. Porous fences have to be unburied both upwind and downwind to avoid dune growing, sand contamination of the infrastructure corridor, and the contamination of the railway. Analogously, sand accumulated inside the volume-like SMM has to be removed from dyke shoulder or ditch cutting. Due to their features and location, solid barriers generally enable easier and cheaper sand removal with respect to other kinds of Path SMMs. Apart from the common heavy machines, some *Sand Removal Machines* (SRMs) have been ad-hoc conceived in the last decade in order to remove trapped sand around line-like infrastructures, such as the sand cutter and blower, e.g. [210].

2.3.5 Receiver Sand Mitigation Measures

Receiver SMMs are located directly along or over the infrastructure (e.g. along the embankment shoulder or on railway track). Such measures necessarily interact with and depend on the track components (e.g. rail, sleepers or slab, ballast) and the railway functional requirements (e.g. rail gauge, safety distance from the track). Based on the working principle, Receiver SMMs can be further divided into two types:

1. the aerodynamic-based measures that reduce the sand action by controlling windblown sand transport or promoting erosion;
2. the sand-resistant measures, addressed to increase the sand resistance of the track system components rather than avoiding sand sedimentation.

In other words, the aerodynamic-based SMMs aim at eliminating the accumulated sand around the receiver, while the sand-resistant SMMs are intended to increase the receiver resistance to the sedimented sand.

Aerodynamic-Based

The very first example of an SMM intended to control the windblown sand transport is the jet roof proposed in [198] (Figure 2.24 a). Such a working principle has been further proposed in patent applications by several inventors for both windblown sand, e.g. Figure 2.24 (b) [103] and snow mitigation, e.g. Figure 2.24 (c) [207].

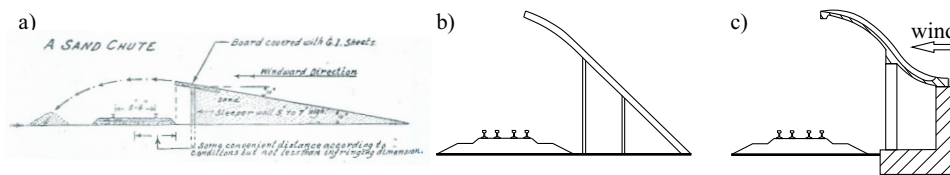


Figure 2.24: Aerodynamic-based Receiver SMMs: jet roofs. a) Historical example from [198], b) patent redrawn from [103], c) patent redrawn from [207].

The working principle of the jet roofs relies on four common steps: i.) acceleration of the multiphase flow along the upwind artificial slope; ii.) lift-off of the particles at the jet roof trailing edge; iii.) crossing of the particles over the infrastructure; and iv.) sedimentation of the particles downwind the infrastructure. This conjectured transport mechanism seems physically sound for windblown snow, where the convective contribution of the wind flow largely prevails over the gravitational force acting on the very lightweight snowflakes. Conversely, the gravity force applied on the sand grain is orders of magnitude larger than the one on snowflakes. Hence, the trajectories qualitatively sketched in [198] presumably overestimate the flight length of the sand grains. It is conjectured herein that the sand grains fall and sediment closer to the jet roof trailing edge, i.e. on the railway track. Partially-open or fully-closed tunnels [175, 55], are the straightforward extension of the jet roof concept. They have evident disadvantages with respect to the building costs and the safety issues when extensively applied along railways [105].

Among the measures intended to promote sand erosion on the railway track, the review is given for the particular on-track devices. They include humped sleepers within the conventional ballasted track system (Figure 2.25 d) [203, 268, 201] and humped slab track [266]. Humped slabs have been tested in-situ along the Namibian railway [203] and the Iran railway [264]. The working principle of humped sleepers is based on the well-known Venturi effect. This type of devices rely on the acceleration of the local wind speed induced by the narrowing of the duct in which

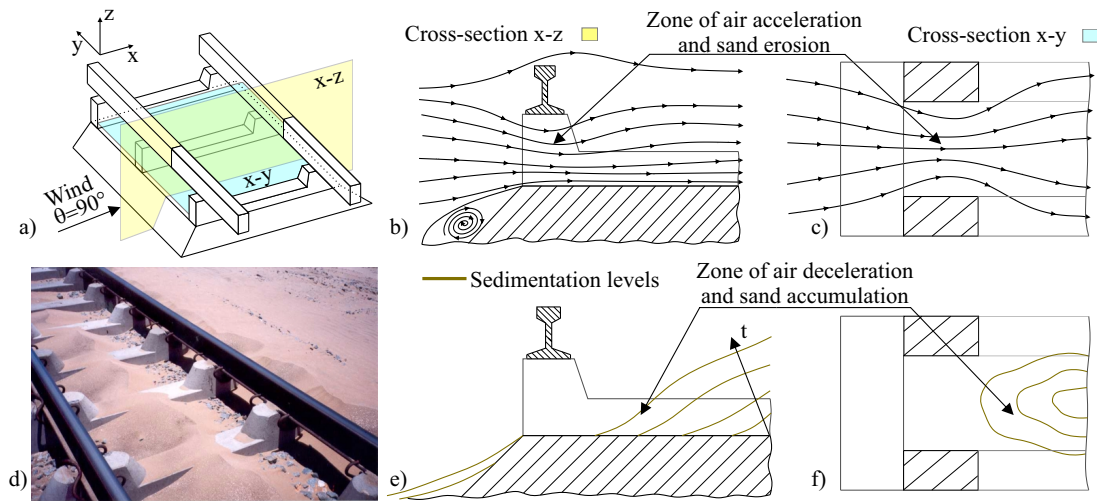


Figure 2.25: Aerodynamic-based Receiver SMMs. Venturi effect-based: a) humped sleepers scheme. Streamlines in the section: x-z (b), x-y (c). d) humped sleepers [reprinted from: 201, with the permission to reuse under a Creative Commons Attribution License]. Qualitative sand accumulation levels in the section: x-z (e), x-y (f).

it flows. Besides acceleration, the flow is redirected towards the track components to be protected (Figure 2.25 b, c). Figure 2.25 (d) qualitatively testifies that the Venturi effect takes place in the openings between the consecutive sleepers and below the rail lower flange. On the one hand, this effect results in the localized erosion of the sand and avoids the full obstruction of the track. On the other hand, local deceleration of the wind flow between the upwind and downwind rails results in the local sand sedimentation, e.g. on signalling balises (Figure 2.25 e, f). In the case of skewed wind directions ($\theta \neq 90^\circ$), it is conjectured here, and investigated in the following chapters of the Thesis, that the Venturi effect weakens since the flow separates in the duct between the two successive humps. It is assumed that the sand accumulates below the rails up to the complete clogging of the SMM. In other words, highly-skewed winds do not see the openings of humped sleepers. Further examples of the measures based on the Venturi effect are the localized-porosity fences with higher porosity in their lower part [144] and the so-called bottom-opening walls [55]. Such measures are intended to be installed in the proximity of railway track in order to promote sand erosion. According to the study in [55], the bottom-opening walls are effective for high wind speeds.

Sand-Resistant

Some components of the track superstructure have been recently ad-hoc modified in order to make them more resistant to the sand action. Several ballastless track systems have been tested along desert railways to avoid ballast contamination SSLs. Among them:

- track systems with longitudinal continuous support, such as the Tubular-Track (T-Track) railway system (Figure 2.26 a). The T-Track system has been developed in South Africa since 1989, installed in the Kingdom of Saudi Arabia deserts in 2008 [168] and in Namibian desert. According to [168], the T-Track systems have a lot of advantages compared to the ballasted railways. The main reason why they are used in desert areas is because they do not exhibit problems related to the ballast fouling. On top of that, initial and maintenance costs are lower;
- the track slab systems with discrete rail support, e.g. RHEDA2000[®], currently installed in the Medina-Mecca high-speed line and shown in Figure 2.26 (b) [167]. The most significant advantages are the high stability of the track, reduced maintenance requirements [169], and suitability for the application in sandy deserts, making them suitable for high-speed railways. However, the initial costs for their construction are higher and it is more difficult to replace parts of the system in case of a failure [137].

The combination of the slab track system and the humped sleepers results in the humped slab track. Its performance is investigated in [266]. According to the study, the height of the humps should be about 80 mm in order to avoid track covering for the orthogonal incoming wind direction ($\theta = 90^\circ$). Moreover, due to the fact that the slab systems are ballastless solutions, the system does not exhibit problems related to the ballast contamination. No results are given for skewed incoming winds.

Ballastless systems, besides the ballast protection against sand contamination, could be alternatively achieved by the application of rigid-polyurethane foam as an in-situ stabilization method [132, 70]. A recent study in [78] addresses the improvement of the ballast performance when the ballast fouling takes place through the mixing of tire derived aggregate with the ballast.

Besides ballast, others components of the track superstructure have been modified in order to withstand the effects of windblown sand:

- sand-induced abrasive wear of sliding components of turnout and reduced durability of lubricants have been addressed by redesigning the switch mechanism and developing lubricant-free, grease-free, or hinge-free products, e.g. the Plate Integrated Roller System (Piroll[®]) or the Hydraulic Switching System (Hydrolink[®]) [137];



Figure 2.26: Sand-resistant Receiver SMMs. The ballastless track slab systems: a) longitudinal continuous support, the T-Track system (explicit publishing permission from the owner of the photo: Giles Wiggs), b) the continuous slab [reprinted from: 164, with the permission from El Confidencial]. c) the lubricant-free turnout [reprinted from: 137, with the permission from Voestalpine].

- the sand-induced rail grinding SSLs have been addressed by increasing the rail head wear and fatigue resistance. Thermal hardening of the steel rails of at least R350HT grade are recommended in [187];
- the sand-induced wheel profiling SSLs are mitigated, at the present state of art, by two strategies:
 - the adoption of suggested multiple rail profiles along the tangent portions of a railway, in order to produce different contact bands on the wheels and distribute the wear across the wheel tread [111];
 - the adoption of the tested railway wheels made of hardened steels specifically designed for the desert environments (SANDLOS H[®]). Their wearing resistance was proved to be higher than the one made of the general-purpose standard steels [86].

Stand alone receiver SMMs are insufficient in most cases to protect the infrastructure against SULS, even if they are effective versus the targeted SSLs. In Figure 2.27 examples of inadequate performances of some receiver SMMs at SULS are given. In Figure 2.27 (a) and (c) there are no Path or Source SMMs coupled with the Receiver SMM. The ballastless track is successful at prevent ballast contamination, but it is ineffective at mitigating partial covering of the track (Figure 2.27 a) or dune encroaching (Figure 2.4 a). The lubricant-free turnouts avoid wearing of their mechanical components. However, the switch in the figure is out of service because of the massive sedimentation between the tapering and the diverging outer rail (Figure 2.27 c). In Figure 2.27 (b) the slab track is coupled with a SVW having low trapping efficiency. Ballast is not contaminated, but the track is partially covered by the windblown sand not trapped by the solid barrier. In general, Receiver SMMs are useful to deal with a small amount of sedimented sand, while the upwind Path SMMs are able to trap most of the incoming sand drift enabling



Figure 2.27: Failure of Receiver SMMs: a) the T-Track covered by sand (explicit publishing permission from the owner of the photo: Ciaran Nash), b) the continuous humped slab covered by sand [reprinted from: 164, with the permission from El Confidential], c) the lubricant-free turnout jammed by sand (courtesy of Astaldi).

efficient performance of the Receiver SMMs.

Sand Removal Machine (SRM) able to move on rails have been ad-hoc conceived in the last decade to clean the rail track from sand in SULTS conditions. Some examples are 46-6 SRM [102] adopted in the Egypt and Iraq railway network and SRM 500 [250] used in the Syrian and Kingdom of Saudi Arabia railway networks. Such SRMs have high nominal clearing capacities (up to 2,300 tons/hr) required in the maintenance at SULTS, if no or low-efficiency Source or Path SMMs are put in place upwind the infrastructure. Both SRMs use plough and brooms to remove sand from the tracks. The capability of SRMs to discharge the sand as far as possible from the railway SMM is another crucial aspect. For that purpose, they are using slewing conveyor belt capable of discharging the sand from 3 to 5 meters away from the track. In order to prevent the large quantities of removed sand to re-enter a new erosion-transport-sedimentation cycle, SRMs should be complemented by the complete procedure for sand disposal. For example, placing it in storage areas far from the railway track where the sand can be stabilized. Even though SRMs help with SULTS, they are almost ineffective versus SSSL, particularly against ballast contamination.

Chapter 3

Methods

In the following chapter a brief overview of the mathematical models, governing equations and numerical approaches within the Finite Volume Method is given. The presented methods are used during the research for the Thesis, but the exhaustive explanation of all the details is omitted because the Thesis does not focus on the development of the models. Additionally, this chapter introduces the optimization procedures and gives mathematical aspects required to understand their working principles.

3.1 Computational Approaches in Turbulent Flows

In the computational models used in the Thesis, it is assumed that the fluids consist of particles with a length scale much smaller than the characteristic scale of the system, but in the same time much larger than the scale of the molecules. Observing the flow at this scale is covered under the *continuum* hypothesis. It is an idealization of the fluids which allows them to be treated as continuous means. In such an approach, the measurable macroscopic quantities related to fluids, e.g. velocity, pressure, density, are modeled by continuous functions and their values can be obtained at every point of the monitored space. However, continuum hypothesis has its limitations, but for the flows interesting to Wind Engineering, thermodynamic conditions at which the hypothesis is valid are satisfied. The number defining if the continuum hypothesis is valid is called the *Knudsen number* (Kn) defined as a ratio of molecular mean path and the characteristic scale of the system. For all the studied cases in the Thesis, the value equals 10^{-8} , it is much smaller than the limit 0.1 and the continuum hypothesis holds.

The effects which describe the flows at the macroscopic level are reflection of what happens at the molecular level. For example, the behavior resulting at conditions outside of the temperature equilibrium, i.e. kinetic energy of the molecules, is recognized as heat conduction at the macroscopic level. Another example is the

behavior at the conditions outside of the convective equilibrium which is recognized as viscosity.

At the macroscopic level, the fluid behavior is highly influenced by the velocity. The first important classification of the flow based on its velocity, or more precisely the ratio of inertial and viscous forces quantified by the Reynolds Number (Re), is *laminar* and *turbulent* flows. At Re much lower than the critical value, the fluid particles follow regular trajectories. In such conditions the flow is considered to be laminar. As Re increases and reaches the critical value the regime of the flow switches from laminar to turbulent. In most cases, the trigger which switches the flow regime are the instabilities at the too large Reynolds numbers.

The second important classification based on velocity, more precisely the ratio of velocity and sound velocity quantified by the Mach number (Ma), is *compressible* and *incompressible* flows. For the lower values of $Ma < 0.3$ the flows are considered incompressible. The most significant characteristic of the flows in such regime is the constant density at temperatures around the referent value. For higher Ma this does not hold and flow becomes compressible.

Clearly, the different regimes of the flow require different mathematical description and consequently numerical approaches to solving the equations. The research presented in this Thesis revolves completely around the highly turbulent, but still incompressible flows.

3.2 Mathematical Model

The fluid particles are defined by their volume V , bounded by the domain Ω . In general, V and Ω can change in both space and time, where:

- spatial coordinates: $\mathbf{x} = (x_1, x_2, x_3)^T$;
- time coordinate: t .

To monitor what happens to a given physical quantity $\phi = \phi(\mathbf{x}, t)$ in the domain, a generic transport equation is defined based on the amount of the quantity exchanged through the boundary of the volume ∂V and the contribution of sources/sinks of ϕ . Based on the way in which the reference system is specified for the transport equation, two approaches are most commonly used: i.) the *Eulerian* approach, in which the reference frame of the volume V is fixed in time and the quantity ϕ is evaluated from the flow of the fluid through this volume; and ii.) the *Langrangian* approach, in which the reference frame is attached to the volume V and travels with it at the velocity of the fluid. In the Thesis, only the Eulerian approach is used and the further description of the equations is given in the Eulerian form.

The generic transport equation for a fixed volume V reads:

$$\frac{\partial}{\partial t} \int_V \phi dV = - \int_{\partial V} \mathbf{n} \cdot (\mathbf{u}\phi + \tilde{\mathbf{F}}_\phi) d\sigma + \int_V s_\phi dV. \quad (3.1)$$

In the equation, $\mathbf{u} = \mathbf{u}(\mathbf{x}, t) = (u_1, u_2, u_3)^T$ is the velocity vector, $\mathbf{F}_\phi = \mathbf{u}\phi$ and $\tilde{\mathbf{F}}_\phi$ are the fluxes of ϕ through the boundary ∂V , caused by convection and diffusion, respectively. \mathbf{n} is the normal unit vector. s_ϕ is the source/sink term of quantity ϕ . The transport equation describes the conservation of the quantity ϕ . Based on the choice of the quantity which is being conserved the generic transport equation takes the form of:

- mass conservation: $\phi = \rho$;
- momentum conservation: $\phi = \rho\mathbf{u}$;
- energy conservation: $\phi = \rho e$, where e is the specific energy of the system.

3.2.1 Mass Conservation

If the generic quantity ϕ is substituted with ρ in Equation (3.1) the mass conservation results:

$$\frac{\partial}{\partial t} \int_V \rho dV = - \int_{\partial V} \mathbf{n} \cdot (\rho\mathbf{u}) d\sigma. \quad (3.2)$$

With the application of the *divergence theorem* the following form is obtained:

$$\frac{\partial}{\partial t} \int_V \rho dV = - \int_V \nabla \cdot (\rho\mathbf{u}) dV. \quad (3.3)$$

Finally, the mass conservation in differential form reads:

$$\frac{\partial \rho}{\partial t} + \nabla \cdot (\rho\mathbf{u}) = 0. \quad (3.4)$$

It is worth stressing at this point that in case of incompressible flows where $\rho = \text{const}$ the mass conservation takes the simplified form:

$$\nabla \cdot \mathbf{u} = 0, \quad (3.5)$$

which states that the divergence of velocity equals 0.

3.2.2 Momentum Conservation

If, in Equation (3.1), the generic quantity ϕ is substituted with $\rho\mathbf{u}$, $\tilde{\mathbf{F}}_\phi = -\mathbf{T}$ (stress tensor) and $s_\phi = \rho\mathbf{b}$ (volumetric forces per unit mass) the momentum conservation results:

$$\frac{\partial}{\partial t} \int_V \rho\mathbf{u} dV = - \int_{\partial V} \mathbf{n} \cdot (\rho\mathbf{u} \otimes \mathbf{u}) d\sigma + \int_{\partial V} \mathbf{n} \cdot \mathbf{T} d\sigma + \int_V \rho\mathbf{b} dV. \quad (3.6)$$

By application of the divergence theorem and further writing it in the differential form, the following equation results:

$$\frac{\partial}{\partial t}(\rho\mathbf{u}) = -\nabla \cdot (\rho\mathbf{u} \otimes \mathbf{u}) + \nabla \cdot \mathbf{T} + \rho\mathbf{b}. \quad (3.7)$$

From the properties of the divergence operator it follows:

$$\nabla \cdot (\rho\mathbf{u} \otimes \mathbf{u}) = \mathbf{u}\nabla \cdot (\rho\mathbf{u}) + \rho\mathbf{u}\nabla\mathbf{u},$$

and combining it with the mass conservation, the (3.7) can be equivalently written as:

$$\rho\frac{\partial\mathbf{u}}{\partial t} = -\rho\mathbf{u}\nabla\mathbf{u} + \nabla \cdot \mathbf{T} + \rho\mathbf{b}. \quad (3.8)$$

For the *Newtonian fluids*, in which the viscous stresses are linearly proportional to the local strain rate, e.g. air and water, the stress tensor \mathbf{T} is defined as:

$$\mathbf{T} = -\left(p_s + \frac{2}{3}\mu\nabla \cdot \mathbf{u}\right)\mathbf{I} + 2\mu\mathbf{D}. \quad (3.9)$$

In order, μ is the dynamic viscosity, \mathbf{I} is the identity tensor, and p_s is the static pressure. $\mathbf{D} = \frac{1}{2}[\nabla\mathbf{u} + (\nabla\mathbf{u})^T]$, is the deformation gradient tensor. In the equations where the temperature is not of interest and is considered constant, the viscosity μ can be treated as a constant as well. The following expression results:

$$\nabla \cdot \mathbf{T} = -\nabla p_s - \frac{2}{3}\mu\nabla(\nabla \cdot \mathbf{u}) + \mu\nabla(\nabla \cdot \mathbf{u}) + \mu\Delta\mathbf{u},$$

from which Equation (3.7) becomes, for a Newtonian fluid:

$$\frac{\partial}{\partial t}(\rho\mathbf{u}) + \nabla \cdot (\rho\mathbf{u} \otimes \mathbf{u}) + \nabla p_s - \frac{1}{3}\mu\nabla(\nabla \cdot \mathbf{u}) - \mu\Delta\mathbf{u} - \rho\mathbf{b} = 0. \quad (3.10)$$

In the equation the following characteristic terms occur:

- the temporal derivative: $\frac{\partial}{\partial t}(\rho\mathbf{u})$,
- the convective derivative: $\nabla \cdot (\rho\mathbf{u} \otimes \mathbf{u})$,
- the part of the diffusive derivative related to compressibility of the fluid: $-\frac{1}{3}\mu\nabla(\nabla \cdot \mathbf{u})$, which equals 0 for incompressible flows,
- the part of the diffusive derivative related to the viscous flow: $-\mu\Delta\mathbf{u}$, where $\mu = \text{const}$,
- sink and source: ∇p_s and $-\rho\mathbf{b}$.

3.2.3 Energy Conservation

If, in Equation (3.1), the generic quantity ϕ is substituted with ρe , $\tilde{F}_\phi = -\mathbf{T} \cdot \mathbf{u} - \mathbf{q}_h$ (vector form of mechanical work and heat fluxes) and $s_\phi = \rho \mathbf{b} \cdot \mathbf{u} + \rho Q_h$ (work by gravity and heat source) the energy conservation results:

$$\frac{\partial}{\partial t}(\rho e) = -\nabla \cdot (\rho e \mathbf{u}) + \nabla \cdot (\mathbf{T} \cdot \mathbf{u}) + \rho \mathbf{b} \cdot \mathbf{u} - \nabla \cdot \mathbf{q}_h + \rho Q_h, \quad (3.11)$$

This equation is here mentioned only, because the energy conservation and the study of the flows where temperature has a significant role is not covered by this Thesis.

3.2.4 Constitutive Laws

The two scalar (mass and energy) and a single vector (momentum) conservation laws listed above have more unknowns than the equations. To close such system of equations, i.e. make the numbers of unknowns and equations the same, additional constitutive laws have to be included. These laws strictly depend on the fluid. In the case of Newtonian fluids, the following is introduced:

- the equation of internal energy: $e_i = e_i(p_s, T)$, stating that internal energy is fully defined by the two state variables. The total specific energy of the system can then be defined as $e = \frac{1}{2} \rho \mathbf{u}^2 + \rho e_i$;
- the equation of state: $\rho = \rho(p_s, T)$, stating that density is completely defined by two variables of state;
- the Fourier's law of heat conduction: $\mathbf{q}_h = -\lambda \nabla T$, stating that the conduction of heat through the material is oppositely oriented and proportional to the temperature gradient and proportional to the diffusion coefficient λ ;
- the Newton's law of viscosity: $\mathbf{T} = -\left(p_s + \frac{2}{3} \mu \nabla \cdot \mathbf{u}\right) \mathbf{I} + 2\mu \mathbf{D}$, stating that the strain tensor consists of pressure and viscous part, where the viscous part is linearly proportional to the gradient of velocity.

By taking the relations into account the system of the equations defining the flow of Newtonian fluids gets closed.

3.2.5 Turbulence Modelling

Turbulence is the property of most flows in nature and engineering applications. It is worth stressing that turbulence is the property of the flow and not the fluid itself. Moreover, if Re is large enough, most of the turbulence dynamics are the

same for different fluids, whether they are liquids or gases. The strict definition of turbulence does not exist, and in literature when trying to define turbulence, the main characteristics of the turbulent flows are given instead:

- Turbulent flows are *continuum phenomenon*. Briefly, this means that the smallest scales in turbulent flows are still much larger than the molecular scale.
- Re higher than the critical is the required criterion for turbulent flows. They mostly occur as instabilities of initially laminar flows when Re becomes too high. Such instabilities are connected to a combination of contributions of viscous and inertial effects described by the momentum conservation equation. Due to the mathematical complexity of non-linear partial differential equations, it is not possible to obtain a closed form analytical solution of such equations with current level of mathematical tools.
- The turbulent structures, called *eddies*, are present in the flow at a range of spatial and time scales.
- Turbulent flows are *dissipative*. The dissipative character is mainly related to the fact that eddies require constant inflow of energy to maintain themselves. The eddies in turbulent flow break apart into the smaller eddies. This process continues until the smallest scale, the so-called *Kolmogorov scale*, completely dissipates due to viscosity into the internal energy of the fluid.
- From the perspective of engineering applications, *diffusivity* of turbulence is the most important characteristic of turbulent flows. It causes increased rate of mixing and increased rate of mass, momentum and energy transport. Without an expressed diffusive character of the flow, the flow is not turbulent, i.e. flows which look irregular, but are not diffusive are not turbulent.
- Turbulent flows are *three-dimensional, rotational, time dependent* and *irregular*. For example, a phenomenon of great importance for turbulence is the *vortex stretching* which is intrinsically three-dimensional phenomenon and is absent in two-dimensional flows. Such flows are characterized by increased vorticity. Moreover, the flow structures change in time even if the flow at the inlet of the domain does not.

To capture the essence of turbulent flows with numerical models, the complete range of turbulent scales can be accounted for by directly solving discretized Navier-Stokes set of equations (mass and momentum conservation). The Direct Numerical Simulations (DNS) have to be complemented by the fine enough spatial discretization to capture the smallest Kolmogorov scale of the flow. Additionally, the time discretization has to be fine enough to capture the smallest time scale. From the

numerical point of view, such modelling of the flow is very expensive and is rarely used in the engineering applications nowadays.

The more common approach in engineering applications is Large Eddy Simulations (LES). In this approach filtering of the spatial scales is used with a goal of directly resolving the larger scales of the flow which carry the most turbulent energy, the so-called *super-grid scales*. The rest of the scales, which in the first place cause the DNS approach to be too numerically expensive, are taken into account by statistical approaches. These scales are called *sub-grid scales*. The spatial filtering is done by the spatial discretization itself. As the numerical grid gets finer, the range of sub-grid scales decreases. In the limit case, for a very fine discretization, LES approaches DNS.

The most applied statistical approach to solving turbulence is the *Reynolds Averaging*. Generally speaking, the generic variable ϕ at a given location x_i which is transported by a transport equation can be split into its mean $\bar{\phi}$ and fluctuating components ϕ' .

$$\phi(\mathbf{x}, t) = \bar{\phi}(\mathbf{x}) + \phi'(\mathbf{x}, t), \quad (3.12)$$

where the time average at a given location \mathbf{x} is defined as:

$$\bar{\phi}(\mathbf{x}) = \frac{1}{T} \int_t^{t+T} \phi(\mathbf{x}, t) dt, \quad T_1 \ll T \ll T_2. \quad (3.13)$$

In order, T is the interval of the averaging, T_1 is the time period of the largest turbulent scale and T_2 is the time scale of the slow fluctuations, large enough not to be regarded as turbulence. Applying the averaging on the incompressible set of Navier-Stokes equations, the following expression is obtained:

$$\nabla \cdot \bar{\mathbf{u}} = 0, \quad (3.14)$$

$$\frac{\partial}{\partial t}(\bar{\mathbf{u}}) + \nabla \cdot (\bar{\mathbf{u}} \otimes \bar{\mathbf{u}}) = \mathbf{g} - \nabla \bar{p}_s + \nabla \cdot (\nu \nabla \bar{\mathbf{u}}) - \nabla \cdot (\overline{\mathbf{u}'\mathbf{u}'}), \quad (3.15)$$

where $\bar{\mathbf{u}}$ is the averaged velocity, \bar{p}_s the averaged pressure and ν the air kinematic viscosity. The last term, defined as an average of the product of fluctuating components of velocity is called the *Reynolds stress tensor*. It results from the averaging of the convective term in which the average of the product is performed:

- $\overline{\phi'} = 0$;
- $\overline{\phi_1 \phi_2} = \overline{(\bar{\phi}_1 + \phi'_1)(\bar{\phi}_2 + \phi'_2)} = \bar{\phi}_1 \bar{\phi}_2 + \overline{\phi'_1 \phi'_2}$;

the last term is the covariance of the quantities ϕ_1 and ϕ_2 and it only equals 0 when the terms are not correlated, which is not the case in turbulent flows. The Reynolds stress tensor cannot be expressed with the averaged components of velocities. This introduces new unknowns to the system of equations. To close

the system of equations within the computational models used in this Thesis, the *Boussinesq hypothesis* is adopted to modelling of the Reynolds stress tensor:

$$\overline{\mathbf{u}'\mathbf{u}'} = \nu_t(\nabla\mathbf{u} + (\nabla\mathbf{u})^T) + \frac{2}{3}k\mathbf{I}, \quad (3.16)$$

where k is the specific turbulent kinetic energy defined as:

$$k = \frac{1}{2}\overline{\mathbf{u}' \cdot \mathbf{u}'}. \quad (3.17)$$

ν_t in Equation (3.16) is the eddy viscosity. Many different turbulence models based on Reynolds averaging exist where the definition of ν_t differs. In the Thesis the so-called k - ω Shear Stress Transport (SST) model is used. The specific turbulent kinetic energy k and the specific dissipation of the kinetic turbulent energy ω are computed from the corresponding transport equations. For the sake of completeness and description of the Reynolds-averaged Navier-Stokes (RANS) equations, the complete three-dimensional, incompressible, steady-state set used in the simulations in the Thesis, written with the Einstein notation is given:

$$\frac{\partial \bar{u}_i}{\partial x_i} = 0, \quad (3.18)$$

$$\bar{u}_j \frac{\partial \bar{u}_i}{\partial x_j} = -\frac{1}{\rho} \frac{\partial \bar{p}}{\partial x_i} + \frac{\partial}{\partial x_j} \left[\left(\nu + \nu_t \right) \left(\frac{\partial \bar{u}_i}{\partial x_j} + \frac{\partial \bar{u}_j}{\partial x_i} \right) \right], \quad (3.19)$$

$$\bar{u}_j \frac{\partial k}{\partial x_j} = \frac{\partial}{\partial x_j} \left[\left(\sigma_k \nu_t + \nu \right) \frac{\partial k}{\partial x_j} \right] + \tilde{P}_k - \beta^* k \omega, \quad (3.20)$$

$$\bar{u}_j \frac{\partial \omega}{\partial x_j} = \frac{\partial}{\partial x_j} \left[\left(\sigma_\omega \nu_t + \nu \right) \frac{\partial \omega}{\partial x_j} \right] + C_{\omega_1} \frac{\omega}{k} P_k - C_{\omega_2} \omega^2 + (1 - F_1) \frac{2\sigma_\omega}{\omega} \frac{\partial k}{\partial x_i} \frac{\partial \omega}{\partial x_i}. \quad (3.21)$$

\tilde{P}_k is the source term of k and is modeled by a limiter. The limiter prevents the build-up of turbulence in low velocity regions and is defined as:

$$\tilde{P}_k = \min(P_k, 10\beta^*k\omega), \quad \text{where} \quad P_k \approx \nu_t \left(\frac{\partial \bar{u}_i}{\partial x_j} + \frac{\partial \bar{u}_j}{\partial x_i} \right) \frac{\partial \bar{u}_i}{\partial x_j}.$$

In the k - ω SST model the turbulent kinematic viscosity ν_t is defined as:

$$\nu_t = \frac{a_1 k}{\max(a_1 \omega, S F_2)}. \quad (3.22)$$

The details regarding the blending functions F_1 and F_2 , and the values of the main model constants β^* , σ_k , σ_ω , C_{ω_1} , C_{ω_2} , S and a_1 are omitted herein. For the complete description, the interested readers can find them in [166]. The 3D version of the equation set is defined for $i, j = [1, 2, 3]$, while the degenerate 2D set drops the

third degree of freedom resulting in $i, j = [1, 2]$.

Such model has been tested by many authors in the light of the state of art. In fact, RANS approach is perfectly adapted to simulate the time-averaged flow features responsible for the long-term morphodynamics of sand dunes, e.g. in [152, 6, 38, 149], and around railways [270, 173]. In the Thesis, the $k - \omega$ SST turbulence model is selected because of its accuracy in detecting the inflection points [165, 166]. The model has been previously adopted in simulation of similar bluff-body geometries and fundamental topographical forms [38] or windblown sand solid barriers [39, 115]. The wall treatment of the sandy surfaces is modelled by the sand-grain roughness wall functions. They are adopted because of their proven accuracy in environmental CWE, e.g. [24]. Such wall functions are completely adequate in perspective of the study as shown in the previous 3D simulations of sand dune aerodynamics, e.g. in [152, 124, 123, 38]. In particular, these are modified standard wall functions [141] with the modification of wall roughness [48]. The sand grain roughness height is defined as $k_s = 9.793z_0/C_s$, where z_0 is the aerodynamic roughness length and $C_0 = 0.5$ the roughness constant.

Modelling of turbulence in multi-phase flows differs because of the interactions between the phases and the characteristic phenomena between the particles which affect the turbulence of the continuous phase. In windblown sand, such phenomena are the particle-wall collisions and the inter-particle collisions. According to the study in [190], these phenomena can be modeled by the effective viscosity of the sand phase $\nu_{eff,s}$. $\nu_{eff,s}$ is defined as the sum of the molecular sand viscosity ν_s , turbulent sand viscosity $\nu_{t,s}$ and the term which takes into account the inter-particle collisions $\nu_{c,s}$. According to the study in [156], $\nu_{c,s}$ should be a scalar isotropic function of the strain rate tensor \mathbf{D} , i.e. it only depends on the sand volume fraction and the invariants of \mathbf{D} . These phenomena in turn affect the wind phase through the coupling terms in the mass, momentum and energy equations. To appropriately capture the physics of the turbulence in multi-phase flows, the turbulence model has to be modified as well. An example is given in [99], where a detailed description is given on the modulation of the $k-\varepsilon$ model. It has been developed for multi-phase flows in stirred vessels with much higher volume fractions of the suspended phase compared to the wind-blown sand. The recent example of the turbulence response to the particle related phenomena for windblown snow is given in [32]. Even though sand and snow have significantly different physical properties, their transport by wind is modeled by similar set of equations.

The low volume fraction in windblown sand justifies the use of the non-modulated $k-\omega$ SST turbulence model within the Thesis. Moreover, in the Thesis the focus is on the conceptual design, the preliminary design and the shape optimization, which are iterative processes and require a high number of simulations. Coupled multi-phase model which takes into account the turbulence modulation is, in this regard, too expensive. However, at the present stage of the design, the results are

relevant and accurate because only the necessary conditions for erosion and sedimentation are required when comparatively discussing the performance assessment of different SMMs in the presented stages of the design. At these conditions, the corresponding SMM has the maximum performance for a given geometry.

3.2.6 Initial and Boundary Conditions

To fully prescribe the conditions under which partial differential equations are solvable, Initial conditions (IC) and Boundary conditions (BC) are required. In general, two types of boundary conditions exist: i.) *Numerical BC*; and ii.) *Physical BC*. Numerical BC can be further classified in Fixed value BC (the so-called *Dirichlet BC*), the Fixed gradient BC (the so-called *Von Neumann BC*), and the combinations of the two (the so-called *Robin BC*). In the Dirichlet BC the value of the variable is specified at the boundary. Conversely, the Von Neumann BC specifies the variable gradient at the boundary. The initial conditions for a generic variable ϕ are prescribed for every \mathbf{x} in the domain Ω :

$$\phi(\mathbf{x},0) = \phi_0(\mathbf{x}), \quad \forall \mathbf{x} \in \Omega. \quad (3.23)$$

The Dirichlet and Von Neumann boundary conditions for a generic variable ϕ are defined for every \mathbf{x} at the boundary Γ_D and Γ_N , respectively:

$$\begin{cases} \phi(\mathbf{x}, t) = g(\mathbf{x}, t), & \forall \mathbf{x} \in \Gamma_D, \\ \left(\frac{\partial \phi}{\partial \mathbf{n}} \right) = \mathbf{h}(\mathbf{x}, t), & \forall \mathbf{x} \in \Gamma_N. \end{cases} \quad (3.24)$$

Physical boundary conditions are defined from the combination of the Numerical boundary conditions applied to different variables. The physical boundary conditions prescribed for the Navier-Stokes equations, and their brief explanation are listed bellow. More details can be found in [125]:

- *Inlet* boundary: to fully describe the inlet of the boundary, velocity is fixed (Dirichlet BC) and pressure set to zero gradient (Von Neumann BC). Values of turbulence parameters at inlet are described with the Dirichlet BC.
- *Outlet* boundary: to describe the outlet boundary and satisfy the mass conservation in the same time, the pressure is fixed at the outlet, while velocity is set to the zero gradient BC. Values of the turbulence parameters at the outlet are described with the zero gradient BC.
- *No-slip* condition at impermeable walls: this condition describes the variables at the impermeable walls. In the no-slip condition the velocity of the fluid is set equal to the velocity of the wall. Additionally, due to the fact that there is no flow through the impermeable walls, pressure is set to the zero gradient condition.

- *Symmetry plane*: symmetry plane forces the normal component of the variable gradient to be equal to zero at that boundary.
- *Cyclic/periodic* conditions: periodic boundaries are treated as physically-connected, but numerically-split boundaries, i.e. the variables are exactly the same on the two mutually periodic boundaries.
- *Wall functions* [223]: wall functions are used to model velocity in the first grid layer attached to the walls. At the walls, velocity has prescribed value by the no-slip boundary condition. Therefore, turbulent parameters are prescribed at the wall instead. To set wall functions, special attention should be paid to the dimensionless wall distance n^+ which besides velocity, depends on the numerical grid. For wall functions to give accurate velocity, the center of the first cell from the wall should be put in the logarithmic turbulence sublayer ($n^+ > 30$). Wall functions are used to avoid very thin layers of the numerical grid at the wall needed to properly resolve the velocity gradient.
- *Turbulence parameters*: inlet turbulence parameters should be prescribed in equilibrium with the velocity. Such a combination ensures that the ABL does not further develop in the computational domain.

3.3 Finite Volume Method

The process of numerical discretization can be split into two parts: i.) *the discretization of the domain*, where the time and space is split into discrete parts defined by the spatial and time step, respectively; and ii.) *the discretization of the equations* in which continuous partial differential equations are split into a set of corresponding discrete algebraic equations. The *Finite Volume Method* (FVM) has the following properties:

- It is based on the discretization of the integral form of the conservation equations and uses the divergence theorem to transition from volume to surface integrals.
- The space is discretized in the form of numerical grid. The grid consists of three-dimensional *control volumes* with a finite volume. In general, the control volumes can take a polyhedral shape with the number of its neighbors equal to the number of its faces as shown in Figure 4.6.
- The time is discretized in the form of a fixed or variable time step Δt .
- The variables are stored in the *centroid* of the control volume P and linearly vary through it $\phi(\mathbf{x}) = \phi_P + (\mathbf{x} - \mathbf{x}_P) \cdot \nabla \phi_P$. To complete the variation of the variable with the behavior in time, the similar linear expression is assumed

$\phi(t + \Delta t) = \phi^t + \Delta t \left(\frac{\partial \phi}{\partial t}\right)^t$. This variation ensures the second-order accurate method. The coordinates of the centroid \mathbf{x}_P satisfy the following expression: $\int_{V_P} (\mathbf{x} - \mathbf{x}_P) dV = 0$.

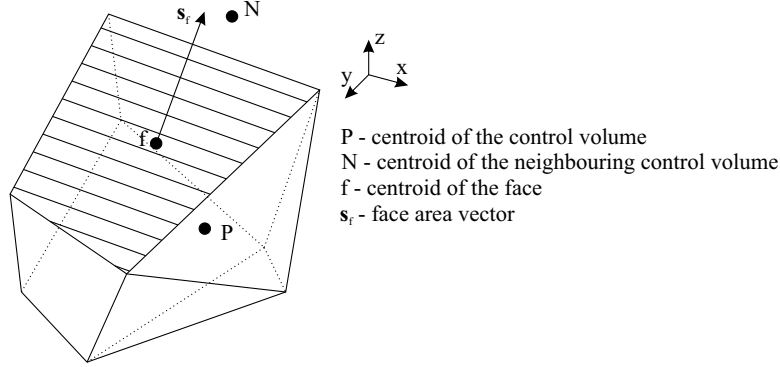


Figure 3.1: General polyhedral control volume in FVM. Redrawn from [125].

The goal of the discretization is to write a set of equations, e.g. the Navier-Stokes equations, in the form able to be iteratively solved by linear solvers:

$$\mathbf{A}\mathbf{x} = \mathbf{b}. \quad (3.25)$$

\mathbf{A} is the $N \times N$ matrix containing the coefficients of the terms which depend on the unknown \mathbf{x} . The diagonal coefficients are related to the terms which depend on the variable prescribed in the *owner* control volume P , while the off-diagonal terms depend on the variable prescribed in the *neighbor* control volume N . \mathbf{x} is the $N \times 1$ vector of the variables ϕ . \mathbf{b} is the $N \times 1$ vector of the solution containing the free terms in the discretized equations, i.e. the coefficients which do not multiply the variable. In such a way the system is described by the N number of linear algebraic equations, each prescribed for a single control volume of the grid.

3.3.1 Discretization of the Convective Term

The convection term of the generic transport equation in the integral form after the application of the divergence theorem is written as:

$$\int_V \nabla \cdot (\mathbf{u}\phi) dV = \int_S \mathbf{n} \cdot (\mathbf{u}\phi) dS. \quad (3.26)$$

In the following the subscript f corresponds to the variable which is specified at the centroid of the face. The convective term can be rewritten as the sum of the integrals over individual faces i :

$$\sum_i \int_S \mathbf{n}_i \cdot \mathbf{u}_{e,i} \phi_i dS_i. \quad (3.27)$$

The generic variable ϕ linearly varies over the face of the cell in the second order accurate discretization. This results in the following expression:

$$\sum_i \int_S \mathbf{n}_i \cdot \mathbf{u}_{f,i} (\phi_{f,i} + (\mathbf{x}_i - \mathbf{x}_{f,i}) \nabla \phi_{f,i}) dS_i. \quad (3.28)$$

From the definition of the centroid, a part of the integral equals 0, i.e. $\mathbf{n}_i \cdot \nabla \phi_{f,i} \int_S (\mathbf{x}_i - \mathbf{x}_{f,i}) dS_i = 0$. Therefore, the final form of the convective term is:

$$\sum_i F_i \phi_{f,i}, \quad (3.29)$$

where $F_i = \mathbf{n}_i \cdot \mathbf{u}_{f,i}$ and $S_{f,i} = \mathbf{s}_i \cdot \mathbf{u}_{f,i}$ represents the normalized mass flux through a face. In the expression, \mathbf{s}_i is the *face area vector*, i.e. a vector with the magnitude equal to the area of the face and the direction of its normal. From the final form of the term it can be concluded that the convective term is accounted for by summation of the product of fluxes through the faces and the corresponding variable transported by the flux. The generic variables required to calculate the convective term are prescribed at the centroids of faces. These values are calculated by interpolation schemes taking into account the values at the centroid of the monitored cell and its neighbors. An example of *Central Differencing* scheme is shown in Figure 3.2. In this example, the velocity at the face is computed from the following relation:

$$\phi_f = f_x \phi_P + (1 - f_x) \phi_E, \quad (3.30)$$

where:

$$f_x = \frac{\overline{fE}}{\overline{PE}}. \quad (3.31)$$

The contributions to the matrix \mathbf{A} in Equation (3.25) can be finally computed.

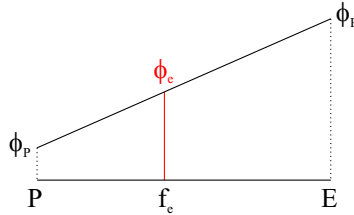


Figure 3.2: Face interpolation - central differencing scheme.

$\sum_i F_i \phi_{f,i}$ is added as a diagonal coefficient, while the off-diagonal coefficients for each corresponding neighboring cell is $F_i (1 - f_{x,i})$.

3.3.2 Discretization of the Diffusion Term

The diffusion term in the integral form reads:

$$\int_V \nabla \cdot (\nu \nabla \phi). \quad (3.32)$$

By applying the divergence theorem and taking into account the linear variation of velocity over the cell and its faces, in a similar way as shown for the convective term, the diffusion term can be rewritten as:

$$\int_V \nabla \cdot (\nu \nabla \phi) = \sum_i \nu_{f,i} \mathbf{s}_i \cdot \nabla \phi \quad (3.33)$$

One way of the gradient computation for orthogonal grids reads:

$$\mathbf{s}_i \cdot \nabla \phi_f = S_f \frac{\phi_N - \phi_P}{P - N}. \quad (3.34)$$

For non-orthogonal grids, an error occurs in the estimation of the gradient computed in this way. To account for the error, the non-orthogonal correctors are included in the definition of the gradient. For the detailed description of different gradient calculation methods, the non-orthogonality error and the definition of the corrector see: [125].

3.3.3 Discretization of the Source/Sink Term

A constant source/sink term in the generic transport equation s_ϕ is simply discretized in FVM as:

$$\int_V s_\phi dV = s_\phi V_P. \quad (3.35)$$

This means that in order to account for a constant source/sink of the generic variable, the source/sink value is multiplied by the corresponding volume of the cell. The contribution of sources/sinks is added in the right hand side (**b**) of the Equation (3.25), because the coefficients defining the term do not include the generic variable.

3.3.4 Interpolation Schemes

In the section above dealing with the discretization of the convection term, *Central Differencing* interpolation scheme is introduced to calculate the values at face centroids. Depending on the accuracy, stability and, in general, the physical properties of the transported variables, a range of interpolation schemes exist. The nodes used to derive the expressions for these schemes are shown in Figure 3.3.

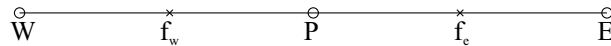


Figure 3.3: Face interpolation - definition of nodes.

Besides central differencing, the most used interpolation schemes are listed:

1. *Upwind differencing scheme:*

$$\phi_{f,e} \approx \begin{cases} \phi_P & \text{if } \mathbf{u}_{f,e} > 0 \\ \phi_E & \text{if } \mathbf{u}_{f,e} < 0 \end{cases} \quad (3.36)$$

Upwind differencing interpolation scheme is a first order accurate scheme which introduces error in form of numerical diffusion to the solution.

2. Upwind schemes of higher order:

- (a) *Linear upwind differencing scheme:* this is a scheme analogous to the central differencing scheme, but it is centered on the two upwind nodes. In the case $\mathbf{u}_{f,e} > 0$ it reads:

$$\phi_{f,e} \approx \phi_P f_x + \phi_W(1 - f_x), \quad f_x = \frac{x_{f,e} - x_W}{x_P - x_W}. \quad (3.37)$$

This is a second order upwind differencing interpolation scheme which introduces error in the form of numerical dispersion to the solution.

- (b) *QUICK:* in this scheme, the value of the variable ϕ between x_P and x_E is interpolated by a parabola. Therefore, three points have to be included in the interpolation. For $\mathbf{u}_{f,e} > 0$ the scheme reads:

$$\phi_{f,e} \approx \phi_P + f_{x,1}(\phi_E - \phi_P) + f_{x,2}(\phi_P - \phi_W), \quad (3.38)$$

with

$$f_{x,1} = \frac{(x_{f,e} - x_P)(x_{f,e} - x_W)}{(x_E - x_P)(x_E - x_W)}, \quad f_{x,2} = \frac{(x_{f,e} - x_P)(x_E - x_{f,e})}{(x_P - x_W)(x_E - x_W)}.$$

This is a quadratic upwind interpolation with third order of the truncation error.

Besides accuracy, one of the most important characteristic of numerical schemes is boundedness. The boundedness is strictly required in the transport of scalars which physically cannot exhibit negative values, e.g. turbulent kinetic energy, volume fraction, temperature etc. Therefore, it is necessary to obtain bounded solution from the transport equations of such scalars. In the Thesis, the convection term is discretized by the Limited Linear scheme, a 2nd order accurate, bounded, Total Variation Diminishing (TVD) scheme resulting from the application of the Sweby limiter [228] to the central differencing in order to enforce the monotonicity criterion. For the list of other bounded numerical schemes see: [125].

3.3.5 Discretization of the Temporal Derivative Term

Discretization in time is done by prescribing a time step Δt and applying a discretization method on the temporal derivative term which in integral form reads:

$$\int_t^{t+\Delta t} \int_{V_P} \frac{\partial \phi}{\partial t} dV dt, \quad (3.39)$$

where, if control volumes do not change in time, the temporal derivative takes the form:

$$\int_t^{t+\Delta t} \left(\frac{\partial \phi}{\partial t} \right)_P V_P dt. \quad (3.40)$$

Depending on the way temporal derivative is approximated, different time discretization schemes occur:

- *Implicit Euler method:*

$$\left(\frac{\partial \phi}{\partial t} \right)_P = \frac{\phi_P^n - \phi_P^o}{\Delta t}, \quad (3.41)$$

where n is the new and o is the old time instance ($n = o + \Delta t$). This expression is directly obtained from the expansion of ϕ_P^o in the *Taylor series* and truncating second and higher order terms. It results in a scheme with numerical diffusion occurring as an error.

- *Second order implicit Euler method:*

$$\left(\frac{\partial \phi}{\partial t} \right)_P = \frac{3\phi_P^n - 4\phi_P^o + \phi_P^{oo}}{2\Delta t}, \quad (3.42)$$

where oo represents a time step before the o ($n = o + \Delta t = oo + 2\Delta t$). In such a way a generic variable is approximated with a parabola through three points in time, n , o and oo . Such method is second order accurate with numerical dispersion as the corresponding numerical error.

3.4 Optimization Approach

In general, optimization is a process of minimizing (or maximizing) a goal function $G(\mathbf{x})$. In mathematical terms, this can be expressed by Eq. 3.43, where \mathbf{x} is the design variable vector, which satisfies constraints on design variables and responses [35]:

$$\begin{aligned} & \text{minimize : } G(\mathbf{x}) \\ & \mathbf{x} \in \mathbb{R}^n \\ & \text{subject to : } U \geq (\text{or } =) f_i(\mathbf{x}) \geq (\text{or } =) L \quad \text{where } i = 0, 1, \dots, M. \end{aligned} \quad (3.43)$$

f_i is one of the M number of constraints with its upper limit U and lower limit L . For a vector of design variables to be valid, it has to satisfy all the linear/non-linear equality/inequality constraints.

3.4.1 General Work-Flow of Aerodynamic Optimization

All the essential parts of the optimization process are combined in the work-flow schematically shown in Figure 3.4. The process is split into 4 main parts. In pre-

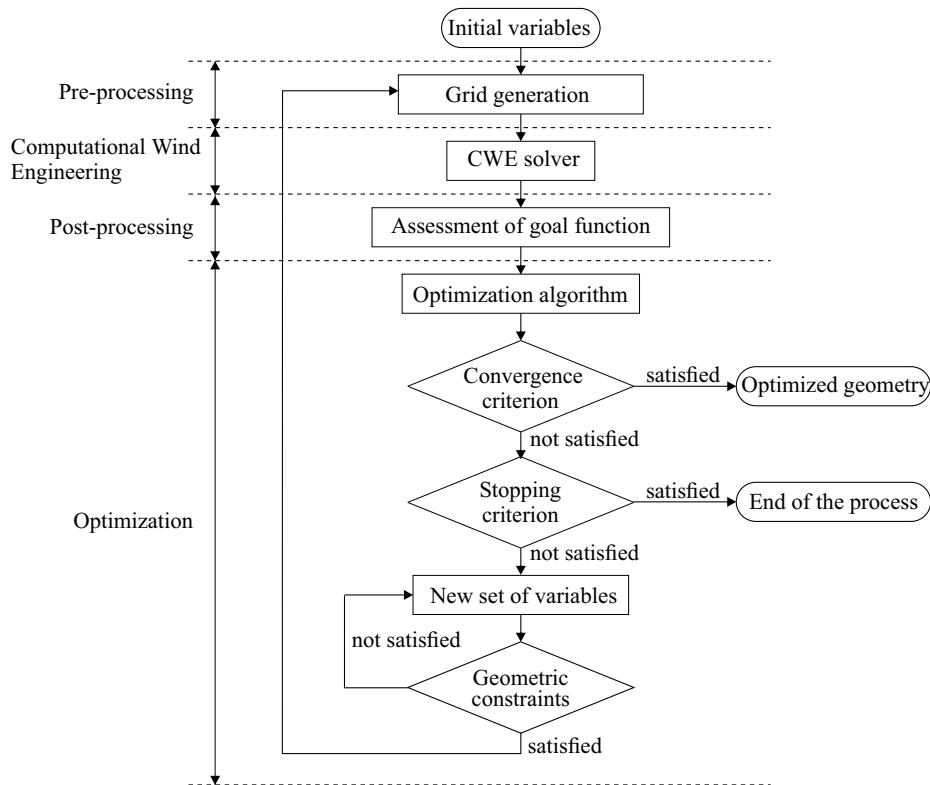


Figure 3.4: Work-flow of the optimization process.

processing, the numerical grid is automatically generated from the design variables. In the CWE part the wind flow is simulated around the geometry. In the post-processing part the relevant flow fields are used to evaluate the aerodynamic metrics and the goal function. The optimization part is the only part which significantly changes for different optimization methods. The complete optimization loop stops when either the convergence criterion is met and the optimal geometry is found, or the maximum number of function evaluations set in the stopping criterion is reached. In the Thesis, the convergence threshold is set based on the weighted residual of the goal function and equal to 10^{-4} for three successive iterations. The

maximum number of function evaluations is set equal to 25 for gradient-based, and 100 for genetic algorithm optimization. Conversely, if the stopping criteria are not met, a new set of variables is chosen based on the specified algorithm. Additional geometric constraints are checked in order to verify that the new set of variables satisfies them. The geometrically valid set of variables enters the new iteration of the loop.

3.4.2 Gradient-Based Optimization

Gradient-based optimization is a popular local optimization method which exploits gradients of the goal function to reach the local minimum. In the Thesis, a common adaptation of the GBO called *Method of Feasible Directions* is used. GBO algorithms are best suited for efficient navigation to the local minimum in the vicinity of the initial point. The two main steps of GBO are the calculation of gradient and stepping in the direction of the gradient. In mathematical terms, the gradient is defined as follows:

$$\nabla G(\mathbf{x}) = \left(\frac{\partial G(\mathbf{x})}{\partial x_1}, \frac{\partial G(\mathbf{x})}{\partial x_2}, \dots, \frac{\partial G(\mathbf{x})}{\partial x_n} \right), \quad (3.44)$$

where $G(\mathbf{x})$ is the goal function. The gradient is computed in the numerical form. The initial simulation is carried out and the value of the initial goal function is computed. Subsequent simulations are carried out for a geometry with the known change in the design variables. The obtained difference in the goal function, coupled with the known change in the design variables allows the computation of the gradient and the progression to the next iteration of GBO. The stepping in the direction of the gradient is defined as:

$$G(\mathbf{x})_{i+1} = G(\mathbf{x})_i - \eta \nabla G(\mathbf{x}), \quad (3.45)$$

where η is the gradient step. The gradient step is always a positive real number that allows the progression from the initial point x_i to the new point x_{i+1} . In the Thesis, $\eta = 0.05$ is adopted.

3.4.3 Genetic Algorithm Optimization

Genetic algorithm is a global method which mimics the Darwin's theory of evolution. There are several applications of GAO coupled with CWE analysis in the environmental engineering literature, e.g. [180, 100, 261]. The work-flow of GAO adopted herein is shown in Figure 3.5. The initial step consists of the selection of a random initial population and the assessment of the goal function for each individual. The population size is one of the main parameters affecting computational cost and convergence, and is set to 10 herein. *Reproduction* includes *crossover* and

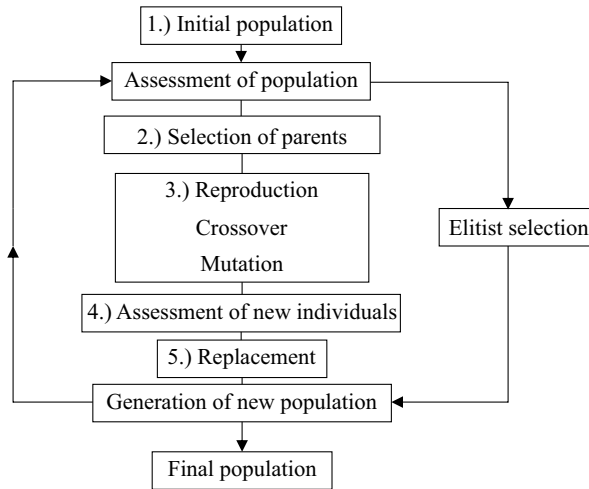


Figure 3.5: Work-flow of genetic algorithm optimization.

mutation, which take place in the following order: i.) crossover is applied with a fixed probability on the chosen parents; ii.) if crossover is applied, mutation is applied with a fixed probability to the new individuals; iii.) if crossover is not applied, mutation is applied with a fixed probability to the parents. The crossover rate specifies the probability of crossover being performed to generate a new offspring. Mutation is performed by modifying the value of the design variables by a given percentage. After the reproduction process, the goal function for the newly-generated offspring is evaluated. In the *replacement* process the current population and the newly-generated individuals are combined to create a new population. In the study, this is done in the form of the *elitist selection*. A defined number of the best individuals from the initial population are directly transferred to the new population. The remaining population is filled by the best offspring and remaining parents.

For more details, the interested readers are referred to [219]

3.4.4 Aerodynamic Optimization in Civil Engineering: an Overview

Aerodynamic Optimization has attracted growing interest of the scientific community over the past 60 years. Consequently, several automated design optimization procedures and algorithms are available nowadays, recently reviewed in [221]. Due to the continuous advancements in computational resources, optimization has become an important stage in aerodynamic design with applications in many industrial fields, e.g. aerospace [112], turbomachinery [145], automotive [74], and train aerodynamics [174], energy harvesting, internal pipe and cavity flows, among

others. Application to the field of wind and structural engineering suffers a relative delay, mainly induced by the high computational costs related to the simulation of turbulent, high-Reynolds wind flow around bluff-bodies [7] and simulation of ABL [22]. Shape optimization is applied on a wide range of different geometries. From the studies of general shapes, e.g. optimization of trapezoidal bluff-cylinders [45, 160] and recent shape optimization of circular cylinders [130]; to applications in Civil Engineering where the main focus is put on optimization of the aerodynamic shape of buildings [25, 22, 76, 77, 69], and bridge decks [58, 57].

In all of these studies, the computational cost saving is pursued by adopting Surrogate-Based Optimization (SBO). In SBO, relatively inexpensive surrogate model replaces the expensive goal function. Therefore, the search for the optimal solution is carried out on the surrogate model, which has to be defined in advance, based on the adequate number of simulations performed on the original goal function [22]. The type and application of surrogate model, and the total number of the calibration simulations are of utmost importance, and can drastically affect the accuracy of the optimization [194, 89]. Variety of different surrogate approaches are employed in wind engineering applications, e.g. basic *Kriging* [22, 58], *Multi-fidelity co-Kriging* [69], *Artificial Neural Network based surrogate* [77]. The sampling strategy to define the surrogate model is most commonly the random point generation [77] or optimal Latin hypercube sampling [22]. The number of sampling points in the reviewed literature significantly varies between the cases; from 15 [22, 58] up to 200 [77].

In the studies above, GAO is preferred a priori to GBO because of its general robustness in handling large design spaces characterized by multiple local minima and/or discontinuities. To compensate for relatively high number of function evaluations required by GAO compared to GBO, they are coupled with the less expensive surrogate models.

The optimization objective is generally defined in the form of multiple goal functions from the simulated aerodynamic metrics, e.g. drag and lift coefficients and their fluctuations [22, 77, 69, 130]. Conversely, in [57] a single goal function is evaluated as the summed volume of bridge components, while the aerodynamic metrics are taken into account as design variables.

In a general modelling perspective, windblown sand phenomena should be simulated by accounting for both wind and sand flow. In an engineering perspective, at the detailed design stage, the accurate barrier performance shall be assessed by means of physical tests, i.e. full-scale field tests in windy and sandy environments or by scaled WT tests with incoming drifting sand [44]. Alternatively, its performance can be assessed by means of multiphase CWE simulations [190, 155] by adopting time evolving free sand-surface boundary conditions. Both WT tests and multiphase simulations are not affordable within the preliminary design phase and related optimization studies because of their high cost. In the Thesis, the SMM performance is estimated by means of purely aerodynamic metrics defining

the region where the local wind flow induces sand accumulation, as defined in [40]. Indeed, the SMMs have maximum sand trapping performances without sedimented sand around them, and sand sedimentation involves the monotonic decrease of their performances [44]. Hence, single-phase CWE simulations are able to estimate the maximum SMM performance. Moreover, even if the aerodynamic metrics are expected to be approximated, they are able to describe the relative performances of different alternative solutions, as demonstrated in [40]. Throughout the Thesis wind profile at the inlet is modeled as the ABL having in mind that the SMMs are low-rise structures mounted on the ground surface, and the vertical change of velocity is of utmost importance.

Conversely, most of the studies cited above adopt two-dimensional computational domains that refer to horizontal planes far from the ground level, for applications to high-rise buildings, or to vertical planes around bridge decks far from the ground surface. Consistently with the assumption above, in such studies uniform incoming wind is adopted at the inlet boundary: in other terms, the ABL is not accounted for during optimization. In the same computational cost-saving perspective, most of the studies adopt RANS approach to turbulence modeling. Higher fidelity turbulence models, such as LES, are only partially adopted in [69] and in full in [77], when the minimization of the fluctuating wind forces is the optimization goal, or one of the objectives. In the Thesis, single-phase simulations modeled by the steady RANS approach are adopted having in mind that: i.) unsteady fluid phenomena can be neglected in the barrier aerodynamic assessment since sand mass transport happens at a much larger time scale than turbulence characteristic time scales; ii.) reference is made to equivalent static wind force corresponding to the extreme effects of the turbulent wind to assess the cost of the barrier. The whole adopted computational model has been validated using accurate WT tests in [38] for the same class of aerodynamic problems, i.e. a nominal 2D bluff-body immersed in a turbulent ABL. The same computational model has been adopted to study aerodynamic behavior of windblown sand solid barriers in [39]. Additionally, RANS has been widely used for comparable configurations in dune aerodynamics analysis [150, 6, 38, 149].

3.5 Computational Wind Engineering and Wind Tunnel Testing in Railway Aerodynamics: an Overview

Generally speaking, the aerodynamic behavior of the railway is a combined result of the aerodynamic features of substructure and superstructure, and their interactions. In this perspective, the *substructure* is treated throughout the Thesis as the grouping of embankment and, if present, ballast bed. Compared to the

geometric shapes, substructure can be simplified by an overall ridge with stepped inclined slopes. The *superstructure* is an ensemble of the track system components that rest on the substructure, such as sleepers or slab, and rails.

The *substructure aerodynamics* shares some common flow features with nominally two-dimensional *fundamental landforms*, such as trapezoidal ridges, ideal transverse dunes, sloped escarpments and forward-facing step as the limiting case of the latter. The flow around these forms has been widely studied since the end of the Seventies by the WT tests [34, 33, 217], and later by the CWE simulations [62, 181, 222]. Taken as a whole, these studies testify that the wind flow along the top surface of the form depends on the inclination of the upwind slope and the height of the form with respect to the incoming wind velocity profile. The first attempts in geomorphology sciences, especially the ones addressed to relate the wind flow and the morphodynamics of the basic forms, are by far more recent. The aerodynamics of the ideal transverse dune has been recently studied both experimentally and computationally, see e.g. [152, 38] and cited references therein. The study in [109] provides a detailed overview of previous studies on escarpment aerodynamics in geomorphological literature, complemented by additional references in fluid dynamics. In addition, the study simulates the flow around forward-facing steps with different heights and under differently-yawed incoming flow.

Several studies in aerodynamics explicitly refer to *railway substructures*, since the pioneering field tests in [13], WT tests in [14] and [36], followed by the first CWE simulations in [270]. Herein, they are first categorized with respect to the *field of application*. Most of them are mainly focused on train aerodynamics under cross wind: the WT tests in [227] and [211], the systematic WT campaign in [26, 49, 233], the computational simulations in [121], and the hybrid WT-CWE coupled approach in [66] and [178]. Study in [271] deals with the simulation of the wind flow around the substructure, with a goal to ground the design of in-situ anemometric monitoring layout. Some other studies specifically address the wind-induced erosion of the embankment, i.e. the WT tests in [36], and the computational simulations in [270]. Sand transport, erosion and sedimentation around the embankment are tentatively discussed by wind+sand WT test in [255] and two-phase CWE simulations in [173].

The *results* of the studies above depend on the field of application and related objectives. The studies in train aerodynamics mainly focus on pressure and forces acting on the rolling stock, where the embankment is included as a geometric feature that can affect the train aerodynamics. A limited number of such studies directly investigate the local flow around the substructure without a train model: study in [49] provides anemometric measurements of the speed-up ratio at the top of a single track with 3:2 (horizontal:vertical) sloped, 6 m-high embankment for seven values of yaw angle. The study clearly shows that speed-up ratio monotonically increases as wind gets more perpendicular to the embankment, up to 1.3 for perpendicular wind.

Study in [178] analyzes the velocity field of the simulated flow around a single-track, 3:2 sloped, 1, 3 and 5 m-high embankments under two yaw angles. It discusses the conditions under which the *Prandtl's independence principle* holds for swept embankments at yaw angles, in the wake of experimental evidence in [13, 14]. This principle is based on the proofs of Prandtl and other authors [189, 212, 127] that the application of the so-called boundary-layer approximation to a steady, incompressible flow of yawed wind over a cylinder with infinite span-wise length results in the set of equations which does not depend on the span-wise velocity component of the incoming flow. For the details of the proof that the principle holds for wings of infinite span-wise length see [251]. Prandtl's independence principle is in the Thesis confirmed for standard railway geometry. The obtained wall shear stresses for different yaw angles, when properly rescaled, show exactly the same trends in the flow-wise and span-wise direction, i.e. it is independent of the span-wise component of the inlet velocity.

In [271] a detailed analysis is provided of both instantaneous and time-averaged flow quantities around the whole double-track, 3:2 sloped, 5, 3 and 1 m-high embankments and at the in-situ monitoring points, in line with the goals of the study. The aerodynamic studies about wind-induced erosion and sedimentation are ultimately and specifically focused on the distribution of the wind shear stresses at the embankment surface, and its comparison to the threshold value above which erosion conditions occur [10, 197]. The measurement of such state variable is challenging in WT tests. The early study in [36] is limited to providing the pressure coefficient distribution and the mean wind velocity along and around a single track, with 3:2 sloped, 8 m high embankment under orthogonal wind. The recent article [255] includes the wind velocity field around a 3:2 sloped trapezoidal ridge, as a drastic simplification of a railway embankment. Conversely, the field of shear stresses is easily calculated from CWE simulations. The article [270] complements the pressure coefficient distribution with the streamline field visualization and the shear stress distribution around and along a single track, 3:2 sloped embankment under orthogonal wind at different Reynolds numbers. Surprisingly, in [173] shear stress distribution along the adopted single track is not presented. Moreover, a quite unconventional 2:3.5 sloped embankment is adopted as a referent geometry.

On the one hand, the *experimental setup and computational models* are adapted to application field and flow quantities of interest. In particular, computational models adopted for train aerodynamics and monitoring layout aim at capturing the instantaneous flow features and aerodynamic forces besides the time-averaged ones: coherently, LES is adopted in [178], *Detached Eddy Simulation* (DES) in [271], while a RANS approach is used in [66] and [121]. CWE studies devoted to erosion and sedimentation are focusing on the time-averaged flow features responsible for the long-term morphodynamics of the sand surface. In the light of this, in [270] and [173] the steady RANS approach is adopted, even if the common choice of the standard $k-\varepsilon$ [140] model looks questionable, because of its well-known

low accuracy in simulating position of the inflection points. On the other hand, minimum requirements have to be respected by WT tests and CWE simulations to guarantee similarity requirements regardless of the specific goals of the study. Among them, the geometric similarity of the substructure and the extension of the experimental/computational domain are of utmost importance. The substructure includes both embankment and ballast bed in most of the WT and CWE studies, except in [255] and [121], where only the embankment is present. The scaling of the substructure model in WT is carefully considered in studies devoted to train aerodynamics. The WT campaigns in [26, 49, 233] systematically address this issue, by fulfilling requirements on *Blockage Ratio* (BR) and *Aspect Ratio* (AR) set by standards ($BR < 15\%$ in) [85], technical specification ($BR < 10\%$ in) [235] and the best practices. The following values are used: $BR \leq 2\%$ and $AR \approx 19$ in [49], $BR \approx 4\%$ and $AR \approx 26$ in [233]. Moreover, study in [233] systematically discusses the tip effects at the ends of the embankment, by testing different end layouts (e.g. wall-to-wall, finite length with and without noses, among others). It follows that the wall-to-wall models are the most suited ones and show the closest results compared to the real world measurements.

The transfer from the train aerodynamics to the erosion-sedimentation studies is not accurately and precisely defined, e.g. $BR = 8\%$ and $AR = 15$ in [36], but $BR = 20\%$ and $AR = 4.8$ in [255]. Except for the pioneering study in [270], and the recent one in [173], CWE simulations are usually carried out in three-dimensional domains for wind direction orthogonal to the substructure. The along-track dimension of the domain varies for orthogonal wind direction from $2H$ in [271] to $25H$ in [178], where H is the overall height of the substructure. A sensitivity study about the domain along-track dimension for a skew angle equal to 50° is mentioned in [178], but results are given only for embankment with train.

The *superstructure aerodynamics* is overlooked in literature. Its effects on train aerodynamics are probably negligible, but it is expected that they play a prominent role in windblown sand erosion/sedimentation along the track, and the knowledge gained from the flow around the superstructure to be a relevant background for the design of receiver SMMs. The lack of knowledge follows from the multiscale features of the resulting modelling problem. In particular, rails and other superstructure components have a characteristic spatial scale (dozen of cm) that differs by two orders of magnitude from the characteristic scale of the substructure. It follows that simplified rails are included only in the largest scale models of few WT tests, e.g. [49, 233, 178], but their similarity requirements and aerodynamic effects are not discussed. Most of the CWE models do not include any component of the track system [270, 271, 178, 121], because of the high number of cells resulting from the spatial discretization around them, and the significant computational cost of the simulations in turn. Only very recently an attempt is made to account for rails in the computational model in [173]. The study deals with the effects on the wind-sand flow in the gaps obtained by removing the upper part of the ballast bed between

the successive sleepers. In order to reduce the computational cost, intrinsically 3D flow around the track is simplified by two 2D simulations. The 2D domains are defined in the vertical planes at the midpoints between the two successive sleepers and the two successive gaps. Such an approach is clearly ill-posed in aerodynamic terms. Indeed, the width of gaps and sleepers in the railway direction is close to the rail and gap height, so nominally 2D flow cannot develop along the rail direction, not even in the time-averaged terms. The problem defined in such a way is not only ill-posed under yawed incoming winds, but also under winds orthogonal to the railway spanning direction.

Within the Thesis, to perform all of the simulations the open source code *OpenFoam*© [249] is used. The available computational resources consist of 18 processing cores on *Intel(R) Core(TM) i7 CPU 860 @ 2.80GHz*. The optimization algorithms in the presented study are carried out with the open-source optimization toolbox *Dakota*© [1].

Chapter 4

Computationally-Based Design of Innovative Path Sand Mitigation Measures

Parts of the work presented in this chapter are published by the author in a peer-reviewed article [115].

This Chapter covers the application of the general design framework on *Shield for Sand* barrier, in particular the detailed design and the optimization. The shape of the barrier, in the form of the conceptual and preliminary design, has been previously patented by the *SMaRT* team. The Chapter starts with the introduction of the conceptual, preliminary and detailed design of the SMM where its aerodynamic working principle is defined. In this section, the adopted design variables, the goal function and the significant contributions to the goal function are presented. The physical and production constraints are detailed as well. Finally, the shape optimization process is thoroughly described.

4.1 Conceptual and Preliminary Design of *Shield for Sand*

The shape optimization is carried out on the patented *Shield for Sand* solid barrier [41]. Figures 4.1 (a) and (b) show the conceptual design and render of the barrier respectively. The *Shield for Sand* cross-section includes three components: i.) a generic foundation (A); ii.) a lower quasi-vertical part (B); and iii.) an upper windward concave deflector (C). The barrier overall height H depends on the specific construction site, namely the magnitude of the incoming sand drift. Each component ensures a specific functional requirement of the SMM. The foundation weight counteracts the overturning moment induced by the the wind load and the passive pressure of the upwind-trapped sand. The quasi-vertical part allows an easy

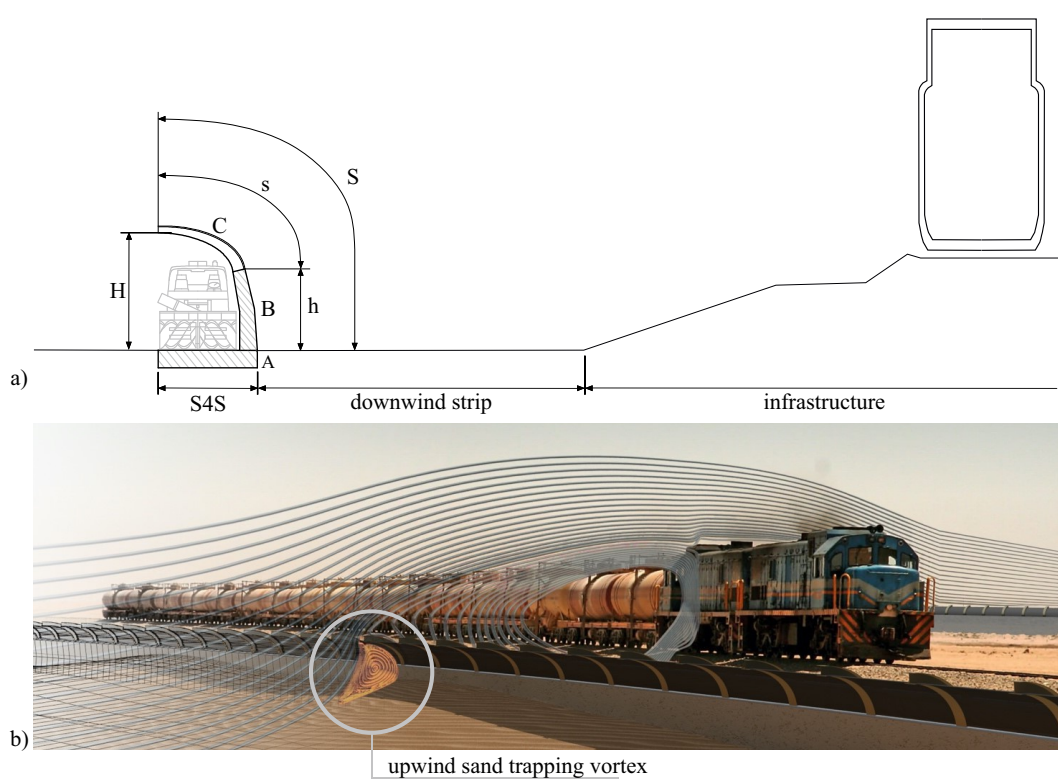


Figure 4.1: Shield for Sand conceptual design (a) and a render along a desert railway line (b).

sand removal and maintenance with an SRM, e.g. sand ploughs or sand blowers. The upper windward concave deflector induces an upwind recirculation and reverses the flow close to the ground, necessarily inducing sand sedimentation in the vicinity of the inflection point and sedimentation or backward erosion between the inflection point and the barrier. As a result, sand sedimentation occurs upwind the barrier where $|\tau_w| < \tau_t$ [39, 44], and backward erosion where $\tau_w > -\tau_t$. In the light of this, the upwind recirculation vortex behaves as a sand trapping vortex. The shape of the deflector is expected to deeply affect aerodynamics of the SMM. The deflector in Figure 4.1 (a) is obtained during the conceptual design by an heuristic approach; its shape follows a spline with multiple control points. The geometry shown in the figure is used as the reference baseline geometry to comparatively assess how well the geometry from the optimization process performs. It is labeled #0 in the following and its shape is defined by $h/H = 0.33$ and $s/H = 1.12$. The choice of the construction methods and materials do not change the shape of the barrier or the performance.

4.1.1 Detailed Design and Optimization Setup

Detailed design of the barrier significantly differs in the way geometry is generated from the preliminary design. It is designed having in mind construction simplicity and cost saving, while maintaining or the improving aerodynamic performance. The goal of this stage is to find suitable semi-finished products which approximate the geometry of barrier and are relatively cheap. The cost of barrier is of utmost importance because *Shield for Sand* is adopted to prevent SULS over long stretches of railway infrastructure. Figure 4.2 depicts the detailed design of *Shield for Sand* barrier. It is assembled from 5 construction members, as annotated in the Figure:

1. corrugated steel panels;
2. precast reinforced concrete L-profiles;
3. refilling soil;
4. light concrete foundation;
5. stabilized ground.

The functional part of the barrier consist of corrugated circular steel panels of constant radius (1) replacing the spline-like deflector defined in the preliminary design. Depending on the desired accuracy of the geometry approximation the number of panels varies. In the Thesis, in order to keep the design as simple as possible only two scenarios are adopted: $N=1$ where the deflector consists of a single panel; and $N=2$ where the deflector consists of two panels. The straight vertical part of the barrier and foundation are coupled in a single construction member in a form of L-profile (2). The L-profile has a deflected tip with radius equal to the first panel allowing the joint of the panels and the concrete wall. From the figure it can be seen that the barrier is positioned in the excavation which is refilled with the soil on top of the horizontal L-profile surface. The amount of refilling soil (3) depends on the magnitude of aerodynamic moments wind is exerting on the geometry. Therefore, the dimensions of excavation follow from the computed mass. Conversely, light concrete foundation (4) and stabilized ground (5) depend on the geotechnical features and have to be adjusted to the particular construction site.

The total height of the barrier H can vary in order to obtain different sand trapping capacity and meet different sand drift conditions along the railway alignment. The constructions members are rescaled accordingly. However, in the optimization, the height is kept constant in order to perform pure shape optimization. In analogy to the detailed design, two alternative design solutions are considered, as sketched in Figures 4.3 (a) and (b). The parts of the detailed design which do not affect the aerodynamics of the barrier are excluded in the definition of the geometry and are tackled only in the definition of the cost.

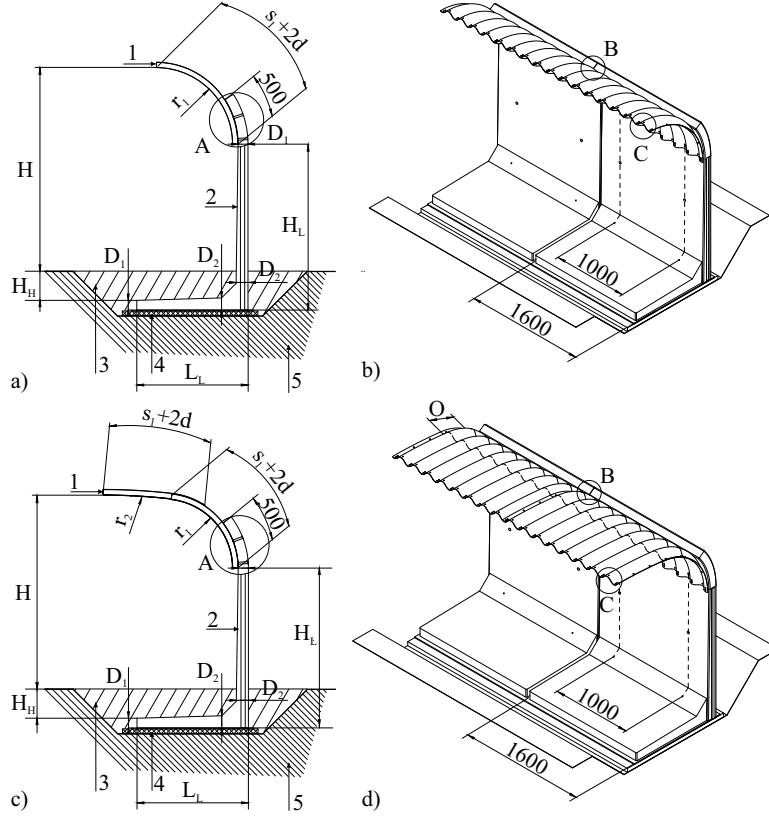


Figure 4.2: Detailed design for $N=1$ scenario: (a) cross-section; (b) isometric view. $N=2$ scenario: (c) cross-section; (d) isometric view.

In Figure 4.3, all the geometrical parameters are detailed. Among them, the height of the vertical wall h and the arc lengths of the panels s_i are adopted as *design variables*, while the central angles α_i , tangency angle α_t , radii r_i and overall curvilinear length S are *derived parameters*. *Geometrical constraints* are introduced to discard undesired shapes, and to ensure the functionality of the barrier. Vertical wall and adjacent arcs share common tangent lines at control points P_i , to ensure the smooth shape between the transition of different parts. The design variables are constrained directly within the following ranges: $0.18 \geq s_i/H \geq 0.53$ and $0.325 \geq h/H \geq 0.65$, where the lower bound on h/H allows unobstructed sand removal. Additional constraints are imposed on derived parameters: i.) $S = h + \sum_{i=1}^N s_i \geq H$, ensuring the total curvilinear length S of the barrier to be longer than or equal to its height H ; ii.) $\sum_{i=1}^N \alpha_i \leq \pi/2$, ensuring that the height of the free end of the deflector is equal to H . *Manufacturing constraints* apply to r_i in order to allow cold bending ($r_i \geq r_m$, being $r_m = 634$ mm). Moreover, they ensure that the thickness of the steel panels t_i obeys standard discrete values of the product.

In the following, the main bulk parameters are denoted by capital letters. L

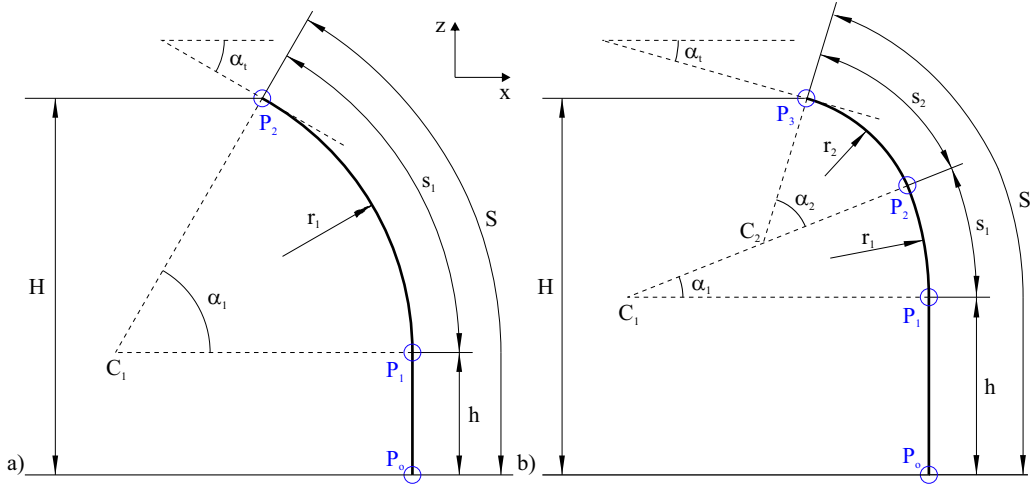


Figure 4.3: Above ground geometrical setup with one (a) and two (b) steel panels.

refers to the horizontal lengths, while H to the vertical ones. Subscripts R and S refer to recirculation and sedimentation zones, respectively, while subscripts u and d distinguish between upwind and downwind position along the x -direction.

The *goal function* is generally defined as $G = c/p$, where c and p are the barrier cost and performance metrics, respectively. Most commonly, as testified by the literature review of the optimization processes in previous chapter, goal function in wind engineering contains only the performance metric, e.g. lift or drag coefficient, mass of the system, etc. Cost is included in this study because, in order to satisfy the main goal of Path SMMs it has to be erected for a number of kilometers. In such a way, a proper protection can be ensured for long stretches of railway in SULS conditions. Hence, slight reduction of the cost per meter of the barrier can result in high overall cost reduction. The sand trapping *barrier performance* p is estimated by aerodynamic metrics only. In particular, the distribution of τ_w/τ_t over the ground surface upwind the barrier. Performance of the barrier defines the maintenance cost. Higher the performance, lower the frequency of maintenance resulting in the lower related costs. Analogously to the definition of sand sedimentation criteria and the working principle of Path SMMs, the performance of the *Shield for Sand* is proportional to the potential sedimentation length upwind the barrier. By additionally taking the stagnation point at the barrier upwind surface into account, the cross-sectional sedimentation area A_S is defined instead of the sedimentation length (see Figure 4.4 a, where the corresponding dimensions of the sedimentation and recirculation areas are annotated). A_S is bounded by the profile of the barrier below the stagnation point, and the sedimentation length, i.e. $A_S \propto L_{S,u}H_{S,u}$. As proven in [40], A_S is linearly proportional to the recirculation area $A_R \propto L_{R,u}H_{R,u} = H_{S,u}$, where $L_{R,u}$ and $H_{R,u} = H_{S,u}$ are the along-wind horizontal and

cross-wind vertical dimensions of the upwind sand trapping vortex, respectively. Herein, the barrier performance is finally adopted as $p = A_R$ having in mind the comparative perspective of the study.

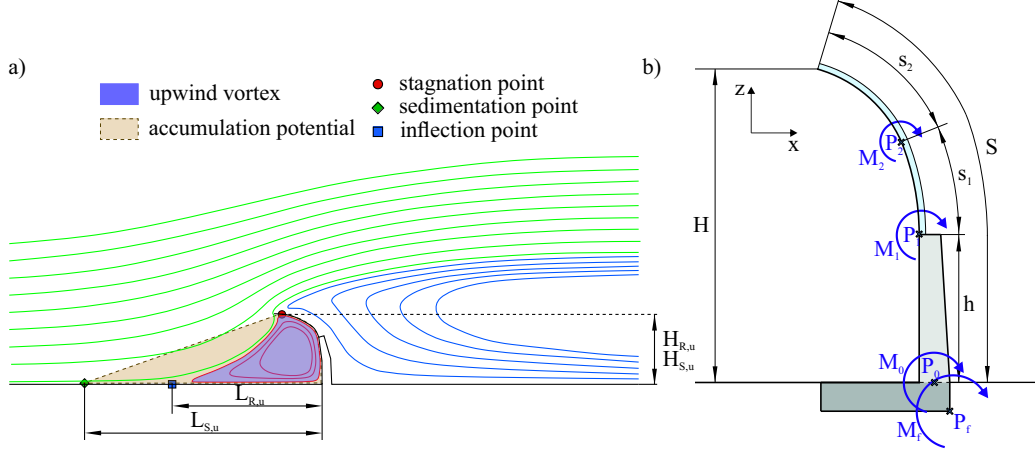


Figure 4.4: Mean streamlines around *Shield for Sand* baseline solution, structures and characteristic lengths of the local flow, after [39] (a). Structural parameters, with wind-induced bending and overturning moments (b).

The overall *barrier cost*, among others, includes shipping, labour, and material costs. These costs depend, to a different extent, on actual specific site, and industrial and economic scenarios. Material costs do not vary as much. For the sake of generality and comparability, the optimization is carried out by considering the material costs only. The barrier cost c follows from the cost of materials per unit weight, and from the barrier total weight. The ratio between the steel unit cost and the reinforced concrete unit cost is set $c_s/c_{rc} = 44$. Weights follow from dimensioning of the elements, that mainly depends on wind-induced loads, and passive pressure of the trapped sand. In the optimization, the aerodynamic wind loads are considered only, coherently with the aerodynamic nature of the research. The design bending moments M_i induced by the wind and design overturning moment M_f are assessed at pivot points P_i , for $i = 0, 1, 2$, and P_f , respectively (see Figure 4.4 b). Clearly, the higher M_i and M_f , the higher the construction cost c . Component cross-sections and global equilibrium have been verified by referring to [83]. Design moments are assessed at peak stagnation pressure q_p related to the basic wind velocity $u_b = 30$ m/s, and wind exposure factor $c_e(z) = 1 + 7/\ln(z/z_0)$. Wind load partial safety factor is set equal to $\gamma = 1.5$, while steel resistance partial safety factor is set equal to $\gamma_s = 1.05$.

Cost and performance are both functions of the barrier size and shape. In other words, the problem has an intrinsic multi-objective nature captured by a single goal function. Two different optimization methods are used. If the response of

the goal function is monotonic and continuous, GBO is selected because of its fast convergence. Conversely, if the response of the goal function contains multiple local minima, GAO is preferred.

4.2 Specific Computational Approach

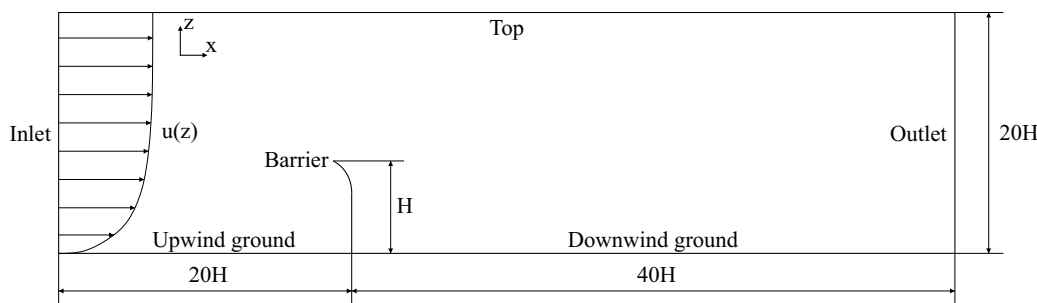


Figure 4.5: 2D computational domain (not in scale). All the lengths are given in relation to barrier height H . $u(z)$ -line represents the incoming logarithmic velocity profile.

The adopted 2D computational domain is shown in Figure 4.5. The computational domain includes the flat ground both upwind and downwind the barrier, and the barrier itself. All the quantities at the inlet boundaries are indicated as far-field, defined in a way which resemble the environmental conditions in arid regions. The upwind far-field is modeled by means of inlet boundary conditions: Von Neumann condition is used for pressure, while Dirichlet conditions are imposed on u , k and ω . The far-field incoming wind velocity profile is prescribed using the log-law $u(z) = \frac{u_*}{\kappa} \log\left(\frac{z+z_0}{z_0}\right)$, where $\kappa = 0.41$ is the Von Kármán constant, u_* is the friction velocity, z_0 is the aerodynamic roughness length. The profiles of $k(z)$ and $\omega(z)$ are set according to [200] in order to replicate the neutral ABL. Such a combination of velocity and turbulence parameters at the inlet are in equilibrium, i.e. the wind profile does not develop in the domain. At outlet, for all the flow parameters zero-gradient condition is imposed. No-slip conditions are imposed at the ground surfaces and at barrier wall. The convection terms are discretized by means of the so-called Limited Linear scheme, a 2nd order accurate, bounded, Total Variation Diminishing (TVD) scheme resulting from the application of the Sweby limiter [228] to the central differencing in order to enforce the monotonicity criterion. SIMPLE algorithm is used for pressure-velocity coupling.

Far-field aerodynamic roughness length at the inlet is set equal to $z_0 = \cdot 10^{-2}$ m, while the ground aerodynamic roughness length of the upwind and downwind strips is set equal to $z_{0,g} = \cdot 10^{-3}$ m because of the ground grading in the neighborhood of the infrastructure. The far-field wind shear velocity is set equal to

$u_* = \sqrt{\tau_w/\rho} = 0.82$ m/s, where τ_w is the shear stress at the ground surface. Such a value of u_* is appropriately chosen in order to exceed the threshold resulting from the chosen diameter of sand. For example, the upper limit of sand granulometry $d = 0.5$ mm results in $u_{*t} = 0.4$ m/s [197], and is still significantly overshoot by the chosen wind profile. From the logarithmic wind profile, It directly follows that $Re_H = Hu_H/\nu \in [1.7 \cdot 10^6, 3.7 \cdot 10^6]$ for a barrier height equal to $2 \leq H \leq 4$ m. In the supercritical turbulent regime, significant Re effects are not expected.

Space discretization and definition of geometry for the optimization is done according to Figure 4.3 (a) and (b). In both scenarios, the vertical concrete wall extends from control point P_0 to P_1 . If the position of P_0 point is fixed at the origin of coordinate system, the coordinates of $P_1 = (0, h)$ follow directly. The vertical tangency at point P_1 ensures the center of the first arc to be at the same height as P_1 , at the distance r_1 from it ($C_1 = (-r_1, h)$). The coordinates of point $P_2 = (C_{1,x} + r_1 \cdot \cos\alpha_1, C_{1,z} + r_1 \cdot \sin\alpha_1)$ follow. The definition of the N=1 scenario stops here. To add another arc to the geometry, additional points have to be defined. The position of second arc center is computed from the constraint of tangency at point P_2 . If two circular arcs are tangent at a point, their radi-vectors are parallel through that point. From this, the two coordinates of the second center can be written: $C_{2,x} = P_{2,x} - r_2/r_1(P_{2,x} - C_{2,x})$; and $C_{2,z} = P_{2,z} - r_2/r_1(P_{2,z} - C_{2,z})$. The coordinates of $P_3 = (C_{2,x} + r_2 \cdot \cos\alpha_2, C_{2,z} + r_2 \cdot \sin\alpha_2)$ follow.

To finalize the definition of geometry, radii and circle angles have to be defined. In the N=1 case the following relation can be written: $H = h + s_1/\alpha_1 \cdot \sin(\alpha_1)$. The value at which the relation is satisfied is adopted as α_1 . Radius of the first arc follows $r_1 = s_1/\alpha_1$. In the N=2 case, the similar relation can be written: $H = h + s_1/\alpha_1 \cdot \sin\alpha_1 + s_2/\alpha_2(\sin\alpha_2 - \sin\alpha_1)$. Additional constraint is taken in account here to close the equation $\alpha_1 + \alpha_2 = 90^\circ$, i.e. $\alpha_t = 0$. The choice of this constraint is justified at the beginning of Section 4.3.2. These relations prove that with the adopted constraints the design variables are sufficient to compute the derived parameters and, therefore, the complete geometry of the barrier.

The two scenarios are used to specify the position of non-permeable wall boundary conditions in Figure 4.6 which are marked by the thick black line. The red lines represent the characteristic control lines used to generate the grid and keep its satisfying quality. The structure of the control lines depends on the curvature of the deflector. For low circular angles the grid is defined in the same way as for the limit SVW case (Figure 4.6 a). Conversely, the deflector with high circular angles are discretized with the so-called *OH* topology, preferred for the discretization of circular arcs (Figure 4.6 b). The position of red lines in both cases is related to the geometry of barrier. The automatic grid generation within the optimization procedure is carried out by a script controlling *blockMesh* utility within *OpenFOAM*®. To simplify grid generation and to assure high grid quality, barrier is modeled as a panel with zero thickness.

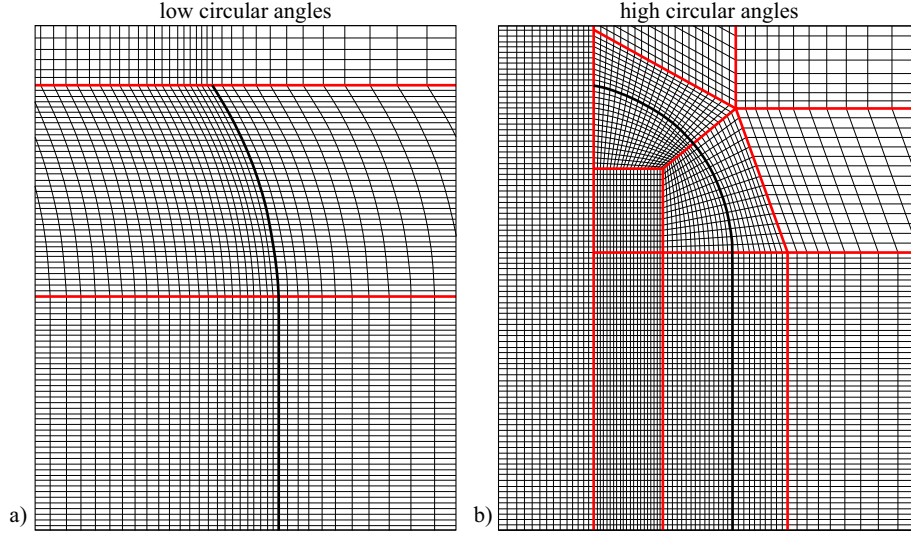


Figure 4.6: Automatically-generated numerical grids: a) around a barrier with low circular angle; b) around a barrier with high circular angle.

The resulting grids are completely structured, i.e. consisting of hexahedral control volumes. The grid is refined along the ground and at the barrier walls, so that the height n_w of the wall-adjacent cell: i.) provides a sufficiently high grid resolution in the normal direction n to the surface in order to adequately resolve the gradients of flow parameters, ii.) complies with the wall function requirement on dimensionless wall unit $30 < n^+ = n_p u^* / \nu < 200$, where $n_p = n_w / 2$ is the cell center height. In the present study, a further need rises in relation to computational efficiency, because of the large number of simulations required for the optimization process. For analogous accuracy, efficiency is pursued by cost savings made possible by relatively coarse computational grid. The requirement (i) is satisfied when the n_w is as small as possible. Conversely, the requirement (ii) suggests large n_w . The second requirement is setting the range from which n_w can be chosen. To find the best value of n_w , a preliminary study on grid dependency was carried out. The initially-selected grid was the finest which satisfies the requirements (i) and (ii), i.e. $n^+ = 30$. The grid density which is finally adopted results from grid coarsening, until the significant changes in the results occur, or the limit of $n^+ = 200$ is violated. The retained value of the cell height $n_w = 0.0125H$ results in a satisfying balance among requirements, being the one for which the main aerodynamic metrics are in the range from 2% to 5% compared to the finest grid. The average of the resulting n^+ equals ≈ 100 . The total number of control volumes depends on the geometry of the barrier around which the grid is created, and ranges from 30,000 to 50,000.

4.3 Preliminary Sensitivity Study

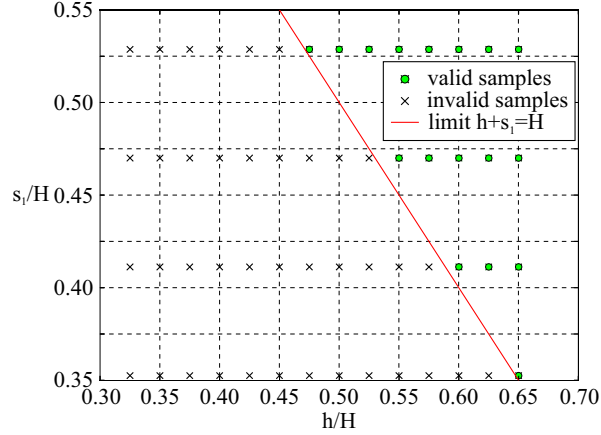
A systematic sensitivity study is carried out before optimization. First, it is intended to provide a sound phenomenological insight in the effects of the design parameters on the flow field. Second, it aims at evaluating the trend of the performance and cost, as well as of the goal function, and at recognizing emerging trends versus other parameters, if any. Third, the sensitivity study is carried out to select a priori the most suited optimization method in the light of the trend of the goal function, and to prove a posteriori that the optimization converges to the optimal solution. The preliminary sensitivity study is carried out for both alternative design solutions ($N = 1$ and $N = 2$). The same quantities are adopted as design variables within both, the preliminary study and the optimization process.

For the sake of generality, in the following, all the design variables and the results are made dimensionless by referring to the quantities H (the height of the barrier), u_H (the incoming wind speed at the barrier height), ρ (air density). Moreover, performance and cost metrics, as well as the goal function, are normalized by referring to the corresponding quantities of the baseline solution from preliminary design in order to highlight comparative nature of the optimization. In the following results, parameters related to the baseline solution are marked by subscript 0. The shape of the baseline solution is patented and the details about the shape are presented in [41].

4.3.1 Preliminary Sensitivity Study for the One-Panel Deflector

Figure 4.7 shows the sampling of the design parameters h and s_1 for the preliminary study for $N=1$. The sampling covers the ranges $0.325 \leq h/H \leq 0.65$ and $0.35 \leq s_1/H \leq 0.53$ by uniform discrete steps $\Delta_h/H = 0.025$ and $\Delta_{s_1}/H = 0.05875$. 17 valid cases result when all the constraints are satisfied, bounded from the invalid cases by the constraint $s_1 + h = H$.

Figure 4.8 collects fields of the flow variables relevant to the barrier performances, with reference to three samples. Sample #1 has a low overall curvilinear length very close to H ($s_1/H = 0.353$ and $h/H = 0.65$). In other terms, its geometry is the closest to the SVW limit case ($s_1/H + h/H = 1$) among the evaluated samples. Conversely, sample #3 is the one with the maximum curvilinear length ($s_1/H = 0.53$ and $h/H = 0.65$). Finally, sample #2 is the intermediate case ($s_1/H = 0.41$ and $h/H = 0.625$). Figure 4.8 (a) shows the mean streamlines in a wide region around the barrier. Two main coherent flow structures are recognized: an upwind vortex and a very large downwind vortex, that extends over about $15H$ in the wake. While the downwind vortex does not significantly vary, both the x -wise and z -wise length of the upwind vortex depends on the design parameters. Corresponding erosion and sedimentation zones along the ground level


 Figure 4.7: $N = 1$ - Sampling plan for sensitivity study.

complement the figure. Figures 4.8 (b) and (c) show a close-up view around the barrier, in particular the mean streamlines of the wind flow (b) and contours of the turbulent dissipation rate ω filled by vorticity color map (c). Besides the outer quasi-irrotational free flow (green streamlines, $\omega \approx 0$), and the upwind and downwind main clockwise vortices (red and blue streamlines, low ω), both streamlines and ω contours point out in detail the small secondary vortex downwind the barrier (orange streamlines, very low ω), and the shear flow (yellow streamlines, high ω) corresponding to the attached and separated boundary layer. Boundary layer is initially attached to the ground surface upwind the inflection point; it is separated adjacent to the upwind vortex (between the inflection and the stagnation points); then it is reattached along the upper part of the barrier upwind surface (between the stagnation point and the barrier free end); finally it is separated at the sharp edge of the barrier free end. Recirculating flows have significant effect on wind-blown sand transport. In fact, vortices modify both magnitude and direction of the wind shear stresses τ_w . The sedimentation lengths $L_{S,u}$ and $H_{S,u}$ as well as recirculation lengths $L_{R,u}$ and $H_{R,u}$ progressively increase from the sample #1 to the sample #3 due to the windward migration of the sedimentation point.

Wind-induced pressure field on the barrier is directly resulting in the wind action, affecting the barrier structural sizing and cost. Figures 4.9 (a) and (b) show the distributions of the aerodynamic pressure coefficient $C_p = \frac{p-p_\infty}{1/2\rho u_H^2}$ along upwind and downwind surfaces of the barrier, respectively. C_p distributions for the valid samples are sorted in increasing order of s_1/H , with an emphasis on the samples selected in Figure 4.8. In general, the mean pressure along the barrier surfaces is directly related to the curvature of the time-averaged flow streamlines along the same surface, i.e. the shape and the length of the recirculation regions [43]. The $C_{p,d}$ distribution along the downwind surface is almost constant and does not change

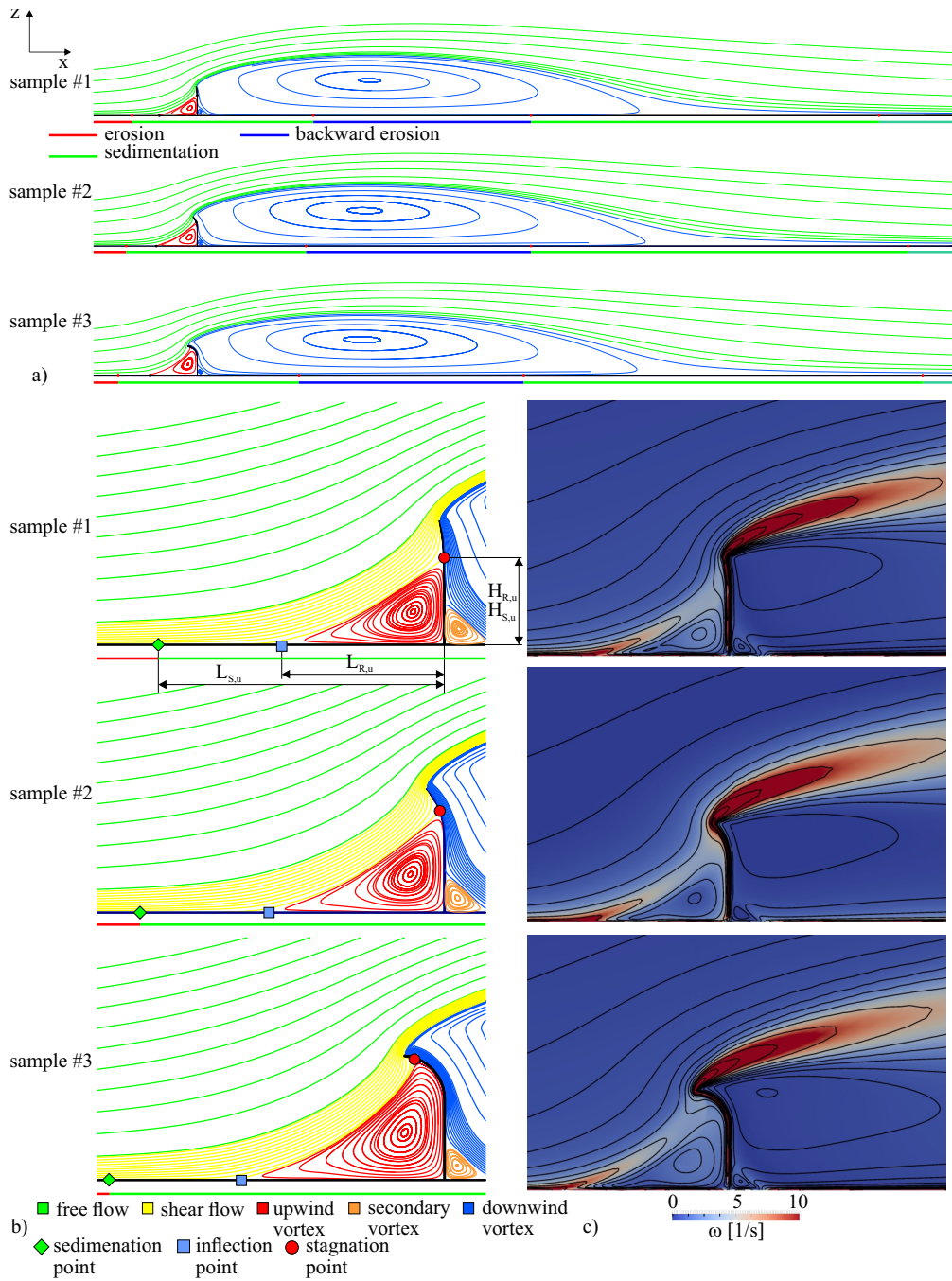


Figure 4.8: $N = 1$ - Flow structures and characteristic quantities around differently shaped barriers: limit case close to SVW (a), example between two limit cases (b), most deflected simulated case (c).

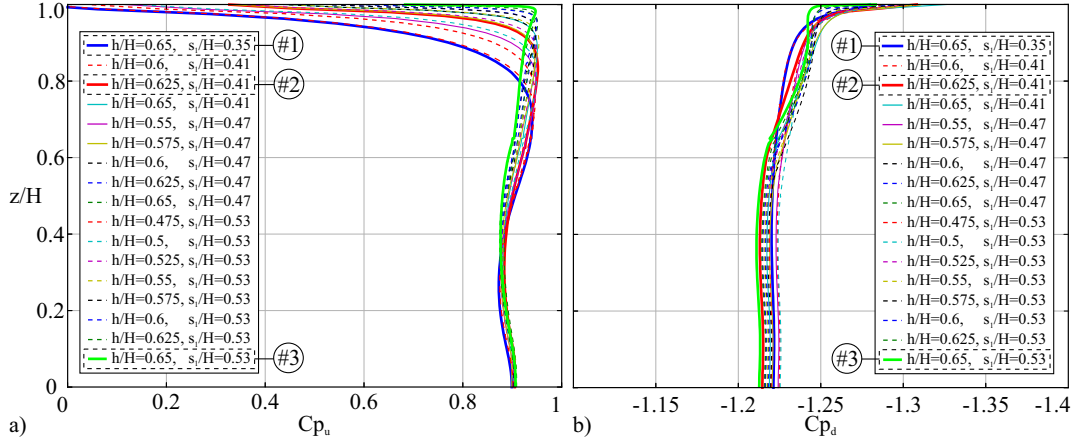


Figure 4.9: $N = 1$ - Pressure coefficient over barrier height: upwind surface (a), downwind surface (b).

significantly by varying the design parameters (see Figure 4.9 b), consistently with the nearly constant shape and size of the downwind main vortex. Only a slight pressure recovery takes place along the upper part of the rear surface ($z/H > 0.7$) for significantly curved deflectors ($s_1/H > 0.41$, e.g. samples from #2 to #3). The $C_{p,u}$ distribution along the upwind surface is mainly characterized by the height of the stagnation point, i.e. z position where the maximum pressure occurs along the upwind surface. The curve corresponding to the sample #1 identifies the stagnation point at the lowest tested height. As the curvilinear length increases, the stagnation point moves towards the top of the barrier. The Sample #3 induces the highest stagnation point, almost at the deflector free end. It is worth recalling that the stagnation point of the baseline conceptual design of *Shield for Sand* nearly corresponds to the deflector free end $z = H$ [39]. Below the stagnation point the upwind vortex is adjacent to the upwind surface, and $C_{p,u}$ is almost constant and independent from the design parameters. Conversely, above the stagnation point the boundary layer is reattached and the flow outside it is progressively accelerated, what in turn decreases $C_{p,u}$. In short, the higher the stagnation point, the longer the upwind surface exposed to high and z -wise constant pressure distribution.

In order to discuss the effects of the design parameters s_1 and h more concisely, local quantities are integrated into bulk performance metrics (see Figure 4.10) and cost metrics (see Figure 4.11). $L_{R,u}/L_{R,u,0}$, $H_{R,u}/H_{R,u,0}$ and $A_R/A_{R,0}$ are plotted versus s_1/H and h/H in Figures 4.10 (a), (b) and (c), respectively.

The longest $L_{R,u}$ and $H_{R,u}$ are obtained for the highest curvilinear length of the barrier. The relative increase of $H_{R,u}$ with the increase in the design parameters is higher than $L_{R,u}$, i.e. high vertical wall and long curved deflector effectively elevate the stagnation point. The increase in design parameters has a less dramatic, but

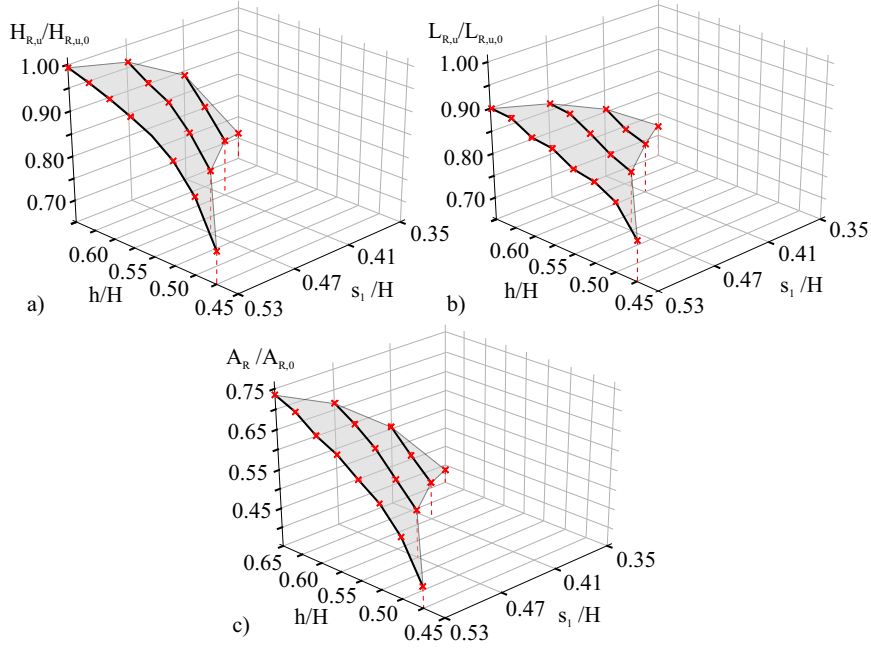


Figure 4.10: $N = 1$ - Bulk metrics related to performance: along-wind projection $L_{R,u}$ (a), vertical projection $H_{R,u}$ (b), and recirculation area A_R (c) of the upwind sand trapping vortex.

still significant effect in moving the inflection point farther from the barrier. The adoption of a single panel nearly approaches the baseline stagnation height and recirculation length, i.e. $H_{R,u} \approx H_{R,u,0}$ and $L_{R,u} = 0.9L_{R,u,0}$. However, a significant relative performance gap remains in terms of A_R (Figure 4.10c), where the value ranges in $0.5 \leq A_R/A_{R,0} \leq 0.75$. The bulk cost metrics are presented in Figure 4.11(a) and (b) where the normalized aerodynamic moments $M_1/M_{1,0}$ and $M_0/M_{0,0}$ are plotted respectively, versus s_1/H and h/H . M_1 linearly increases as s_1 increases, while it is nearly constant versus h . In other terms the almost constant suction versus s_1 along the downwind surface (Figure 4.9 b) prevails over the pressure reduction along the deflector upwind surface (Figure 4.9 a). M_0 shows a quadratic trend versus both s_1 and h . The reason of such a trend is manifold, i.e. the increase in the overall curvilinear length of the barrier increases both the resultant aerodynamic force and its leverage. Moreover, the height of the stagnation point is a quadratic function of both s_1 and h (Figure 4.10 a). The higher the stagnation point, the longer the curvilinear length of the upwind surface subjected to high and constant pressure (Figure 4.9 a). The results about aerodynamic moments are encouraging; i.e. wind forces are significantly lower compared to the baseline solution; $0.1 \leq M_1/M_{1,0} \leq 0.25$, and $0.55 \leq M_0/M_{0,0} \leq 0.65$.

To complete the assessment of the $N = 1$ sample within the sensitivity study,

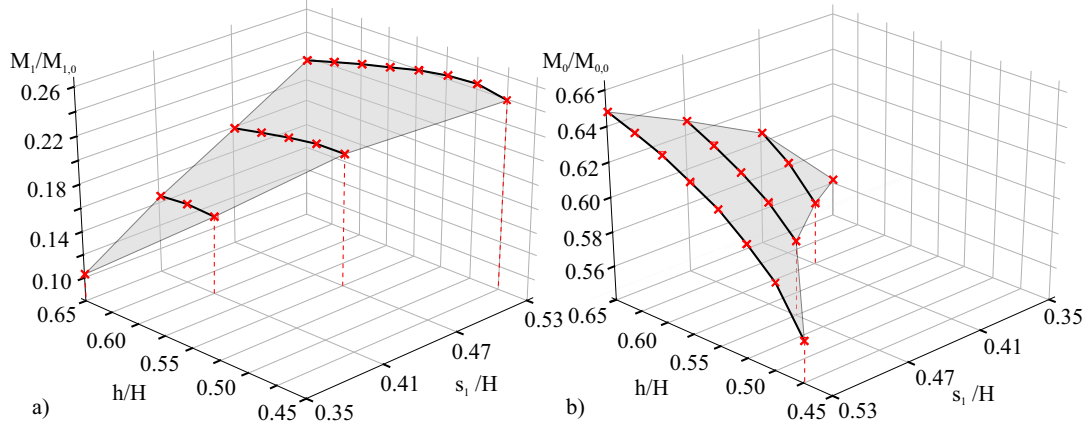


Figure 4.11: $N = 1$ - bulk metrics related to cost: moment M_1 at the deflector base (a), overall base moment M_0 (b).

their position is shown on the c/c_0 - p/p_0 plane in Figure 4.12 (a), complemented with the streamlines around the selected samples in Figure 4.12 (b). In Figure

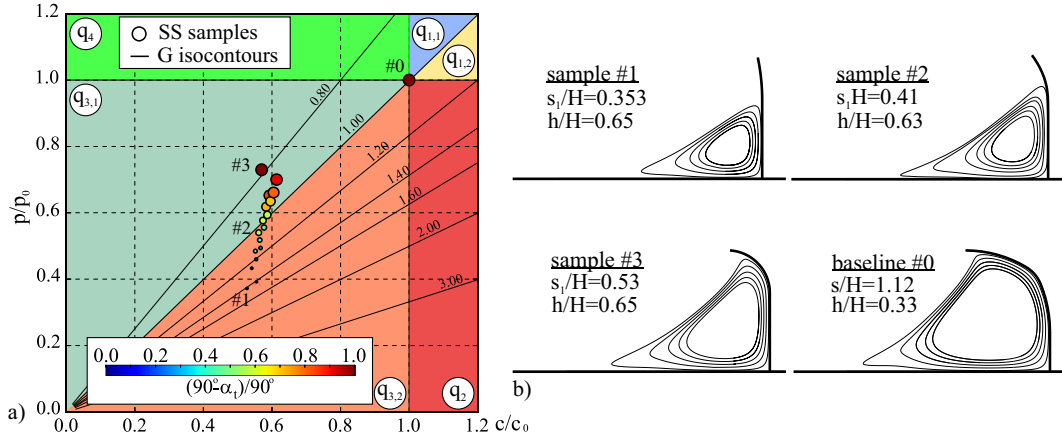


Figure 4.12: $N = 1$ - Synopsis of the sensitivity study (SS): samples in the cost-performance plane (a), streamlines around selected samples (b).

4.12 (a) each circle corresponds to a single sample. Its size and filling color both correspond to a value of chosen derived parameters. The size is proportional to the overall curvilinear length S of the barrier, while the filling color corresponds to the normalized tangency angle of the free end of the deflector $(90 - \alpha_t)/90$. The c/c_0 - p/p_0 plane is divided into 6 regions based on the normalized values of cost, performance, and goal function with respect to the *Shield for Sand* baseline solution #0 at coordinates (1,1). The regions are labeled $q_{i,j}$, where i represents the

quadrant and j a specific sector of the i -th quadrant. The quadrant q_1 includes the samples characterized by the higher cost and the higher performance with respect to the ones corresponding to the baseline solution, i.e. $c/c_0 > 1$ and $p/p_0 > 1$. The quadrant q_2 includes the samples characterized by the higher cost and the lower performance with respect to the ones corresponding to the baseline solution, i.e. $c/c_0 > 1$ and $p/p_0 < 1$. The quadrant q_3 includes the samples characterized by the lower cost and the lower performance with respect to the ones corresponding to the baseline solution, i.e. $c/c_0 < 1$ and $p/p_0 < 1$. The quadrant q_4 includes the samples characterized by the lower cost and the higher performance with respect to the ones corresponding to the baseline solution, i.e. $c/c_0 < 1$ and $p/p_0 > 1$. In short, the quadrants q_2 and q_4 host the worst and best scenarios, respectively. The first and third quadrants are further split according to the the bisector corresponding to the isocontour $G/G_0 = 1$. In particular, $q_{1,1}$ and $q_{3,1}$ correspond to $G/G_0 < 1$, while $q_{1,2}$ and $q_{3,2}$ correspond to $G/G_0 > 1$. Results of the preliminary study for $N=1$ are all clustered in the third quadrant q_3 , i.e. both cost and performance of the samples are always lower than the baseline solution. Hence, results are encouraging in a genuine design perspective. Cost-to-performance values are lower than the baseline solution ($G/G_0 < 1$, sub-quadrant $q_{3,1}$). However, this is due to the significant cost reduction, rather than the performance growth.

For all the samples, the steel panel and r.c. wall thicknesses are equal to the ones of the baseline solution ($t_{s1}/t_{s,0} = 1$ and $t_h/t_{h,0} = 1$). Hence, the cost reduction results from the shorter overall curvilinear length, and from the height increase of the cheaper r.c. vertical wall. Interestingly, clear and emerging positive correlation of the goal function G and the free end tangency angle α_t is observed, i.e. the lower α_t , the lower G . In other terms, when the deflector free end has the horizontal tangent, the stagnation point moves up to the barrier free end at $z = H$. As a result, $H_{R,u}$ and A_R are the highest resulting in the lowest G (sample #3). In general, a highly-bended one-piece deflector with horizontal free end reduces the barrier cost-to-performance ratio.

Finally, the normalized goal function G/G_0 is plotted in Figure 4.13 versus the design parameters s_1 and h . By fixing h or s_1 alternatively, the goal function monotonically and smoothly decreases versus the other design parameter. A well-defined minimum $\check{G}/G_0 = 0.79$ (red circle in Figure 4.13) occurs at $h/H = 0.65$ and $s_1/H = 0.53$. Such a trend reflects the phenomenological reading provided by Figures 4.8 and 4.9. For all the samples, changes of the design parameters do not result in a switch of an aerodynamic regime, i.e. the flow topology does not vary qualitatively, while changes occurs only in the size of the flow structures and the position of the stagnation and inflection points. In short, the baseline *Shield for Sand* barrier is a high-degree-of-bluffness body and the corresponding optimization is less challenging than the cases studied in, e.g. [58] or [69], characterized by the transition from high- to low-degree-of-bluffness aerodynamics during the optimization process resulting in non-monotonic objective functions.

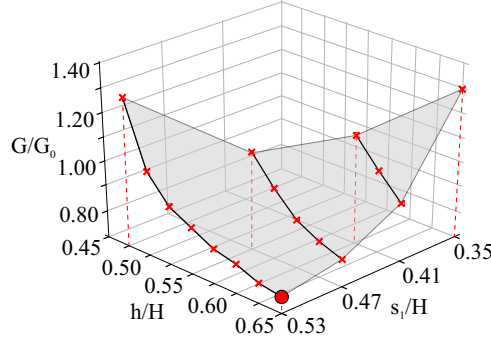


Figure 4.13: $N = 1$ - Trend of the goal function versus the design parameters.

4.3.2 Preliminary Sensitivity Study for the Two-Panel Deflector

In the light of the emerging dependency of the goal function on the free end tangency angle α_t (Figure 4.12), in the following $\alpha_t = 0$ is set as a further geometrical constraint. This allows to compute the derived parameters from the following design variables h , s_1 , s_2 . The sampling of the design space covers the ranges $0.325 \leq h/H \leq 0.65$, $0.18 \leq s_i/H \leq 0.53$ by uniform discrete steps $\Delta_h/H = 0.025$ and $\Delta_{s_i}/H = 0.05875$. 429 valid cases result when all the constraints are satisfied. Bearing in mind the robustness of the aerodynamic behavior of the *Shield for Sand* barrier, the phenomenological insight on how the design parameters affect the flow field is not provided for $N = 2$. Figure 4.14, summarizes the results obtained from the sensitivity study for $N = 2$ on the c/c_0 - p/p_0 plane, analogously to Figure 4.12. Most of the samples are still clustered in the $q_{3,1}$ sub-quadrant, where cost-to-performance values are lower than the baseline solution, analogously to the results of $N = 1$. Nevertheless, a significant number of the samples are located in the upper part of $q_{3,1}$, e.g. $0.9 \leq p/p_0 < 1$, $0.7 \leq c/c_0 < 1$; and in the q_4 quadrant where cost is lower and performance higher compared to the baseline solution. These samples occur in two point clouds. The cloud of better performing samples is positioned along the $G/G_0 = 0.8$ isocontour (e.g. samples #4, #5, #6), while the second develops almost parallel to the former, shifted to the higher cost and consequently lower G/G_0 (e.g. samples #2 and #3). It follows that samples having the same performance do not necessarily exhibit the same goal function (e.g. samples #2 and #6). On the one hand, this confirms that performance-based optimization would only partially capture the nature of the design problem, and further suggests that the cost has to be in the definition of the goal function. On the other hand, the non-trivial trend of the samples suggests that a deeper insight into performance and cost metrics is needed.

Overall, the performance ranging in $0.6 \leq p/p_0 \leq 1.15$ is higher than what is

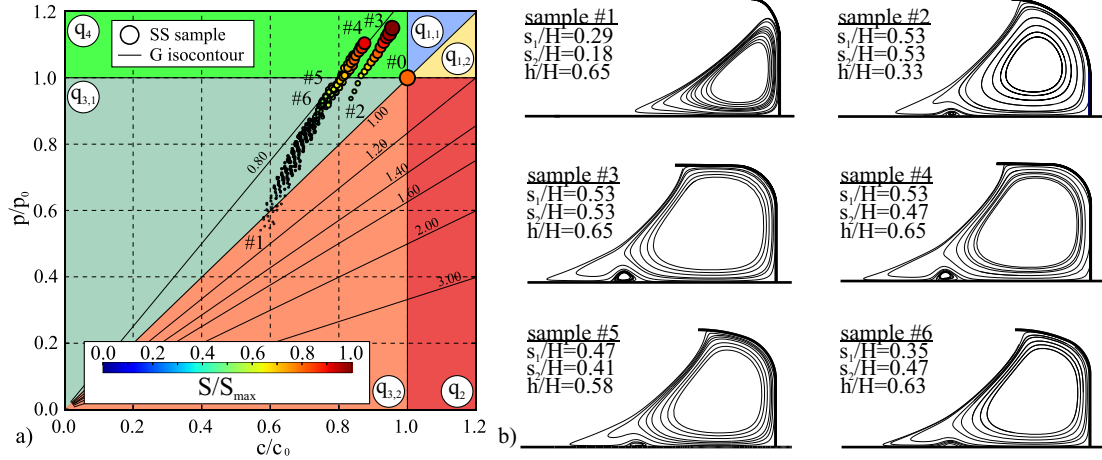


Figure 4.14: $N = 2$ - Synopsis of the sensitivity study (SS): samples in the cost-performance plane (a), streamlines around selected samples (b).

obtained for $N = 1$. Moreover, for about 30 samples the performance is higher than the baseline solution ($p/p_0 > 1$). From the results, performance is directly proportional to the overall curvilinear length S of the barrier, as shown by size and filling color of the circles in Figure 4.14 (a). However, barriers with nearly the same overall curvilinear length (e.g. samples #5 and #6, $1.45 \leq S/H \leq 1.46$) have different performance because of the different shapes and resulting size of the trapping vortex.

The addition of the second panel results in higher cost ($0.6 \leq c/c_0 \leq 0.95$) compared to $N = 1$. Conversely, it is still lower than the cost of the baseline solution ($c/c_0 < 1$). Due to the much different material unit costs, higher vertical wall made of r.c. significantly contributes to the overall cost reduction. However, barriers with the same r.c. vertical wall height and thickness (e.g. samples #3 and #4, $h/H = 0.65$) have different overall costs due to the length of the deflector. Indeed, all the samples in the second, smaller cloud of samples have the same maximum arc lengths ($s_1/H = 0.53$, $s_2/H = 0.53$), even if the curvature varies, e.g. #2 and #3 in Figure 4.14 (b). The long span of the cantilever induces high aerodynamic moment M_1 , thick steel panel adjacent to the r.c. wall ($t_{s1}/t_{s,0} = 1.2$), and higher cost in turn. Conversely, the samples in the bigger and better performing cloud of samples (samples #4, #5 and #6) have the steel panel thicknesses equal to the one of the baseline case ($t_{s1}/t_{s,0} = 1$ and $t_{s2}/t_{s,0} = 1$). Bubble plot in Figure 4.15 (a) shows the trend of the sampled normalized goal function G/G_0 versus the design variables h , s_1 , s_2 . For the clearer visualization, point style rather than their size varies to highlight different ranges of G/G_0 . Figures 4.15 (b), (c) and (d) plot G/G_0 versus two design parameters at a time, with the remaining parameter is set to a

constant value.

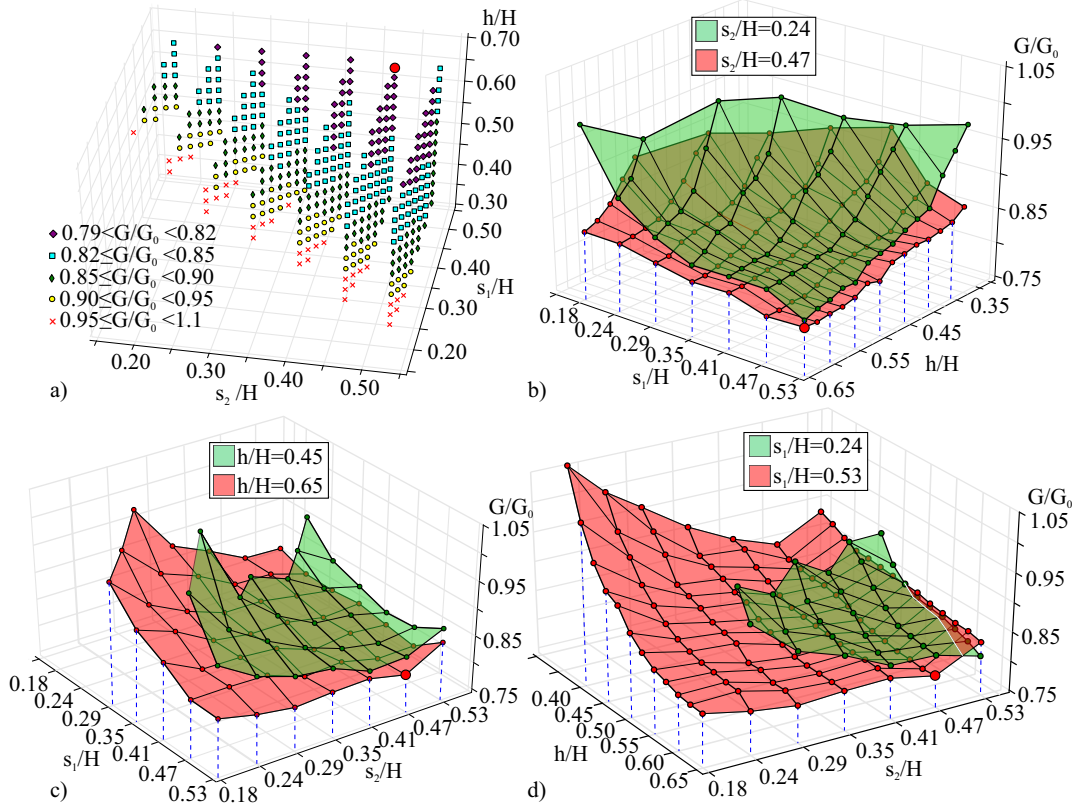


Figure 4.15: $N = 2$ - Trend of the goal function in the overall design space (a), trend of the goal function versus pairs of the design parameters (b,c,d).

Overall, the range of variation of G/G_0 for $N = 2$ ($0.79 \leq G/G_0 \leq 1.1$) is narrower than for $N = 1$ ($0.79 \leq G/G_0 \leq 1.3$), due to the additional constraint on α_t . The robust aerodynamic behavior of the barrier keeps the trend of G/G_0 variation smooth versus the design parameters, analogously to $N = 1$. However, the trend is no longer fully monotonic, and the local plateaux of minima occurs. Even if the global minimum $\check{G}/G_0 = 0.79$ can be numerically assessed at $s_1/H = 0.53$, $s_2/H = 0.47$, and $h/H = 0.65$ marked by the red circle in Figure 4.15, multiple samples having $0.79 < G/G_0 < 0.82$ are highlighted by purple diamonds. They occur at relatively high values of h , s_1 and s_2 , with an exception for the highest values of s_1 and s_2 ($s_1/H = s_2/H = 0.53$), where G/G_0 locally increases. Such varying trend results from the cumulative contributions of three design parameters instead of two as in $N = 1$. The response of the goal function for $N = 2$ case makes it more challenging than $N = 1$ in the optimization perspective.

4.4 Optimization

The optimization approaches used for $N = 1$ and $N = 2$ are selected a priori in the light of the goal function responses observed from the preliminary studies, i.e. plots in Figure 4.13 and Figure 4.15. GBO is selected for $N = 1$ because of the monotonic and smooth trend of the goal function, making optimization affordable by this well established approach. Both GBO and GAO are employed for $N = 2$ to compare their accuracy and efficiency, bearing in mind the G function is no longer fully smooth and monotonic, and optimization is more challenging. In particular, two GBO runs are carried out, to test its robustness depending on the initial solution.

Figure 4.16 (a) shows the trend of the goal function versus the function evaluations for both $N = 1$ and $N = 2$. The sensitivity study also allows to estimate a posteriori the error along the optimization process by referring to the distance $\Delta_i = |\check{G} - \phi_i|/G_0$ between the sampled minimum $\check{G} = 0.79$ and ϕ_i , where $\phi_i = G_i$ for GBO, while $\phi_i = \bar{G}_i$ and $\phi_i = \min(G_i)$ for GAO, being \bar{G}_i and $\min(G_i)$ the average and the minimum value of the goal function over the individuals of the i -th population. Figure 4.16 (b) plots the distance Δ versus the iterations i .

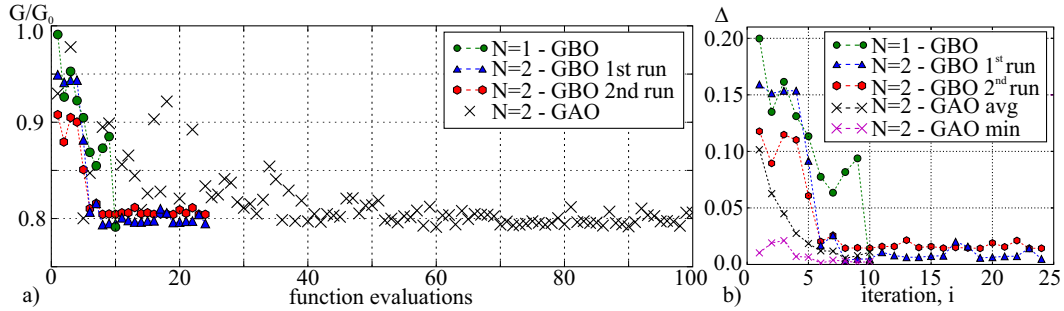


Figure 4.16: GBO and GAO objective function for each function evaluation (a) and estimated error (b).

As expected, for $N = 1$, GBO converges quickly, i.e. after 10 function evaluations only, and it reaches the sampled global minimum \check{G} , i.e. $\Delta_{10} = 0$ (Figure 4.16 b). Similarly, for any initial solution for $N = 2$, the GBO quickly reaches convergence plateaux. However, the set convergence criterion is not numerically fulfilled because of the low convergence threshold, and consequently reaching maximum number of evaluations for both runs. More interestingly, close but different G minima are found from different initial solutions, namely $G/G_0 = 0.795$ and $G/G_0 = 0.804$ for first and second runs, respectively. In other words, GBO converges to a particular local minimum depending on the initial set of design variables. However, the estimated error is in both cases lower than 2%. The trend towards convergence is visible for GAO, although a larger number of function evaluations are required to

qualitatively reach the plateau (≈ 50 , Figure 4.16 a). The mean distance over the sixth population ($i = 6$, Figure 4.16 b) is of the same order of magnitude as the one obtained with GBO, while the minimum distance over the last population ($i = 10$) is equal to about 0.1%.

Figure 4.17 displays the optimization paths in the $c - p$ plane analogously to Figures 4.14 (a) and 4.15 (a). Figure 4.17 (a) summarizes the sample clouds from sensitivity analysis for reference. The GBO and GAO successive evaluations along the optimization paths are shown in the same plane in Figures 4.17 (b), (c) and (d). 7th, 8th, and 9th GAO populations are not plotted for the sake of clarity. For

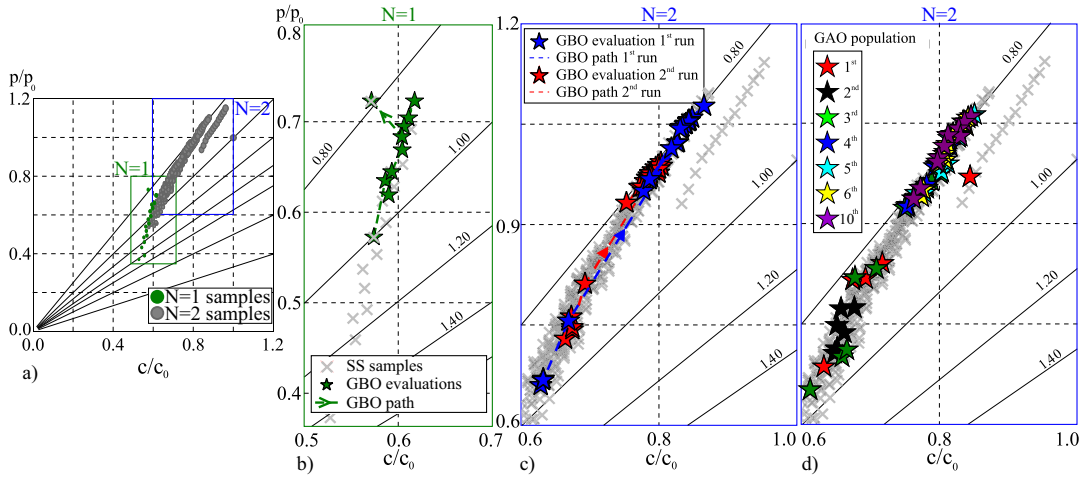


Figure 4.17: Summary of the samples from the sensitivity study (SS) on the $c/c_0 - p/p_0$ plane (a), GBO and GAO paths for $N = 1$ (b) and $N = 2$ (c,d).

$N = 1$, optimization starts from a poor initial solution close to the border of $q_{3,1}$ and $q_{3,2}$ sub-quadrants ($G/G_0 = 1$). The optimization path proceeds across $q_{3,1}$ significantly increasing performance, while slightly increasing cost. The minimum ($G/G_0 = \hat{G}/G_0 = 0.79$) is reached in the final step where the low cost is recovered, equivalent to the cost of the initial shape.

For $N = 2$, both GBO paths continuously tend to $G/G_0 = 0.8$ isocontour by a significant increase of both performance and cost. In other words, the last GBO evaluations and the two minima share almost constant values of G/G_0 , but differ in both performance and cost ($p/p_0 \approx 1.1$; $c/c_0 \approx 0.85$ and $p/p_0 \approx 0.97$; $c/c_0 \approx 0.8$, for first and second run, respectively). GAO starts from dispersed individuals of the 1st population, including a single sample lying in the cloud corresponding to the thicker steel panel. Overall, the next populations develop with the same trend of the GBO runs. The individuals in the last population have nearly the same G values ($G/G_0 \approx [0.79, 0.81]$), but significantly differ in cost ($c/c_0 \approx [0.78, 0.85]$)

and performance ($p/p_0 \approx [0.95, 1.06]$). These differences reflect the intrinsic multi-objective nature of the problem, and translate in the different nearly-optimal shapes of the barrier.

The characteristic shapes obtained by the optimization are shown in Figure 4.18 for $N = 1$ and $N = 2$. For the easier comparison the shapes are complemented by the shape of the baseline solution. The GBO optimal shapes corresponding

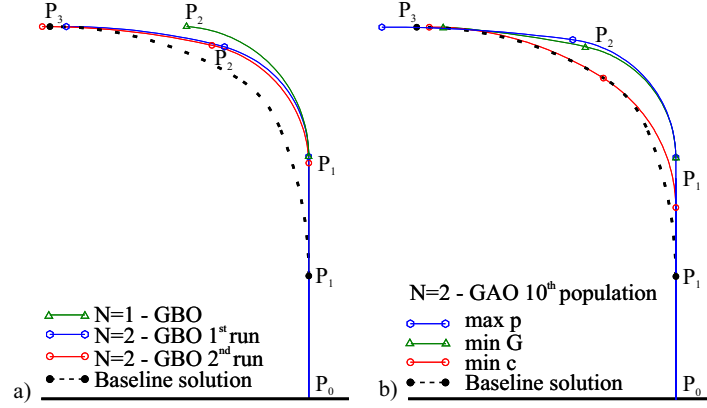


Figure 4.18: Optimal shapes from GBO (a) and GAO (b).

to the optimal design parameters are shown in Figure 4.18 (a). The GAO optimal shape corresponds to the single individual of the last population with minimal G/G_0 . Additionally, the shape of the cases with the maximum performance and the minimum cost obtained by GAO are included in the same figure. Overall, all the optimal shapes have a higher vertical wall with respect to the baseline solution. The shape for $N = 1$ has the shortest overall curvilinear length, and the deflector curvature is close to the high curvature of the baseline solution. For $N = 2$ the GBO runs result in very similar optimal shapes ($s_1/H = 0.400$, $s_2/H = 0.438$, $h/H = 0.65$), and ($s_1/H = 0.455$, $s_2/H = 0.479$, $h/H = 0.633$), having deflector curvature higher than the baseline solution. Conversely, GAO results in three distinct shapes, where: i.) the optimal shape is close to the GBO optimal shapes ($s_1/H = 0.411$, $s_2/H = 0.502$, $h/H = 0.65$); ii.) the shape corresponding to the maximum performance is close to the optimal one, but has the largest curvilinear length ($s_1/H = 0.459$, $s_2/H = 0.514$, $h/H = 0.65$); and iii.) the shape corresponding to the minimum cost is the closest to the baseline shape, even if its maximum deflector curvature is higher ($s_1/H = 0.407$, $s_2/H = 0.506$, $h/H = 0.513$).

In brief, the following remarks outline the most significant findings of the chapter. One-panel deflector is efficiently optimized by the gradient-based approach. The optimal solution dramatically reduces construction costs, but does not improve the aerodynamic performance of the baseline solution. Application of the

fast-converging gradient-based algorithm is possible because of the monotonic response of the goal function. For the two-panel deflector, the optimization allows the reduction of construction costs and, in the same time, increase in performance compared to the baseline barrier. Conversely to the one-panel deflector, the response of the goal function is highly non-monotonic and the gradient-based optimization is not a suitable algorithm in search for the optimal solution. Nonetheless, the gradient-based optimization can be adopted to quickly improve the design in vicinity of the initial shape. The search for the optimal family of solutions is performed by adopting genetic algorithm approach. A number of shapes have been found with nearly equivalent minimum value of the goal function. The same class of aerodynamic problems can be approached with the same method, i.e. sand sedimentation around high-degree-of-bluffness barriers where abrupt changes in their aerodynamic regime do not take place within the design space.

Chapter 5

Computationally-Based Design of Innovative Receiver Sand Mitigation Measures

Parts of the work presented in this chapter are published by the author in a peer-reviewed article [114].

This Chapter covers the research done on the topic of conceptual and preliminary design of innovative Receiver SMM *Sand Blower*. The Chapter starts with the detailed definition of the adopted unmitigated railway infrastructure and the geometry of SMM taken into account. The best performing unmitigated systems are subjected to the design of the new SMM, in particular the standard railway system and the humped sleepers. Drawbacks and advantages are critically discussed and results are comparatively assessed.

5.1 Field Evidences of Sand Sedimentation Patterns around Railways

The defined windblown sand transport directly depends on the local properties of the wind flow, mainly its gradient at the sandy surface. Any obstacle to wind flow changes the sand action in turn. Hence, in arid and sandy environments, a local obstacle changes the wind flow and generates its own sand sedimentation pattern. A selection of such patterns along railways is shown in Figure 5.1. They were observed during site visits along railways in Iran (Bam - Zahedan line, Figure 5.1 b, c and f), Algeria (Redjem Demouche - Mecheria line, Figure 5.1 d, e and g), and Namibia (Aus - Lüderitz line, Figure 5.1 a, h and j, Swakopmund - Walvis Bay line, Figure 5.1 i [201]). A great database of ≈ 2000 photos has been collected during the site visits and the presented photos show the most reoccurring sand sedimentation patterns. In all of the figures, the wind direction is from left to right.

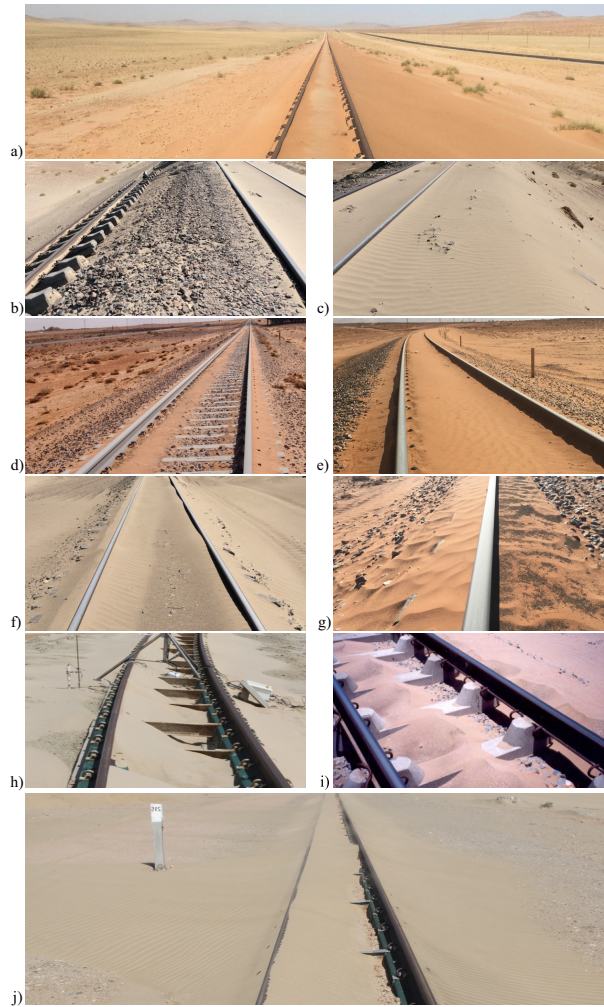


Figure 5.1: Observed sand sedimentation patterns around railways. General patterns around the railway (a) and the substructure (b, c). Local Patterns around standard railway system (d, e). Different granulometry of sedimenting particles (f, g). Local patterns around non-conventional track systems (h,i). Pattern due to yawed incoming wind (j). Inferred prevailing wind directions from left to right in all pictures. Photocredits: pictures a, h, j - C. Nash and G. Wiggs, University of Oxford, SMaRT members; pictures b, c, f - F. Genta, Astaldi Company, SMaRT partner organization; pictures d, e, g - M. Horvat, C. Nash and R. Nuca, SMaRT early stage researchers; picture i - [201], with the permission to reuse under a Creative Commons Attribution License.

First, the morphological reading of the presented patterns allows to preliminary categorize recurrent sedimentation scenarios, tentatively recognize the incoming wind and railway geometrical features that affect them, and drive the selection of

the setups for computational simulations. Second, the local wind conditions which cause them can be qualitatively inferred, although observed sedimentation patterns are not systematically accompanied by the in-situ anemometric measurements of the wind speed.

A new assessment metric to account for the sand erosion and sedimentation conditions is defined $\tau^* = \frac{\tau_x}{|\tau_x|} \frac{|\tau|}{\tau_t}$. It is a dimensionless form of wall shear stresses which besides the magnitude, takes into account the direction with respect to the incoming wind flow at the inlet. Three characteristic conditions result: i.) windward erosion (from now on simply called erosion, $\tau^* > 1$); ii.) sedimentation ($1 > \tau^* > -1$); and iii.) backward erosion ($\tau^* < -1$). Backward erosion occurs in the recirculation regions and has the potential to transport the sand from the downwind side, towards the railway infrastructure.

Global sedimentation pattern around the whole railway is shown in Figure 5.1 (a). Across the far-field around the railway the windblown sand transport takes place at equilibrium, i.e. the eroded vertical flux from the surface is the same to the sedimented one. This results in the ground surface being sand-free. Conversely, close to the railway, the geometry acts as a ground-mounted obstacle, locally disturbs the wind velocity profile, non-equilibrium conditions arise and sedimentation prevails. A sandy corridor along the railway in some sense proves that the railway causes its own sand problems.

Sedimentation around the substructure is exemplified in Figures 5.1 (b) and (c), where the same railway segment is observed from the upwind and downwind side, respectively. A typical asymmetric erosion and sedimentation pattern can be easily observed along the side slopes of the high-rise embankment: the upwind one is in the prevailing erosion regime, because of the flow speedup; conversely, the downwind slope is fully covered by sedimented sand, because it lies in the reversed flow region characterized by the lower kinetic energy. In this case the upwind rail acts as a sharp watershed between erosion and sedimentation, i.e. its head induces a massive boundary layer separation. This separation mode cannot be generalized, because other features are expected to affect it, e.g. the height and edge roundness of the embankment and ballast bed among others. However, it is expected that the global aerodynamics and morphodynamic can be affected by the local perturbations of the track components.

Local sedimentation patterns around the standard ballasted track system are detailed in Figures 5.1 (d) and (e). Clear differences can be observed between them and the previous case with regard to the local sedimentation around rails and along the gauge. In particular, sand sedimentation occurs upwind the upwind rail in Figures 5.1 (d) and (e), while the same does not hold in Figure 5.1 (b). Such a difference could be ascribed to the effects of the low-rise embankment and sharp edges of the ballast bed, among other causes. This suggests that the local aerodynamics and morphodynamic are affected by the global perturbations of the substructure. In

summary, the strong coupling between the local and global phenomena is conjectured. Furthermore, the two local patterns in Figures 5.1 (d) and (e) are different, even though they occur around the same geometry and for the same sand granulometry. In particular, the gauge is partially sand-free in 5.1 (d), while a thin and quasi-uniform sand layer occurs in 5.1 (e). It is conjectured herein that such differences can partially occur due to the different incoming sand drift, wind speeds, and related values of the wall shear stresses τ_w . In addition, Figures 5.1 (f) and (g) shed some light on natural segregation of the grains with different diameters or of sand and organic particles around the upwind rail. Clear sorting between the fine white sand and the coarser gray sand can be seen in Figure 5.1 (e). In Figure 5.1 (f) the organic particles with lower density sediment in the different area than the rest of the sand. Such field evidences clearly confirm that the particle diameter, density, and consequently τ_t significantly affect the sedimentation patterns.

Local sedimentation patterns around the non-conventional track systems are shown in Figures 5.1 (h) and (i). Figure 5.1 (h) refers to the Tubular-Track system (T-Track[®]). A large amount of sand is unintentionally trapped within the gauge, notably downwind the upwind rail. This phenomenon is suspected to be triggered by the high continuous concrete beams on which the rails are mounted, and the massive boundary layer separation induced by them. The superstructure in case of T-Tracks is ≈ 3 times higher than the one in the standard railway system. Figure 5.1 (i) shows the non-conventional humped sleepers. The sand-free ballast surface below the rails confirms that the desired Venturi effect locally takes place, the wind flow is accelerated through the gaps, and the sand is eroded. However, the undesired sedimentation occurs along the mid part of the gauge in the form of sand piles. It is conjectured herein that this is due to the jet-flow expansion and deceleration at the outlet of the upwind gap.

A local sedimentation pattern under the yawed incoming wind is shown in Figure 5.1 (j). The incoming wind direction, non-orthogonal to the alignment is testified by the direction of the sand ripples upwind the railway. Ripples span in the direction perpendicular to the wind direction. Ripples are also clearly visible along the gauge and downwind the track, but their direction differs from the upwind ones. This evidence suggests that the railway causes the deflection of the local wind flow, analogously to what has been proven, e.g. in [16] and [110], with a reference to dunes and forward facing step, respectively. The sedimentation pattern under the yawed wind in Figure 5.1 (j) significantly differs in the shape from the one under the orthogonal wind (Figure 5.1 h), although both patterns refer to the same substructure, track system and sand characteristics.

The ensemble of the field evidences discussed above confirms the huge variety of the sedimentation patterns. It is conjectured that they mainly depend on the geometry of the substructure and superstructure, velocity magnitude and yaw angle of the incoming wind speed, sand diameter and related mechanical features. The

effects of such parameters are systematically investigated in the following computational study.

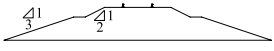
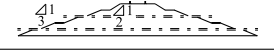
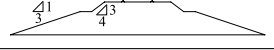
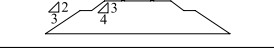
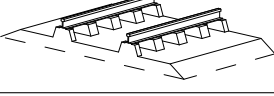
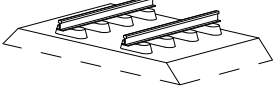
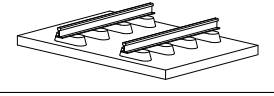
5.2 Setup of the Study

To properly setup the study and the computational approach, boundary conditions and geometry of the studied cases have to resemble the real life conditions which occur in desert and arid regions.

5.2.1 Railway Systems

The adopted railway systems result from multiple combinations of different substructures and superstructures. Their geometries are selected among the ones currently used in railway construction, and observed during site visits along desert railways. All of the resulting cases are listed in Table 5.1. The table is split into

Table 5.1: Synopsis of conventional and non-conventional railway systems.

case ID	RS	AR_E	H_E	AR_B	θ_0	geometrical scheme
0	—	—	—	—	90	
<i>EB.1</i>	<i>EB – SS</i>	3 : 1	1.2	2 : 1	90, 75, 60, 45	
<i>EB.2</i>	<i>EB – SS</i>	3 : 1	12	2 : 1	90	
<i>EB.3</i>	<i>EB – SS</i>	3 : 1	1.2	4 : 3	90	
<i>EB.4</i>	<i>EB – SS</i>	3 : 2	1.2	2 : 1	90	
<i>EB.5</i>	<i>EB – SS</i>	3 : 2	1.2	4 : 3	90	
<i>NC.1</i>	<i>E – CB</i>	3 : 1	1.2	—	90	
<i>NC.2</i>	<i>E – SB</i>	3 : 1	1.2	—	90	
<i>NC.3</i>	<i>EB – HS</i>	3 : 1	1.2	2 : 1	90, 75, 60, 45	
<i>NC.4</i>	<i>E – HS</i>	3 : 1	1.2	—	90, 75, 60, 45	

two parts. The first one (from cases EB.1 to EB.5) includes RS with the standard substructure and superstructure. The second one (from cases NC.1 to NC.4) collects RS with the non-conventional superstructure. For the sake of clarity, each

case is accompanied by a scheme of its geometry. For the sake of brevity, the constant values of the geometric parameters are given in Figure 5.2. In particular, the standard gauge equal to 1,435 mm, and 172 mm high Vignole UIC 60 rails are adopted. Besides the geometric parameters, the tested yaw angles θ_0 are listed for each of the cases. The main varying parameters are indicated by capital letters.

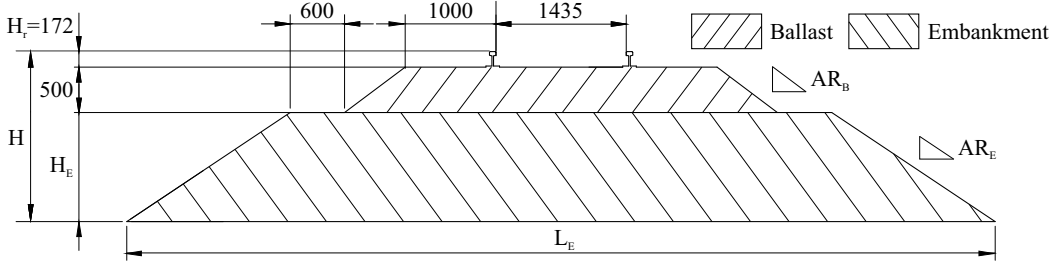


Figure 5.2: Values of common geometrical parameters in mm, with reference to EB.1 cross section.

Analogously to the optimization study presented in the previous chapter, letter L stands for the horizontal dimensions, H for the vertical dimensions. AR denotes the Aspect Ratio of the corresponding slope, subscript E refers to the embankment, B to the ballast and r to the rail.

Substructure is denoted by EB when it includes both embankment and ballast bed, while only the letter E stands for ballastless systems. AR_E and AR_B do not vary continuously because of the earthworks construction constraints. The most common discrete values are adopted and detailed in Table 5.1. Low ($H_E = 1.2$ m) and high ($H_E = 12$ m) embankments are tested as well. Additionally, case ID 0 is considered, where rails are laid directly on natural ground. This case is intentionally excluded from the list of RS because it does not follow the railway construction practice, where a compacted subgrade of minimum thickness is always prescribed. Case 0 is conceived as an aerodynamic reference, i.e. as a geometrical and aerodynamic limit case where the substructure has no effects on the aerodynamics of the railway system.

Standard superstructure includes rails supported by the standard sleepers embedded in the ballast bed. Hence, sleepers do not affect the wind flow. Non-conventional RS couple a single substructure geometry with four different types of superstructures: i.) ballastless embankment with continuous beams (E-CB), analogous to the track system described in [168] and shown in Figure 5.1 (h); ii.) ballastless embankment with slotted beams (E-SB) adopted as an intermediate step between (i. E-CB) and (iii. E-HS); iii.) embankment with ballast and humped sleepers (EB-HS), analogous to the track system described in [203, 202] and shown in Figure 5.1 (i); and iv.) ballastless embankment with humped slab (E-HS), analogous to the track system described in [264]. The height of the beams in E-CB and E-SB is equal to 190 mm. The height of the humps in EB-HS and E-HS is equal to

$H_h = 140$ mm. The total height of the railway system H includes humps or beams, if any, and is adopted as the aerodynamic reference scale in the following.

5.2.2 Setup of the Vanes

The Receiver SMM, *Sand Blower*, is designed in form of S-shaped guiding vanes applied to the standard sleepers (SS) and the so-called humped sleepers (HS). A general geometry is shown in Figure 5.3 (a). To distinguish dimensions of the vanes from dimensions of RS they are annotated by lowercase letters. For example, $L_{B,u}$ is the horizontal distance from the foot of the upwind rail to the ballast upwind sharp edge which is covered by the vane. Conversely, $l_{B,i}$ is a horizontal dimension of the vane over the inclined part of the ballast. The dimensions of the vane geometry for all the tested configurations are systematically presented in Figure 5.3 (b).

From the upwind side, the horizontal dimension l_v of the vane is fixed at the values of $1l_{B,i}$, $0.5l_{B,i}$ and 0. The values correspond to the leading edge of the vane having the same x -coordinate as the foot of the ballast, middle of the ballast slope, and the sharp edge of the ballast, respectively. The trailing edge is positioned either at the same x -coordinate as the foot of the rail, or where the vane intersects the safety gauge of the train. This ensures the safe operating conditions of the traffic.

Important parameter of the vane is the ratio of areas at the vane's inlet and outlet AR_v . This ratio is completely defined by the geometry of RS, h and h_v . h is the vertical dimension of the vane. It equals $2H_r$, $1H_r$ or 0. h_v is the vertical distance at which the trailing edge is positioned with respect to the upper ballast surface. It equals $4H_r$, $2H_r$ or 0. From the dimensions of the cases presented in Figure 5.3, AR_v ranges from 2 in the case of HS.1 to 7 in the cases with $h_v = 0$ and $h = 2H_r$, i.e. HS.3, HS.6, HS.7, HS.6s.

The further modification of the S shaped vane is done in form of the 250 mm gap on the selected cases HS.6 and HS.8. The resulting cases are distinguished by the subscript s, i.e. HS.6s and HS.8s. The HS.6s geometry is further adopted for 3D simulations. The 3D model of the geometry is presented in Figure 5.3 (c). The 3D vane is designed in a way which adopts the 2D cross-section, with the span-wise dimension of 5 periods of the humped sleepers RS ($5W$, where $W = 600$ mm). The vane is attached and secured between the rails and the humps. A well-performing configuration from the preliminary design of the SMM should be further complemented by support beams near the leading edge of the vane, but for the sake of simplicity and its negligible aerodynamic effects at the presented stages of the design, they are omitted in the following simulations.

5.2.3 Specific Computational Approach

The adopted 3D computational domain is shown in Figure 5.4 (b). The domain includes flat ground both upwind and downwind the studied geometry, and the

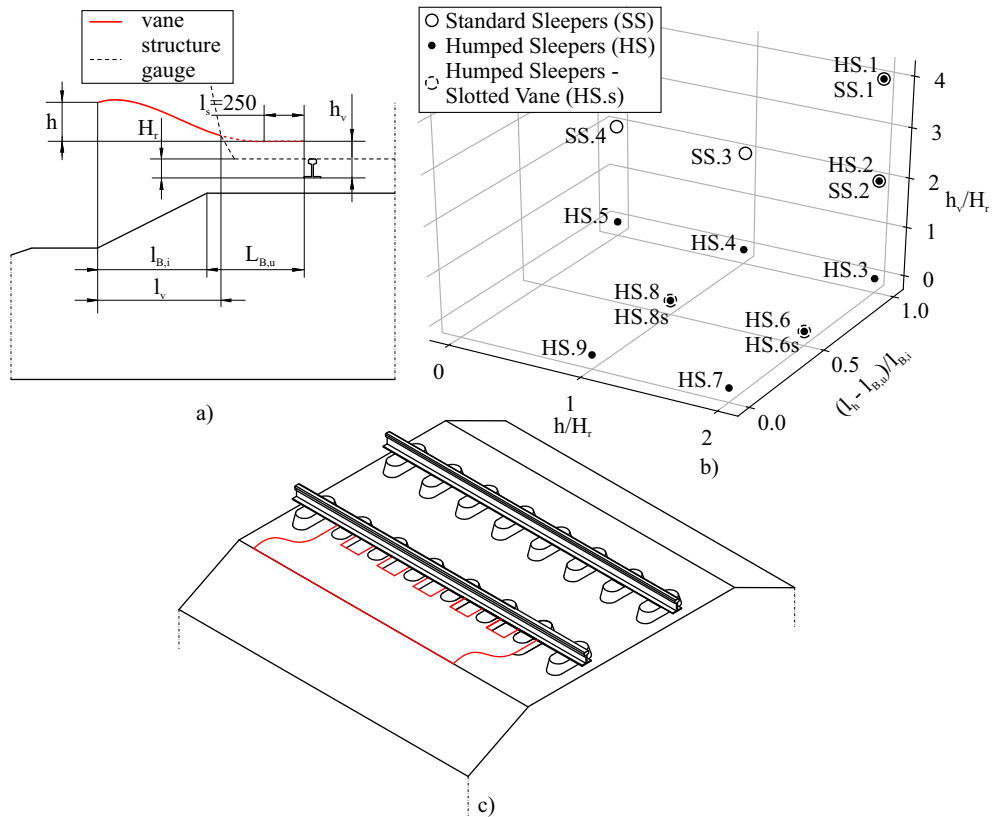


Figure 5.3: Synopsis of vane geometries. a) General 2D case; b) main geometrical vane parameters of the studied cases; c) 3D vane geometry.

geometry itself. The origin of the coordinate system is set at the far-field ground

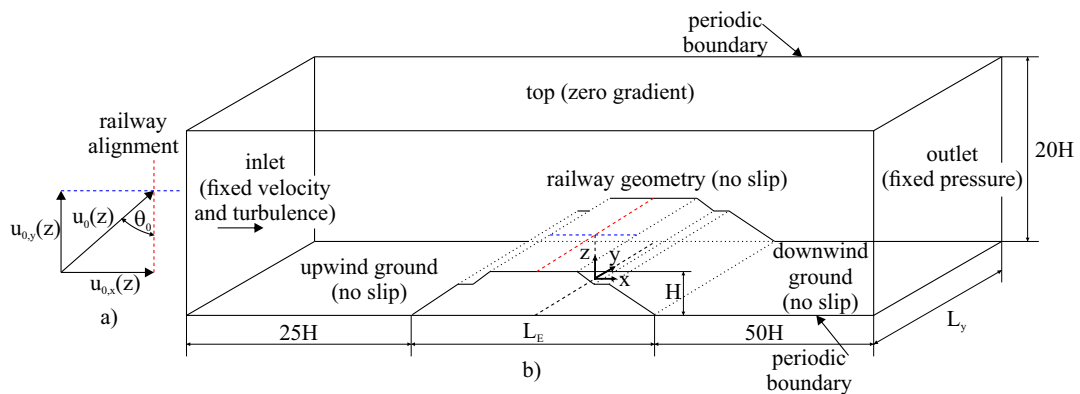


Figure 5.4: Scheme of computational domain and boundary conditions (not in scale - superstructure not drawn for the sake of clarity).

level, positioned so that the $y - z$ vertical plane includes the geometry longitudinal axis. The geometry is arranged in the domain so that its longitudinal axis is normal to the domain lateral faces. The distance to the inlet boundary is equal to $25H$, H being the overall height of the studied geometry. The distance from the geometry to the outlet boundary is $50H$. The height of the domain is equal to $20H$. Such distances are set equal to or larger than the ones adopted in previous computational studies on the analogous applications [e.g. 38, 178, 271], and are by far large enough to avoid influences of boundary conditions on the results. The track-wise size L_y is set in the wake of a preliminary study or literature review, in general. The study conducted in the preliminary study of *Sand Blower* deals with 2D simulations, where domain results from $L_y = 1$ m combined with a single layer of cells in the track-wise direction. In such a way a general 3D case is reduced to a 2D case.

Physical boundary conditions used at the boundaries are specified in Figure 5.4. The related state variables prescribed at inlet are indicated by the subscript 0. u_0 , k_0 and ω_0 at inlet are imposed by the following Dirichlet BC to simulate the neutral ABL. The velocity profile is prescribed using the log-law $u_0(z) = \frac{u_{*,0}}{\kappa} \log\left(\frac{z+z_0}{z_0}\right)$, where $\kappa = 0.41$ is the *Von Kármán* constant, $u_{*,0}$ the shear velocity, z_0 the aerodynamic roughness length. The details of the profiles of $k_0(z)$ and $\omega_0(z)$ can be found in the study [200]. Such combination of velocity and turbulence is in equilibrium, ensuring that the specified profiles do not further develop in the domain (see Subsection 5.4.1 for the proof).

Lateral domains are treated differently for the 3D and 2D domains. In the 3D domains, two different approaches are used. For most of the simulations, both lateral boundaries are treated as periodic. In the simulation of *Sand Blower* with perpendicular winds, one boundary is treated as the symmetry b.c. while the other is treated the zero gradient boundary. 2D simulations are defined by the generic 2D boundaries imposed at the quasi-3D domains which ensure that the set of equation is treated as a 2D set.

Generally speaking, two approaches can be adopted to account for the relative angle of attack between the railway and the incoming wind direction. In the first, the wind direction is kept constant while the railway is rotated around the vertical axis. Such an approach is commonly adopted in the WT tests, and in some computational studies. Alternatively, the railway alignment is fixed in place, while the wind direction at the inlet is varied. In this Thesis, the second approach is chosen. The inlet velocity u_0 is split into its cross-wind and track-wise components, respectively: $u_{0,x}(z) = u_0(z) \cdot \sin(\theta_0)$ and $u_{0,y}(z) = u_0(z) \cdot \cos(\theta_0)$, where θ_0 is the yaw angle with respect to the railway longitudinal axis y (Figure 5.4 a). In such a way, the wind direction is directly specified at the inlet and the periodic boundaries are propagating the direction throughout the domain. The combination of the railway arrangement in the domain and adopted b.c. at the inlet and side surfaces allow to keep the same spatial grid for any yaw angle, and to avoid tip effects at the end

of the embankment. Conversely, the first approach does not offer the mentioned advantages, as discussed in [233] and [178].

5.2.4 Incoming Wind Flow and Sand Features

The incoming wind flow adopted in the simulations reflects the actual desert conditions. The ground aerodynamic roughness length is set equal to $z_0 = 3 \cdot 10^{-3}$ m, according to the recommendations given in [83]. The incoming far-field wind shear velocity is set equal to $u_{*,0} = \sqrt{\tau_0/\rho} = 0.82$ m/s. Such a value is appropriately chosen in order to exceed the erosion threshold shear velocity u_{*t} for the sand grain diameters in the range $d \in [0.063, 1.2]$ mm [197], i.e. windblown sand transport occurs upwind the railway. The resulting reference wind speed at the rail height varies in the range $12.5 \leq U_H \leq 16.7$ m/s, and the corresponding Reynolds number $Re_H = H \cdot U_H/\nu$ in $1.88 \cdot 10^6 \leq Re_H \leq 2.12 \cdot 10^7$. Such values, together with the railway sharp-edged geometry, suggest that the flow is within the Reynolds super-critical regime, so that the significant Reynolds effects are not expected to take place for any of the cases. To take into account the incoming wind not perpendicular to the alignment, simulations are carried out with the yaw angle different than $\theta_0 = 90^\circ$. $\theta_0 = 75^\circ, 60^\circ, 45^\circ$ are adopted for EB.1, NC.3 and NC.4 cases (Table 5.1). The same conditions are applied in the simulations of *Sand Blower*.

The adopted sand diameter d is equal to 0.2 mm. This is the average value of diameters measured at the sites visited and presented in Figure 5.1. The corresponding mean value of the erosion threshold shear stress is equal to $\tau_t = 0.09$ Pa [197].

The windblown sand erosion/sedimentation is mainly triggered by the local ratio of the wind-induced wall shear stress and the sand threshold shear stress $|\tau_w|/\tau_t$. Figure 5.5 graphs the τ_0/τ_t ratio for the varying incoming wind velocity at 10 m height and the varying sand diameter. The surface above the isocontour $\tau_0/\tau_t = 1$ corresponds to the $U_{10} - d$ pairs that induce erosion. In order to discuss potential erosion/sedimentation patterns in different environmental conditions, one can vary d and τ_t in turn, or equivalently U_{10} and τ_0 in turn. $d = 0.2$ mm is kept constant throughout the study (the thick black line in Figure 5.5), while U_{10} is varied to sample four different classes in the Beaufort Scale (red points in Figure 5.5): #1-BS 4 moderate breeze, $\tau_0/\tau_t = 1.5$; #2-BS 5 fresh breeze, $\tau_0/\tau_t = 3$; #3-BS 6 strong breeze, $\tau_0/\tau_t = 6$; #4-BS 8 gale, $\tau_0/\tau_t = 12$. Within the supercritical aerodynamic regime, the wind flow can be quantified by flow variables in dimensionless form because of the aerodynamic similarity, as it is done in many engineering areas, e.g. lift and drag coefficients. The dimensionless skin friction coefficient $C_f = 2|\tau_w|/\rho U_{10}^2$ is obtained directly from simulations. Later, the local ratio $|\tau_w|/\tau_t$ is obtained for the adopted instances of the Beaufort scale by making C_f dimensional again with the reference to the desired velocity: $\tau_{\#i}(x, y, z) = C_f(x, y, z) \frac{1}{2} \rho U_{10, \#i}^2$.

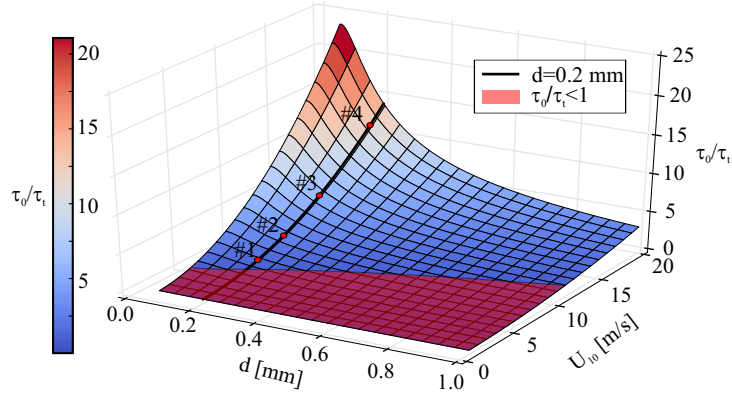


Figure 5.5: Ratio τ_0/τ_t at the inlet boundary as a function of d_s and U_{10} .

5.3 Generation of the Numerical Grids

The space discretization for every simulation performed within **Chapter 5** is accomplished by a fully-structured grid consisting of hexahedral control volumes. An example of a 3D grid with a slice in the vertical $x - z$ plane and a resulting discretization at the ground boundaries are shown in Figure 5.6 (a) and (b). The grid topology shown in the slice (Figure 5.6 b) is extruded in the track-wise direction by a constant step equal to $\Delta_y = 0.026H$, H being the total height of the geometry. The resulting grid at the ground surface is shown in the same figure. The following

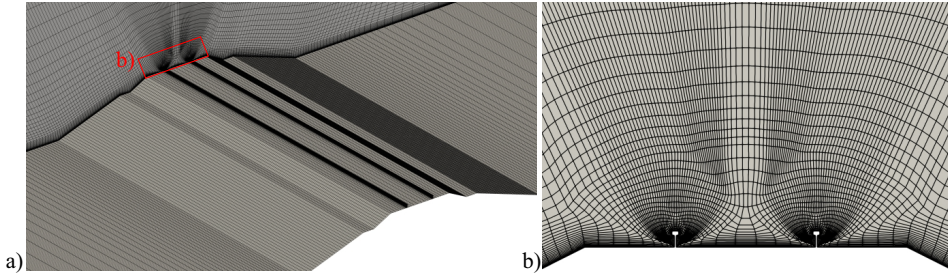


Figure 5.6: Numerical grid around the ground and side surfaces of a standard railway (a), close up view around the rail (b).

criteria have led the grid generation and, in particular, its refinement around the ground and the railway: i.) the geometry of the rail web and rail head is precisely discretized (Figure 5.6 b) in order to accurately simulate the local flow around them. Bridging between the different geometrical scales and related grid densities is a demanding goal, i.e. the rail height is about $1/6600$ the along-wind size of the whole domain; ii.) the overall control volume number is limited and the related computational cost have to be affordable in the framework of a wide parametrical

study; iii.) the cell aspect ratio is kept lower or equal to 100, close to the ground and far from the railway; iv.) the height n_w of the wall-adjacent cells provides a sufficiently high grid resolution in the normal direction n to the surface in order to adequately resolve the gradients of flow variables; and v.) n_w complies with the wall function requirement on the dimensionless wall unit $30 < n^+ = n_p u^* / \nu < 200$, being $n_p = n_w / 2$ the cell center height. In order to satisfy the criteria (iv) and (v), the wall unit is in the range $100 \leq n^+ \leq 200$ for all the simulations. The overall control volume number of the resulting grid depends on the overall height H of the railway and on the adopted railway system. For the sake of conciseness, reference is made here to the grid shown in Figure 5.6, composed by 6.8 million control volumes.

The convection term is discretized by means of the so-called Limited Linear scheme, a 2nd order accurate, bounded, Total Variation Diminishing (TVD) scheme resulting from the application of the Sweby limiter [228] to the central differencing scheme in order to enforce the monotonicity criterion. SIMPLE algorithm is used for pressure-velocity coupling.

5.4 Results

The goal of the section is twofold. First, to show the aerodynamic behavior of the unmitigated railway systems and to quantify their aerodynamic performance. Second, to show the striking differences in the erosion-sedimentation patterns once the *Sand Blower* is applied.

5.4.1 Unmitigated Railway Systems

The results dealing with the unmitigated railway systems generally analyze how different railway systems in a combination with different incoming winds modify the wind flow and the potential sand sedimentation/erosion conditions around the railway. For the sake of clarity, results are classified according to the scale to which different phenomena correspond to: i.) the global scale; and ii.) the local scale, the quantities of the latter being designated with subscript r (rail). Consistently, the global and the local spatial lengths are given in their dimensionless form with reference to the the whole railway height H and the rail height H_r , respectively. Velocity is always normalized with the reference to the velocity U_H . At the global scale, the flow is analyzed within the subdomain $-7H \leq x \leq +16H$: it includes the overall railway system and the downwind reversed flow region. At the local scale, the focus is put on the subdomain $-11H_r \leq x \leq +11H_r$ which closely corresponds to the upper horizontal surface of the ballast bed or embankment. Analogously to the previous chapter, subscripts R and S refer to the recirculation and sedimentation zones, respectively. Subscripts u , m and d distinguish between

the upwind, mid-gauge, and downwind position along the x -direction. For instance, $L_{R,dr}$ is the horizontal length of the local downwind recirculation.

Preliminary Study

Specific and punctual benchmarking on the railway embankment with track system and without rolling stock has not been carried out, because of the lack of the publicly available, high-quality, fully-described WT tests and related measurements of the local flow variables relevant to the present application. However, the whole computational model has been fully-validated in [38] against the accurate, local WT measurements for the same class of aerodynamic problems, i.e. the high-Re turbulent flow around a 3D-bluff-fundamental landform mounted on the desert surface, characterized by the boundary layer separation and reattachment. The adopted computational model is exactly the same in all its parts, i.e. turbulence model and boundary conditions, numerical approach, type of computational domain and spatial grid.

The preliminary study is intended to set the most suited track-wise length L_y under the yawed incoming wind, in order to increase the computational efficiency. The preliminary study is carried out on EB.1 case under the widest amplitude of the yaw angle $\theta_0 = 45^\circ$ regarded as the most challenging setup. Three values are tested in geometrical progression, $L_y = 40H$, $20H$, and $10H$. The x -wise distributions of

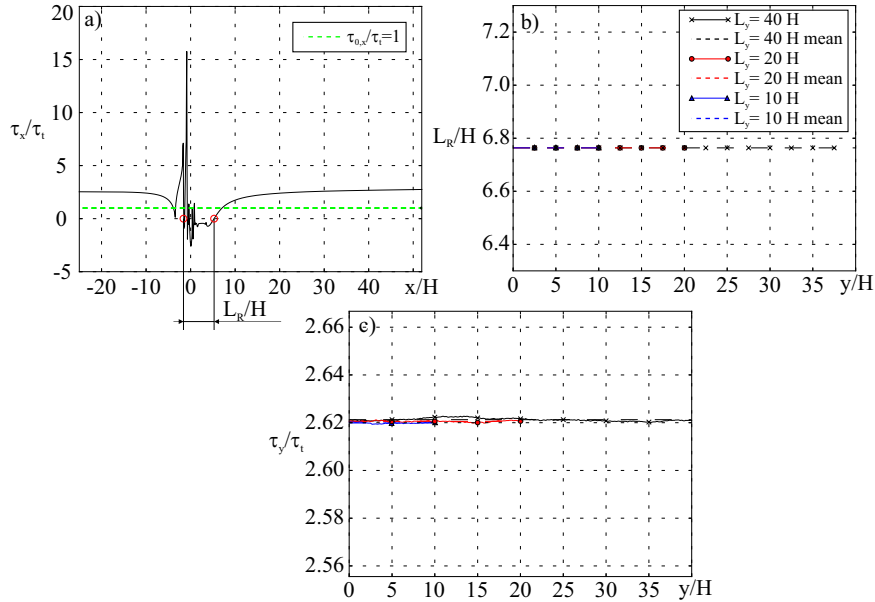


Figure 5.7: Grid sensitivity to domain track-wise length L_y .

the normalized x -component of the wall shear stress at $y = 0$ are graphed Figure 5.7(a) for every value of L_y . Two remarks follow:

- the adopted upwind $L_{x,u}$ and downwind $L_{x,d}$ windward lengths are long enough to guarantee no changes in the flow far upwind and downwind the railway, and proof is given that the velocity and turbulence profiles at the inlet and the outlet are in equilibrium;
- the three distributions overlap, i.e. no significant effects are induced by L_y in the considered range.

The distance of the reattachment point downwind the track (recirculation length in the following) is equal to $L_R = 6.78H$ at the central section. The L_R/H distribution along the y -direction in Figure 5.7 (b) testifies that the reattachment point position is constant track-wise, i.e. the flow is 2D, and that it is not affected by the L_y value. Slight and negligible oscillations occur along the track-wise distribution of the normalized y -component of the wall shear stress sampled at $x/H = 5$ (Figure 5.7 c). From the presented, it is concluded that the results obtained with the shortest crosswind length $L_y = 10H$ do not significantly differ compared to the ones obtained by adopting larger domains. Such a length is much smaller than the one adopted by [178] ($L_y = 25H$) thanks to the adopted combination of the computational domain and b.c. Although even shorter L_y values could be envisaged, $L_y = 10H$ is adopted in the following because of its acceptable computational cost.

Effects of Substructure with the Conventional Ballasted Track

For the sake of brevity, the main features of the flow field around the whole railway are shown in Figure 5.8 for the EB.1 case only. Figure 5.8 (a) shows the flow topology by means of the streamlines coupled with the vorticity field. The boundary layer shows high vorticity magnitude. Its large-scale separation involves the main clockwise vortex R_d . Such recirculation area is bounded by two inflection points defined as points at which $|\tau_w| = 0$. The separation point of R_d occurs at the downwind sharp edge of the ballast bed, while the reattachment point occurs far downwind the railway. The outer free flow is quasi-irrotational. The profiles of the dimensionless velocity components (u_x/U_H and u_z/U_H) are given in Figure 5.8 along the four selected vertical lines (p1, p2, p6, p7) around the substructure and the three lines (p3, p4, p5) close to the track. Profiles are given for every EB.SS case. p1 shows the upward flow deflection induced by the substructure, that results in decreased u_x and $\partial u_x/\partial z|_{z=0}$, and potentially in sand sedimentation. At p2 the flow is significantly accelerated in terms of both u_x/U_H and u_z/U_H and their z -derivative at the ground: the erosion condition is qualitatively achieved. The acceleration is the most significantly affected by H at lower $(z - z_g)/H$ (EB.2 case). The effects of AR_E and AR_B on u_z/U_H is greater than on u_x/U_H . p6 and p7 lay in the undisturbed flow for case 0, while they are within the substructure wake for the EB.SS cases. p6 crosses the recirculation region, and the large negative z -derivative of u_x at the ground is expected to induce backward erosion. p7 is

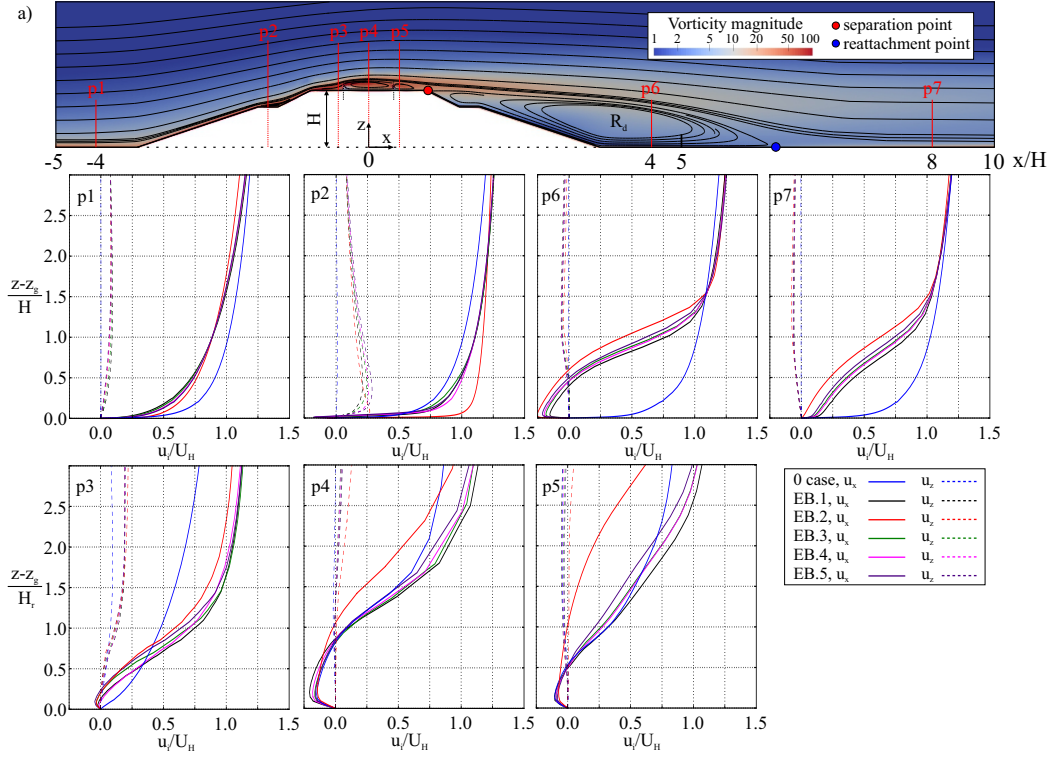


Figure 5.8: Wind flow around railway: a) Streamlines and vorticity; p1)-p7) vertical profiles of the velocity components at different positions across the railway system.

located slightly downstream the reattachment of the boundary layer, and the weak z -derivative of u_x potentially promotes sedimentation. Along both lines, negative u_z/U_H is weakly affected by the substructure geometry, and reflects the downward flow induced by the recirculation. At p3-5, the velocity components and their z -derivatives close to the ground are weakly affected by the substructure geometry, i.e. the local flow is mostly driven by the rails. Even for the case 0, the velocity profiles are close to the others. At the elevations approximately higher than the rail ($(z - z_g)/H_r > 1$), u_x/U_H is sensitive to the substructure geometry. In particular, for the case EB.2 at p5 the rail-induced effects on the x -velocity profile almost vanish and the embankment-induced separation prevails. In order to check and discuss the condition for sand erosion/sedimentation, Figure 5.9 focuses on the shear stress field along the ground and substructure surface. As in Figure 5.8, only the EB.1 case is shown for the sake of conciseness. The flow topology is included in Figure 5.9 (a) for the reference. Global flow features are observed around the whole railway at the substructure scale. The distribution of the skin friction coefficient C_f is plotted in Figure 5.9 (b). It is further rescaled in the dimensionless ratio τ^* in Figure 5.9 (c) to account for the effect of four incoming reference speeds U_{10} on the potential sand erosion/sedimentation conditions without the need of the additional

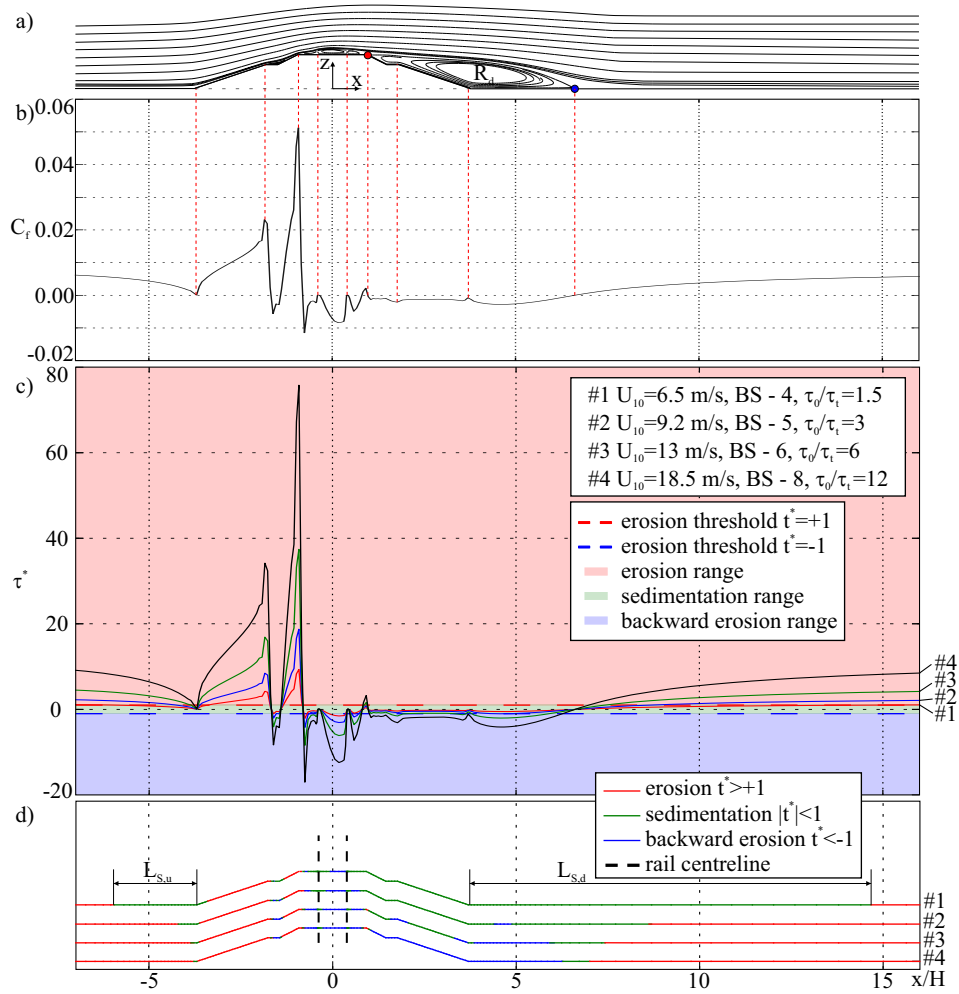


Figure 5.9: Global flow features and potential sedimentation zones: a) reference flow topology; b) skin friction coefficient; c) shear stresses for different incoming reference velocities; d) potential sedimentation, erosion and backward erosion zones.

computational simulations. In the perspective of the study, the key values are $\tau^* = \pm 1$ (the erosion thresholds). The corresponding points, called sedimentation points, are positioned at the sand surface where the transition between sedimentation and erosion is expected. The value of τ^* in Figure 5.9 (c), directly gives the sand sedimentation, erosion and backward erosion patterns in Figure 5.9 (d). Considerably different sedimentation patterns take place in the downwind recirculation zone, and upwind the substructure to a lesser extent. In general, as U_{10} increases, both erosion and/or backward erosion zones replace the sedimentation, i.e. the sedimentation areas shorten and the erosion ones grow. In particular, the downwind faces of embankment and ballast lay in the downwind recirculation zone. For the lowest value of U_{10} (#1) such faces are entirely in the sedimentation zone. As

U_{10} increases (#2, #3), localized short backward erosion zones take place. For the highest U_{10} (#4), these zones coalesce, and the downwind face is entirely backward eroded. The upwind slopes of the embankment and ballast lay in the erosion zone for all the cases, because of the local flow acceleration. The upwind embankment and ballast feet are the exceptions because of the local flow deceleration and the small local recirculation zone, respectively. As U_{10} progressively increases, the sedimentation zones shorten upwind the embankment foot, while the backward erosion takes place along the horizontal surface between the embankment and ballast. In

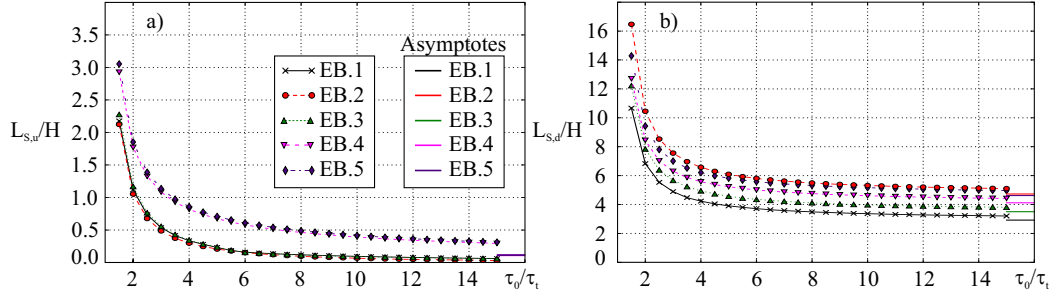


Figure 5.10: Global upwind (a) and downwind (b) sedimentation lengths.

order to synthetically quantify the effects of the incoming flow on the global sedimentation/erosion/backward erosion, two lengths are defined in Figure 5.9 (d): i.) the upwind sedimentation/backwards erosion length $L_{S,u}$ measured from the first sedimentation point to the upwind foot of the embankment; and ii.) the downwind sedimentation/backwards erosion length $L_{S,d}$ measured from the downwind foot of the embankment to the last sedimentation point. Both lines are defined between a fixed geometric point and a flow-dependent sedimentation point. The lengths are plotted in Figure 5.10 versus τ_0/τ_t with a much denser sampling. Additionally, case EB.1 is compared with other cases of standard railway geometry in order to point out the effects of the different substructure geometry. Both $L_{S,u}/H$ and $L_{S,d}/H$ monotonically decrease as τ_0/τ_t increases for all the cases, and tend to asymptotic values for $\tau_0/\tau_t \rightarrow \infty$. The horizontal asymptotes are equal to 0 for $L_{S,u}/H$ in cases EB.1, EB.2 and EB.3, while $L_{S,u}/H$ in the other cases and $L_{S,d}/H$ tend to values different than 0. In order to explain this, it is preliminary worth stressing that the position of the inflection points does not change in the rescaled graphs of τ^* , while the position of the sedimentation points depends on the incoming wind speed U_{10} (Figure 5.9 d). Hence, as τ_0/τ_t increases, τ^* the curve is steeper, so that the x -distance between the inflection point and its neighboring sedimentation points decreases. At the limit case $\tau_0/\tau_t \rightarrow \infty$, such a distance tends to 0. It follows that in the case of the recirculation conditions, the sedimentation points collide into the corresponding inflection point, and L_S tends to the distance between the fixed geometrical point and the inflection point. In the case of the flow deceleration, the

inflection point does not occur, sedimentation points collide into the fixed geometric point and $L_S \rightarrow 0$. In the light of this, graphs in Figure 5.10 (a) prove that the upwind recirculation occurs in front of the embankment for the cases EB.4 and EB.5, while it does not for the cases EB.1, EB.2 and EB.3. In other terms, the embankments with aspect ratio $AR_E = 3 : 2$ lead to a reversed flow at their foot, while the gentler embankments $AR_E = 3 : 1$ simply cause the flow deceleration. Additionally, the embankment height H_E and the ballast slope AR_B have no significant influence on the upwind sedimentation length, as testified by the grouping of the curves with equal AR_E . All the curves of $L_{S,d}$ (Figure 5.10 b) are clearly distinct, although they share the same trend. It follows that all the substructure parameters affect the sedimentation downwind the embankment. The steeper the embankment (AR_E , e.g. compare EB.1 and EB.4) and the ballast bed (AR_B , e.g. compare EB.1 and EB.3), the longer $L_{S,d}/H$. In spite of this common trend, the effect of the steeper embankment is twice the one of the steeper ballast, in average over the whole range of τ_0/τ_t . The influence of H_E is evaluated by comparing the EB.1 and EB.2 cases. An increase of 10 times the height of the embankment results in an increase of 1.5 time of $L_{S,d}/H$. An analogous effect is obtained by increasing, at the same time, both AR_E and AR_B (compare EB.2 and EB.5) for every value of τ_0/τ_t . Local flow features are observed along the track at the rail scale. In Figure 5.11 all the EB-SS cases, together with the case 0, are shown analogously to Figures 5.8 (a) and 5.9 (d). Vorticity coupled with the streamlines are shown in the left column, while the right column shows the sedimentation, erosion and backward erosion zones. Each row of the figure corresponds to a single EB-SS case. The different flow conditions shown in the right column are in order #1, #2, #3 and #4, from top to the bottom. Three significant local flow coherent structures develop: i.) the upwind local vortex $R_{u,r}$, positioned upwind the upwind rail; ii.) the middle local vortex $R_{m,r}$, occupying the gauge; and iii.) the downwind local vortex $R_{d,r}$, located downwind the downwind rail. Additional secondary vortices appear in some cases upwind and downwind the rails. From the cases 0, EB.1 and EB.2 it can be seen that the height of the substructure affects the shape of of the mid-rail vortex $R_{m,r}$ and the position of its center. For the lowest $H_s = 0$ (case 0), it is downwind the upwind rail, for $H_s = 1.7$ m (case EB.1) it moves at about the middle of the gauge, while for the highest $H_s = 12.5$ m (case EB.2), it shifts towards the downwind rail. The lower the substructure, the flatter all the vortices, and the shorter the x -length of the downwind one $R_{d,r}$. Significant difference arises in the topology of $R_{d,r}$ in EB.2, where it coalesces with the downwind global vortex R_d . All the features above are due to the significantly different direction of the flow just outside the boundary layer at its separation point in correspondence with the upwind rail. In particular, the local upward flow does not allow the flow to reattach at the downwind surface of the ballast. No significant differences in the flow structure occur for the rest of the cases (EB.3, EB.4, EB.5) compared to the EB.1 case, i.e. AR_E and AR_B do not qualitatively affect the local topology of the flow. The right

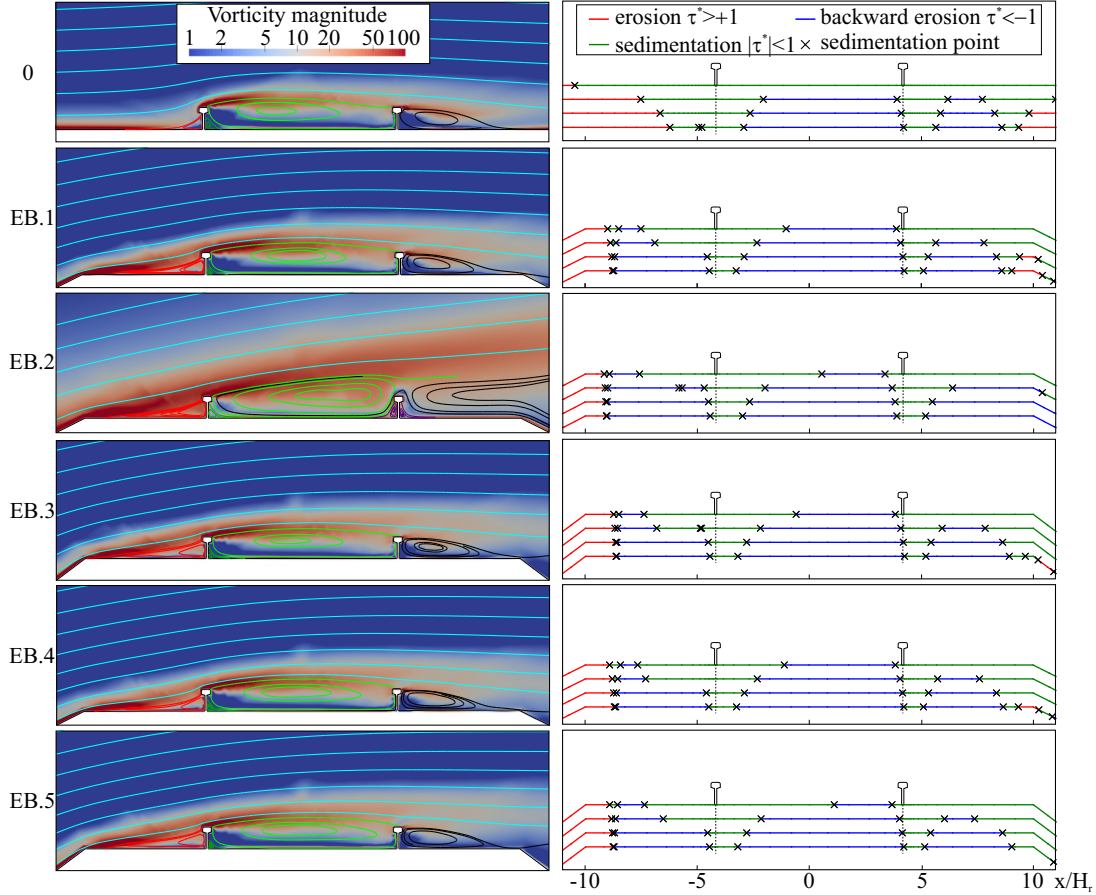


Figure 5.11: Local flow patterns (left column) and potential sedimentation, erosion and backward erosion zones (right column).

column of Figure 5.11 testifies that for each recirculation zone, many sedimentation and backward erosion zones occur, and they significantly depend on the incoming flow speed. Three general rules can be outlined: i.) the ballast upwind sharp edge is constantly eroded, because of the flow speedup; ii.) along the recirculation zones, sedimentation and backward erosion take turns, depending on the streamline curvature close to the wall and to the incoming speed; and iii.) the eventual reattachment point along the ballast downwind surface (e.g. in 0, EB.1, EB.3, EB.4, EB.5) results in the sequence of backward erosion-sedimentation-erosion, where the latter is strongly dependent on the extent of the reattachment and the incoming speed (e.g. in 0, EB.1, EB.4). Due to the alternating and varying sedimentation and erosion zones, the corresponding bulk areas (A_S and A_E) are defined instead of a single sedimentation or erosion length. The areas are expressed as the integrals of sedimentation and erosion zones, respectively, along the whole ballast upper horizontal surface A_u ($-10 \leq x/H_r \leq 10$), and are further divided by A_u itself. The

resulting dimensionless bulk quantities A_S/A_u and A_E/A_u can vary in the range $[0, 1]$. The backward erosion area straightforwardly follows from the previous ones as $A_{BE} = A_u - (A_S + A_E)$. A_S/A_u and A_E/A_u are plotted versus τ_0/τ_t in Figures 5.12 (a) and (b), respectively. The case 0 behaves significantly differently than the

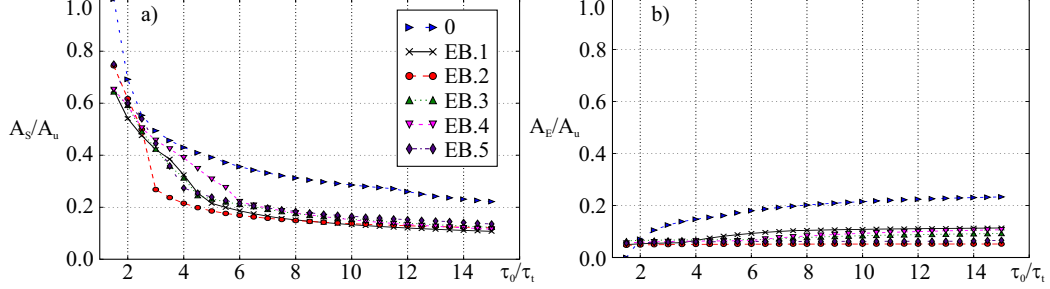


Figure 5.12: Local erosion (a) and sedimentation (b) normalized areas for EB.SS cases.

other cases. Sedimentation occurs everywhere for the lowest $\tau_0/\tau_t = 1.5$, while both A_S/A_u and A_E/A_u are higher than in the other EB-SS cases for higher τ_0/τ_t . This behavior mainly results from the lack of backward erosion upwind the upwind rail for every τ_0/τ_t (Figure 5.11). The other EB-SS cases slightly differ for the low-to-moderate values $\tau_0/\tau_t \leq 6$, where the rate of change of A_S/A_u depends in general on the local switch from sedimentation to erosion. For higher values $\tau_0/\tau_t > 6$ the local sedimentation/erosion pattern along the track is nearly constant and does not dramatically depend on the substructure geometry.

Effects of Non-Conventional Track Systems

The aerodynamic and sedimentation behavior of the non-conventional RS listed in Table 5.1 under the orthogonal wind is discussed in this section. All the cases share the same substructure adopted in EB.1. Except for NC.1, all the cases considered have periodic track-wise varying geometry, because of the humped sleepers/slab and the gaps among them. The spacing between them is the same and equal to $W = 0.6$ m. From the aerodynamic point of view, the humps make the whole railway a bluff-body with small periodic perturbations. Therefore, 3D local flow is expected. Analogous setups have been studied in literature during the last decade, adopted to control the flow around bluff-cylinders under uniform incoming flow. Interested readers are referred to the review papers [56] and [65], and the references therein. For such a class of flow, the periodic structures in the wake result from perturbations. In particular, the study [135] recently showed that the largest flow structures in the wake can have a track-wise length scale λ not necessarily equal to the wavelength of the periodic perturbations ($\lambda \geq W$ for the present application). In order to check the possible periodicity in the wake of the humps

and to evaluate its track-wise length scale, u_y/U_H velocity component is plotted versus y/W along the sampling line in Figure 5.13. The track-wise sampling line

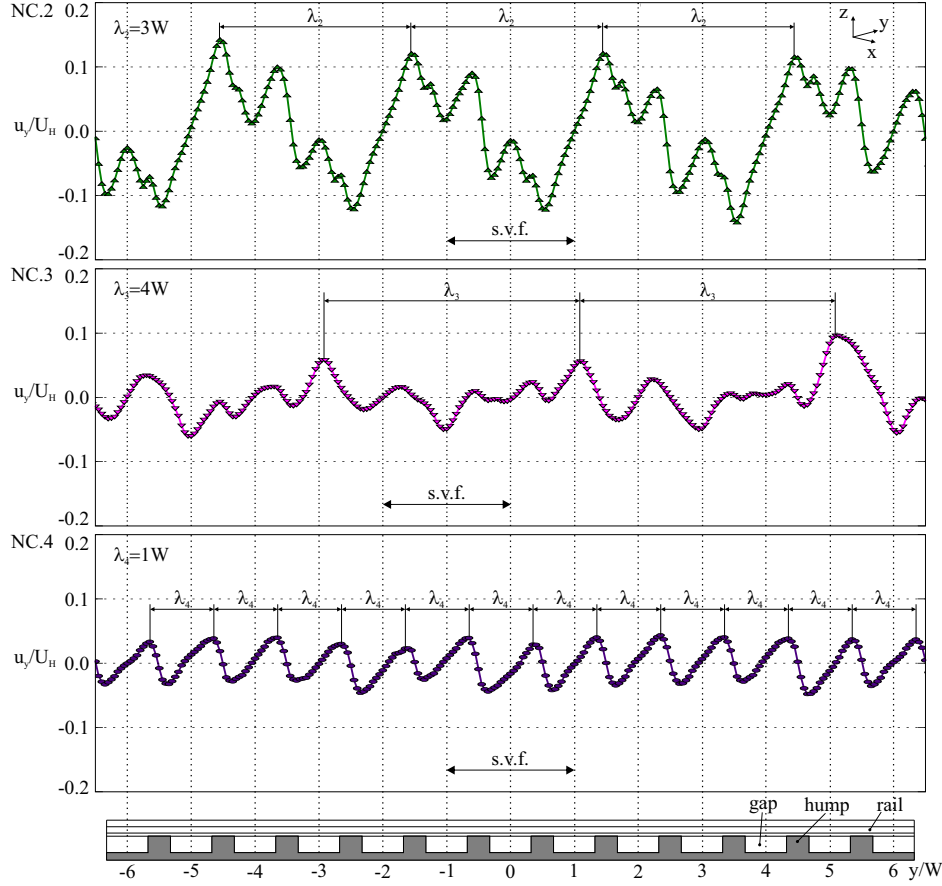


Figure 5.13: u_y velocity component along the track-wise direction for non- conventional 3D superstructures (NC.2-NC.4). s.v.f. refers to the streamline visualization field.

is located half of the hump length downwind the upwind hump, and at the height from the ballast bed equal to half of the hump. Three emerging flow features can be easily recognized. They clearly and significantly depend on the hump shape and on the presence of the ballast bed. First, the track-wise length scale significantly varies, being $\lambda_2 = 3W$, $\lambda_3 = 4W$ and $\lambda_4 = W$ for NC.2, NC.3, and NC.4 respectively. Second, the maximum magnitude of u_y/U_H differs among the cases as well, being the highest for NC.2., while NC.3 and NC.4 share approximately the same value. Third, the same track-wise periodic trend is qualitatively different. The flow around the ballastless humped slab (NC.4) is almost perfectly periodic, and the local flow almost symmetric with respect to the mean vertical plane of each gap, i.e. $u_y = 0$). The flow around the rounded humped sleepers (NC.3) is not

periodic, it seems characterized by multiple length scales. The adjacent gaps show recurrent sequence of the positive-nil-negative-nil u_y vectors. The flow around the sharp-edged slotted beams (NC.2) is nearly periodic, but the u_y distribution along λ is asymmetric and featured by a recurrent sequence of the positive-nil-negative u_y vectors. In order to shed more light on the 3D features of the local flow, the patterns are visualized in Figure 5.14 along a $2W$ -long segment, named streamline visualization field (s.v.f.) in Figure 5.13. For the sake of readability, a domain equal to whole λ is omitted for NC.2 and NC.3. The flow around EB.1 case is included for aerodynamic reference, together with the 2D flow around the NC.1 case. The left column corresponds to the domain around the upwind rail, while the right column to the downwind rail. The flow direction at the solid walls is visualized by means of the Line Integral Convolution (LIC) [46] applied to the τ_w vector field. Each visualization field is further split in the middle along the y axis. The right half is dedicated to streamlines, while the left side to the selected separation, reattachment, and stagnation lines and point obtained from the τ_w field. To keep the cases in the figure comparable, the streamlines are seeded always in the same relative position and with the same seeding density for the more complex cases (NC.2-4). The flow structures do not develop in the track-wise direction for NC.1, resulting in a 2D flow. The recirculation zones are larger than in EB.1 because of the higher blockage effect of the continuous beams. The upwind and downwind recirculation zones are qualitatively the same as in the EB.1 case, except for the additional smaller recirculation zones along the top flat surfaces of the continuous beams. Between the rails the flow is split into the large clockwise recirculation and the significant secondary counter-clockwise recirculation. The bounds of the recirculation zones correspond to the separation, reattachment and stagnation straight lines. The stepped geometry of the continuous beams and the top rails involves the doubling of the local recirculation, and the corresponding stagnation and reattachment lines at both upwind and downwind side. The upwind flow structure among the cases NC.2-NC.4 is overall the same (Figure 5.14, left column). The straight separation lines testify that the flow is 2D far upwind the railway system. The reattachment line around the upwind humps is not straight and is qualitatively different for the humps with sharp or smoothed edges. For all the cases, the stagnation occurs on both the upwind hump and rail surface, analogously to NC.1. Instead of a line, the stagnation is pointwise because of the 3D flow. The stagnation point on the upwind hump face is nearly at the same height for all the cases. Conversely, the stagnation point on the rail web corresponds to the mid plane of the gap. The higher the momentum of the accelerated flow along the gap, the lower its position. On top of the humps a pair of counter rotating vortices with the vertical axis of rotation occur. Because of their effect, the separation line along the rail head is no longer straight. In spite of its very complicate topology, the flow around the downwind humps (Figure 5.14, right column) can be overall described by a single remark, i.e. the interaction between the impinging jet flow induced by the upwind

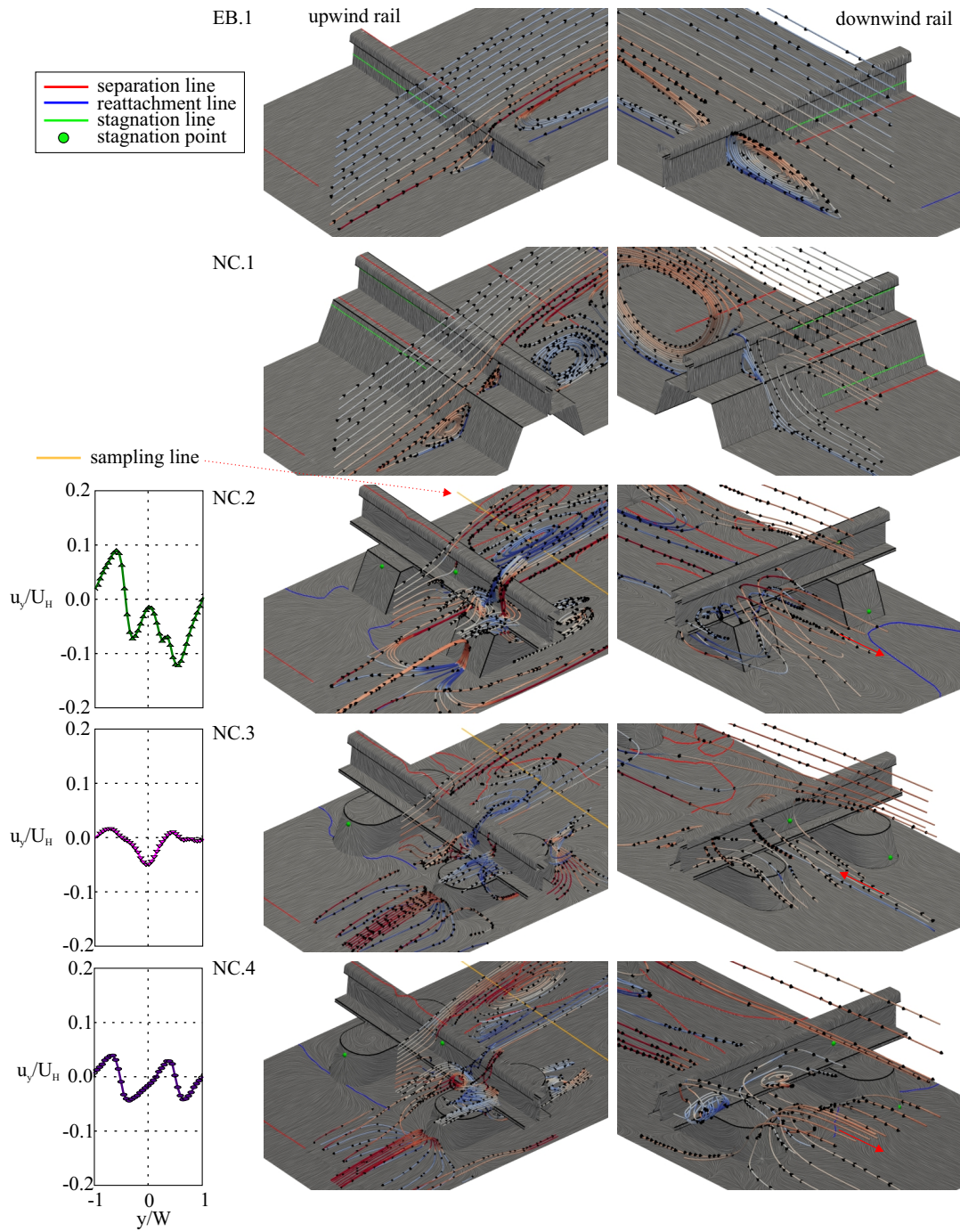


Figure 5.14: Flow patterns for NC cases (incoming wind from left to right).

gap and the reversed flow along the downwind ballast surface induced by the global recirculation downwind the substructure. In the cases NC.2 and NC.4 the jet flow

prevails, while in NC.3 the reversed flow supersedes. The consequences are manifold. First, the flow along the downwind gap is windward in NC.2 and NC.4, while it is reversed in NC.3 (the red arrows in Figure 5.14). Second, the local flow results in the different position of stagnation points on the rail web. It corresponds to the one on the hump in NC.2 and NC.4, while it is located at the mid plane of the gap in NC.3. Third, the separation lines along the gauge are nearly directed flow-wise and develop from one hump to the other in NC.2 and NC.4. In NC.3, the separation line along the gauge is deviated along the y axis and moved upwind by the reversed flow entering the downwind gap. The 3D flow fields described above deeply impact the sedimentation, erosion and backward erosion patterns around the railway track surface. They are shown in Figure 5.15 by plan views. The upper surface of the continuous beams (NC.1) and the humps (NC.2-NC.4) are excluded for the sake of clarity. The large secondary recirculation along the gauge in NC.1

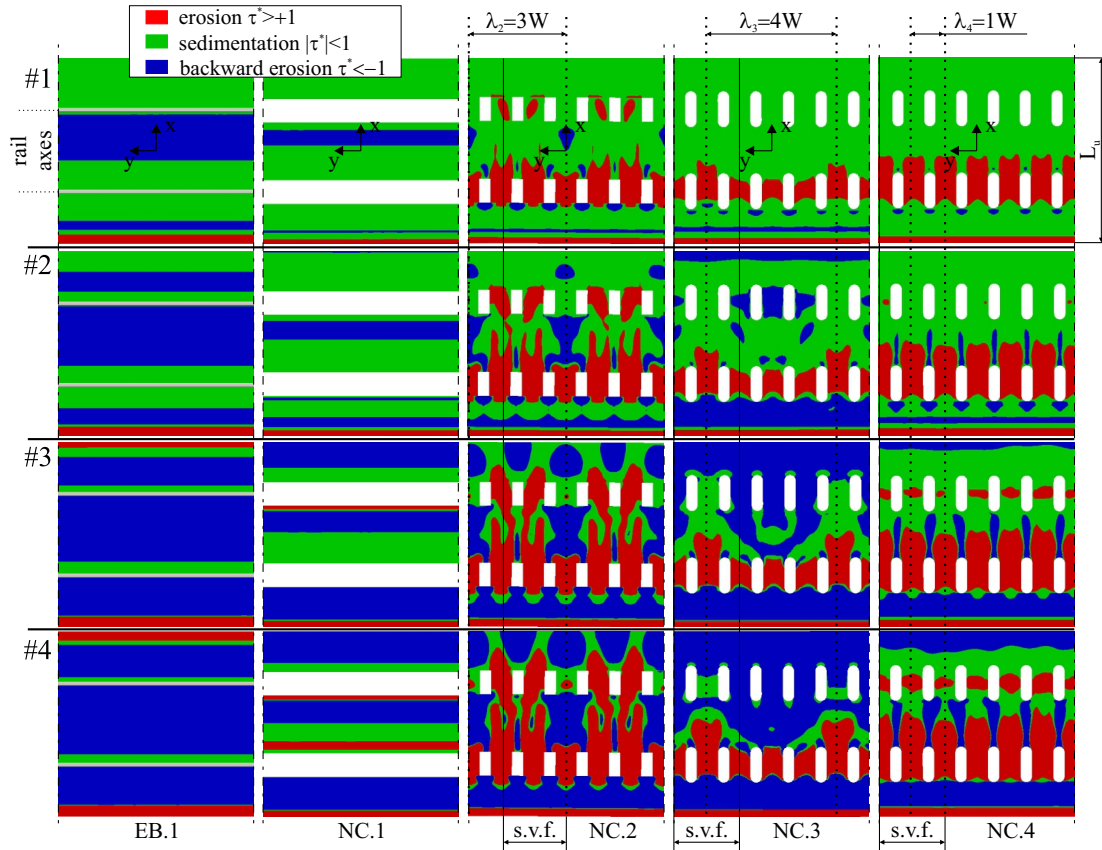


Figure 5.15: Potential sedimentation, erosion and backward erosion patterns for NC cases (incoming wind from bottom).

leads to the corresponding sedimentation zone wider than in EB.1 for every incoming wind speed. The intricate 3D flow described in NC.2-NC.4 leads to the sand

sedimentation patterns which vary both track-wise and along-wind in turn. The patterns periodically repeat track-wise with the same aerodynamic wavelength λ_i . The windward flow through both upwind and downwind gaps in NC.2 and NC.4 results in the erosion patches under the downwind rail too. Such erosion zones already occur in NC.2 for the lowest considered wind speed (#1), and progressively enlarge as the wind speed increases. From #3, upwind and downwind, the erosion zones coalesce, and the along-wind "sand erosion channels" take place for two gaps at each track-wise period. In NC.4, even though the erosion at the downwind gaps prevails over the sedimentation for high speed (#3-#4), it never merges with the erosion at the upwind gap. The reversed flow across the downwind gap in NC.3 induces extensive sedimentation along the gauge and around the downwind humps for lower speed (#1), progressively replaced by the backward erosion zones as the wind speed increases (#2-#4). Although these patterns only show the distribution of necessary conditions for sedimentation, erosion, and backward erosion, they allow to conjecture the expected windblown sand dynamics. The sand erosion channels, as the one in NC.2 is the most promising scenario, because they permit the free passage of the sand through the superstructure. The erosion at the upwind gap and the backward erosion at the downwind one as in NC.3 is expected to move the sand from the downwind rail towards the middle of the gauge, i.e. to trap the sand at the track. Such a scenario explains the field evidence shown in Figure 5.1 (i), and partially defeats the purpose of the ballasted humped sleepers. All the cases discussed above are synthetically compared by means of the dimensionless bulk quantities A_S/A_u and A_E/A_u in Figure 5.16. Even though NC.3 case has the

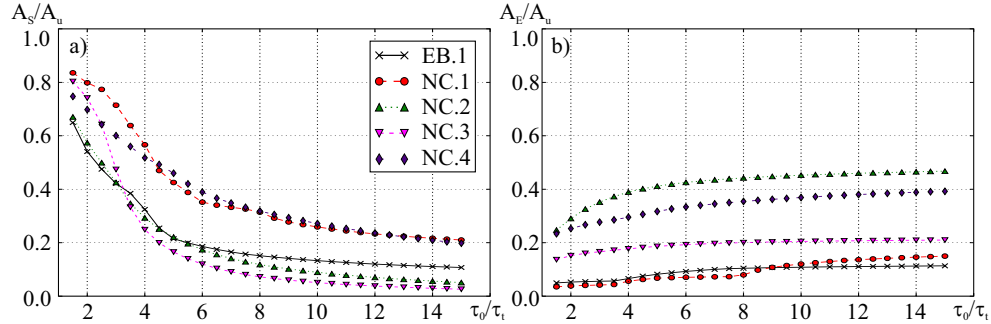


Figure 5.16: Local erosion (a) and sedimentation (b) normalized areas for NC cases.

lowest sedimentation area for $\tau_0/\tau_t > 4$, most of the erosion occurs in the backward direction. NC.2 shows relatively low sedimentation and the highest erosion in the whole range of τ_0/τ_t . The NC.4 case shows high erosion, but also very high sedimentation. The worst scenario is observed in NC.1, that combines the highest sedimentation with the lowest erosion. The standard railway system has intermediate performance in terms of sedimentation, but it shows very low erosion. In the light of this, the best performances under orthogonal incoming wind are observed

for NC.2 and NC.4.

Effects of the Yaw Angle

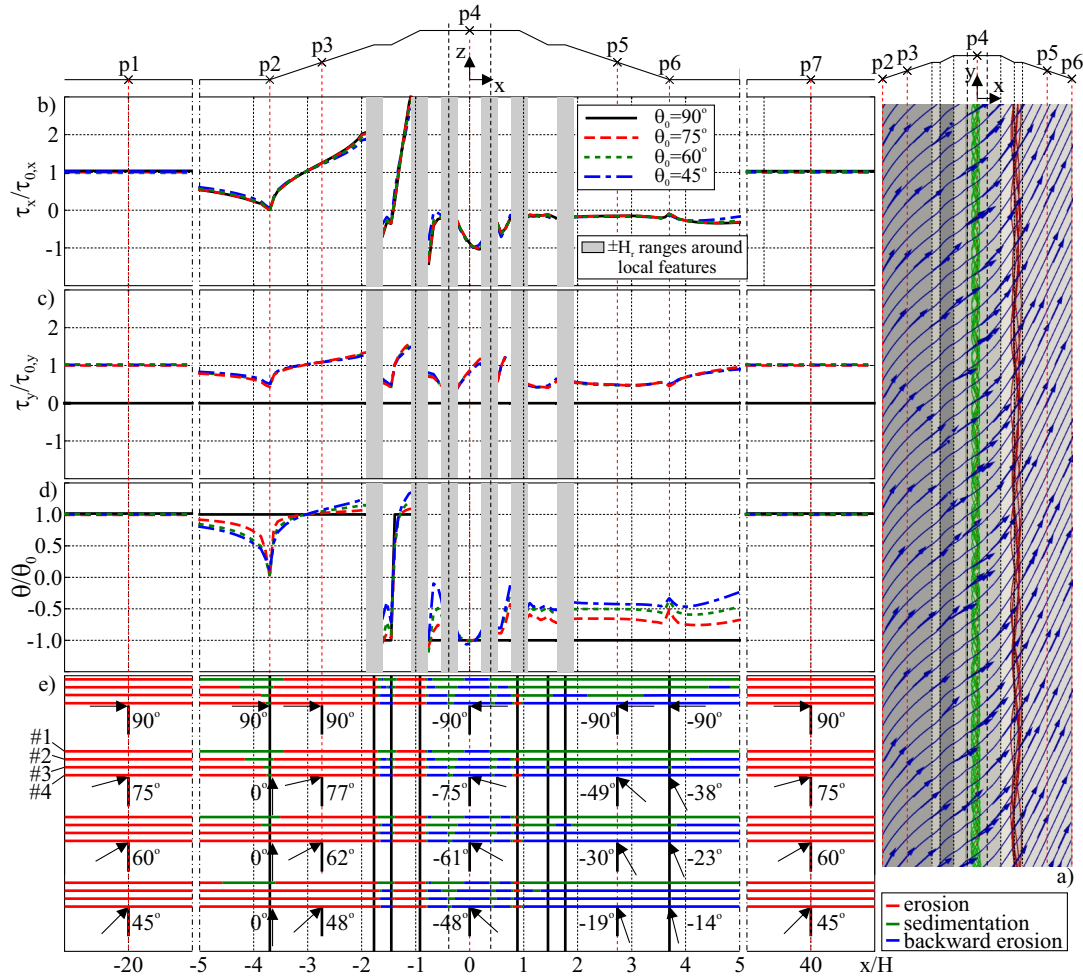


Figure 5.17: Effects of differently-yawed wind flow on standard RS (EB.1) aerodynamics.

In the light of the above, the effects of the yaw angle θ_0 of the incoming wind are evaluated for few cases only: the conventional track system (EB.1), and the two non-conventional track systems (NC.3 and NC.4). For the sake of conciseness, the global aerodynamics is scrutinized for EB.1 only in Figure 5.17. The global flow field is visualized by the streamlines in plan view for the most yawed wind ($\theta_0 = 45^\circ$) in Figure 5.17 (a). Blue streamlines are seeded in the outer free flow just outside the boundary layer, while the red and green ones develop in the recirculation regions downstream the superstructure and between the rails, respectively. The outer flow is clearly deflected downwind the railway, where the angle shift

occurs $\Delta\theta \approx 20^\circ$. Such a feature echoes the known flow deflection downwind the transverse desert and coastal dunes, discussed in [16] and the references therein. The red and green streamlines confirm the global and local separation of the boundary layer. Additionally, they testify that the resulting recirculating flow is highly swirled. Such structure is similar to the so-called *helical* or *corkscrew* vortices in the near wake of the transverse desert and the coastal dunes, as discussed, measured and simulated in [240], [64] and [123]. The deflected outer flow and swirled recirculating flow coexist, unlike suggested by the seminal conceptual model proposed in [229] for the downwind-side flow of the aeolian dunes. In the spirit of the study, the effects of the yaw angle are further scrutinized by referring to the x and y components of the shear stress at ground. τ_x and τ_y components are normalized by the corresponding component at the inlet, and plotted versus the x axis in Figure 5.17 (b) and (c), respectively. Gray stripes hide the highly localized effects induced by the sharp edges and rails in the narrow ranges ($\pm H_r$), where the results are unreadable at the adopted scale because of the very high gradients of τ_w . Two significant behaviors are observed. First, the normalization leads to the overlapping of all the curves. The results prove that *Prandtl's independence principle* [209] holds for the turbulent flow around railway embankments [13, 178] far from the local perturbations. Second, the change in the magnitude of $\tau_x/\tau_{0,x}$ is approximately twice the change of $\tau_y/\tau_{0,y}$. Moreover, τ_y never changes the sign, i.e. τ_x is the sole cause of the switch between the potential erosion and backward erosion. The local angle between the alignment direction and the resultant τ_w vector follows from its components $\theta = \text{atan}(\tau_y/\tau_x)$. The distribution of θ/θ_0 is graphed in Figure 5.17 (d). Under the incoming orthogonal wind, θ takes only two values, i.e. $\theta = \pm 90^\circ$, where $\theta = -90^\circ$ correspond to reversed flow. Continuous distributions occur under the yawed winds, due to the fact that the τ_w components vary differently. Such distributions prove that the boundary layer flow is locally deflected, and that the local switch in direction depends on the yaw angle. In particular, all the distributions reach $\theta/\theta_0 = 0^\circ$ at the upwind foot of the embankment, because of the x -wise deceleration. At the upwind foot, the local flow perfectly aligns with the railway. The flow deflection at the upwind embankment foot is qualitatively analogous to the one observed in the field measurements along the beach dune and discussed in [17], [110] and the cited references therein. The local boundary layer flow direction θ is explicitly given in Figure 5.17 (e) by the arrows and the amplitudes at the selected positions p1-p7. p1 and p7 are located far upwind and downwind respectively, p4 in the middle of the railway system, p3 and p5 in the middle of the upwind and downwind slope of the embankment, and p2 and p6 at the upwind and downwind embankment foot respectively. In the same figure, the potential erosion, sedimentation, and backward erosion patterns under the 4 yaw angles and the 4 reference speeds (#1-#4) are given as well. Two main remarks follow. First, for a given wind speed, the more yawed the incoming wind, the smaller the sedimentation zones. In other terms, skewed winds induce wider erosion and/or backward

erosion under the same speed. For instance, at the embankment upwind foot (p2) sedimentation occurs at every speed when $\theta = 90^\circ$, but the track-wise erosion takes place starting with strong breeze (#3) for $\theta = 60^\circ$, and with fresh breeze (#2) for $\theta = 45^\circ$. The track-wise sand flow made possible by such erosion conditions is recognized along the toe of the coastal dunes termed *along-shore transport* [e.g. 241]. Analogously, along the embankment downwind slope (p5) backward erosion takes place uniquely under gale wind (#4) for $\theta = 90^\circ$, but nearly the track-wise erosion ($\theta = -14^\circ$) starting with fresh breeze (#2) for $\theta = 45^\circ$. In spite of the significant differences in the substructure geometry and the track system, the case $\theta_0 = 45^\circ$ qualitatively echoes to the field evidence shown in Figure 5.1 (j), where the ripples suggest the local wind direction at around $\theta \approx 45^\circ$ upwind the railway, and at much lower negative $\theta \approx -20^\circ$ downwind.

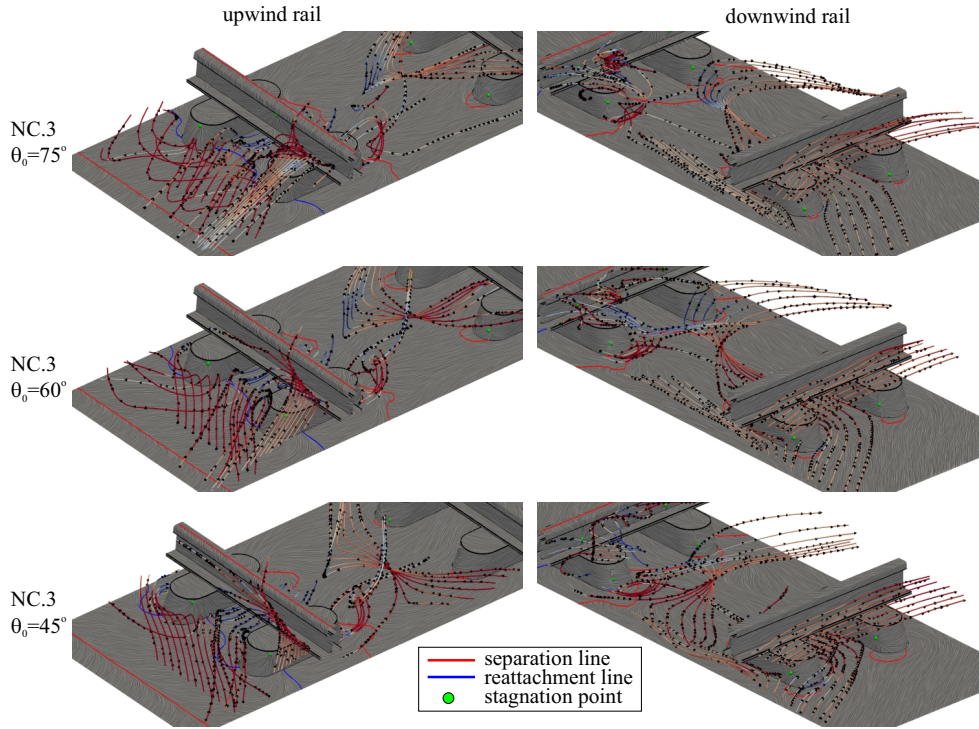


Figure 5.18: Flow patterns for NC.3 cases at different yaw angles.

The effects of yawed wind flow on the non-conventional superstructure are presented for cases NC.3 and NC.4. In Figures 5.18 and 5.19 the aerodynamic structures are comparatively presented for different θ_0 . From the comparison of the flows approaching the upwind and downwind rail it can be seen that the flow deflection occurs at the different superstructures as well. As the wind gets more yawed, the flow at the downwind rail gets more adjacent to the rail. By comparing the position of the separation lines at the upwind rail of the NC.4 case it is clear that the

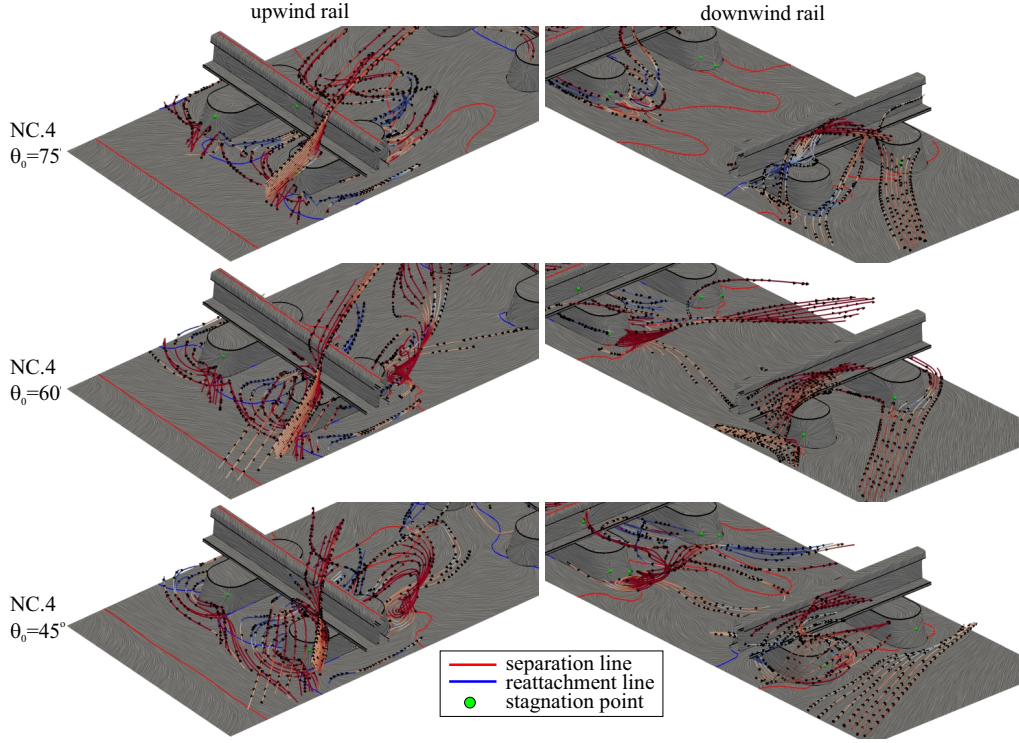


Figure 5.19: Flow patterns for NC.4 cases at different yaw angles.

recirculation zone shrinks as winds gets more yawed. For the NC.3 case the recirculation length is larger, and constant for different θ_0 . Similarly to the perpendicular winds, the flow is reattached just upwind the rail, as marked by the reattachment line. A contribution to the accelerated flow comes from the flow which is deflected just upwind the rail, at the position of the humps. The pair of the counter-rotating vortices at the upwind humps disappear. For both superstructure configurations, NC.3 and NC.4, at $\theta_0 = 75^\circ$, the arch vortex is present, represented by the pair of counter-rotating vortices in the wake of the humps. As the wind gets more yawed, i.e. $\theta_0 = 60^\circ$ and 45° , the arch vortex is replaced by a single recirculation zone with the vertical axis of rotation. All the θ_0 instances at NC.3 are characterized by the immediate separation of the accelerated flow just after the humps. This results in the downwind rails being trapped in the global recirculation zone. For the NC.4 case, such condition occurs at $\theta_0 = 60^\circ$. Conversely, at $\theta_0 = 45^\circ$ and 75° the flow reattaches upwind the downwind rail and enters the downwind gap, suggesting the occurrence of the erosion zones under the downwind rail instead of the backward erosion zone. The position of the stagnation points at the upwind humps for both NC.3 and NC.4 changes with the direction of the wind. The position tentatively corresponds to the part of the hump where its geometry is perpendicular to the incoming wind direction. Moreover, the stagnation points at the rail web disappear for $\theta < 75^\circ$ where the wind gets more parallel to the rail spanning direction. At the

downwind rail, similar positions of the stagnation points occur. The ones at the humps get slanted with the wind directions while the ones at the rail web disappear. The observed aerodynamic behavior is complemented by the potential sedimenta-

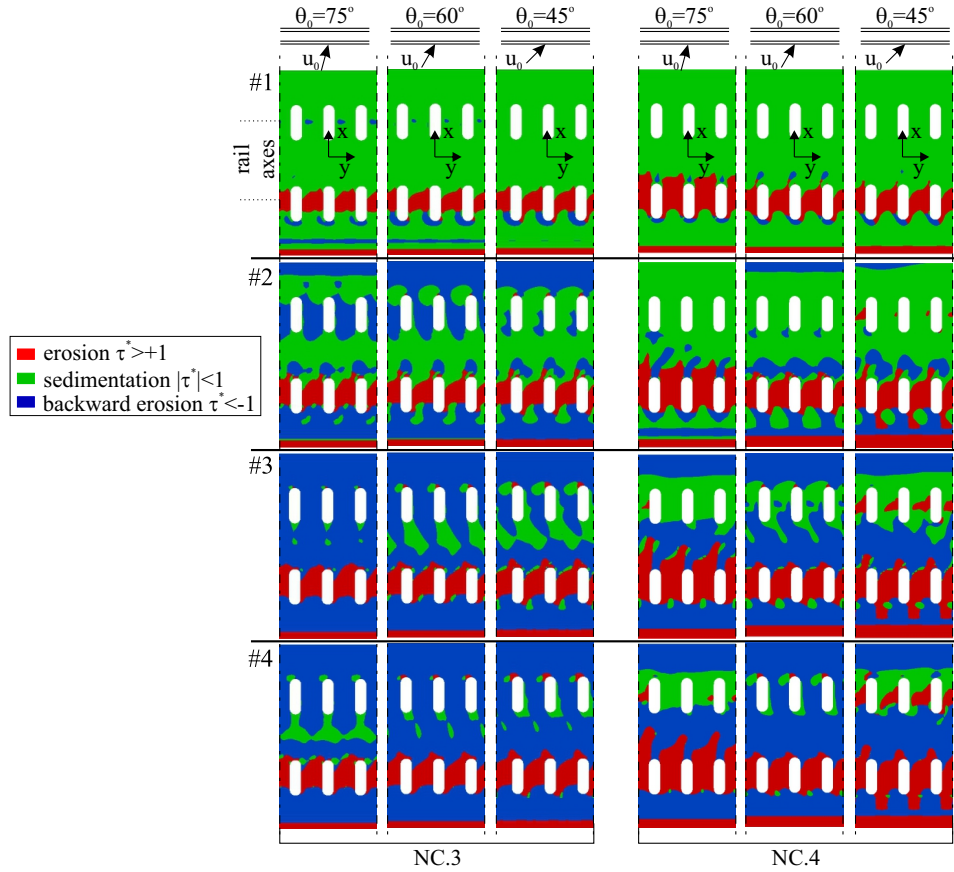


Figure 5.20: Potential sedimentation, erosion and backward erosion patterns along non-conventional railway systems under differently yawed wind-flow (incoming wind from below).

tion, erosion and backward erosion patterns shown for the different θ_0 in Figure 5.20. The simulated patterns are overall complex, and locally highly sensitive to both the yaw angle and the track system. Nevertheless, some general features can be synthetically outlined. First, the patterns remain periodic in the track-wise direction also under the yawed winds but, unlike the orthogonal wind, the track-wise wavelength λ equals the the spacing between humps W . Second, the shape of the sedimentation zones and the occurrence of the backward erosion zones around the downwind humps for the higher speed (#2 to 4) suggest the local flow direction in their wake. As anticipated from the comparison of the aerodynamic structures, the flow is reversed for NC.3 at all the θ_0 and the sand is expected to be eroded towards the gauge at the downwind rail. For NC.4 the fact that the local flow is windward

at $\theta_0 = 75^\circ$ and $\theta_0 = 45^\circ$ is further proven by the windward erosion zones. The reversed flow at $\theta_0 = 60^\circ$ is resulting in the backward erosion zones. Third, as the wind speed increases, sedimentation is generally replaced by backward erosion, while erosion remains nearly constant or slightly decreases (NC.4, $\theta_0 = 75^\circ$, upwind the gaps). The pattern for the case NC.3- $\theta_0 = 75^\circ$ -#4 remarkably recalls the field evidence observed for the same track system and shown in Figure 5.1 (i): both gaps are eroded, and the combination of the sediment transport from the upwind and downwind gaps results in almost x -symmetric, y -periodic piles of sand within the gauge.

All the discussed cases are synthetically compared by means of the dimensionless sedimentation and erosion areas in Figure 5.21. The #1-4 curves are given for each case versus θ_0 . In general, the cases show the highest sedimentation lev-

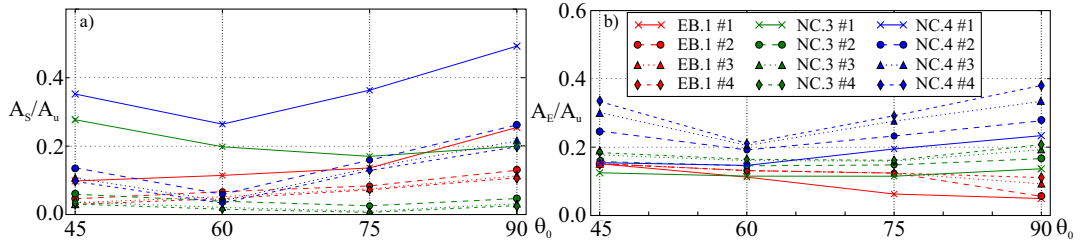


Figure 5.21: Sedimentation (a) and erosion (b) normalized areas for selected cases under differently-yawed wind flow.

els under the perpendicular winds, which are proven to be the most critical with respect to the sand covering. As the angle increases, sedimentation unexpectedly drops. Changes in the incoming wind velocity have little influence on the trend of the curves, while they generally translate/scale the curves w.r.t. the vertical axis. In particular, sedimentation and erosion on the standard railway system (EB.1) are weakly sensitive to θ_0 , i.e. erosion slightly increases for more yawed winds, and sedimentation progressively decreases. NC.3 is nearly insensitive to θ_0 , except for the sedimentation at #1, where A_S/A_u singularly increases as the yaw angle decreases. The case NC.4 is the most sensitive to the changes in yaw angle in both erosion and sedimentation. Interestingly, the trend of the curves is not linear, and the local minima occur at $\theta_0 = 60^\circ$ because of the reversed flow around the downwind humps, as discussed in Figure 5.20.

5.4.2 Preliminary Design of the Receiver Sand Mitigation Measure

The observed trends and the knowledge gathered during the study of the unmitigated RS resulted in the several ideas for the design of SMM. In the following,

the application of the innovative design is applied on two RS; first, the standard (EB.1) and second, the non-conventional RS with the humped sleepers (NC.3).

Preliminary study is carried out in the form of 2D simulations to test the new design idea in a semi-heuristic, trial-and-error approach. The goal is to manipulate the wind flow around the rails in order to increase the aerodynamic performance. Once again, the performance is based on the map of wall shear stresses over the upper substructure surface, analogously to the assessment of the unmitigated RS.

Standard Sleepers

The main idea of applying a guiding vane on railway with the standard sleepers is to accelerate the recirculation flow in between the gauge. The accelerated mid-gauge recirculation should, in theory, extend the corresponding backward erosion zone. Even though, in such condition, the sand remains trapped, the pointwise signaling equipment which are positioned at the middle of the gauge get passively cleaned from the sand for a wider range of τ_0/τ_t .

In Figure 5.22 each row corresponds to a SS case as listed in Figure 5.3 (b). Additionally, case SS.0 is included which corresponds to the unmitigated SS railway. The speed-up ratio, defined as a $U/U_0(H)$, where U is a local magnitude of the velocity field and $U_0(H)$ is magnitude of inlet velocity at the height H , is coupled with the streamlines in the left column of Figure 5.22. The aerodynamics is complemented with the sedimentation, erosion and backward erosion zones in the right column for the different wind conditions, #1, #2, #3 and #4 from top to bottom. In general, with increase in τ_0/τ_t the erosion zones extend while sedimentation shrink.

Three significant local coherent structures develop for the SS.0 case, similarly to the previously tested 3D simulations (first row of Figure 5.22): i.) the upwind local vortex $R_{u,r}$; ii.) the middle local vortex $R_{m,r}$; and iii.) the downwind local vortex $R_{d,r}$. Additional secondary vortices appear in some cases upwind and downwind the rails. As expected, the 2D simulations resemble quite well the results of the 3D cases for the nominally 2D standard railway geometry.

Adding a guiding vane upwind the railway significantly changes the flow structure. For all the SS cases, a pair of counter rotating vortices develop at the suction side of the vane. At the pressure side the flow is accelerated and deflected. The accelerated flow (colored in green) approaches the gauge and is intended to accelerate the recirculation $R_{m,r}$, and in turn extend the backward erosion zone. In SS.1 a secondary vortex appears in between the gauge causing the erosion zones upwind the main backward erosion zone. From the perspective of protecting the equipment in the middle of the gauge this is not a desired phenomenon, because the sand gets transported from the both sides towards the middle of the gauge. Strikingly different flow occurs for in SS.2 when h_v is reduced. The angle of the accelerated

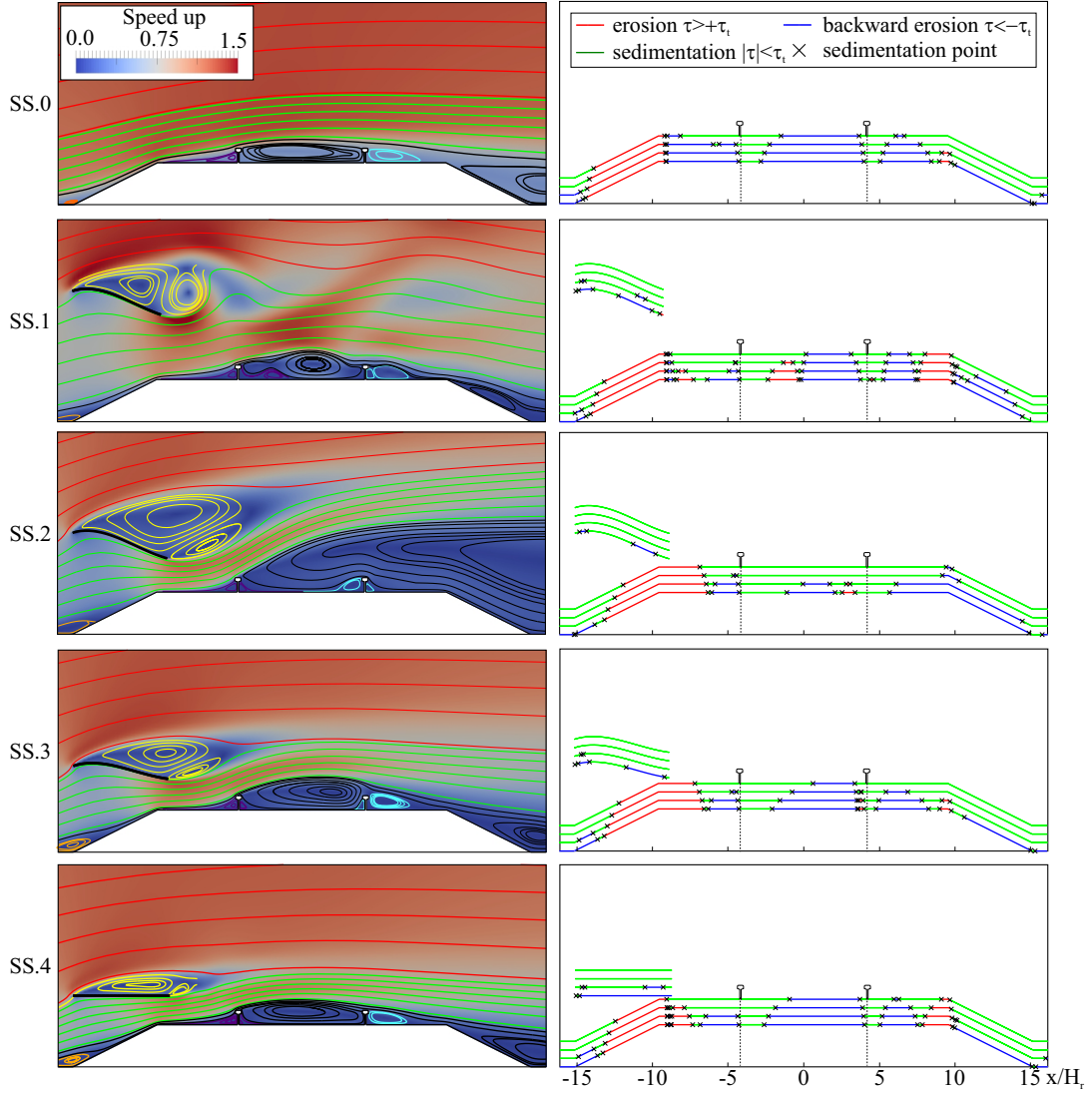


Figure 5.22: Local flow features in terms of aerodynamics (left column) and potential sedimentation, erosion and backward erosion zones (right column) for SS cases.

flow leaving the vane moves the separation point of the global downwind recirculation flow to the head of the upwind rail. Such a condition leads to significantly reduced kinetic energy of the flow in between the gauge. Hence the reduction of the erosion zones in between the gauge for a given τ_0/τ_t . While keeping the same h_v and reducing the vertical dimension of the vane h in SS.3, the angle at which the accelerated flow leaves the vane becomes more horizontal. This leads to retrieving qualitatively the same flow field compared to the unmitigated measure. However,

the aerodynamic performance is still lower than for the unmitigated case.

The final attempt to increase the performance is done in the form of reducing the h to 0, i.e. making the vane horizontal as can be seen in SS.4. The aerodynamic performance increases compared to the SS.3 case, but it is still not better than the already well-performing unmitigated case. The geometry of the standard railway superstructure and the already large backward erosion zone in-between the rails make the further improvements impossible at the present time. The backward erosion covers $\approx 60\% - 80\%$ of the surface for wide range of wind velocity magnitudes at the inlet (#1 – #4).

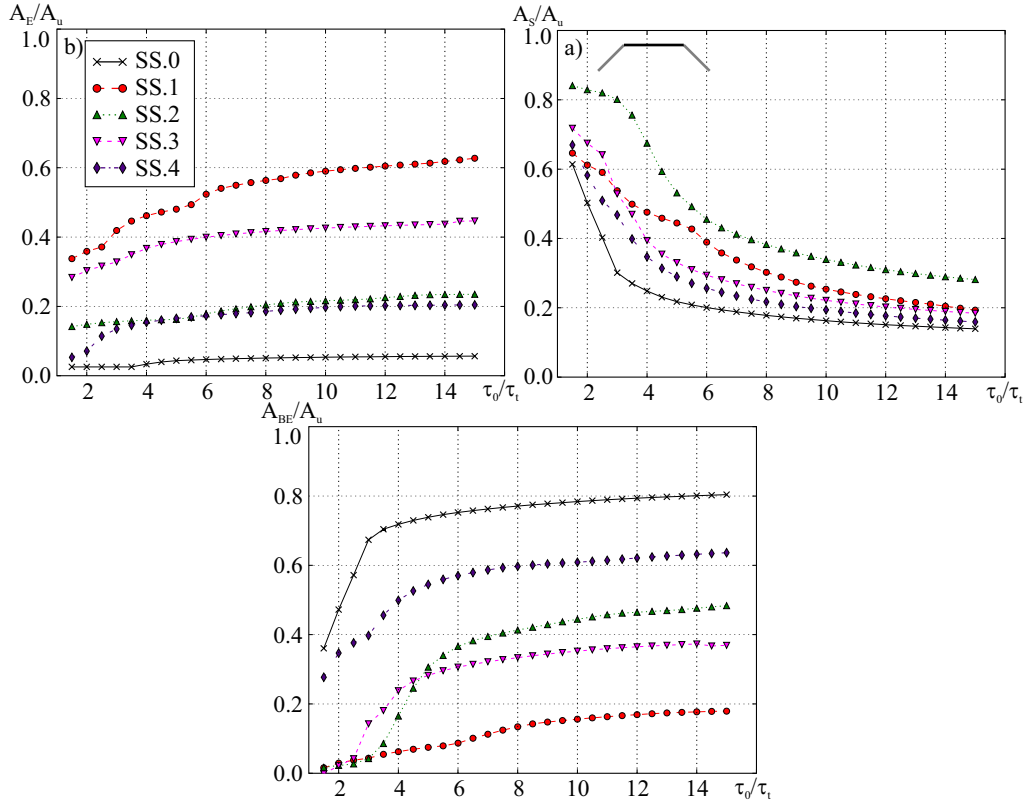


Figure 5.23: Graphs of erosion (a), sedimentation (b), and backward erosion (c) for SS cases integrated over the upper ballast surface.

To quantify the performance of the *Sand Blower* at the SS system, the erosion A_E , sedimentation A_S , and backward erosion A_{BE} zones are integrated over the ballast upper surface A_u and presented in their dimensionless form. The areas are in order presented in Figure 5.23 (a), (b) and (c). The integration over the whole ballast surface is not given because of its lower relative importance compared to the upper surface. From the perspective of sand mitigation and keeping the railway signaling equipment free of sand the performance over the upper surface is essential.

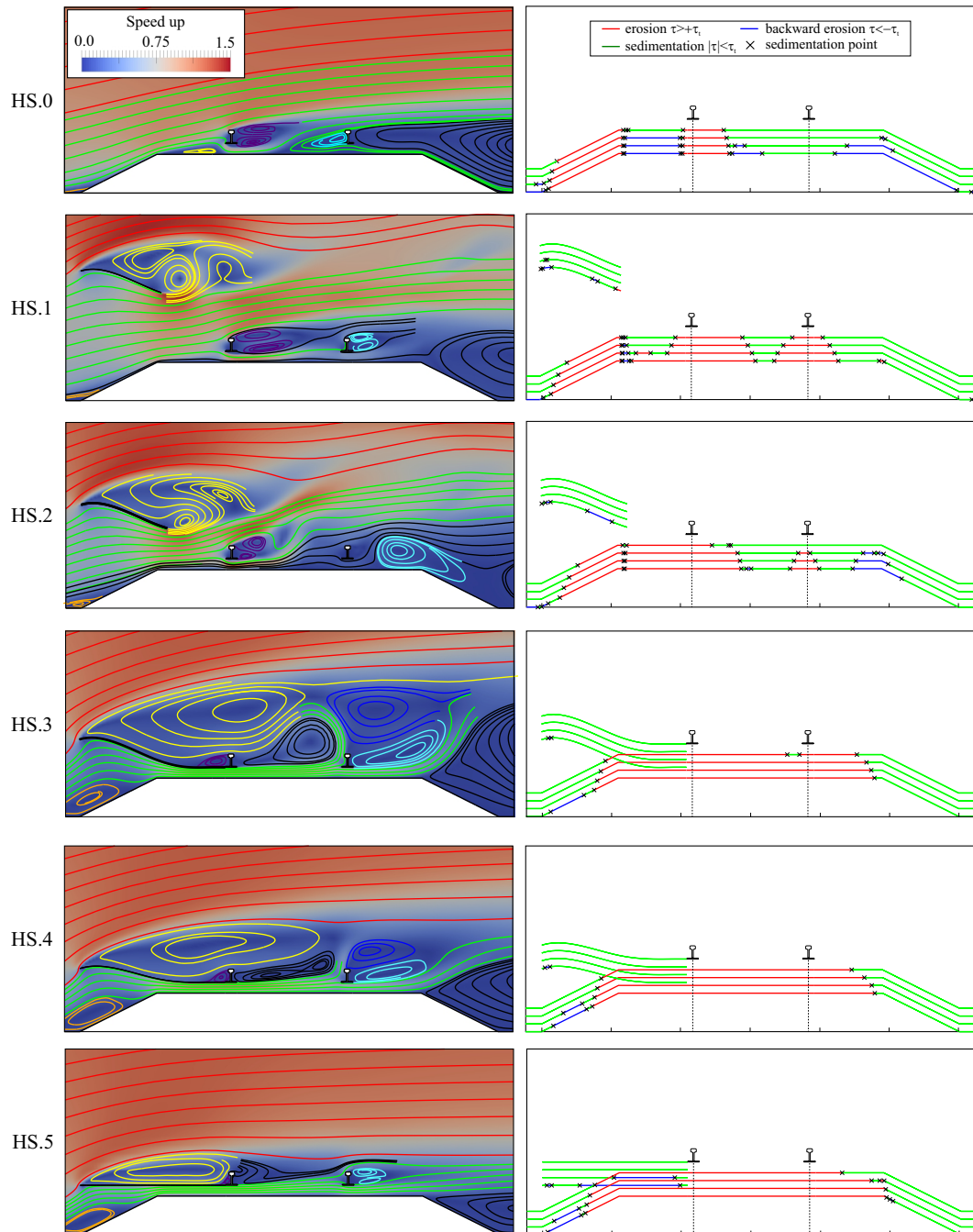
From the graphs it can be seen that the unmitigated railway for the most part retains the highest percentage of backward erosion and the lowest percentage of sedimentation for a given τ_0/τ_t . This means that from all of the cases, the application of the chosen vane geometries to the SS geometry reduces the aerodynamic performance. Hence, the application of the vanes at the SS system is, at this point of research not suggested.

Humped Sleepers

The geometry of the SS systems does not leave a lot of room for the aerodynamic improvement. Hence, the guiding vanes have been applied to the HS system. The initial idea of the unmitigated HS system is to accelerate wind in the gaps between the rails and ballast. As shown in the study of unmitigated railways and confirmed by the results of the 2D simulation in the first row of Figure 5.24, the solution works well at the upwind rail. The separation of the flow occurs in between the gauge, leaving the downwind rail in the recirculatory flow and in turn, the combination of the sedimentation and backward erosion zone. The idea of the *Sand Blower* is to force the flow to be attached in between the gauge giving the optimal sand erosion-sedimentation conditions.

Figure 5.24 is created analogously to the one presented for the SS cases. The general 2D structure of the flow around the unmitigated HS geometry (HS.0) consists of the small vortex at the upwind slope of ballast (orange), the vortex upwind the upwind gap (yellow), a pair of counter rotating vortices downwind the upwind rail bounded by the accelerated flow and the flow over the rail (purple), and a big global recirculation zone with the separation point in the middle of the gauge (black and green). The vanes in the next two rows, HS.1 and HS.2, are geometrically equivalent to the cases SS.1 and SS.2. Adding the vane completely changes the flow topology in between the gauge compared to the HS.0. The flow downwind the vane consists of two counter rotating vortices, similarly to the SS cases. The most significant contribution of the vane is that the flow does not separate along the gauge and stays attached to the ground over whole upper ballast surface. Subsequently, massive improvements occur in the erosion-sedimentation-backward erosion patterns. In both of the cases, besides the upwind rail, the erosion zone occurs under the downwind rail as well.

The next improvement is done by attaching the vane to the foot of the upwind rail. For all the cases with the attached vane ($h_v = 0$; HS.3-HS.6s) the flow topology is qualitatively the same and very complex. It consists of a much bigger vortex at the upwind ballast slope (orange), a main vane recirculation (yellow) with a smaller secondary recirculation just in front of the upwind rail (purple), a single recirculation in between the gauge (black), and a pair of counter rotating vortices downwind the downwind rail (blue and light blue). It can be seen that all of the $h_v = 0$ vanes erode the upper ballast surface completely.



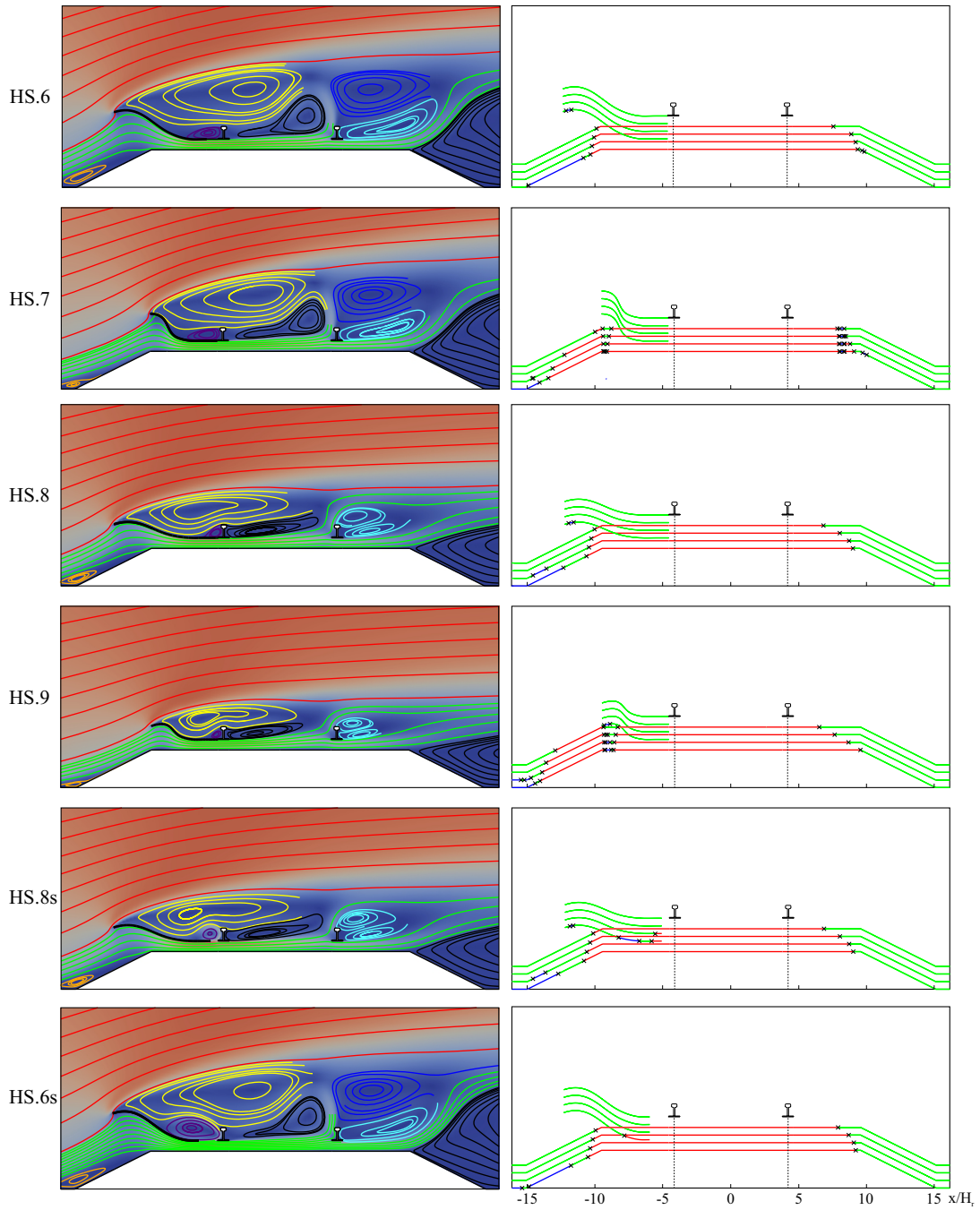


Figure 5.24: Local flow features in terms of aerodynamics (left column) and potential sedimentation, erosion and backward erosion zones (right column) for HS cases.

The next couple of steps are done in the attempt to reduce the size of the

vane while keeping the same performance in the cost-reducing perspective. In HS.4 and HS.5 the height h of the vanes is reduced. The corresponding figures in the right column show that the erosion performance at the upper ballast surface is approximately the same compared to the case HS.3. Conversely, the horizontal length l is reduced in cases HS.6 and HS.7. In HS.6 the erosion performance is the same compared to the previous cases. A drawback is observed for the case HS.7 with the lowest l . At the upwind sharp edge of the ballast, a small sedimentation zone occurs for all the inlet wind velocities #1 – #4. To avoid a possibility of the vane getting clogged by the sand, this solution is discarded. Analogous aerodynamic behavior occurs for the case HS.9 where both h and l of the vane are reduced. It can be concluded that the shortest l results in a small recirculation bubble which in turn results in the sand sedimentation zone at the sharp ballast edge.

By taking the above into account, two solutions are selected, the case HS.6 and HS.8. For both the cases, an additional simulation is performed with a gap between the trailing edge of the vane and the upwind rail. The function of the gap is to allow the sand, which potentially overshoots the vane, to enter the accelerated flow and be eroded across the railway system. There is no significant differences between the performances of the vane with and without the gap. The only difference is the size of the secondary vortex developing on the vane (purple). In a safety perspective HS.6s is the chosen geometry. HS.6s is the solution with the highest $h = 2H_r$ which has twofold function: i.) it makes the sand overshooting the least probable; and ii.) it preserves the steepest slope of the vane geometry with the angle higher than the sand repose angle ($\approx 30^\circ$) allowing the sand to avalanche to the lower portions of the vane. In such a way, the sand flux crossing the vane is reduced and the vane is being passively cleaned.

The quantification of the aerodynamic performance is given in Figure 5.25 in form of the integrated dimensionless erosion, sedimentation and backward erosion areas. Figure 5.25 shows the expected trends in general. As τ_0/τ_t increases, sedimentation gets lower and erosion/backward erosion higher. The cases without the vane attached to the rail (HS.1 and HS.2) show similar behavior to the unmitigated case in sedimentation. Because the flow in HS.1 and HS.2 is reversed at the downwind rail compared to the unmitigated rail, erosion is much higher. The cases with the vane attached ($h_v = 0$) show better results compared to the others. The following conclusions can be outlined: i.) the HS cases show very low values of sedimentation, i.e. reaching 0-level at $\tau_0/\tau_t \approx 5 - 6$, leaving the ballast upper surface completely eroded; ii.) these solutions are almost insensitive to the changes in τ_0/τ_t , with only slight differences observed at low values of τ_0/τ_t ; iii.) the only case, besides the unmitigated HS.0, for which a significant backward erosion zone occurs (HS.2) can be immediately discarded and declared as the worst tested solution; and iv.) the selected HS.6s case is confirmed to be in the narrow band of the best performing cases, proving that it is a suitable solution to be further improved.

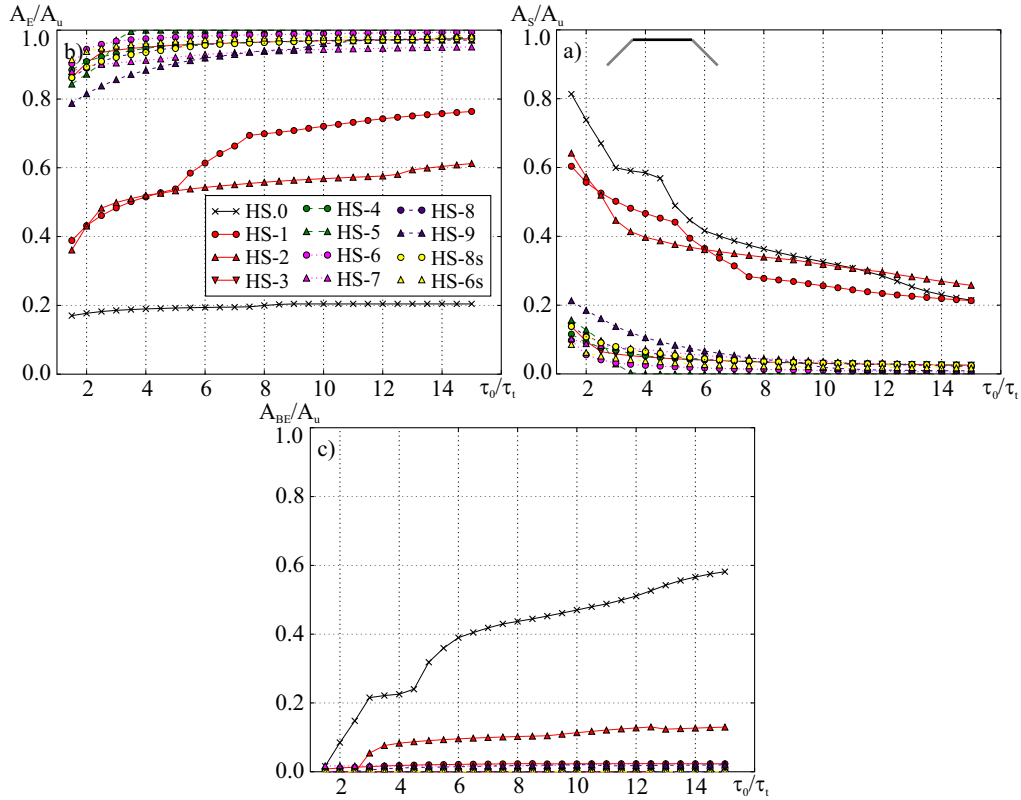


Figure 5.25: Graphs of erosion (a), sedimentation (b), and backward erosion (c) for HS cases integrated over the upper ballast surface.

5.4.3 Final Performance Assessment of the Receiver Sand Mitigation Measure

To finalize the assessment of *Sand Blower* applied to humped sleepers, further 3D simulations are performed to take into account the 3D flow effects which occur around the humps and the joints of the vane and the infrastructure. The promising results were the motivation to name the 3D adaptation of the shape HS.6s '*Sand Blower*' (see Figure 5.3 c). The adopted track-wise size of *Sand Blower* equals 5 sizes of the HS geometric period W , with the cross-section of the HS.6s vane. However, the track-wise length of the SMM can be adapted to the equipment it is protecting. For example, 3 gaps should suffice for the protection of signaling balise, but a longer ≈ 20 m length is required for the protection of switches and turnouts. Figure 5.26 plots the streamlines of the local flow around the *Sand Blower*. To make the figure clearer, the flow visualization is presented from the two views; the upwind rail in the left column and the downwind rail in the right column. For the sake of comparison, the same visualization is presented for unmitigated SS and HS

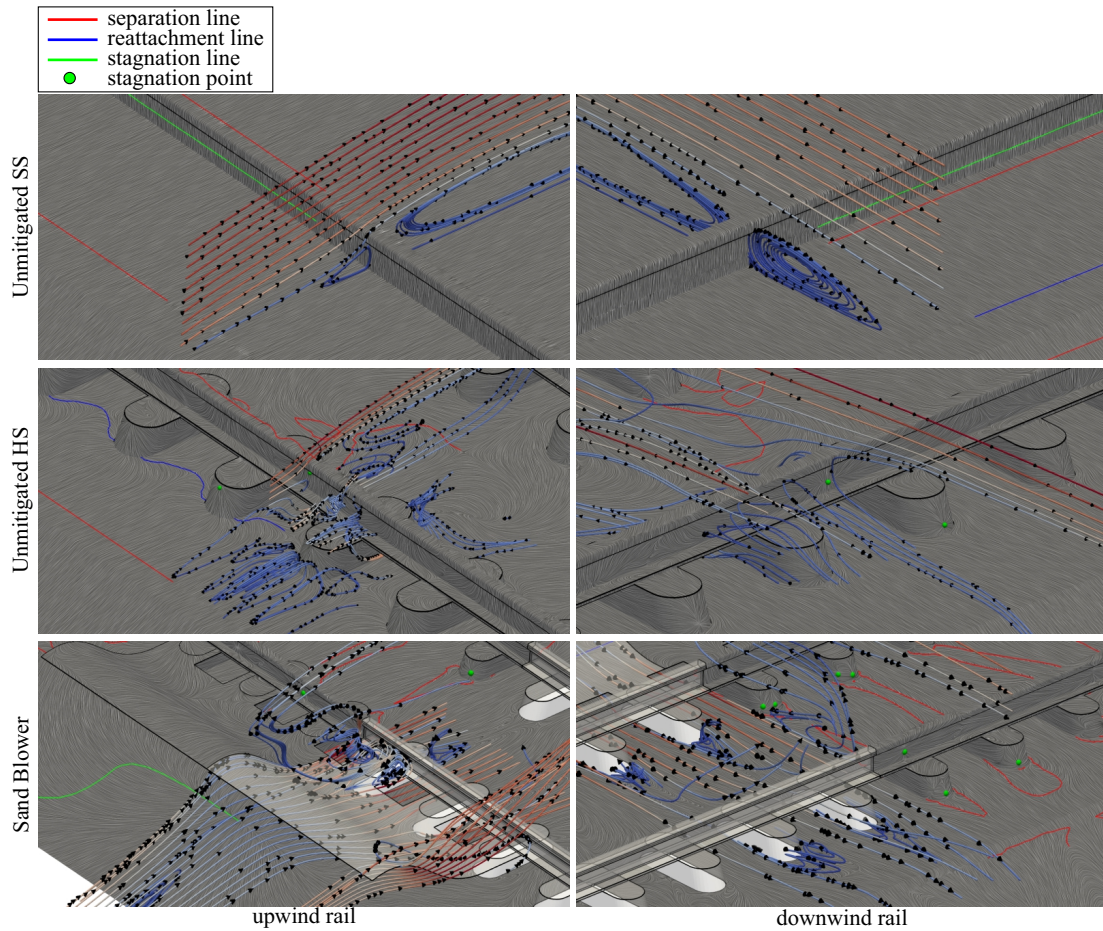


Figure 5.26: Flow patterns for unmitigated SS, HS and *Sand Blower* cases (incoming wind from left to right).

cases. It can be seen that the 3D flow around the SS geometry is qualitatively the same as presented for the 2D cases, i.e. the streamlines are positioned at the vertical $x - z$ plane and the third y - component of the flow does not occur.

The flow in the unmitigated HS case is already presented in the section about the unmitigated railway systems (NC.3) and is here included as a reference only. In brief, the flow is accelerated under the upwind hump. The part of the flow entering the gaps is following their geometry and it separates in the middle of the gauge. From the presented it can be seen that the general idea of the flow given by the 2D simulations is confirmed, but the 3D effects which occur at the gaps are expected to have significant effect on the erosion/sedimentation/backward erosion patterns.

The flow structures change when *Sand Blower* is applied to the unmitigated HS geometry. The majority of the flow is accelerated under the upwind rail and

enters the gauge without the recirculation zone occurring upwind the humps. A small fraction of it escapes through the gap and is dragged into the recirculation zone downwind the vane. At the joints of the upwind rail and the *Sand Blower*, pairs of counter rotating vortices occur with the vertical axis of rotation. Additional swirling with the windward axis of rotation occurs at the track-wise tips of the *Sand Blower* caused by the pressure difference at the suction and pressure side of the vane. The figure confirms that the good aerodynamic behavior of the flow observed in the 2D cases, occurs in the 3D simulations as well. The accelerated flow remains attached to the upper ballast surface and leaves the gauge under the downwind rail. Exception can be seen for the flow just upwind the downwind humps. The humps force a smaller fraction of the flow to separate in the gauge. Additionally, in the wake of each hump, an arch vortex appears.

Moreover, to get a better idea of the complex flow, the ballast surface, half of the railway and half of the *Sand Blower* are marked with the LIC of the wall shear stresses vector field. Such representation shows the local direction of the flow at every point of the surface. If the condition for sand erosion is satisfied $|\tau^*| > 1$, the direction of the erosion is locally parallel to the LIC lines.

The 3D flow fields described above deeply impact the sedimentation, erosion and backward erosion patterns around the railway track surface. They are shown in Figure 5.27 by plan views. The patterns which occur at the unmitigated SS case are qualitatively the same as the ones presented for the 2D cases. The patterns in unmitigated HS case further prove the 3D structure of the flow. The upwind gap is in the erosion zone where the humped sleepers work well from the sand mitigation point of view. Conversely, the downwind rail is in the backward erosion conditions, similarly to the *Sand Blower* case past the track-wise tips, i.e. the blue patters visible for *Sand Blower* case at #3 and #4. For the unmitigated case, the erosion at the upwind gap and the backward erosion at the downwind gap is expected to move the sand from the both rails towards the middle of the gauge, i.e. trapping sand at the track. Such a scenario partially defeats the purpose of the ballasted humped sleepers which are designed to keep the gauge free from sand. The most significant contribution of the *Sand Blower* is the reversal of the backward erosion zone at the downwind rail and turning it into the erosion zone. In such a way, the erosion patches under the upwind and downwind rail get connected and allow the free passage of the sand across the gauge. This occurs even for the very low inlet values of the wind speed (from #1). Additionally, the erosion passages are extended to the downwind portions of the upper ballast surface. The small sedimentation-backward erosion patches occur in between the upwind and downwind humps, and downwind the downwind humps as a consequence of the flow structures which develop upwind and in the wake of the humps. This being said, the results shown for the 2D cases, correspond relatively well to the cross sections in between the humps. A slight drop of performance compared to the 2D cases is observed because of the sedimentation-backward erosion zones which occur

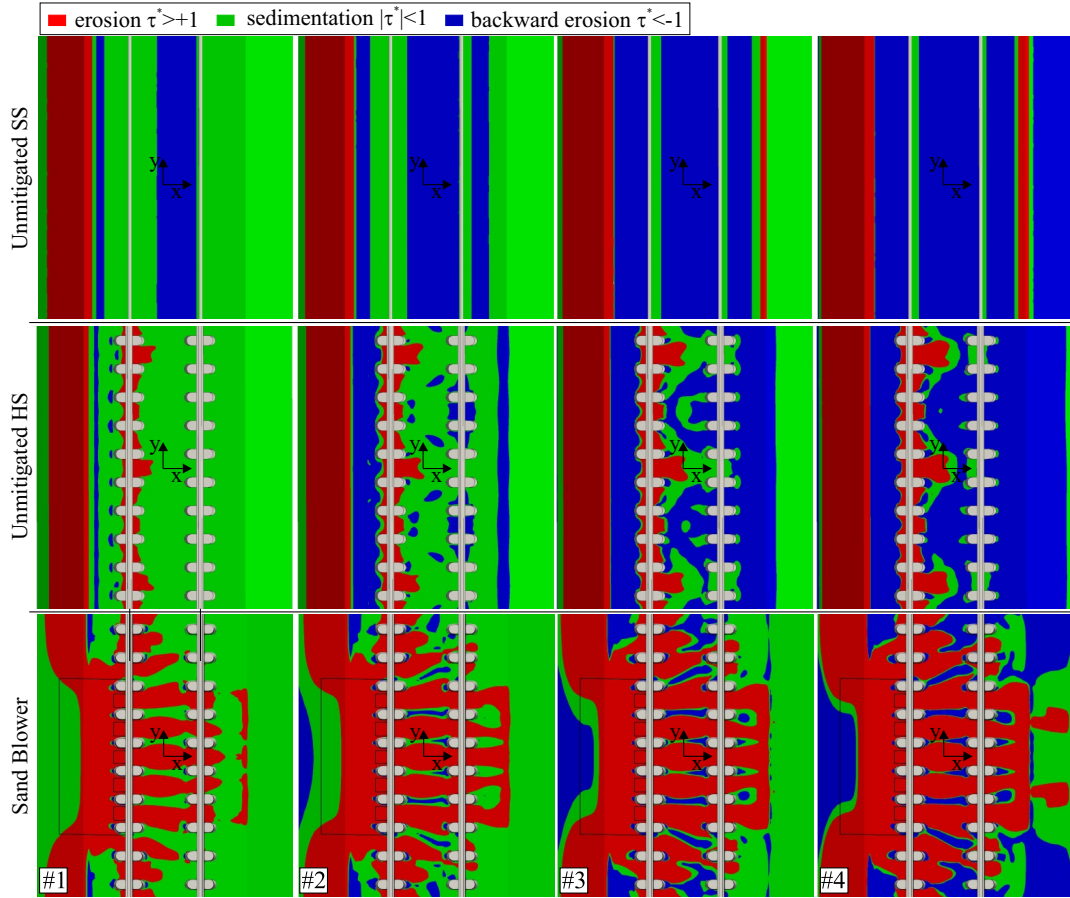


Figure 5.27: Potential sedimentation, erosion and backward erosion patterns for unmitigated SS, HS and *Sand Blower* cases (incoming wind from left to right).

around the humps. The performance of the *Sand Blower* is quantified in Figure 5.28. The results are compared with the 3D simulations of the unmitigated SS and HS railway systems. The sedimentation graph in Figure 5.28 (b) shows the need of the further aerodynamic performance improvement of humped sleepers. In particular, the HS system works better for the higher τ_0/τ_t compared to the SS system, but for $\tau_0/\tau_t < 3.5$ the sedimentation is lower for the SS cases. Conversely, the *Sand Blower* case exhibits the lowest values of sedimentation for all the τ_0/τ_t values and converges to the approximately same low value as the unmitigated HS case. Figure 5.28 (a) confirms the best behavior of *Sand Blower* from the selected cases. The A_E/A_u is strikingly much higher than for the other cases and ranges in [0.7,0.9]. Conversely, erosion at the unmitigated cases is not influenced much by the change in τ_0/τ_t and is kept in the narrow range around 0.1 and 0.2 for the SS and HS case, respectively. To make it completely clear, the additional graph of the

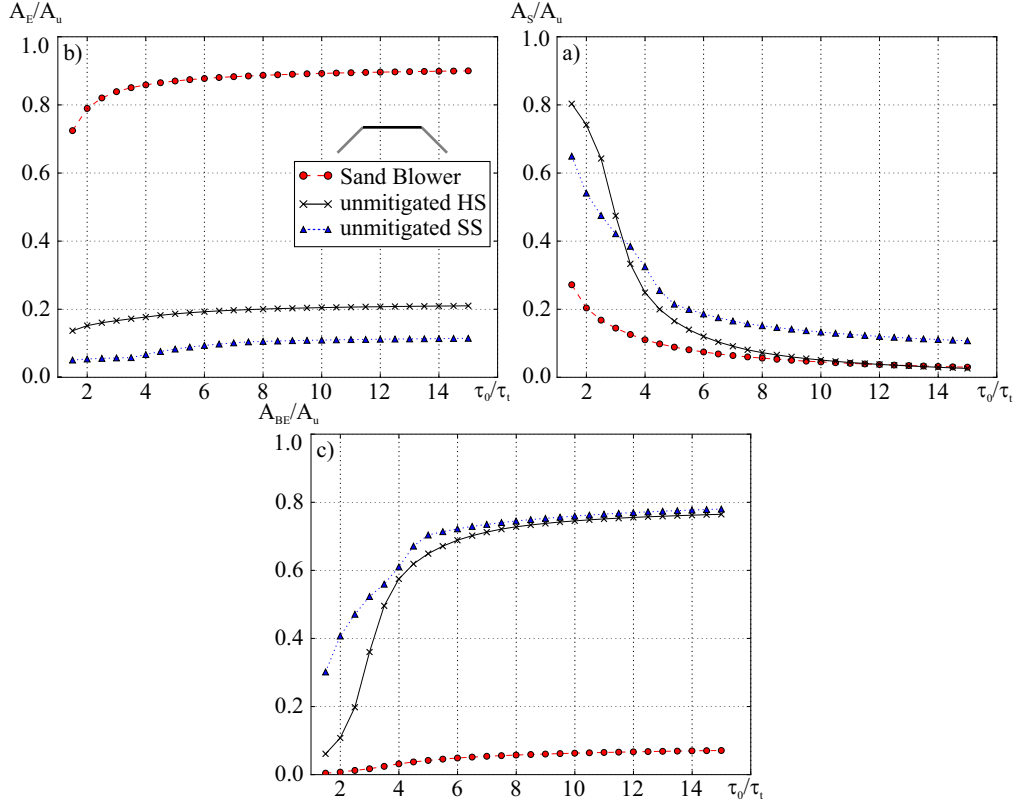


Figure 5.28: Local erosion (a), sedimentation (b) and backward erosion (c) normalized areas for *Sand Blower*.

backward erosion area is included in Figure 5.28 (c). The figure shows that the lack of erosion for the unmitigated HS case is substituted by a large percentage of backward erosion. To summarize, *Sand Blower* case shows the best behavior at all of the performance metrics.

5.4.4 Performance Assessment of the Receiver Sand Mitigation Measure under Yawed Winds

The effects of the yaw angle have been tested for the same angles as the unmitigated railway, i.e. $\theta_0 = 90^\circ$, 75° , 60° , and 45° . In the cost-reducing perspective a narrower *Sand Blower* geometry has been tested. Instead of track-wise dimension of 5 humped sleeper gaps used for perpendicular wind, 4 gaps are used instead.

From Figure 5.29 it can be seen that in general, the erosion zones get skewed under the upwind rail compared to the perpendicular wind. Compared to the unmitigated HS system under differently-yawed winds, an improvement is clear. The sand erosion zones under the upwind and downwind rails are still connected

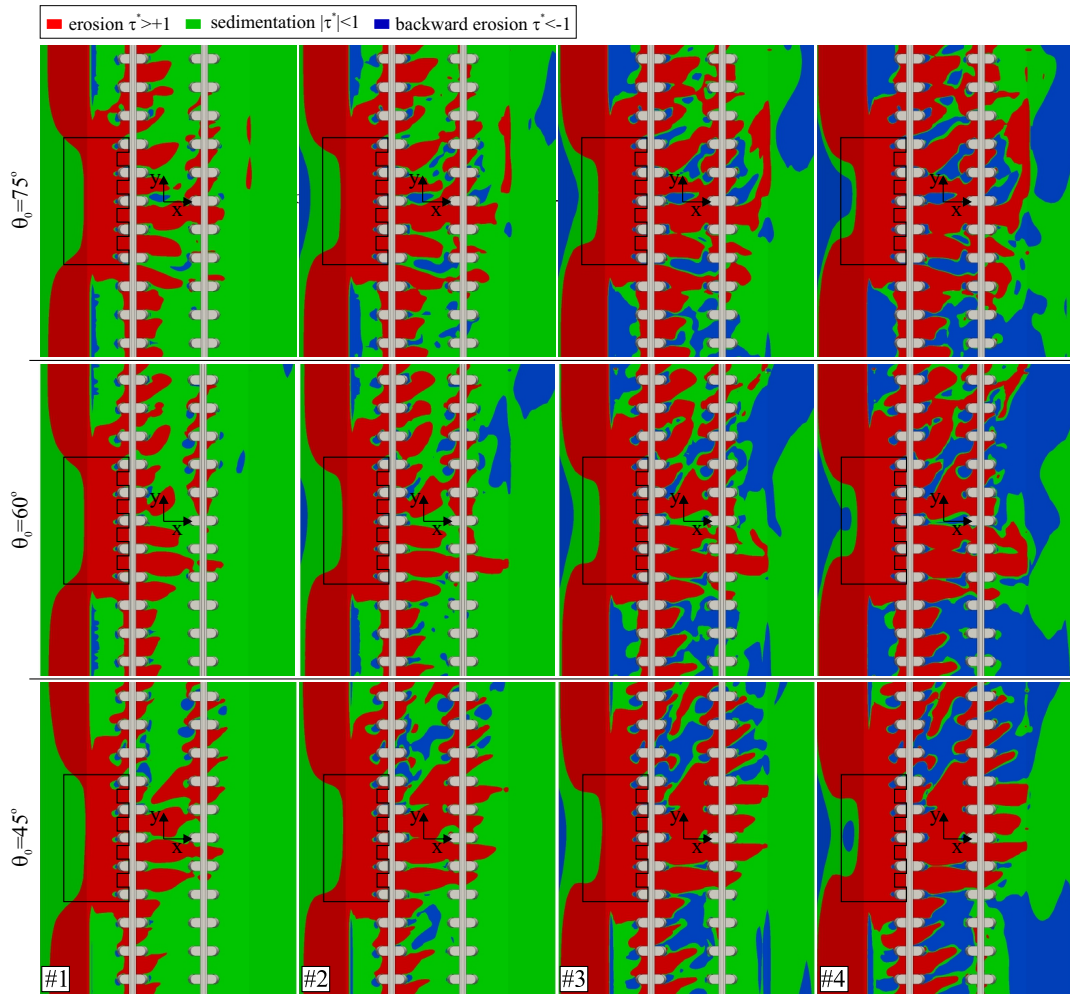


Figure 5.29: Potential sedimentation, erosion and backward erosion patterns for unmitigated SS, HS and *Sand Blower* cases at different yaw angles.

and the mid-gauge separation is avoided. The results show, that for the *Sand Blower* track-wise dimension of 4 gaps, three perpendicular erosion channels occur connecting the rails for every tested θ_0 . 75% of the *Sand Blower* track-wise length has connected sand erosion zones, ensuring the unobstructed transport of the sand over the gauge. This behavior occurs because the humps act as the additional guiding vanes which ensure the wind to enter the gaps perpendicularly, allowing for partially retrieving of the same sand erosion-sedimentation-backward erosion patterns as for the perpendicular wind.

The qualitatively observed drop in averaged performance for yawed winds is quantified in Figures 5.30 (a), (b) and (c) where plots of normalized sedimentation, erosion and backward erosion are plotted, respectively. The averaging is performed

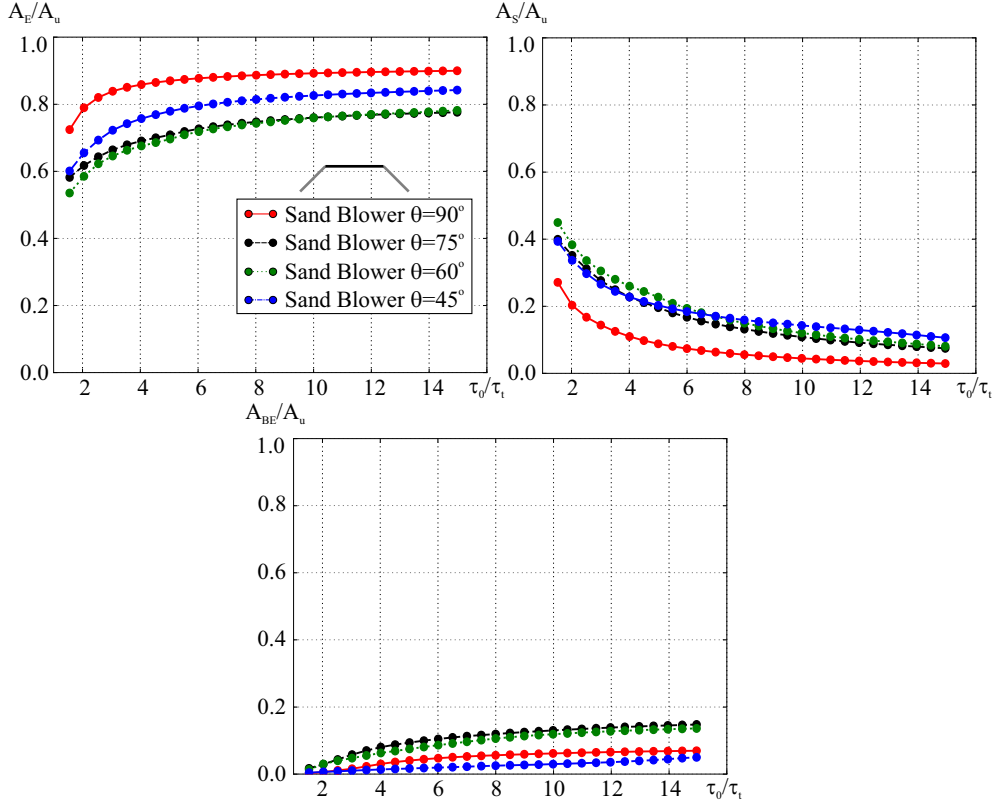


Figure 5.30: Averaged values of local erosion (a), sedimentation (b) and backward erosion (c) normalized areas for *Sand Blower* at different yaw angles.

over the whole track-wise dimension of *Sand Blower*. Compared to the perpendicular wind, there is less erosion present for yawed winds on the expense of increased sedimentation and backward erosion percentage. Interestingly, the averaged erosion closest to the perpendicular winds is observed for the highest skewed winds, $\theta_0 = 45^\circ$. This occurs because of significant reduction of the backward erosion zones compared to the other yawed cases. The averaged backward erosion for $\theta_0 = 45^\circ$ is even lower than what is observed for the perpendicular wind. Conversely, for this case the averaged sand sedimentation is comparatively the same as for $\theta_0 = 60^\circ$ and 75° . Even though the averaged performance metrics are worse compared to the perpendicular wind, they are still much better compared to the unmitigated HS and SS systems.

The significant track-wise variability has to be discussed for the proper assessment of the *Sand Blower* under differently-yawed winds. To see what happens, the individual averaging for each gap is plotted for the three performance metrics in Figures 5.31, 5.32 and 5.33 for $\theta_0 = 75^\circ$, $\theta_0 = 60^\circ$, and $\theta_0 = 45^\circ$, respectively. The results for each gap are complemented with the values of the whole track-wise

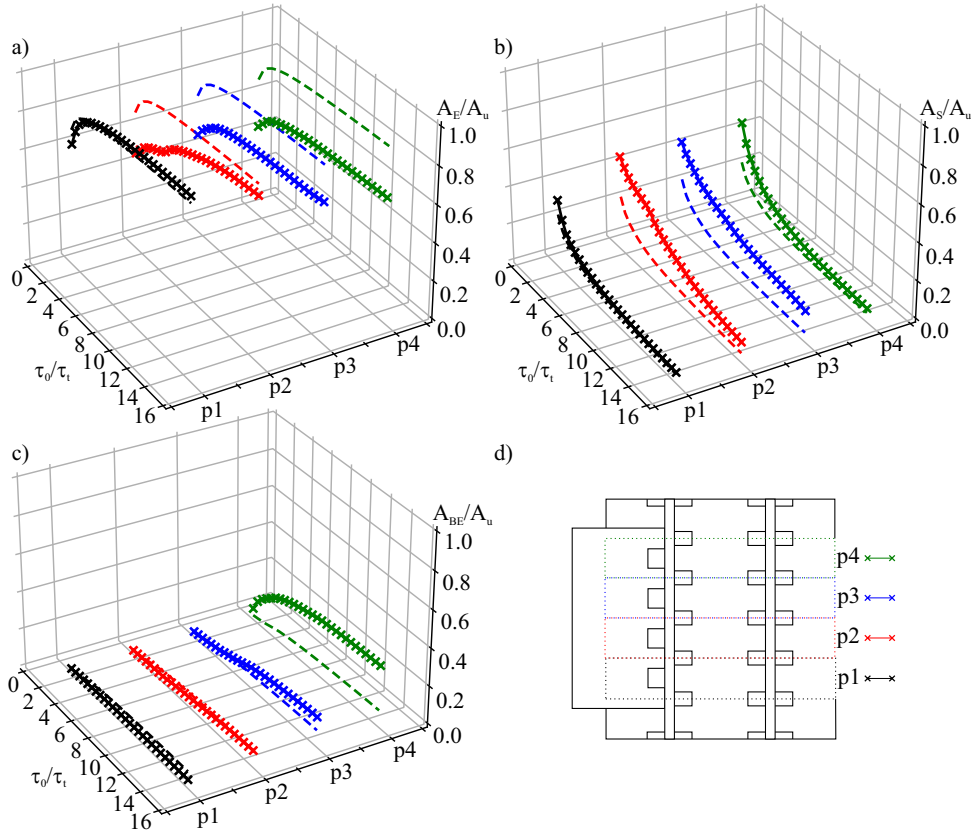


Figure 5.31: Local erosion (a), sedimentation (b) and backward erosion (c) normalized areas for *Sand Blower* at $\theta_0 = 75^\circ$ for a given gap presented in subfigure (d).

average for the perpendicular wind. The gaps are named $p1 - 4$ whose position is defined in Figure 5.31 (d). The same figure is redundantly included in Figures 5.32 and 5.33 to allow easier reading of the results. At $\theta_0 = 75^\circ$ the best performing gap is the gap $p1$. The erosion, sedimentation and backward erosion overlaps with the average computed for the perpendicular wind. At $\theta_0 = 60^\circ$ the best performing gap which overlaps with the average at the perpendicular wind is $p2$. Conversely, at $\theta_0 = 45^\circ$ the gaps $p2$, $p3$ and $p4$ are relatively close to the performance of the perpendicular wind.

In conclusion, *Sand Blower* performs well under wide range of yaw angles. The study explains and quantifies reasons why the relatively worse performance occur when the metrics are averaged over the whole track-wise domain. However, this only means that the track-wise dimensions of *Sand Blower* has to be further investigated and that the precise positioning of the measure is of utmost importance. The fact that at least 25% of L_s performs the same as for the perpendicular wind and the rest

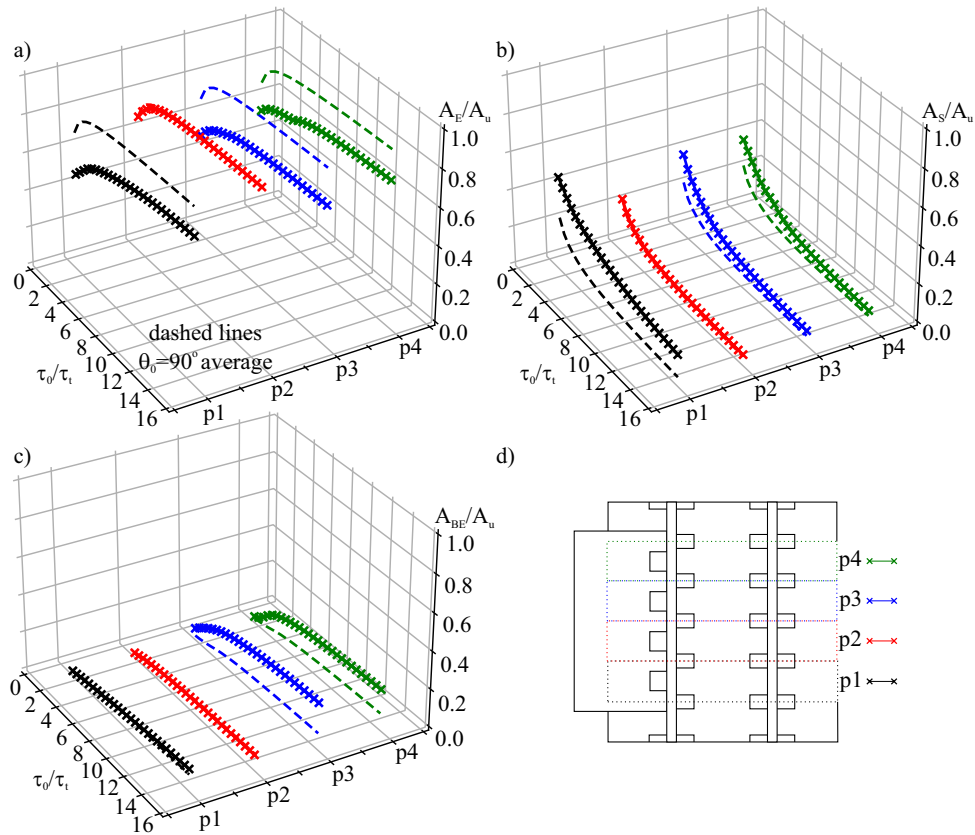


Figure 5.32: Local erosion (a), sedimentation (b) and backward erosion (c) normalized areas for *Sand Blower* at $\theta_0 = 60^\circ$ for a given gap presented in subfigure (d).

75% relatively well with discrepancy up to 20% for erosion, 10% for sedimentation and backward erosion is further encouraging in the perspective of applying *Sand Blower* in the real world desert conditions. Even better performance and less variation is expected for longer L_s .

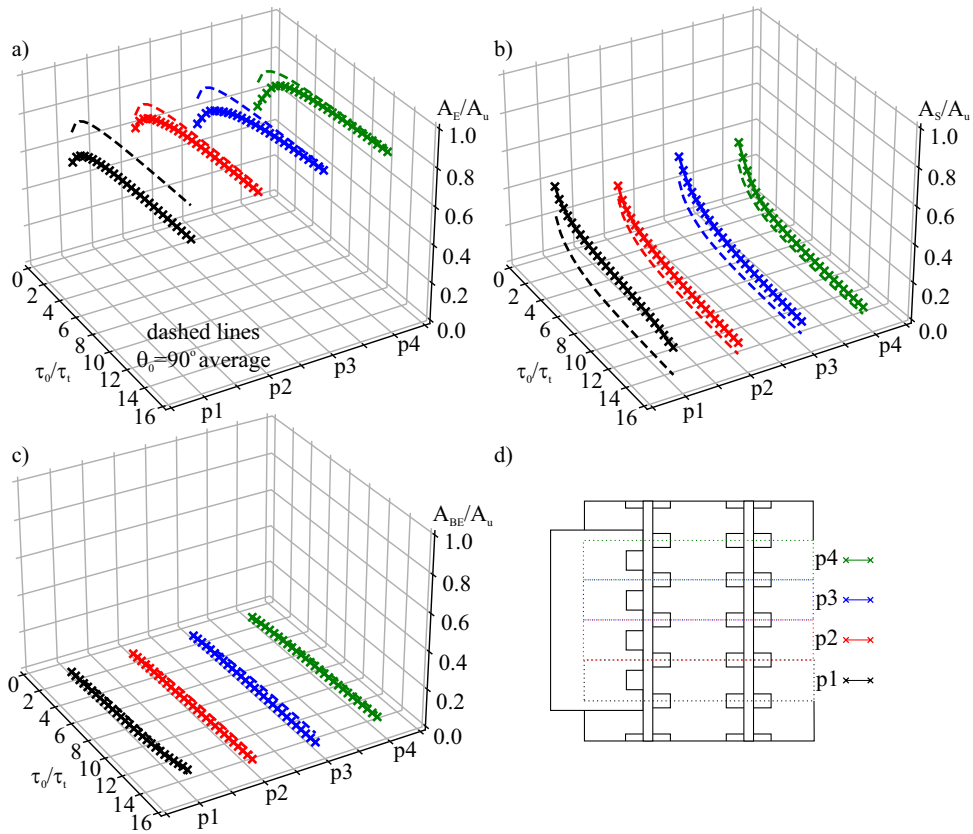


Figure 5.33: Local erosion (a), sedimentation (b) and backward erosion (c) normalized areas for *Sand Blower* at $\theta_0 = 45^\circ$ for a given gap presented in subfigure (d).

Chapter 6

Conclusion

Infrastructure built in deserts and arid areas acts as an obstacle to transported windblown sand and in turn disturbs the equilibrium between sand erosion and sedimentation. Any changes in velocity profiles necessarily leads to changes in sand transport. Therefore, each obstacle creates a local sand sedimentation/erosion pattern around itself. The negative effects of sedimented sand were recognized since the late nineteenth century, and are nowadays the environmental limiting factors that are inherent in safety and serviceability of current and future railway projects.

The research done within the PhD Thesis aims at approaching the problem setting and problem solving of windblown sand sedimentation around railways in rigorous engineering terms grounded on the deep knowledge of the aerodynamic behavior of railways and SMMs. The first step has been done in the form of a state of art review. A wide overview of the existing scientific and technical literature on the topic is provided and intended to: i.) give an updated multidisciplinary map of the evolving state of art to researchers; and ii.) give a structured background to railway owners, designers, general contractors and railway operators in order to properly set up project terms of reference, and most suited design solutions. The overview is given through: i.) addressing windblown sand as an environmental variable action; ii.) the classification of its effects in an original framework based on windblown Sand Limit States; and iii.) the categorization of the SMMs proposed up to now in an innovative Source-Path-Receiver scheme. The innovative classification of SMMs is given according to their relative position to the infrastructure. Such classification in the same time distinguishes the working principles of different mitigation measures. Several significant outlines can be drawn:

- the does not focus on Source SMMs despite their wide use against desertification process at regional scales. Instead, the focus is put on the SMMs whose working principle relies on the local control and modification of the wind and sand flow around the railway;
- a number of Path SMMs are proposed in literature and some of them are

extensively adopted in practice since the same building components are already employed in the production of other types of barriers (e.g. noise or wind barriers). While porous fences are widely studied in literature, publicly available studies about solid barriers are scarce;

- working principle of porous fences involves a significant amount of sand bleed through the unburied fence leading to the contamination of the railway corridor. This makes the maintenance longer and more costly. Conversely, solid barriers comply with the practical requirement of preventing sand accumulation in the railway corridor by keeping high trapping efficiency upwind the solid barrier even at high accumulation levels. From an economic point of view, this requirement is of utmost importance and should be ensured by careful aerodynamic design based on understanding of the barrier aerodynamic behavior;
- Receiver SMMs are built in direct contact with railway superstructure and have to comply with its functional requirements. The Receiver SMMs are not widely employed because its application necessarily involves a global rethinking of the superstructure components (i.e. sleepers, rail, signalling devices) and rolling stock to be adapted to arid environmental conditions. Bearing in mind that these components results form a 150 year long optimization in European and North American countries, the modifications cannot be envisaged in a short time scale. Research and development programs on longer time scale are required.

Besides the few remarkable exceptions, the rigorous quantitative assessment of SMMs performances is still missing in the scientific literature and technical practice. This is due to the inherent multiscale and multiphysics nature of the involved phenomena, the scaling and measurements difficulties in experimental tests and the modelling and numerical difficulties in computational simulations. In the , the attempt is made to solve the issues related to the insufficient transfer of knowledge between the different scientific communities interested in the topic of sand mitigation.

The two following subsections are given in order to separate the outlines of the research done on the improvements of Path and Receiver SMMs, in particular their problem setting, design, performance assessment and optimization.

6.1 Outlines of Path SMMs

The **Chapter 4** discusses aerodynamic shape optimization of solid sand barriers in turbulent atmospheric boundary layer. A specific barrier, *Shield for Sand*, is approached by the two initial design solutions. For each of them, the optimization

is carried out in the wake of extensive sensitivity studies, aimed at understanding the aerodynamic response of the barrier. Indeed, this is required because the response of the goal function to the changes in design variables defines the most suited optimization algorithm.

One-panel deflector is efficiently optimized by the gradient-based approach. The optimal solution dramatically reduces construction costs, but does not improve the aerodynamic performance of the baseline solution. Application of the fast-converging gradient-based algorithm is possible because of the monotonic response of the goal function.

For the two-panel deflector, the introduction of additional variables allows the reduction of construction costs and, in the same time, increase in performance compared to the baseline barrier. Conversely to the one-panel deflector, the response of the goal function is highly non-monotonic and the gradient-based optimization is not a suitable algorithm in search for the optimal solution. Nonetheless, the gradient-based optimization can be adopted to quickly improve the design in vicinity of the initial shape. The search for the optimal family of solutions is performed by adopting genetic algorithm approach. A number of shapes have been found with nearly equivalent minimum value of the goal function. The choice of the final solution among them remains in charge of the designer, in the light of the specific needs of individual projects. The same class of aerodynamic problems can be approached with the same method, i.e. sand sedimentation around high-degree-of-bluffness barriers where abrupt changes in their aerodynamic regime do not take place within the design space.

The final performance assessment is still left to be done. The further assessment can be carried out in different forms, e.g. in the form of full scale field tests in windy and sandy environments, scaled wind tunnel tests with incoming drifting sand, or CWE simulations accounting for the multiphase characteristics of windblown sand. Moreover, the final assessment can be adjusted to individual projects in the form of more general goal function. The form c^n/p^m , where $n \neq m$, enables to account for different relative importance of cost and performance.

6.2 Outlines of Receiver SMMs

The first part of **Chapter 5** contributes to the increase in knowledge about the flow around railway tracks, and the resulting potential sand sedimentation patterns. The study critically compares the aerodynamic behavior and related potential sand sedimentation/erosion patterns for different combinations of railway substructures and track systems usually adopted in arid environments. The reading of the simulated flow field allows to point out the geometrical features of the railway substructure and superstructure with the most significant impact, and to understand the aerodynamic phenomena that induce necessary conditions for sand erosion and

sedimentation. The potential sand sedimentation/erosion patterns depend not only on the flow dimensionless metrics usually employed in aerodynamics, but also on the ratio between the local shear stress and the sand erosion threshold value. Bulk dimensionless metrics of the sedimentation, erosion, and backward erosion allow to synthetically and generally define the performances for different railway systems. In a synthetic design perspective, the most relevant results are outlined:

- low-rise, gentle-sloped substructures are recommended to reduce sand sedimentation around the whole railway, notably downwind;
- large sedimentation and small erosion zones potentially occur around standard ballasted track system. Hence, alternative superstructures are needed in desert regions;
- track systems including humped sleepers/slab are promising solutions to promote sand erosion;
- the flow around humped sleepers/slab is strongly three-dimensional, very sensitive to the shape of the humps, and to the aerodynamic interaction with ballast bed, if present. Accordingly, the erosion performance of humped sleepers/slab are affected by both substructure and superstructure geometry;
- accordingly, the erosion performances of humped sleepers/slab are affected by the above, by the yaw angle and speed of the incoming wind;
- in particular, the track system NC.4 shows the best erosion performances, but its sensitivity to wind yaw angle is critical for long railway lines exposed to track-wise variable wind regimes.

The obtained results offer a well-defined framework for performance assessment, and the obtained results introduce a solid phenomenological background. The adopted RANS-based computational model paves the way to the early stage, conceptual design of retrofitting measures for existing track systems, or of innovative track components for desert railways, possibly integrated by effective Receiver SMM(s) intended to further promote sand erosion on the track surface. More accurate approaches to the performance assessment of track and receiver SMMs are still to be developed to meet the engineering needs for the final assessment of the design solutions. These tools include, among others: i.) more sophisticated, unsteady CWE simulations by LES able to predict sedimentation/erosion intermittency, as recently proposed in [37]; ii.) multiphase wind-sand computational models able to simulate the dynamics of wind, saltating sand and sand accumulation/erosion profile, as reviewed in [156] and applied in [154]; iii.) high-quality, well-documented WT tests fulfilling similarity requirements about railway embankment and track system, barrier, wind and sand saltation layer, to be used for final verification

and CWE validation; and iv.) accurate and robust measurement techniques to be adopted during long-term field trials.

The second part of **Chapter 5** deals with the application of the guiding vanes to the existing railway systems with standard and humped sleepers in order to increase their aerodynamic performance. The computationally-based approach is used as a suitable tool to conceive the idea and to improve it in the form of preliminary design. Different geometric variations have been tested in a semi-heuristic approach and the solution *Sand Blower* is critically assessed. The final remarks can be outlined:

- the unmitigated geometry of standard sleepers does not allow for significant increase in initial relatively high aerodynamic performance;
- the unmitigated geometry of humped sleeper system performs well at the upwind rail, but the mid-gauge flow separation induces undesired backward erosion at the downwind rail trapping the sand in-between the gauge;
- application of *Sand Blower* to humped sleeper system significantly increases the aerodynamic performance in terms of reducing areas of sedimentation and backward erosion, increasing the area of erosion, forcing the flow to be attached on the ballast surface in between the gauge and in turn connecting the erosion patches at upwind and downwind rail.

Such solution is from the industrial point of view not expensive, it is relatively easy to be built and is intended to protect local pointwise railway equipment. The study presents the preliminary design phase of the *Sand Blower* with the future perspective of additional detailed design, optimization and final performance assessment.

Bibliography

- [1] B. M. Adams et al. *Dakota, A Multilevel Parallel Object-Oriented Framework for Design Optimization, Parameter Estimation, Uncertainty Quantification, and Sensitivity Analysis: Version 6.9 User's Manual*. updated: November 13, 2018. Optimization and Uncertainty Quantification Department. July 2014. URL: <https://dakota.sandia.gov/sites/default/files/docs/6.9/Users-6.9.0.pdf>.
- [2] R. M. Al Rumaih. “Conquering the deserts”. In: *Railway Gazette International* 165.8 (2009), pp. 46–48.
- [3] A. A. Alghamdi and N. S. Al-Kahtani. “Sand Control Measures and Sand Drift Fences”. In: *Journal of Performance of Constructed Facilities* 19.4 (2005), pp. 295–299. DOI: [10.1061/\(ASCE\)0887-3828\(2005\)19:4\(295\)](https://doi.org/10.1061/(ASCE)0887-3828(2005)19:4(295)).
- [4] B. Andreotti, P. Claudin, and S. Douady. “Selection of dune shapes and velocities. Part 1: Dynamics of sand, wind and barchans”. In: *The European Physical Journal B - Condensed Matter* 28 (2002), pp. 321–339. DOI: [10.1140/epjb/e2002-00236-4](https://doi.org/10.1140/epjb/e2002-00236-4).
- [5] S. Anurag. “Problems in maintenance of Indian railway in deserts and possible solutions”. In: *UIC workshop on desert railways*. 2008, pp. 67–82.
- [6] A. D. Araújo et al. “Numerical modeling of the wind flow over a transverse dune”. In: *Scientific Reports - Nature* 3.2858 (2013). URL: <https://www.nature.com/articles/srep02858>.
- [7] M. M. Asghari and R. Kargarmoakhar. “Aerodynamic Mitigation and Shape Optimization of Buildings: Review”. In: *Journal of Building Engineering* 6 (2016), pp. 225–235. DOI: [10.1016/j.jobe.2016.01.009](https://doi.org/10.1016/j.jobe.2016.01.009).
- [8] I. Asi et al. “Stabilization of Dune Sand Using Foamed Asphalt”. In: *ASTM Geotechnical Testing Journal* 25.2 (2002), pp. 168–176. DOI: [10.1520/GTJ11360J](https://doi.org/10.1520/GTJ11360J).
- [9] J. Al-Awadhi, A. Al-Helal, and A. Al-Enezi. “Sand drift potential in the desert of Kuwait”. In: *Journal of Arid Environments* 63 (2005), pp. 425–438. DOI: [10.1016/j.jaridenv.2005.03.011](https://doi.org/10.1016/j.jaridenv.2005.03.011).

- [10] R. A. Bagnold. *The Physics of Blown Sand and Desert Dunes*. Methuen, 1941. DOI: [10.1007/978-94-009-5682-7](https://doi.org/10.1007/978-94-009-5682-7).
- [11] W. Baines. “Effects of velocity distribution on wind loads and flow patterns on buildings”. In: *Wind effects on buildings and structures*. 1963.
- [12] C. Baker. “A review of train aerodynamics Part 2 - Applications”. In: *The Aeronautical Journal* 118.1202 (2014), pp. 345–382. DOI: [10.1017/S0001924000009179](https://doi.org/10.1017/S0001924000009179).
- [13] C. Baker. “The determination of topographical exposure factors for railway embankments”. In: *Journal of Wind Engineering and Industrial Aerodynamics* 21.1 (1985), pp. 89–99. DOI: [10.1016/0167-6105\(85\)90035-2](https://doi.org/10.1016/0167-6105(85)90035-2).
- [14] C. Baker. “Train aerodynamic forces and moments from moving model experiments”. In: *Journal of Wind Engineering and Industrial Aerodynamics* 24.3 (1986), pp. 227–251. DOI: [10.1016/0167-6105\(86\)90024-3](https://doi.org/10.1016/0167-6105(86)90024-3).
- [15] C. G. Bates. *Windbreaks: Their Influence and Value*. Tech. rep. US Dept. of Agriculture, Forest Service, 1911.
- [16] B. O. Bauer et al. “Critical Reflections on the Coherent Flow Structures Paradigm in Aeolian Geomorphology”. In: *Coherent Flow Structures at Earths Surface* (2013), pp. 111–134. DOI: [10.1002/9781118527221.ch8](https://doi.org/10.1002/9781118527221.ch8).
- [17] B. O. Bauer et al. “Wind direction and complex sediment transport response across a beach-dune system”. In: *Earth Surface Processes and Landforms* 37.15 (2012), pp. 1661–1677. DOI: [10.1002/esp.3306](https://doi.org/10.1002/esp.3306).
- [18] A. M. Behbahani. “Hazard and risk assessment of wind erosion and dust emissions in Denmark - a simulation and modelling approach”. PhD thesis. University of Basel, Faculty of Science, 2015. URL: <http://edoc.unibas.ch/38575/>.
- [19] R. Bellefontaine et al. “The African Great Green Wall project - What advice can scientists provide?” In: *CSFD Topical issue, French Scientific Committee on Desertification*. Montpellier, 2012.
- [20] P. Y. Belly. *Sand movement by wind*. Tech. rep. US Army - Corps of engineers, 1964.
- [21] B. Ben Salem. “Mulching Technique of Dune Fixation: the layer system”. In: *Sand Dune Stabilization, Shelterbelts and Afforestation in Dry Zones*. Food and Agriculture Organization of the United Nations. Rome, 1985.
- [22] E. Bernardini et al. “The Transport of Sand by Wind”. In: *Journal of Wind Engineering and Industrial Aerodynamics* 144 (2015), pp. 154–164. DOI: [10.1016/j.jweia.2015.03.011](https://doi.org/10.1016/j.jweia.2015.03.011).
- [23] A. Bernardino et al. “Water Channel Study of Flow and Turbulence past a Two Dimensional Array of Obstacles”. In: *Boundary Layer Meteorology* 155.1 (2015), pp. 73–85. DOI: [10.1007/s10546-014-9987-2](https://doi.org/10.1007/s10546-014-9987-2).

- [24] B. Blocken, J. Carmeliet, and T. Stathopoulos. “CFD evaluation of wind speed conditions in passages between parallel buildings - effect of wall-function roughness modifications for the atmospheric boundary layer flow”. In: *Journal of Wind Engineering and Industrial Aerodynamics* 95.9-11 (2007), pp. 941–962. DOI: [10.1016/j.jweia.2007.01.013](https://doi.org/10.1016/j.jweia.2007.01.013).
- [25] S. Bobby et al. “A complete performance-based optimization framework for the design of tall buildings”. In: *11th International Conference on Structural Safety and Reliability*. New York, USA, 2013.
- [26] M. Boccione et al. “Crosswind action on rail vehicles: wind tunnel experimental analyses”. In: *Journal of Wind Engineering and Industrial Aerodynamics* 96.5 (2008), pp. 584–610. DOI: [10.1016/j.jweia.2008.02.030](https://doi.org/10.1016/j.jweia.2008.02.030).
- [27] K. K. Bofah and K. G. Al-Hinai. “Field tests of porous fences in the regime of sand-laden wind”. In: *Journal of Wind Engineering and Industrial Aerodynamics* 23 (1986), pp. 309–319. DOI: [10.1016/0167-6105\(86\)90051-6](https://doi.org/10.1016/0167-6105(86)90051-6).
- [28] N. Boulghobra. “Climatic data and satellite imagery for assessing the aeolian sand deposit and barchan migration, as a major risk sources in the region of In-Salah (Central Algerian Sahara)”. In: *Arabian Journal of Geosciences* 9.450 (2016). DOI: [10.1007/s12517-016-2491-x](https://doi.org/10.1007/s12517-016-2491-x).
- [29] N. Boulghobra, N. Koull, and T. Benzaoui. “Four decades period of climatic data for assessing the aeolian hazard in the region of Touggourt (Low Algerian Sahara)”. In: *Geographia Technica* 11.1 (2016), pp. 13–22. URL: http://www.technicalgeography.org/pdf/1_2016/03_boulghobra.pdf.
- [30] Fattoum L. Boulghobra N. Saifi M. “Sand encroachment in the Saharan Algeria; the not declared disaster - Case study: In-Salah region in the Tidikelt”. In: *Planet@Risk* 3.1 (2015), pp. 72–76. URL: <https://planet-risk.org/index.php/pr/article/view/172>.
- [31] J. W. Boulton et al. “Assessing Risks to Infrastructure Projects in the Middle East from Drifting and Blowing Sand Using WRF”. In: *World Weather Open Science Conference*. 2014. URL: <https://www.wmo.int/pages/prog/arep/wwrp/new/wwosc/documents/2014.08.07WWOSC-Boulton.pdf>.
- [32] Z. Boutanios and H. Jasak. “Two-way coupled Eulerian-Eulerian simulations of drifting snow with viscous treatment of the snow phase”. In: *Journal of Wind Engineering and Industrial Aerodynamics* 169 (2017), pp. 67–76. DOI: [10.1016/j.jweia.2017.07.006](https://doi.org/10.1016/j.jweia.2017.07.006).
- [33] A. J. Bowen. “The prediction of mean wind speeds above simple 2D hill shapes”. In: *Journal of Wind Engineering and Industrial Aerodynamics* 15.1-3 (1983), pp. 259–270. DOI: [10.1016/0167-6105\(83\)90196-4](https://doi.org/10.1016/0167-6105(83)90196-4).

- [34] A. J. Bowen and D. Lindley. “A wind tunnel investigation of the wind speed and turbulence characteristics close to the ground over various escarpment shapes”. In: *Boundary-Layer Meteorology* 12.12 (1977), pp. 259–271. DOI: [10.1007/BF00121466](https://doi.org/10.1007/BF00121466).
- [35] S. Boyd and L. Vandenberghe. *Convex Optimization*. Cambridge University Press, 2004. URL: http://stanford.edu/~boyd/cvxbook/bv_cvxbook.pdf.
- [36] Z. Boyin et al. “A research on wind erosion simulation test on railway embankment in surface layer”. In: *Journal of Wind Engineering and Industrial Aerodynamics* 44.1-3 (1992), pp. 2699–2700. DOI: [10.1016/0167-6105\(92\)90062-F](https://doi.org/10.1016/0167-6105(92)90062-F).
- [37] P. M. Brito et al. “Prediction of erosion intermittency using Large Eddy Simulation”. In: *Geomorphology* 364 (Sept. 2020), p. 107179. DOI: [10.1016/j.geomorph.2020.107179](https://doi.org/10.1016/j.geomorph.2020.107179).
- [38] L. Bruno and D. Fransos. “Sand transverse dune aerodynamic: 3D coherent flow structures from a computational study”. In: *Journal of Wind Engineering and Industrial Aerodynamics* 147 (2015), pp. 291–301. DOI: [10.1016/j.jweia.2015.07.014](https://doi.org/10.1016/j.jweia.2015.07.014).
- [39] L. Bruno, D. Fransos, and A. Lo Giudice. “Solid barriers for windblown sand mitigation: Aerodynamic behavior and conceptual design guidelines”. In: *Journal of Wind Engineering and Industrial Aerodynamics* 173 (2018), pp. 79–90. DOI: [10.1016/j.jweia.2017.12.005](https://doi.org/10.1016/j.jweia.2017.12.005).
- [40] L. Bruno, M. Horvat, and L. Raffaele. “Windblown sand along railway infrastructures: A review of challenges and mitigation measures”. In: *Journal of Wind Engineering and Industrial Aerodynamics* 177 (2018), pp. 340–365. DOI: [10.1016/j.jweia.2018.04.021](https://doi.org/10.1016/j.jweia.2018.04.021).
- [41] L. Bruno, L. Preziosi, and D. Fransos. “A deflecting module for an anti-sand barrier, a barrier thus obtained and a protection method from wind-blown sand. WO 2016/181417 A1”. PCT International Application WO 2016/181417 A1. 2016.
- [42] L. Bruno, L. Preziosi, and D. Fransos. “Saudi Landbridge Railway Project - Sand Mitigation Study - Sand Mitigation Measure Efficiency Final Report”. Internal report to Italferr S.p.a. July 2014.
- [43] L. Bruno, M.V. Salvetti, and F. Ricciardelli. “Benchmark on the Aerodynamics of a Rectangular 5:1 Cylinder: An overview after the first four years of activity”. In: *Journal of Wind Engineering and Industrial Aerodynamics* 126 (2014), pp. 87–106. DOI: [10.1016/j.jweia.2014.01.005](https://doi.org/10.1016/j.jweia.2014.01.005).

- [44] L. Bruno et al. “Shield for Sand: an Innovative Barrier for Windblown Sand Mitigation”. In: *Recent Patents on Engineering* 12.3 (2018), pp. 237–246. DOI: [10.2174/1872212112666180309151818](https://doi.org/10.2174/1872212112666180309151818).
- [45] J. Burman et al. “Assessment of response surface-based optimization techniques for Unsteady flow around bluff bodies”. In: *9th AIAA/ISS- MO Symposium on Multidisciplinary Analysis and Optimization*. Atlanta, Georgia, 2002.
- [46] B. Cabral and L. C. Leedom. “Imaging vector fields using line integral convolution”. In: *SIGGRAPH '93*. New York, USA: ACM Press, 1993, pp. 263–270. DOI: [10.1145/166117.166151](https://doi.org/10.1145/166117.166151).
- [47] I. A. Carrascal et al. “Dynamic behaviour of high-speed rail fastenings in the presence of desert sand”. In: *Construction and Building Materials* 117 (2016), pp. 220–228. DOI: [10.1016/j.conbuildmat.2016.05.023](https://doi.org/10.1016/j.conbuildmat.2016.05.023).
- [48] T. Cebeci and P. Bradshaw. *Momentum transfer in boundary layers*. Wash DC Hemisphere Publ Corp N Y McGraw-Hill Book Co, 1977. URL: <https://www.worldcat.org/title/momentum-transfer-in-boundary-layers/oclc/1036773246>.
- [49] F. Cheli et al. “Wind tunnel tests on train scale models to investigate the effect of infrastructure scenario”. In: *Journal of Wind Engineering and Industrial Aerodynamics* 98.6-7 (2010), pp. 353–362. DOI: [10.1016/j.jweia.2010.01.001](https://doi.org/10.1016/j.jweia.2010.01.001).
- [50] G. Chen et al. “3D numerical simulation of wind flow behind a new porous fence”. In: *Powder Technology* 230 (2012), pp. 118–126. DOI: [10.1016/j.powtec.2012.07.017](https://doi.org/10.1016/j.powtec.2012.07.017).
- [51] J. Cheng and C. Xue. “The sand-damage-prevention engineering system for the railway in the desert region of the Qinghai-Tibet plateau”. In: *Journal of Wind Engineering and Industrial Aerodynamics* 125 (2014), pp. 30–37. DOI: [10.1016/j.jweia.2013.11.016](https://doi.org/10.1016/j.jweia.2013.11.016).
- [52] J. Cheng et al. “Characteristics of the disastrous wind-sand environment along railways in the Gobi area of Xinjiang, China”. In: *Atmospheric Environment* 102 (2015), pp. 344–354. DOI: [10.1016/j.atmosenv.2014.12.018](https://doi.org/10.1016/j.atmosenv.2014.12.018).
- [53] J. Cheng et al. “Disturbance of the inclined inserting-type sand fence to wind-sand flow fields and its sand control characteristics”. In: *Aeolian Research* 21 (2016), pp. 139–150. DOI: [10.1016/j.aeolia.2016.04.008](https://doi.org/10.1016/j.aeolia.2016.04.008).
- [54] J. Cheng et al. “Effect of hanging-type sand fence on characteristics of wind-sand flow fields”. In: *Wind and Structures* 22.5 (2016), pp. 555–571. DOI: [10.12989/was.2016.22.5.555](https://doi.org/10.12989/was.2016.22.5.555).

- [55] J. Cheng et al. “Unloading Characteristics of Sand-drift in Wind-shallow Areas along Railway and the Effect of Sand Removal by Force of Wind”. In: *Scientific Reports* 7.41462 (2017). DOI: [10.1038/srep41462](https://doi.org/10.1038/srep41462).
- [56] H. Choi, W.-P. Jeon, and J. Kim. “Control of Flow Over a Bluff Body”. In: *Annual Review of Fluid Mechanics* 40 (2008), pp. 113–139. DOI: [10.1146/annurev.fluid.39.050905.110149](https://doi.org/10.1146/annurev.fluid.39.050905.110149).
- [57] M. Cid Montoya, S. Hernandez, and F. Nieto. “Shape optimization of streamlined decks of cable-stayed bridges considering aeroelastic and structural constraints”. In: *Journal of Wind Engineering and Industrial Aerodynamics* 177 (2018), pp. 429–455. DOI: [10.1016/j.jweia.2017.12.018](https://doi.org/10.1016/j.jweia.2017.12.018).
- [58] M. Cid Montoya et al. “CFD-based aeroelastic characterization of streamlined bridge deck cross-sections subject to shape modifications using surrogate models”. In: *Journal of Wind Engineering and Industrial Aerodynamics* 177 (2018), pp. 405–428. DOI: [10.1016/j.jweia.2018.01.014](https://doi.org/10.1016/j.jweia.2018.01.014).
- [59] V. Conforti et al. “Proceedings 11th World Congress on Railway Research”. In: *World Weather Open Science Conference*. Milan, 2016.
- [60] W. M. Cornelis and D. Gabriels. “Optimal windbreak design for wind-erosion control”. In: *Journal of Arid Environments* 61.2 (2005), p. 315. DOI: [10.1016/j.jaridenv.2004.10.005](https://doi.org/10.1016/j.jaridenv.2004.10.005).
- [61] H. Davarzani et al. “Study of the effect of wind speed on evaporation from soil through integrated modeling of the atmospheric boundary layer and shallow subsurface”. In: *Water Resources Research* (2014). DOI: [10.1002/2013WR013952](https://doi.org/10.1002/2013WR013952).
- [62] D. M. Deaves. “Computations of wind flow over two-dimensional hills and embankments”. In: *Journal of Wind Engineering and Industrial Aerodynamics* 6.1-2 (1980), pp. 89–111. DOI: [10.1016/0167-6105\(80\)90024-0](https://doi.org/10.1016/0167-6105(80)90024-0).
- [63] A. R. Dehghani-Saniij et al. “Sea spray icing phenomena on marine vessels and offshore structures: Review and formulation”. In: *Ocean Engineering* 132 (2017), pp. 25–39. DOI: [10.1016/j.oceaneng.2017.01.016](https://doi.org/10.1016/j.oceaneng.2017.01.016).
- [64] I. Delgado-Fernandez et al. “Field characterization of three-dimensional lee-side airflow patterns under offshore winds at a beach-dune system”. In: *Journal of Geophysical Research: Earth Surface* 118.2 (2013), pp. 706–721. DOI: [10.1002/jgrf.20036](https://doi.org/10.1002/jgrf.20036).
- [65] C. Demartino and F. Ricciardelli. “Aerodynamics of nominally circular cylinders: A review of experimental results for Civil Engineering applications”. In: *Engineering Structures* 137.15 (2017), pp. 76–114. DOI: [10.1016/j.engstruct.2017.01.023](https://doi.org/10.1016/j.engstruct.2017.01.023).

- [66] B. Diedrichs et al. “Crosswind stability of a high-speed train on a high embankment”. In: *Proceedings of the Institution of Mechanical Engineers, Part F: Journal of Rail and Rapid Transit* 221.2 (2007), pp. 205–225. DOI: [10.1243/0954409JRRT126](https://doi.org/10.1243/0954409JRRT126).
- [67] W. Dierickx, W. M. Cornelis, and D. Gabriels. “Wind Tunnel Study on Rough and Smooth Surface Turbulent Approach Flow and on Inclined Wind-screens”. In: *Biosystems Engineering* 86.2 (2003), pp. 151–166. DOI: [10.1016/S1537-5110\(03\)00120-X](https://doi.org/10.1016/S1537-5110(03)00120-X).
- [68] K Dierks. *Namibia’s Railway System*. Sept. 2004. URL: http://www.klausdierks.com/Namibia_Rail/.
- [69] F. Ding and A. Kareem. “A multi-fidelity shape optimization via surrogate modeling for civil structures”. In: *Journal of Wind Engineering and Industrial Aerodynamics* 178 (2018), pp. 49–56. DOI: [10.1016/j.jweia.2018.04.022](https://doi.org/10.1016/j.jweia.2018.04.022).
- [70] T. Dölçek. “Mechanical Behavior of Polyurethane Stabilized Fouled Ballast (PSFB)”. MA thesis. Geological Engineering at the University of Wisconsin, 2014. URL: http://minds.wisconsin.edu/bitstream/handle/1793/69518/MS_Thesis_Dolcek_Tolga.pdf.
- [71] Z. Dong et al. “A wind tunnel simulation of the mean velocity fields behind upright porous fences”. In: *Agricultural and Forest Meteorology* 146.11 (2007), pp. 82–93. DOI: [10.1016/j.agrformet.2007.05.009](https://doi.org/10.1016/j.agrformet.2007.05.009).
- [72] Z. Dong et al. “Aeolian sand transport: a wind tunnel model”. In: *Sedimentary Geology* 161 (2003), pp. 71–83. DOI: [10.1016/S0037-0738\(03\)00396-2](https://doi.org/10.1016/S0037-0738(03)00396-2).
- [73] Z. Dong et al. “Controlling blown sand along the highway crossing the Taklimakan Desert”. In: *Journal of Arid Environments* 57.3 (2004), pp. 329–344. DOI: [10.1016/j.jaridenv.2002.02.001](https://doi.org/10.1016/j.jaridenv.2002.02.001).
- [74] L. Dumas. *CFD-based optimization in Automotive Aerodynamics, Optimization and Computational Fluid Dynamics*. Springer, 2008.
- [75] A. Ebrahimi and A. K. Keene. “Maintenance Planning of Railway Ballast”. In: *Proceedings of the AREMA Conference*. Minneapolis, 2011.
- [76] A. Elshaer, G. Bitsuamlak, and A. E. Damatty. “Aerodynamic shape optimization for corners of tall buildings using CFD”. In: *14th International Conference on Wind Engineering (ICWE)*. Porto Alegre, Brazil, 2015.
- [77] A. Elshaer, G. Bitsuamlak, and A. El Damatty. “Enhancing wind performance of tall buildings using corner aerodynamic optimization”. In: *Engineering structures* 136 (2017), pp. 133–148. DOI: [10.1016/j.engstruct.2017.01.019](https://doi.org/10.1016/j.engstruct.2017.01.019).

- [78] M. Esmaeili, P. Aela, and A. Hosseini. “Experimental assessment of cyclic behavior of sand-fouled ballast mixed with tire derived aggregates”. In: *Soil Dynamics and Earthquake Engineering* 98 (2017), pp. 1–11. DOI: [10.1016/j.soildyn.2017.03.033](https://doi.org/10.1016/j.soildyn.2017.03.033).
- [79] M. Esmaeili, J. Zakeri, and S. A. Mosayebi. “Effect of sand-fouled ballast on train-induced vibration”. In: *International Journal of Pavement Engineering* 15.7 (2013), pp. 635–644. DOI: [10.1080/10298436.2013.818146](https://doi.org/10.1080/10298436.2013.818146).
- [80] EN 1990 European Committee for Standardization. *Eurocode: Basis of structural design*. Tech. rep. 2002.
- [81] EN 1991-1-2 European Committee for Standardization. *Eurocode 1: Actions on structures - Part 1-2: General actions - Actions on structures exposed to fire*. Tech. rep.
- [82] EN 1991-1-3 European Committee for Standardization. *Eurocode 1: Actions on structures Part 1-3 General actions - Snow Loads*. Tech. rep.
- [83] EN 1991-1-4 European Committee for Standardization. *Eurocode 1: Actions on structures - Part 1-4: General actions - Wind actions*. Tech. rep.
- [84] EN 1991-1-5 European Committee for Standardization. *Eurocode 1: Actions on structures - Part 1-5: General actions - Thermal actions*. Tech. rep.
- [85] EN14067-6 European Committee for Standardization. *Railway Applications - Aerodynamics - Part 6: Requirements and Test Procedures for Cross Wind Assessment*. Tech. rep. 2010.
- [86] M. Faccoli et al. “Effect of desert sand on wear and rolling contact fatigue behaviour of various railway wheel steels”. In: *Wear* 396-397 (2018), pp. 146–161. DOI: [10.1016/j.wear.2017.05.012](https://doi.org/10.1016/j.wear.2017.05.012).
- [87] F. Feldman and D. Nissen. “Alternative testing method for the measurement of ballast fouling: percentage void contamination.” In: *Proceedings of the Conference on Railway Engineering*. Railway Technical Society of Australia. Wollongong, Australia, Oct. 2002, pp. 101–109.
- [88] E. A. Finney. *Snow control on the highways*. Tech. rep. Michigan Engineering Experiment Station Bulletin No. 57, 1934.
- [89] A. I. J. Forrester and A. J. Keane. “Recent advances in surrogate-based optimization”. In: *Progress in Aerospace Sciences* 45 (2009), pp. 50–79. DOI: [10.1016/j.paerosci.2008.11.001](https://doi.org/10.1016/j.paerosci.2008.11.001).
- [90] S.G. Fryberger and G. Dean. “A Study of Global Sand Seas”. In: ed. by McKee E. D. 1979. Chap. Dune forms and wind regime, pp. 137–155.
- [91] K. Futsuhara and M. Mukaidono. “Realization of a fail-safe train wheel sensor using electromagnetic induction”. In: *IEEE Transactions on Instrumentation and Measurement* 38.2 (1989), pp. 421–426.

- [92] G. Al-Gassim. *SAR - North South Railway Challenges*. 2013. URL: <http://fr.slideshare.net/imadhamoud/gassim-al-gassim-sar-environmental-challenges>.
- [93] A. Giannoulis et al. “Wind loading on vertical panels with different permeabilities”. In: *Journal of Wind Engineering and Industrial Aerodynamics* 107-108 (2012), pp. 1–16. DOI: [10.1016/j.jweia.2012.02.014](https://doi.org/10.1016/j.jweia.2012.02.014).
- [94] J. A. Gillies and N. Lancaster. “Large roughness element effects on sand transport, Oceano Dunes, California”. In: *Earth Surface Processes and Landforms* 38 (2013), pp. 785–792. DOI: [10.1002/esp.3317](https://doi.org/10.1002/esp.3317).
- [95] J. A. Gillies, W. G. Nickling, and J. King. “Aeolian sediment transport through large patches of roughness in the atmospheric inertial sublayer”. In: *Journal of Geophysical Research* 111.F02006 (2006). DOI: [10.1029/2005JF000434](https://doi.org/10.1029/2005JF000434).
- [96] J. A. Gillies et al. “Using solid element roughness to control sand movement: Keeler Dunes, Keeler, California”. In: *Aeolian Research* 18 (2015), pp. 35–46. DOI: [10.1016/j.aeolia.2015.05.004](https://doi.org/10.1016/j.aeolia.2015.05.004).
- [97] L. Gomez and R. Mèndez. “Saudis kick up storm over Spanish group’s high-speed desert rail project”. In: *El País* (2015).
- [98] M.C. Good and P.N. Joubert. “The form drag of two-dimensional bluff-plates immersed in turbulent boundary layers”. In: *Journal of Fluid Mechanics* 31.3 (1968), pp. 547–582.
- [99] A. D. Gosman et al. “Multidimensional Modeling of Turbulent Two-Phase Flows in Stirred Vessels”. In: *AIChE Journal* 38.12 (2019), pp. 1946–1956. DOI: [10.1002/aic.690381210](https://doi.org/10.1002/aic.690381210).
- [100] L. Gosselin, M. Tye-Gingras, and M. Mathieu-Potvin. “Review of utilization of genetic algorithms in heat transfer problems”. In: *International Journal of Heat and Mass Transfer* 52.9-10 (2009), pp. 2169–2188. DOI: [10.1016/j.ijheatmasstransfer.2008.11.015](https://doi.org/10.1016/j.ijheatmasstransfer.2008.11.015).
- [101] A. S. Goudie. “Dust storms: Recent developments”. In: *Journal of Environmental Management* 90 (2009), pp. 89–94. DOI: [10.1016/j.jenvman.2008.07.007](https://doi.org/10.1016/j.jenvman.2008.07.007).
- [102] Al-Burhan Group. *Sand removal machine 46-6*. URL: <http://www.alburhangroup.com/products.php>.
- [103] G. Guangyong and M. Peng. “Wind-preventing sand-throwing wall. CN/102002916 B”. CN/102002916 B. 2012.
- [104] Z. Guo et al. “Wind Erosion Induced Soil Degradation in Northern China: Status, Measures and Perspective”. In: *Sustainability* 6.12 (2014), pp. 8951–8966. DOI: [10.3390/su6128951](https://doi.org/10.3390/su6128951).

- [105] A. Haack. “Current safety issues in traffic tunnels”. In: *Tunnelling and Underground Space Technology* 17 (2002), pp. 117–127. DOI: [10.1016/S0886-7798\(02\)00013-5](https://doi.org/10.1016/S0886-7798(02)00013-5).
- [106] M. Heffernan. “Engineering Earth - The Impacts of Megaengineering Projects”. In: ed. by S.D. Brunn. Springer Netherlands, 2010. Chap. Shifting Sands: The Trans-Saharan Railway. DOI: [10.1007/978-90-481-9920-4](https://doi.org/10.1007/978-90-481-9920-4).
- [107] J. C. Henry. “American Railroad on the Arabian Desert”. In: *Popular Mechanics* 97.4 (1952), pp. 107–110.
- [108] M. E. Hereher. “Assessment of sand drift potential along the Nile Valley and Delta using climatic and satellite data”. In: *Applied Geography* 55 (2014), pp. 39–47. DOI: [10.1016/j.apgeog.2014.09.004](https://doi.org/10.1016/j.apgeog.2014.09.004).
- [109] A. P. Hesp and T. A. G. Smyth. “CFD flow dynamics over model scarps and slopes”. In: *Physical Geography* (2019), pp. 1–24. DOI: [10.1080/02723646.2019.1706215](https://doi.org/10.1080/02723646.2019.1706215).
- [110] P. A. Hesp et al. “Flow deflection over a foredune”. In: *Geomorphology* 230.1 (2015), pp. 64–74. DOI: [10.1016/j.geomorph.2014.11.005](https://doi.org/10.1016/j.geomorph.2014.11.005).
- [111] T. Hewitt. “Designing a heavy haul desert railway: lessons learned”. In: *11th International Heavy Haul Conference, (IHHA 2015), Operational Excellence*. Perth, Western Australia, Australia, 21st-24st June 2015, pp. 228–237. URL: <http://railknowledgebank.com/Presto/content/Detail.aspx?ctID=Y3RDb3B5X29mX1RoZXNlcw==&rID=MjgyNw==&ssid=c2NyZWVuSURfMTc2MzM=>.
- [112] R. M. Hicks, E. M. Murman, and G. N. Vanderplaats. *An assessment of airfoil design by numerical optimization*. Tech. rep. NASA Ames Research Center; Moffett Field, CA, United States, 1974.
- [113] S. W. Hong, I. B. Lee, and I. H. Seo. “Modelling and predicting wind velocity patterns for windbreak fence design”. In: *Journal of Wind Engineering and Industrial Aerodynamics* 142 (2015), pp. 53–64. DOI: [10.1016/j.jweia.2015.03.007](https://doi.org/10.1016/j.jweia.2015.03.007).
- [114] M. Horvat, L. Bruno, and S. Khris. “CWE study of wind flow around railways: Effects of embankment and track system on sand sedimentation”. In: *Journal of Wind Engineering and Industrial Aerodynamics* (2020). submitted.
- [115] M. Horvat et al. “Aerodynamic shape optimization of barriers for windblown sand mitigation using CFD analysis”. In: *Journal of Wind Engineering and Industrial Aerodynamics* 197 (2020). DOI: [10.1016/j.jweia.2019.104058](https://doi.org/10.1016/j.jweia.2019.104058).
- [116] S. Hotta and K. Horikawa. “Function of Sand Fence Placed in Front of Embankment”. In: *Coastal Engineering 1990* 2 (1991), pp. 2754–2767. DOI: [10.1061/9780872627765.211](https://doi.org/10.1061/9780872627765.211).

- [117] M. Howard. “The new generation of inductive sensors”. In: *World Pumps* 2013.2 (Feb. 2013), pp. 10–11. DOI: [10.1016/S0262-1762\(13\)70055-5](https://doi.org/10.1016/S0262-1762(13)70055-5).
- [118] B. Indraratna, L. Su, and C. Rujikiatkamjorn. “A new parameter for classification and evaluation of railway ballast fouling”. In: *Canadian Geotechnical Journal* 48.2 (2011), pp. 322–326. DOI: [10.1139/T10-066](https://doi.org/10.1139/T10-066).
- [119] MEED Insight. *Middle East Rail and Metro Projects Report 2014*. Tech. rep. 2014.
- [120] D. Ionescu et al. “Deformation and Degradation Characteristics of Sand-Contaminated Railway Ballast”. In: *Proceedings of the Third International Conference on Railway Technology: Research, Development and Maintenance*. Ed. by J. Pombo. 26. Stirlingshire, UK: Civil-Comp Press, 2016. DOI: [10.4203/ccp.110.26](https://doi.org/10.4203/ccp.110.26).
- [121] I. A. Ishak et al. “Aerodynamic Characteristics Around a Generic Train Moving on Different Embankments under the Influence of Crosswind”. In: *Journal of Advanced Research in Fluid Mechanics and Thermal Sciences* 61.1 (2019), pp. 117–139. DOI: [10.1080/23248378.2018.1424573](https://doi.org/10.1080/23248378.2018.1424573).
- [122] S.p.a. Italferr. *Preliminary Design for Oman National Railway Project - Segment 1 - Oman / UAE border at Al Buraimi - Geotechnical Study: Sand Mitigation Report*. Aug. 2014.
- [123] D. W. T. Jackson et al. “Airflow reversal and alternating corkscrew vortices in foredune wake zones during perpendicular and oblique offshore winds”. In: *Geomorphology* 187.1 (2013), pp. 86–93. DOI: [10.1016/j.geomorph.2012.12.037](https://doi.org/10.1016/j.geomorph.2012.12.037).
- [124] D. W. T. Jackson et al. “Investigation of three-dimensional wind flow behaviour over coastal dune morphology under offshore winds using computational fluid dynamics (CFD) and ultrasonic anemometry”. In: *Earth Surface Processes and Landforms* 36.8 (2011), pp. 1113–1124. DOI: [10.1002/esp.2139](https://doi.org/10.1002/esp.2139).
- [125] H. Jasak. “Error Analysis and Estimation for the Finite Volume Method with Applications to Fluid Flows”. PhD thesis. Imperial College, London, 1996. URL: https://foam-extend.fsb.hr/wp-content/uploads/2016/12/Jasak_PhD_1996.pdf.
- [126] J. W. Johnson, ed. *Federal Inter-Agency Sedimentation Conference*. 970. United States Department of Agriculture Miscellaneous Publication. 1965.
- [127] R. T. Jones. “Effects of sweepback on boundary layer and separation”. In: *NASA Technical Reports, NACA-TR-884* (1947), pp. 487–489. URL: <https://ntrs.nasa.gov/citations/19930091953>.
- [128] N. Junquera. “Shifting sands and 60 million pilgrims: The trials of building an Arabian railway”. In: *El País* (2014).

- [129] Wang K., Jiang J., and Zhang W. “Establishment of Protective System and its Ecological Benefit Along Both Sides of Jing-Tong Railway”. In: *Journal of Desert Research* 9.3 (1989), pp. 1–12.
- [130] K. Karthik et al. “Optimization of bluff bodies for aerodynamic drag and sound reduction using CFD analysis”. In: *Journal of Wind Engineering and Industrial Aerodynamics* 174 (2018), pp. 133–140. DOI: [10.1016/j.jweia.2017.12.029](https://doi.org/10.1016/j.jweia.2017.12.029).
- [131] R. N. Kaul. “Sand dune fixation and afforestation: traditional procedures for dune fixation: the hedge system”. In: *Sand Dune Stabilization, Shelterbelts and Afforestation in Dry Zones*. Food and Agriculture Organization of the United Nations. Rome, 1985.
- [132] A. Keene, T. Edil, and J. Tinjum. “Mitigating Ballast Fouling and Enhancing Rail Freight Capacity”. In: *Technical Repor CFIRE 04-07, National Center for Freight and Infrastructure Research and Education* (Nov. 2012). University of Winsconsin-Madison. URL: http://www.wistrans.org/cfire/documents/FR_CFIRE0407.pdf.
- [133] R.C. Kerr and J. O. Nigra. *Analysis of Aeolian Sand Control*. Arabian American Oil Company, 1951.
- [134] R.C. Kerr and J. O. Nigra. “Eolian Sand Control”. In: *Bulletin of the American Association of Petroleum Geologists* 36.8 (1952), pp. 1541–1573.
- [135] W. Kim and H. Choi. “Effect of the spanwise computational domain size on the flow over a two-dimensional bluff body with spanwise periodic perturbations at low Reynolds number”. In: *Computers and Fluids* 183.15 (2019), pp. 102–106. DOI: [10.1016/j.compfluid.2019.01.006](https://doi.org/10.1016/j.compfluid.2019.01.006).
- [136] J. F. Kok et al. “The physics of wind-blown sand and dust”. In: *Reports on Progress in Physics* 75.10 (2012), p. 106901. DOI: [10.1088/0034-4885/75/10/106901](https://doi.org/10.1088/0034-4885/75/10/106901).
- [137] J. Köllmann. “Railway Operations under Harsh Environmental Conditions – Sand, Dust and Humidity Problems and Technical Solutions / Mitigation Measures”. In: *AHK Workshop Be a Partner of Qatar Rail*. Berlin, 17th April 2013. URL: <http://docplayer.net/22407097-Railway-operations-under-harsh-environmental-conditions.html>.
- [138] T. Kurian and J. H. M. Fransson. “Grid-generated turbulence revisited”. In: *Fluid Dynamics Research* 41.021403 (2009). DOI: [10.1088/0169-5983/41/2/021403](https://doi.org/10.1088/0169-5983/41/2/021403).
- [139] N Lancaster. *Geomorphology of Desert Sand Dunes*. Cambridge, England: Routledge, 1995.
- [140] B. E. Launder and D. B. Spalding. “Mathematical Models of Turbulence”. In: *Academic Press* (1972), p. 169. DOI: [10.1017/S0022112073222048](https://doi.org/10.1017/S0022112073222048).

- [141] B. E. Launder and D. B. Spalding. “The numerical computation of turbulent flows”. In: *Computer Methods in Applied Mechanics and Engineering* 3.2 (1974), pp. 269–289. DOI: [10.1016/0045-7825\(74\)90029-2](https://doi.org/10.1016/0045-7825(74)90029-2).
- [142] S. Lee and H. Kim. “Laboratory measurements of velocity and turbulence field behind porous fences”. In: *Journal of Wind Engineering and Industrial Aerodynamics* 80 (1999), pp. 311–326. DOI: [10.1016/S0167-6105\(98\)00193-7](https://doi.org/10.1016/S0167-6105(98)00193-7).
- [143] C. W. Letchford and J. D. Holmes. “Wind loads on free-standing walls in turbulent boundary layers”. In: *Journal of Wind Engineering and Industrial Aerodynamics* 51 (1994), pp. 1–27.
- [144] B. Li and D. J. Sherman. “Aerodynamics and morphodynamics of sand fences: A review”. In: *Aeolian Research* 17 (2015), pp. 33–48. DOI: [10.1016/j.aeolia.2014.11.005](https://doi.org/10.1016/j.aeolia.2014.11.005).
- [145] Z. Li and X. Zheng. “Review of design optimization methods for turbomachinery aerodynamics”. In: *Progress in Aerospace Sciences* 93 (2017), pp. 1–23. DOI: [10.1016/j.paerosci.2017.05.003](https://doi.org/10.1016/j.paerosci.2017.05.003).
- [146] F. Lianchan. “Railways Built in Deserts and Sand-Prevention in China”. In: *Journal of the China Railway Society* 3 (1984). In Chinese.
- [147] F. Lianchan, L. Jiqing, and D. Yaoquan. “Review on the Prevention of Sand Damages to Railway Line in Desert Areas of China”. In: *Journal of Desert Research* 3 (1994). In Chinese.
- [148] T. Lihui et al. “Characteristics of erosion and deposition of straw checkerboard barriers in alpine sandy land”. In: *Environmental Earth Sciences* 74.1 (2015), pp. 573–584. DOI: [10.1007/s12665-015-4059-6](https://doi.org/10.1007/s12665-015-4059-6).
- [149] I. Lima et al. “Optimal array of sand fences”. In: *Scientific Reports* 7 (2017). DOI: [10.1038/srep45148](https://doi.org/10.1038/srep45148).
- [150] B. Liu et al. “Controlling windblown sand problems by an artificial gravel surface: A case study over the gobi surface of the Mogao Grottoes”. In: *Geomorphology* 134.3-4 (2011), pp. 461–469. DOI: [10.1016/j.geomorph.2011.07.028](https://doi.org/10.1016/j.geomorph.2011.07.028).
- [151] B. Liu et al. “Numerical evaluation of the scale problem on the wind flow of a windbreak”. In: *Scientific Reports* 4 (2014), p. 6619. DOI: [10.1038/srep06619](https://doi.org/10.1038/srep06619).
- [152] B. Liu et al. “Numerical simulation of wind flow over transverse and pyramid dunes”. In: *Journal of Wind Engineering and Industrial Aerodynamics* 99.8 (2011), p. 879. DOI: [10.1016/j.jweia.2011.06.007](https://doi.org/10.1016/j.jweia.2011.06.007).

- [153] Y. Liu. “Establishment and effect of protecting system along the Batou-Lanzhou Railway in the Shapotou Study Area”. In: *Journal of Desert Research* 7.4 (1987). In Chinese with English Abstract, pp. 1–11.
- [154] A. Lo Giudice and L. Preziosi. “A fully Eulerian multiphase model of wind-blown sand coupled with morphodynamic evolution: Erosion, transport, deposition, and avalanching”. In: *Applied Mathematical Modelling* 79 (2020), pp. 68–84. DOI: [10.1016/j.apm.2019.07.060](https://doi.org/10.1016/j.apm.2019.07.060).
- [155] A. Lo Giudice et al. “Modelling Sand Slides by a Mechanics-Based Degenerate Parabolic Equation”. In: *Mathematics and Mechanics of Solid* 24.8 (2018), pp. 2558–2575. DOI: [10.1177/1081286518755230](https://doi.org/10.1177/1081286518755230).
- [156] A. Lo Giudice et al. “Wind-blown particulate transport: A review of computational fluid dynamics models”. In: *Mathematics in Engineering* 1.3 (2019), pp. 508–547. DOI: [10.3934/MINE.2019.3.508](https://doi.org/10.3934/MINE.2019.3.508).
- [157] C. Longjun. “UN Convention to Combat Desertification”. In: *Encyclopedia of Environmental Health* 504-517 (2011).
- [158] R. W. Luebke. “Fencing for controlling accumulation and drifting of snow, sand or other heavier-than-air particles suspended in air currents. US3473786A”. US3473786A. 1967.
- [159] R. Ma et al. “Effectiveness of shelterbelt with a non-uniform density distribution”. In: *Journal of Wind Engineering and Industrial Aerodynamics* 98.12 (2010), pp. 767–771. DOI: [10.1016/j.jweia.2010.07.001](https://doi.org/10.1016/j.jweia.2010.07.001).
- [160] Y. Mack et al. “Multiple surrogates for the shape optimization of bluff body-facilitated mixing”. In: *43rd AIAA Aerospace Sciences Meeting and Exhibit*. Reno, Nevada, 2005.
- [161] J. Mandula, B. Salaiova, and M. Koval’akova. “Prediction of noise from tram traffic in urban units”. In: *Journal of Scientific Papers of Rzeszów University of Technology* 32[180].2 (2000), pp. 237–244. URL: <https://www.infona.pl/resource/bwmeta1.element.baztech-article-BTB2-0047-0097/tab/summary>.
- [162] S. McClure et al. “Shelter effects of porous multi-scale fractal fences”. In: *Journal of Wind Engineering and Industrial Aerodynamics* 163.6-14 (2017). DOI: [10.1016/j.jweia.2017.01.007](https://doi.org/10.1016/j.jweia.2017.01.007).
- [163] W.T. McLaughlin and R.L. Brown. *Controlling Coastal Sand Dunes in the Pacific Northwest*. Tech. rep. US Dept. of Agriculture, 1942.
- [164] R. Méndez. *La arena invade tramos del AVE Medina-La Meca*. 2016. URL: https://www.elconfidencial.com/empresas/2016-03-07/la-arena-invade-tramos-del-ave-a-la-meca-ante-la-paralisis-del-consorcio-espanol_1163269/.

- [165] F. R. Menter. “Two-equation eddy-viscosity turbulence models for engineering applications”. In: *AIAA Journal* 32.8 (1994), pp. 269–289. DOI: [10.2514/3.12149](https://doi.org/10.2514/3.12149).
- [166] F. R. Menter, M. Kuntz, and R. Langtry. “Ten years of industrial experience with the SST turbulence model”. In: *Proceedings of the Fourth International Symposium on Turbulence, Heat and Mass Transfer*. Ed. by K. Hanjalić, Y. Nagano, and J. Tummers. Vol. 4. Turbulence Heat and Mass Transfer Series. Antalya, Turkey: Begell House, Dec. 2003, p. 1208. URL: https://www.researchgate.net/publication/228742295_Ten_years_of_industrial_experience_with_the_SST_turbulence_model.
- [167] P. Merino. “Arabia Saudi: Un reto exigente para la internacionalización de la tecnología española”. In: *Lineas* 80.58-67 (2014). URL: http://www.adif.es/es_ES/comunicacion_y_prensa/doc/UltimoNumero.pdf.
- [168] J. van der Merwe. *T-Track System*. 2013. URL: <http://ttracksaudi.com>.
- [169] G. Michas. “Slab Track Systems for High-Speed Railways”. MA thesis. Stockholm, Sweden: Royal Institute of Technology (KTH), 2012. URL: <https://pdfs.semanticscholar.org/69f8/d0e5d9c8572bad83cfdfae1eb2f00262b20d.pdf>.
- [170] N. J. Middleton and T. Sternberg. “Climate hazards in drylands: A review”. In: *Earth-Science Reviews* 126.48-57 (2013). DOI: [10.1016/j.earscirev.2013.07.008](https://doi.org/10.1016/j.earscirev.2013.07.008).
- [171] D. J. Mitchell et al. “Wind Erosion and Dune Stabilisation in Ningxia, China”. In: *Earth-Science Reviews* (1996). URL: <http://citeseerx.ist.psu.edu/viewdoc/download?doi=10.1.1.550.7819&rep=rep1&type=pdf>.
- [172] D. Mohan and L. Yuanyuan. *Raging sandstorm in Inner Mongolia: Lince was forced to open next day the railway passenger line*. In Chinese. China Radio International. 2010. URL: <http://gb.cri.cn/27824/2010/12/30/5187s3108418.htm>.
- [173] Z. Moyan et al. “Track structure failure caused by sand deposition: Simulation and experimentation”. In: *Aeolian Research* 43 (2020). DOI: [10.1016/j.aeolia.2020.100578](https://doi.org/10.1016/j.aeolia.2020.100578).
- [174] J. Munoz-Paniagua and J. Garcia. “Aerodynamic surrogate-based optimization of the nose shape of a high-speed train for crosswind and passing-by scenarios”. In: *Journal of Wind Engineering and Industrial Aerodynamics* 184 (2019), pp. 139–152. DOI: [10.1016/j.jweia.2018.11.014](https://doi.org/10.1016/j.jweia.2018.11.014).
- [175] F. Naser, C. Baker, and F. Schmid. “A review of railway windblown sand mitigation techniques and a structural analysis of a novel tunneling solution”. In: *International Workshop on Railway Aerodynamics*. University of Birmingham, 2013.

- [176] V. Nathawat and A. Sharda. “Challenges of Track Maintenance in Desert Area - Problems and Remedies”. In: *Permanent Way Bulletin* 32.1 (2005), pp. 1–8.
- [177] J. Nicholson. *The Hejaz Railway*. Stacey International, 2005. DOI: [10.1080/03068370600906481](https://doi.org/10.1080/03068370600906481).
- [178] Y. Noguchi et al. “Numerical and experimental study on the aerodynamic force coefficients of railway vehicles on an embankment in crosswind”. In: *Journal of Wind Engineering and Industrial Aerodynamics* 184 (2019), pp. 90–105. DOI: [10.1016/j.jweia.2018.11.019](https://doi.org/10.1016/j.jweia.2018.11.019).
- [179] T. R. Oke. *Boundary Layer Climates*. Vol. 435. Routledge, 1987. URL: <https://bayanbox.ir/view/6693893538424427706/T.-R.-Oke-Boundary-Layer-Climates-Second-Editio-BookFi.org.pdf>.
- [180] R. Ooka, H. Chen, and S. Kato. “Study on optimum arrangement of trees for design of pleasant outdoor environment using multi-objective genetic algorithm and coupled simulation of convection, radiation and conduction”. In: *Journal of Wind Engineering and Industrial Aerodynamics* 96.10-11 (2008), pp. 1733–1748. DOI: [10.1016/j.jweia.2008.02.039](https://doi.org/10.1016/j.jweia.2008.02.039).
- [181] D. A. Paterson and J. D. Holmes. “Computation of wind flow over topography”. In: *Journal of Wind Engineering and Industrial Aerodynamics* 46-47 (1993), pp. 471–476. DOI: [10.1016/0167-6105\(93\)90314-E](https://doi.org/10.1016/0167-6105(93)90314-E).
- [182] C Paz et al. “Numerical study of the impact of windblown sand particles on a high-speed train”. In: *Journal of Wind Engineering and Industrial Aerodynamics* 145.87-93 (2015). DOI: [10.1016/j.jweia.2015.06.008](https://doi.org/10.1016/j.jweia.2015.06.008).
- [183] M. Pensa, P. Spirito Petrosimo, and G. Spirito Petrosimo. “Barriera Antivento, particolarmente per venti carichi di sabbia. IT1224625”. IT/1224625. 1990.
- [184] J. Pettus Newell. “Sand Guards for Railroad Tracks. US731320”. US/731320. 1903.
- [185] D. A. Phillips. “Analysis of Potential Sand Dune Impacts on Railway Tracks and Methods of Mitigation”. In: *GCC Transport and Railway Conference*. Doha, Qatar, Oct. 2011, pp. 17–19. URL: <http://www.iktissadevents.com/files/events/gtrc/1/presentations/d2-s8-duncan-phillips.pdf>.
- [186] J. S. Plaza, M. L. Barceló, and P. R. de Lema Tapetado. “Sand and Wind: an outline of the study of aeolian action on infrastructure with reference to Haramain High Speed Railway, Makkah–Al-Madinah”. In: *Revista de Obras Públicas* 159.3537 (2012), pp. 7–36. URL: http://ropdigital.ciccp.es/detalle_articulo.php?registro=19202&anio=2012&numero_revista=3537.

- [187] P. Pointner, A. Joerg, and J. Jaiswal. *Definitive guidelines on the use of different rail grades*. Deliverable report D4.1.5GL. EU-Project "Innovative Track Systems" (Innotrack, TIP5-CT-2006-031415), 2009.
- [188] A. K. Pozarlik and J. B. W. Kok. "Numerical Simulation of a Turbulent Flow Over a Backward Facing Step With Heated Wall: Effect of Pulsating Velocity and Oscillating Wall". In: *International Journal of Thermal Sciences* 4.4 (2012). DOI: [10.1115/1.4007278](https://doi.org/10.1115/1.4007278).
- [189] L. Prandtl. On boundary layers in three-dimensional flow. 1946.
- [190] L. Preziosi, D. Fransos, and L. Bruno. "A multiphase first order model for non-equilibrium sand erosion, transport and sedimentation". In: *Applied Mathematics Letters* 45 (2015), pp. 69–75. DOI: [10.1016/j.aml.2015.01.011](https://doi.org/10.1016/j.aml.2015.01.011).
- [191] K. Pye. *Aeolian dust and dust deposits*. Academic Press, 1987.
- [192] K. Pye and H. Tsoar. *Aeolian Sand and Sand Dunes*. Springer, 2009. DOI: [10.1007/978-3-540-85910-9](https://doi.org/10.1007/978-3-540-85910-9).
- [193] J. Qu et al. "Field observations on the protective effect of semi-buried checkerboard sand barriers". In: *Geomorphology* 88.1 (2007), pp. 193–200. DOI: [10.1016/j.geomorph.2006.11.006](https://doi.org/10.1016/j.geomorph.2006.11.006).
- [194] N. V. Queipo et al. "Surrogate-based analysis and optimization". In: *Progress in Aerospace Sciences* 41 (2005), pp. 1–28. DOI: [10.1016/j.paerosci.2005.02.001](https://doi.org/10.1016/j.paerosci.2005.02.001).
- [195] L. Raffaele, L. Bruno, and G. F. Wiggs. "Uncertainty propagation in aeolian processes: From threshold shear velocity to sand transport rate". In: *Geomorphology* 301 (2018), pp. 28–38. DOI: [10.1016/j.geomorph.2017.10.028](https://doi.org/10.1016/j.geomorph.2017.10.028).
- [196] L. Raffaele et al. "Incoming windblown sand drift to civil infrastructures: A probabilistic evaluation". In: *Journal of Wind Engineering and Industrial Aerodynamics* 166 (2017), pp. 37–47. DOI: [10.1016/j.jweia.2017.04.004](https://doi.org/10.1016/j.jweia.2017.04.004).
- [197] L. Raffaele et al. "Windblown sand saltation: A statistical approach to fluid threshold shear velocity". In: *Aeolian Research* 23 (2016), pp. 79–91. DOI: [10.1016/j.aeolia.2016.10.002](https://doi.org/10.1016/j.aeolia.2016.10.002).
- [198] M. A. Rahim. "Behaviour of Drift sand and Method of Dealing with it". In: *Pakistan Engineering Congress*. Vol. 32. 271. 1945.
- [199] J. H. Redding and J. A. Lord. "Designing for the effects of windblown sand along the new Jessah-Riyadh-Dammam expressway". In: *Symposium on Geotechnical Problems in Saudi Arabia*. 1981, pp. 363–395.

- [200] P. J. Richards and S. E. Norris. “Appropriate boundary conditions for computational wind engineering models revisited”. In: *Journal of Wind Engineering and Industrial Aerodynamics* 99.4 (2011), pp. 257–266. DOI: [10.1016/j.jweia.2010.12.008](https://doi.org/10.1016/j.jweia.2010.12.008).
- [201] K. Riessberger. “Heavy Haul in Sand Environment”. In: *IHHA 2015 Conference*. Perth, Australia, June 2015. URL: <https://docplayer.net/144777747-Heavy-haul-in-sand-environment.html>.
- [202] K. Riessberger, E. Guggenberger, and H. Ossberger. “Sleepers having elevated rail fastening as protection against sand coverage”. EP2984230A1. 2016. URL: <https://patents.google.com/patent/EP2984230A1>.
- [203] K. Riessberger and W. Swanepoel. “Specialised Sleepers Combat Sand”. In: *Railway Gazette International* (2005), p. 555. URL: <https://trid.trb.org/view.aspx?id=789500>.
- [204] A.A. Rizvi. “Planning Responses to Aeolian Hazards in Arid Regions”. In: *Journal of King Saud University, Architecture and Planning* 1 (1989), pp. 59–74.
- [205] J. Rodríguez Hernández et al. “Protective barrier for snowstorms, EP2354312A1”. EP2354312A1. 2008.
- [206] M. Saifi, N. Boulghobra, and L. Fattoum. “The Green Dam in Algeria as a tool to combat desertification”. In: *Planet@Risk* 3.1 (2015), pp. 1–4.
- [207] A. Sato and M. Ono. “Snowstorm guard fence structures and jet roofs. US4958806A”. US 4958806 A. 1990. URL: <https://www.google.com/patents/US4958806>.
- [208] R. P. Savage and W. W. Woodhouse. “Creation and stabilization of coastal barrier dunes”. In: *11th International Conference on Coastal Engineering*. London, 1968. DOI: [10.1061/9780872620131.043](https://doi.org/10.1061/9780872620131.043).
- [209] H. Schlichting. *Boundary-layer Theory*. McGraw, H., 1979. DOI: [10.1007/978-3-662-52919-5](https://doi.org/10.1007/978-3-662-52919-5).
- [210] A. Schmidt. *Santera 3000 Technical Sheet*. 2013. URL: <https://www.aebischmidt.com/en/products/street-cleaning/sand-cutter-blower-santera-3000>.
- [211] M. Schober et al. “Wind tunnel investigation of an ICE 3 endcar on three standard ground scenarios”. In: *Journal of Wind Engineering and Industrial Aerodynamics* 98.6-7 (2010), pp. 345–352. DOI: [10.1016/j.jweia.2009.12.004](https://doi.org/10.1016/j.jweia.2009.12.004).
- [212] W. R. Sears. “The Boundary Layer of Yawed Cylinders”. In: *Journal of the Aeronautical Sciences* 15.1 (1948), pp. 49–52. DOI: [10.2514/8.11499](https://doi.org/10.2514/8.11499).

-
- [213] E. T. Selig and J. M. Waters. *Track geotechnology and substructure management*. London: Thomas Telford Services Ltd, 1994.
- [214] Y. Shao. *Physics and Modelling of Wind Erosion*. Springer, 2008. DOI: [10.1007/978-1-4020-8895-7](https://doi.org/10.1007/978-1-4020-8895-7).
- [215] D. J. Sherman and B. Li. “Predicting aeolian sand transport rates: A reevaluation of models”. In: *Aeolian Research* 3 (2012), pp. 371–378. DOI: [10.1016/j.aeolia.2011.06.002](https://doi.org/10.1016/j.aeolia.2011.06.002).
- [216] L. Shi et al. “Three - dimensional Simulation Analysis of Response Law of Windblown Sand Flow around the Railway Culvert”. In: *Aeolian Research* 33.9 (2016), pp. 14–18. URL: https://www.researchgate.net/publication/309769124_Three-dimensional_simulation_analysis_of_response_law_of_wind-blown_sand_flow_around_the_railway_culvert.
- [217] B. Shiau and C. Hsieh. “Wind flow characteristics and Reynolds stress structure around the two-dimensional embankment of trapezoidal shape with different slope gradients”. In: *Journal of Wind Engineering and Industrial Aerodynamics* 90.12-15 (2002), pp. 1645–1656. DOI: [10.1016/S0167-6105\(02\)00276-3](https://doi.org/10.1016/S0167-6105(02)00276-3).
- [218] O. Shuraa. *TerraFirma TF-2000 - Technical Data Sheet*. 2014. URL: <http://www.terrafirma.biz/>.
- [219] D. Simon. *Evolutionary Optimization Algorithms: Biological-Inspired and Population-Based Approaches to Computer Intelligence*. John Wiley and Sons, Ltd, 2013. URL: <https://www.semanticscholar.org/paper/Evolutionary-optimization-algorithms-%3A-and-to-Simon/9abf1effb2092a91c7581f0>
- [220] J. Sinha et al. “Computational Investigation of Control Effectiveness on a Near Transition Open and Closed Axisymmetric Cavity”. In: *Advances in Aerospace Science and Applications* 4.1 (2014), pp. 45–52. URL: https://www.researchgate.net/publication/261988204_Computational_Investigation_of_Control_Effectiveness_on_a_Near_Transition_Open_and_Closed_Axisymmetric_Cavity.
- [221] S. N. Skinner and H. Zare-Behtash. “State-of-the-art in aerodynamic shape optimisation methods”. In: *Applied Soft Computing* 62 (2018), pp. 933–962. DOI: [10.1016/j.asoc.2017.09.030](https://doi.org/10.1016/j.asoc.2017.09.030).
- [222] T.A.G. Smyth. “A review of Computational Fluid Dynamics (CFD) airflow modelling over aeolian landforms”. In: *Aeolian Research* 22 (2016), pp. 153–164. DOI: [10.1016/j.aeolia.2016.07.003](https://doi.org/10.1016/j.aeolia.2016.07.003).
- [223] D. B. Spalding. “A Single Formula for the "Law of the Wall"”. In: *Journal of Applied Mechanics* 28.3 (1961), pp. 455–458. DOI: [10.1115/1.3641728](https://doi.org/10.1115/1.3641728).

- [224] International Organization for Standardization. *ISO 9223 - Corrosion of metal and alloys - Corrosivity of atmospheres - Classification*. 1992.
- [225] C. J. Stigter et al. “Agroforestry solutions to some African wind problems”. In: *Journal of Wind Engineering and Industrial Aerodynamics* 90.10 (2002), pp. 1101–1114. DOI: [10.1016/S0167-6105\(02\)00224-6](https://doi.org/10.1016/S0167-6105(02)00224-6).
- [226] A. S. Stipho. “Aeolian sand hazards and engineering design for desert regions”. In: *Quarterly Journal of Engineering Geology* 25.2 (1992), pp. 83–92. DOI: [10.1144/GSL.QJEG.1992.025.02.02](https://doi.org/10.1144/GSL.QJEG.1992.025.02.02).
- [227] M. Suzuki, K. Tanemoto, and T. Maeda. “Aerodynamic characteristics of train/vehicles under cross winds”. In: *Journal of Wind Engineering and Industrial Aerodynamics* 91.1-2 (2003), pp. 209–218. DOI: [10.1016/S0167-6105\(02\)00346-X](https://doi.org/10.1016/S0167-6105(02)00346-X).
- [228] P. K. Sweby. “High resolution schemes using flux limiters for hyperbolic conservation laws”. In: *SIAM Journal of Numerical Analysis* 21 (1984), pp. 995–1011. URL: <https://www.jstor.org/stable/2156939>.
- [229] M. L. Sweet and G. Kocurek. “An empirical model of aeolian dune lee-face airflow”. In: *Sedimentology* 37.6 (1990), pp. 1023–1038. DOI: [10.1111/j.1365-3091.1990.tb01843.x](https://doi.org/10.1111/j.1365-3091.1990.tb01843.x).
- [230] N. Tennakoon et al. “Assessment of ballast fouling and its implications on track drainage”. In: *11th Australia - New Zealand Conference on Geomechanics: Ground Engineering in a Changing World*. Ed. by G. A. Narsilio, A. Arulrajah, and J. Kodikara. ANZ Geomechanics. 2012, pp. 421–426.
- [231] Terratech. *Railway Sand Drift Abatement*. 2010. URL: <http://www.terratechinfo.com/soil-stabilization-polymer/projects/specialty-applications/railway-sand-drift-abatement>.
- [232] T. Thake. “ERTMS implementation in Saudi Arabia”. In: *International Strategic Rail Forum*. Abu Dhabi, Apr. 2012.
- [233] G. Tomasini, S. Giappino, and R. Corradi. “Experimental investigation of the effects of embankment scenario on railway vehicle aerodynamic coefficients”. In: *Journal of Wind Engineering and Industrial Aerodynamics* 131 (2014), pp. 59–71. DOI: [10.1016/j.jweia.2014.05.004](https://doi.org/10.1016/j.jweia.2014.05.004).
- [234] R. Tresso and D. R. Munoz. “Homogeneous, Isotropic Flow in Grid Generated Turbulence”. In: *Journal of Fluids Engineering* 12256.1 (1999), pp. 51–56. DOI: [10.1115/1.483226](https://doi.org/10.1115/1.483226).
- [235] TSI-HSRST. *Technical specification for interoperability relating to the 'rolling stock' sub-system of the trans-European high-speed rail system, section 4.2.6.3. Crosswind*, pp. 193-195. Tech. rep. Official Journal of the European Union L847132, Directive 2008/232/CE, 2008.

- [236] H. Tsoar, D. G. Blumberg, and Y. Stoler. “Elongation and migration of sand dunes”. In: *Geomorphology* 57 (2004), pp. 293–302. DOI: [10.1016/S0169-555X\(03\)00161-2](https://doi.org/10.1016/S0169-555X(03)00161-2).
- [237] W. R. Tyfour. “Effect of moving sand as a ballast contaminant on rail corrugation: field experience”. In: *International Journal of Environmental Engineering* 6.1 (2014), pp. 15–28. DOI: [10.1504/IJEE.2014.057836](https://doi.org/10.1504/IJEE.2014.057836).
- [238] W. R. Tyfour. “Predicting the Effect of Grinding Corrugated Rail Surface on the Wear Behavior of Pearlitic Rail Steel”. In: *Tribology Letters* 29.3 (2008), pp. 229–234. DOI: [10.1007/s11249-008-9300-y](https://doi.org/10.1007/s11249-008-9300-y).
- [239] UNISIG. *FFFIS for Eurobalise, SUBSET-036 issue 3.0.0, Mandatory Specification, ERTMS*. UNISIG, 2012.
- [240] I. J. Walker and W. G. Nickling. “Dynamics of secondary airflow and sediment transport over and in the lee of transverse dunes”. In: *Progress in Physical Geography* 26.1 (2002), pp. 47–75. DOI: [10.1191/0309133302pp325ra](https://doi.org/10.1191/0309133302pp325ra).
- [241] I. J. Walker et al. “Topographic Steering of Alongshore Airflow over a Vegetated Foredune: Greenwich Dunes, Prince Edward Island, Canada”. In: *Journal of Coastal Research* 22.5 (2006), pp. 1278–1291. DOI: [10.2112/06A-0010.1](https://doi.org/10.2112/06A-0010.1).
- [242] D. M. Wallis. “Freight Train Derails”. In: *Namib Times* (2014). URL: <http://namibtimes.net/freight-train-derails/>.
- [243] T. T. Wang et al. “Numerical simulation of sand load applied on high-speed train in sand environment”. In: *Journal of Central South University* 24 (2017), pp. 442–447. DOI: [10.1007/s11771-017-3446-4](https://doi.org/10.1007/s11771-017-3446-4).
- [244] T. T. Wang et al. “Shelter effect efficacy of sand fences: A comparison of systems in a wind tunnel”. In: *Aeolian Research* 30 (2018), pp. 32–40. DOI: [10.1016/j.aeolia.2017.11.004](https://doi.org/10.1016/j.aeolia.2017.11.004).
- [245] T. T. Wang et al. “The Influence of Wind-Blown Sand on High-Speed Train Aerodynamic Performance”. In: *Proceedings of the Third International Conference on Railway Technology: Research, Development and Maintenance*. Ed. by J. Pombo. Civil-Comp Press, 2016. DOI: [10.4203/ccp.110.51](https://doi.org/10.4203/ccp.110.51).
- [246] X. M. Wang et al. “Has the Three Norths Forest Shelterbelt Program solved the desertification and dust storm problems in arid and semiarid China?” In: *Journal of Arid Environments* 74 (2010), pp. 13–22. DOI: [10.1016/j.jaridenv.2009.08.001](https://doi.org/10.1016/j.jaridenv.2009.08.001).
- [247] X. M. Wang et al. “Shelter effect efficacy of sand fences: A comparison of systems in a wind tunnel”. In: *Journal of Arid Environments* 74 (2010), pp. 13–22. DOI: [10.1016/j.jaridenv.2009.08.001](https://doi.org/10.1016/j.jaridenv.2009.08.001).

- [248] A. Watson. “The control of windblown sand and moving dunes: a review of the methods of sand control in deserts, with observations from Saudi Arabia”. In: *Quarterly Journal of Engineering Geology* 18 (1985), pp. 237–252. DOI: [10.1144/GSL.QJEG.1985.018.03.05](https://doi.org/10.1144/GSL.QJEG.1985.018.03.05).
- [249] H. G. Weller et al. “A tensorial approach to computational continuum mechanics using object-oriented techniques”. In: *Computers in physics* 12.6 (1998), pp. 620–631. DOI: [10.1063/1.168744](https://doi.org/10.1063/1.168744).
- [250] R. Wenty. “The SRM 500 - A high-output sand removal machine for combating sand drifts”. In: *Rail Engineering International* 4 (2017), pp. 9–10.
- [251] J. M. Wild. “The Boundary Layer of Yawed Infinite Wings”. In: *Journal of the Aeronautical Sciences* 16.1 (1949), pp. 41–45. DOI: [10.2514/8.11722](https://doi.org/10.2514/8.11722).
- [252] C. Winchester and C. J. Allen. “Railway Wonders of the World”. In: Amalgamated Press, 1935. Chap. Through Desert and Jungle.
- [253] C. Winchester and C. J. Allen. “Railway Wonders of the World”. In: Amalgamated Press, 1935. Chap. In Northern Africa.
- [254] M. Woldman et al. “Investigating the influence of sand particle properties on abrasive wear behaviour”. In: *Wear* 294-295 (2012), pp. 419–426. DOI: [10.1016/j.jweia.2015.06.008](https://doi.org/10.1016/j.jweia.2015.06.008).
- [255] J. Xiao, Z. Yao, and J. Qu. “Influence of Golmud-Lhasa Section of Qinghai-Tibet Railway on Blown Sand Transport”. In: *Chinese Geographical Science* 25.1 (2015), pp. 39–50. DOI: [10.1007/s11769-014-0722-1](https://doi.org/10.1007/s11769-014-0722-1).
- [256] S. Xie, J. Qu, and Y. Pang. “Dynamic wind differences in the formation of sand hazards at high- and low-altitude railway sections”. In: *Journal of Wind Engineering and Industrial Aerodynamics* 169 (2017), pp. 39–46. DOI: [10.1016/j.jweia.2017.07.003](https://doi.org/10.1016/j.jweia.2017.07.003).
- [257] S. Xie et al. “Formation mechanism and suitable controlling pattern of sand hazards at Honglianghe River section of Qinghai–Tibet Railway”. In: *Natural Hazards* 76.2 (2015), pp. 855–871. DOI: [10.1007/s11069-014-1523-7](https://doi.org/10.1007/s11069-014-1523-7).
- [258] H. B. Xiong et al. “Numerical study on the aerodynamic performance and safe running of high-speed trains in sandstorms”. In: *Journal of Zhejiang University-SCIENCE A* 12 (2011), pp. 971–978. DOI: [10.1631/jzus.A11GT005](https://doi.org/10.1631/jzus.A11GT005).
- [259] L. Xu et al. “Experiment test of wind-sand flow destruction to train tempered glass”. In: *Journal of Central South University (Science and Technology)* 7 (2014), pp. 2489–2495.

- [260] Y. Xu and Y. M. Mustafa. “Using CFD-Based Virtual Sensor Data to Study the Structure of Air Flow behind A Porous Fence”. In: *The Eighth International Conference on Sensor Technologies and Applications*. 2014. URL: https://www.researchgate.net/publication/287310511_Using_CFD-based_virtual_sensor_data_to_study_the_structure_of_air_flow_behind_a_porous_fence.
- [261] Y. Xue, Z. Zhai, and Q. Chen. “Inverse prediction and optimization of flow control conditions for confined spaces using a CFD-based genetic algorithm”. In: *Building and Environment* 64 (2013), pp. 77–84. DOI: [10.1016/j.buildenv.2013.02.017](https://doi.org/10.1016/j.buildenv.2013.02.017).
- [262] H. Yang and C. Shi. “Spatial and temporal variations of aeolian sediment input to the tributaries (the Ten Kongduis) of the upper Yellow River”. In: *Aeolian Research* 30 (2018), pp. 1–10. DOI: [10.1016/j.aeolia.2017.10.002](https://doi.org/10.1016/j.aeolia.2017.10.002).
- [263] Q. G. Yu et al. “Principles of sand dune fixation with straw checkerboard technology and its effects on the environment”. In: *Journal of Arid Environments* 56.3 (2004), pp. 449–464. DOI: [10.1016/S0140-1963\(03\)00066-1](https://doi.org/10.1016/S0140-1963(03)00066-1).
- [264] J. A. Zakeri. “Investigation on railway track maintenance in sandy-dry areas”. In: *Structure and Infrastructure Engineering: Maintenance, Management, Life-Cycle Design and Performance* 8.2 (2012), pp. 135–140. DOI: [10.1080/15732470903384921](https://doi.org/10.1080/15732470903384921).
- [265] J. A. Zakeri and R. Abbasi. “Field investigation of variation of loading pattern of concrete sleeper due to ballast sandy contamination in sandy desert areas”. In: *Journal of Mechanical Science and Technology* 26.12 (2012), pp. 3885–3892. URL: https://www.researchgate.net/publication/257774912_Field_investigation_of_variation_of_loading_pattern_of_concrete_sleeper_due_to_ballast_sandy_contamination_in_sandy_desert_areas.
- [266] J. A. Zakeri, M. Esmaeili, and M. Fathali. “Evaluation of humped slab track performance in desert railways”. In: *Proceedings of the Institution of Mechanical Engineers, Part F: Journal of Rail and Rapid Transit* 225.6 (2011), pp. 566–573. DOI: [10.1177/0954409711403677](https://doi.org/10.1177/0954409711403677).
- [267] J. A. Zakeri and M. Forghani. “Railway Route Design in Desert Areas”. In: *American Journal of Environmental Engineering* 2.2 (2012), pp. 13–18. DOI: [10.5923/j.ajee.20120202.03](https://doi.org/10.5923/j.ajee.20120202.03).
- [268] J. A. Zakeri et al. “Effects of vibration in desert area caused by moving trains”. In: *Journal of Modern Transportation* 20.1 (2012), pp. 16–23. DOI: [10.1007/BF03325772](https://doi.org/10.1007/BF03325772).

- [269] C. L. Zhang et al. “Engineering measures to control windblown sand in Shiquanhe Town, Tibet”. In: *Journal of Wind Engineering and Industrial Aerodynamics* 95 (2007), pp. 53–70. DOI: [10.1016/j.jweia.2006.05.006](https://doi.org/10.1016/j.jweia.2006.05.006).
- [270] J. Zhang, E. Cui, and G. Fu. “Investigation of the flow field and the starting conditions of wind-induced erosion of the railway embankment”. In: *Journal of Wind Engineering and Industrial Aerodynamics* 54-55 (1995), pp. 573–581. DOI: [10.1016/0167-6105\(94\)00073-M](https://doi.org/10.1016/0167-6105(94)00073-M).
- [271] J. Zhang et al. “Detached eddy simulation of flow characteristics around railway embankments and the layout of anemometers”. In: *Journal of Wind Engineering and Industrial Aerodynamics* 193 (2019). DOI: [10.1016/j.jweia.2019.103968](https://doi.org/10.1016/j.jweia.2019.103968).
- [272] K. C. Zhang et al. “Damage by wind-blown sand and its control along Qinghai-Tibet Railway in China”. In: *Aeolian Research* 1.3-4 (2010), pp. 143–146. DOI: [10.1016/j.aeolia.2009.10.001](https://doi.org/10.1016/j.aeolia.2009.10.001).
- [273] N. Zhang, J. H. Kang, and S. J. Lee. “Wind tunnel observation on the effect of a porous wind fence on shelter of saltating sand particles”. In: *Geomorphology* 120 (2010), pp. 224–232. DOI: [10.1016/j.geomorph.2010.03.032](https://doi.org/10.1016/j.geomorph.2010.03.032).
- [274] Z. Zhang, Z. Dong, and S. Chen. “Wind erodibility in eastern Ningxia Province, China”. In: *Environmental Earth Sciences* 68.8 (2013), pp. 2263–2270. DOI: [10.1007/s12665-012-1908-4](https://doi.org/10.1007/s12665-012-1908-4).
- [275] X. Zheng. *Mechanics of Wind-blown Sand Movements*. Springer, 2009. DOI: [10.1007/978-3-540-88254-1](https://doi.org/10.1007/978-3-540-88254-1).

This Ph.D. thesis has been typeset by means of the T_EX-system facilities. The typesetting engine was pdfL^AT_EX. The document class was `toptesi`, by Claudio Beccari, with option `tipotesi=scudo`. This class is available in every up-to-date and complete T_EX-system installation.